AFRL-RZ-WP-TP-2009-2160

THE EFFECT OF VARIABLE GRAVITY ON THE COOLING PERFORMANCE OF A PARTIALLY-CONFINED FC-72 SPRAY

Travis E. Michalak, Kirk L. Yerkes, Scott K. Thomas, and John McQuillen

Electrochemistry and Thermal Sciences Branch
Energy/Power/Thermal Division

JULY 2009

STINFO COPY

AIR FORCE RESEARCH LABORATORY
PROPULSION DIRECTORATE
WRIGHT-PATTERSON AIR FORCE BASE, OH 45433-7251
AIR FORCE MATERIEL COMMAND
UNITED STATES AIR FORCE

REPORT DOCUMENTATION PAGE		*Form Approved* *OMB No. 0704-0188*

The public reporting burden for this collection of information is estimated to average 1 hour per response, including the time for reviewing instructions, searching existing data sources, searching existing data sources, gathering and maintaining the data needed, and completing and reviewing the collection of information. Send comments regarding this burden estimate or any other aspect of this collection of information, including suggestions for reducing this burden, to Department of Defense, Washington Headquarters Services, Directorate for Information Operations and Reports (0704-0188), 1215 Jefferson Davis Highway, Suite 1204, Arlington, VA 22202-4302. Respondents should be aware that notwithstanding any other provision of law, no person shall be subject to any penalty for failing to comply with a collection of information if it does not display a currently valid OMB control number. **PLEASE DO NOT RETURN YOUR FORM TO THE ABOVE ADDRESS**.

1. REPORT DATE *(DD-MM-YY)* July 2009	2. REPORT TYPE Interim	3. DATES COVERED *(From - To)* 14 September 2004 – 5 June 2009
4. TITLE AND SUBTITLE THE EFFECT OF VARIABLE GRAVITY ON THE COOLING PERFORMANCE OF A PARTIALLY-CONFINED FC-72 SPRAY		**5a. CONTRACT NUMBER** IN-HOUSE
		5b. GRANT NUMBER
		5c. PROGRAM ELEMENT NUMBER 62203F
6. AUTHOR(S) Travis E. Michalak and Kirk L. Yerkes (AFRL/RZPS) Scott K. Thomas (Wright State University) John McQuillen (NASA Glenn Research Center)		**5d. PROJECT NUMBER** 3145
		5e. TASK NUMBER 20
		5f. WORK UNIT NUMBER 314520C9
7. PERFORMING ORGANIZATION NAME(S) AND ADDRESS(ES) Electrochemistry and Thermal Sciences Branch (AFRL/RZPS) Energy/Power/Thermal Division Air Force Research Laboratory Propulsion Directorate Wright-Patterson AFB, OH 45433-7251 Air Force Materiel Command United States Air Force	Wright State University Dayton, OH NASA Glenn Research Center Cleveland, OH	8. PERFORMING ORGANIZATION REPORT NUMBER
9. SPONSORING/MONITORING AGENCY NAME(S) AND ADDRESS(ES) Air Force Research Laboratory Propulsion Directorate Wright-Patterson Air Force Base, OH 45433-7251 Air Force Materiel Command United States Air Force		10. SPONSORING/MONITORING AGENCY ACRONYM(S) AFRL/RZPS
		11. SPONSORING/MONITORING AGENCY REPORT NUMBER(S) AFRL-RZ-WP-TP-2009-2160

12. DISTRIBUTION/AVAILABILITY STATEMENT
Approved for public release; distribution unlimited.

13. SUPPLEMENTARY NOTES
PAO Case Number and clearance date: 88 ABW-2009-2202, 26 May 2009.   This document contains no color.

14. ABSTRACT
This thesis discusses the effects of a variable-gravity environment on the performance of a subcooled partially-confined spray. An experiment, consisting of a test chamber, the associated flow loops, and instrumentation, was fabricated and flown on the NASA Reduced-Gravity Testing Platform. This modified KC-135 aircraft followed a parabolic flight path to provide various acceleration levels. The spray chamber contained two opposing nozzles spraying onto Thick Film Resistor (TFR) heaters, which were mounted on insulating glass pedestals. Only the upward facing heater was used during this testing. Thermocouples under the heater in the glass pedestal were used to determine the heater surface temperature. The glass pedestals were surrounded by an annular sump system, which was used to collect and remove the cooling fluid from the test chamber. The fluid used for this testing was FC-72, which is a non-toxic, non-flammable, and non-reactive refrigerant. Due to its dielectric nature, FC-72 was sprayed directly onto the electric thick film heaters. The parametric ranges of this experiment were as follows: Heat flux to the spray, $21.1 \leq q''_{sp} \leq 69.0$ W/cm2; acceleration field, $0.15 \leq a \leq 1.80$ g; coolant volumetric flow rate, $6.18 \leq V \leq 8.94$ ml/s; and coolant subcooling, $23.1 \leq \Delta T_{sc} \leq 31.7$ K. The heat fluxes tested were below the critical heat flux q''_{CHF}. The wall superheat $\Delta T_{sat} = T_s - T_{sat}$ was found to increase with heat input and acceleration, and decrease with subcooling and volumetric flow rate.

15. SUBJECT TERMS
spray cooling, variable gravity, two-phase cooling

16. SECURITY CLASSIFICATION OF:			17. LIMITATION OF ABSTRACT:	18. NUMBER OF PAGES	19a. NAME OF RESPONSIBLE PERSON (Monitor) Travis E. Michalak
a. REPORT Unclassified	**b. ABSTRACT** Unclassified	**c. THIS PAGE** Unclassified	SAR	220	19b. TELEPHONE NUMBER *(Include Area Code)* N/A

Standard Form 298 (Rev. 8-98)
Prescribed by ANSI Std. Z39-18

i

TABLE OF CONTENTS

LIST OF FIGURES

LIST OF TABLES

NOMENCLATURE

a	Acceleration normal to surface, g
A	Heater area, m^2
b	Radius of glass heater post assembly, m
C	Percent dissolved air content by volume, $[V'_{air}/(V'_f+V'_{air})]\times100$
D	Diameter, m
E	Voltage, V
f	Heater conduction loss fraction, $1 - (q''_{sp}/q''_H)$
Fr	Froude number, v^2/aD_d
G	$q'''b^2/((T_{sat}-T_{\infty,wall})k_{htr})$
$G\Delta$	Non-dimensional heat input, $q/(\pi bk_{htr}(T_{sat} - T_{\infty,wall}))$
Ga	Galileo number, $aD_d^3\rho^2/\mu^2$
h	Convective heat transfer coefficient, $W/(m^2\text{-}K)$
H	Layer thickness, m
I	Electrical current, A
k	Thermal conductivity, $W/(m\text{-}K)$
K	k_f/k_{htr}
m	Mass flow rate, kg/s
Nu	Nusselt number, $h_{top}b/k_f$
P	Pressure, N/m^2
q	Power, W
q''	Heat flux, W/cm^2
q'''	Volumetric heat generation, W/m^3
R	Electrical resistance, Ω
T	Temperature, K
v	Droplet velocity, m/s
V	Volumetric flow rate, ml/s

V' Volume, m^3

We   Weber number, $\rho v^2 D_\mathrm{d}/\sigma$

x^* Position variable used in surface temperature formulation, m

Greek symbols

ΔT Temperature difference, K

ΔT_sat Wall superheat, $T_\mathrm{s} - T_\mathrm{sat}$, K

ΔT_sc Fluid subcooling temperature, $T_\mathrm{sat} - T_\mathrm{noz}$, K

θ Non-dimensional temperature, $(T - T_{\infty,\mathrm{wall}})/(T_\mathrm{sat} - T_{\infty,\mathrm{wall}})$

ρ Density, kg/m^3

σ Surface tension, kg/s^2

μ Absolute viscosity, kg/(m-s)

Subscripts

1-φ   Single-phase

2-φ   Two-phase

air   air

b   Point between substrate and heater layers

ch   Chamber

CHF   Critical heat flux

cov   Glass cover layer

d   Droplet

f   Free-stream fluid

H   Heater

htr   Heater layer

int   Heater/pedestal interface

l   Liquid

lf   Lower film

MHF   Minimum heat flux

noz   Nozzle inlet

R   Resistor

s	Surface
sat	Saturation
sc	Subcooling
sen	Sensible heating
sp	Spray
sub	Ceramic substrate layer
t	Point between heater and cover layers
top	Surface of heater
uf	Upper film
v	Vapor
∞,top	Free-stream fluid flowing over heater surface
∞,wall	Free-stream fluid flowing over pedestal wall

1. THE EFFECT OF VARIABLE GRAVITY ON THE COOLING PERFORMANCE OF A PARTIALLY-CONFINED FC-72 SPRAY

1.1. Introduction

The thermal management of high-power, high-flux devices is becoming increasingly difficult. Even with advances in materials and efficiencies, these devices require the dissipation of ever increasing amounts of thermal energy. Many of these devices also have both low thermal mass and tight spatial and temporal isothermality requirements, sometimes less than ±2K. For devices being used for aerospace applications, the systems are additionally required to operate under various acceleration levels. As a result, robust thermal management approaches need to be developed. Spray cooling is a thermal management scheme that has the potential to be a solution to many of these challenges,[1],[2] including the cooling of electronic devices, which often require the removal of high heat fluxes at low surface superheats.[3],[4] However, it is not yet clear what influence variable-gravity environments might have on the behavior of spray cooling systems. Kim[5] stated that gravity can have an effect on the performance of multi-phase thermal management systems, but did not discuss spray cooling. There have been several specialized applications of spray cooling for aerospace applications. For instance, the Space Shuttle Orbiter uses spray evaporators with water and ammonia as the working fluids.[6] This spray system operates in an open-loop configuration, and uses brief pulses of the working fluid, which is nearly completely evaporated.[7] However, for spray cooling to be a viable thermal management technique for widespread aerospace applications, a greater understanding of the behavior of this scheme under variable-gravity conditions needs to be developed, especially using a closed-loop, recirculating system.

In spray cooling, a working fluid is forced through an orifice and atomized into small drops. These drops then impinge on the surface to be cooled and remove large amounts of heat through a combination of single-phase convection and evaporation.[2] Sehmbey et al.[8] identified two types of spray cooling: Pressure atomization and gas-

assisted atomization. In pressure-atomized nozzles, the working fluid is atomized through the pressure drop across the nozzle, whereas with gas-assisted atomization, a high-velocity gas (or vapor) is used to break the working fluid up into droplets. Spray cooling can have many advantages over standard heat spreader/forced air cooling for electronics applications, including improved performance and reduced size and noise.[9] Spray cooling can have advantages over other forms of two-phase cooling as well. Sehmbey et al.[8] suggested that spray cooling heat transfer and q''_{CHF}, the maximum heat transfer obtainable through nucleate boiling, can be ten times higher than values obtained using pool boiling.

Kim[2] discussed heat transfer mechanisms involved in spray cooling, as well as some of the factors that influence the performance of spray cooling, such as surface condition and size, spray pattern and droplet characteristics, working fluid properties, the presence of non-condensable gases, spray inclination, and gravity. Silk et al.[7] also gave an overview of spray cooling research and details on planned future work in variable gravity spray cooling, especially for microgravity applications.

Some of the early efforts into spray cooling found that the characteristics of the spray can have a significant effect on heat transfer performance. The droplets of the spray have to be large enough and move fast enough to reach the surface through any escaping vapor, yet be small enough and move slowly enough that they do not simply bounce off the surface. The amount of excess fluid used should be minimized to keep the liquid film on the surface as thin as possible. This recommendation was due to the fact that the two-phase heat transfer that takes place in spray cooling is optimal when thin-film evaporation occurs, as opposed to the nucleate boiling that takes place in pool boiling.[10],[11] However, it should be noted that Estes and Mudawar[12] found that for sprays with relatively high volumetric fluxes, the boiling curve does not necessarily look like the traditional boiling curve as there was very little change in slope between the single-phase and nucleate boiling regimes. This was attributed to a suppression of nucleate boiling, and the presence of excess fluid, leading to low evaporation efficiency.

Pautsch and Shedd[13] reported that systems that did not use fluid as effectively, and relied more on single-phase cooling, tended to be able to reach higher values of q''_{CHF}. In fact, based on models that were developed from experimental data, it was reported by

Shedd and Pautsch[14] that the heat removal can be primarily attributed to single-phase mechanisms. In contrast, Lin et al.[15] reported that the spray cooling performance could be attributed, in a large part, to nucleate boiling. This conclusion was reached through single-nozzle spray cooling experiments performed with water, methanol, or a combination of water and methanol.

Pais et al.[11] examined the impact of subcooling and flow rate on the performance of spray cooling using air-atomizing nozzles and water. The results showed that a fluid with a larger subcooling, ΔT_{sc}, tends to remove more heat from the surface before the onset of nucleate boiling, while a fluid with a smaller ΔT_{sc} may remove more heat in the region near q''_{CHF}, depending on the spray characteristics. The results also indicated that higher liquid flow rates removed more heat in the region before the onset of nucleate boiling and in the q''_{CHF} region.

Puterbaugh[16] used a test rig similar to that described in Baysinger et al.[17] and Yerkes et al.[18] to test the effect of air dissolved into the working fluid on spray cooling performance. Dissolved air content was measured using a mercury aire-ometer, and was varied between $5\% \leq C \leq 18\%$. It was reported that there was little change in spray cooling heat transfer performance with varying air content for the range of chamber pressures, flow rates, and subcooling levels tested.

Um et al.[19] investigated the effect of heater surface orientation on q''_{CHF} for spray cooling. The various surface orientations are described in Fig. 1.1. Two different air-atomizing nozzles were used to spray water at different liquid flow rates onto a heated surface which could be oriented horizontally facing upward, vertically, or horizontally facing downward. One nozzle had a uniform spray pattern, while the other had a non-uniform spray pattern, with the flow more heavily-concentrated in the center of the pattern. The orientation of the surface showed little effect on q''_{CHF} for the uniform-spray nozzle. There was also little difference noted between the upward- and downward-facing horizontal orientations for the non-uniform spray. However, q''_{CHF} was found to be higher for the vertically-oriented surface than for the horizontally-oriented surface when using the non-uniform spray, and the percentage change in q''_{CHF} was less at higher liquid flow rates.

Lin and Ponnappan[20] reported on the spray cooling performance for an eight-nozzle array spraying on a surface with an area of 2.0 cm^2, using FC-87, FC-72, methanol, and water as the working fluids, at low levels of subcooling (FC-87: $\Delta T_{sc} <$ 0.6°C, FC-72: $\Delta T_{sc} < 3.5$°C, methanol: $2.7 < \Delta T_{sc} < 13.7$°C, water: $3.0 < \Delta T_{sc} < 14.1$°C). It was found that ΔT_{sat} increased with increasing heat flux. Both the heat flux that could be removed at a given ΔT_{sat} and q''_{CHF} increased as volumetric fluxes increased. For the fluorocarbon fluids FC-72 and FC-87, q''_{CHF} was up to 90 W/cm^2. Methanol produced q''_{CHF} of 490 W/cm^2, and for water, q''_{CHF} exceeded the maximum achievable heat flux for this system, which was 500 W/cm^2. The heat transfer coefficient followed a similar trend; water yielded the highest, followed by methanol, and then the fluorocarbon fluids.

Lin et al.[21] reported on the effects of surface orientation on the performance of spray cooling a large area (19.3 cm^2) using a 48-nozzle array. It was reported that both the cooling performance and q''_{CHF} were slightly enhanced for the case of a downward-facing horizontal surface, when compared to a vertical surface. The performance of this setup was also compared to that obtained using the small (2.0 cm^2) area heater from Lin and Ponnappan[20]. The cooling performance of the small-area heater (in an upward-facing horizontal orientation) was more than 30% better than for the vertically-oriented large-area heater.

Lin and Ponnappan[22] also reported on the behavior of large-area spray cooling at different surface orientations. During this effort, an ejector was used to improve the stability of the flow rate by employing the motive flow produced by a gear pump to produce suction at the exit of the condenser, which assisted in ensuring that no vapor was allowed to enter the inlet of the gear pump. The downward-facing horizontal heater had a 5% higher q''_{CHF} than the vertically-oriented heater, and the vertically-oriented heater had a 6% higher q''_{CHF} than the upward-facing horizontal heater.

Rybicki and Mudawar[23] reported on the effects of various parameters including orientation on spray cooling performance. Several correlations were developed in previous works,[12],[24],[25] utilizing upward-facing horizontal surfaces. In this effort, a downward-facing horizontal surface was used with PF-5052 as the working fluid. This new data was found to be described by the same correlations for multiple regions of the boiling curve. Since the same correlations could be applied to all of the data, it was

concluded that the nozzle/surface orientation had little effect on performance, as long as large amounts of liquid were not allowed to build up on the surface in an upward-facing horizontal surface orientation.

Kato et al.[26] examined the effects of both heater orientation (under terrestrial conditions) and acceleration (provided by an aircraft following a parabolic trajectory) on the cooling performance of sprays. Two working fluids were used with the same pressure-atomized nozzle. For water, the spray was found to be uniform, and for CFC-113, the spray was found to be non-uniform. For these experiments, a copper block with a nickel-plated surface was heated to a high temperature, and then cooled down over a period of time consisting of ten parabolas for the flight tests. The flow rate was generated with a pressurized piston/cylinder as opposed to a recirculating closed loop. During the terrestrial heater orientation tests with water, q''_{CHF} was found to be slightly higher for a vertical surface than for an upward-facing horizontal surface. Also, in the transition boiling region (above q''_{CHF}), for a given heat flux, the wall superheat ΔT_{sat} was higher for the vertical surface than for the upward-facing horizontal surface. During parabolic flight testing with CFC-113, q''_{CHF} was found to decrease in reduced gravity, and for a given heat flux, ΔT_{sat} was lower in reduced gravity, especially in the transition region above q''_{CHF}. With water, q''_{CHF} was higher in reduced gravity than in terrestrial or elevated gravity, but for a given heat flux, ΔT_{sat} was again found to be lower in reduced gravity, though this gravity dependence was more pronounced in the region below q''_{CHF} for water. Gravity dependence was not reported for a higher spray volume flux of water.

Sone et al.[27] reported on a continuation of the work by Kato et al.,[26] again using a pressurized piston/cylinder to generate the flow rate. Water and FC-72 were examined, using several different nozzles. Using a transparent Indium Tin Oxide (ITO) heater, the effect of orientation under terrestrial gravity conditions was again studied. For water, heaters oriented both vertically and downward-facing horizontally showed decreased heat transfer when compared to an upward-facing horizontally-oriented heater, while FC-72 sprays did not show an appreciable dependence on heater orientation. Also using this ITO heater, the heat transfer performance of a water spray was shown to be degraded slightly with a reduction in gravity in the region below q''_{CHF}. With this transparent heater, differences were noted between water and FC-72 in the behavior of the impacting

droplets, the liquid film, and the heater surface. The water liquid film was reported to be stagnant, and the thickness seemed to be dependent on gravity or heater orientation. The FC-72 film was more prone to being swept away by impacting droplets, possibly due to significant differences in thermophysical properties such as viscosity and surface tension between water and FC-72.

The results for tests with a copper block heater with a Cr-plated surface were also presented by Sone et al.[27] The heater was heated to a high temperature, and then cooled during the parabolas. For water at low spray volume fluxes, in the region below q''_{CHF} and in the film boiling region above the minimum heat flux point, q''_{MHF}, the heat transfer decreased with a decrease in gravity. For the smallest tested spray volume flux conditions with water in the high ΔT_{sat} region, heat transfer was degraded in reduced gravity. For water with high spray volume fluxes, reducing gravity tended to result in a reduced q''_{CHF}. For FC-72, a spatial variation in gravity dependence was reported. Near the center of the heater, decreasing gravity led to increased q''_{CHF} and enhanced heat transfer in the region below q''_{CHF}, while thermocouples near the edge of the heater showed an opposite effect.

Further experiments were carried out by Yoshida et al.[28] where a copper block heater with a Cr-plated surface and a transparent ITO heater were employed, along with three different nozzles, with water and FC-72. The spray volume fluxes used were small enough that the heater surface was not completely covered by liquid, but remained in a drop-wise evaporation regime, and were again generated using a pressurized piston/cylinder. The copper block heater was used to perform transient cooling tests by heating it up to a high temperature at the beginning of a flight and then cooling it down over a period of ten parabolas. The ITO heater was used to provide steady-state heat transfer results by supplying a set heater power and spraying the surface. Gravity was not observed to have a strong effect on the spray cooling performance in the nucleate boiling regime for either fluid. For water in terrestrial conditions, a downward-facing horizontal heater produced a higher heat flux than an upward-facing horizontal heater. For low spray volume fluxes, q''_{CHF} was not affected by gravity or heater orientation, but q''_{CHF} and heat transfer in the transition boiling region (between q''_{CHF} and the film boiling region) was affected by gravity and heater orientation for higher spray volume fluxes.

6

The strongest effect of gravity and orientation was observed in the q''_{MHF} region and the film boiling region for low We. With a downward-facing heater in both terrestrial and reduced gravity, the heat flux was reduced for these low-We tests.

Golliher et al.[6] used a drop tower located at NASA Glenn Research Center capable of producing 2.2 s of microgravity to study the behavior of a spray striking a flat surface. The experiment was performed with an air-atomized nozzle spraying water onto an aluminum surface, with and without heat input to the surface, and without the use of a recirculating closed loop. Upon striking the surface, the spray was observed to form multiple, separated segments of coalesced liquid, arranged in a repeatable pattern. This has significant implications in the management and removal of any working fluid that is not evaporated during the cooling process. This paper concentrated on the physical behavior of the spray, and did not include information on the cooling performance of the spray system.

Roisman et al.[29] reported on the behavior and splashing of droplets striking a convex surface in microgravity. Three different splash scenarios were identified, and a stability analysis and a non-dimensional analysis were performed to attempt to predict the behavior of these phenomena. Gambaryan-Roisman et al.[30] reported on the behavior of the film produced by the impact of a water spray on a heated convex surface, and the cooling performance of this spray cooling scheme, in normal and reduced-gravity conditions. The flow rates were generated using a pressurized membrane tank, as opposed to a recirculating closed loop. It was found that the film thickness and the shape of the liquid/gas interface were affected by the parameters of the spray. The volumetric flow rate of the water had an impact on the film thickness and the spray cooling performance. The gravity level was found to have an effect on the spray cooling performance, especially for higher water flow rates, and a decrease in spray cooling performance was noted in microgravity.

Rowden et al.[31] described the development of a closed-loop spray system that was designed to mimic an electronics package, and to act as a precursor to future flight test benches for possible testing in microgravity environments. Also presented were the results of modeling efforts examining single bubble growth in a thin liquid film and the behavior of a single droplet of liquid striking a thin film of liquid near a bubble. The

model accounted for the effects of gravity, and the variation in the average Nu = $q''[\sigma/a(\rho_l - \rho_v)]^{1/2}/(\Delta T_{sat}k_l)$ over time was found to be very similar between models using terrestrial gravity and microgravity. From these models, Rowden et al.[31] predicted that experimental data taken in terrestrial gravity may be applicable to microgravity environments. However, Selvam et al.[32] noted that computer modeling of spray cooling is a very complex task, and gave an overview of some of the modeling efforts that have taken place, along with results of the modeling of a vapor bubble growing on a surface. There have been several other modeling efforts described in literature that concentrated mainly on the behavior of individual droplets or vapor bubbles.[33],[34],[35],[36],[37] Cole et al.[38] also presented results of spray cooling modeling, and included both a microscale model to predict behavior of an individual droplet and a macroscale model to predict behavior of a large number of droplets in a spray.

Some of the first research using a closed-loop, recirculating test setup in a variable-gravity environment was accomplished by Baysinger et al.[17] who presented the design and preliminary testing of a variable-gravity spray cooling experiment. The primary purpose of this study was to investigate heat transfer and fluid management issues for a continuous-flow, closed-loop spray cooling system subjected to a variable-gravity environment. Tests were conducted using ITO heaters onboard the NASA KC-135 Reduced-Gravity Research Aircraft, which provided the variable-gravity environment by following a parabolic flight trajectory. This preliminary testing provided much information on the fluid management aspects of variable gravity testing.[39]

Building on the work by Baysinger et al.,[17] Yerkes et al.[18] performed experiments using the same apparatus on the NASA KC-135 with ITO heaters, but with higher heat loads than the previous experiments. For these tests, the parameters ranges reported were: Heat flux, $10.1 \leq q''_{sp} \leq 39.4$ W/cm^2; volumetric flow rate, $5.26 \leq V \leq 10.5$ ml/s; and acceleration, $0.01 \leq a \leq 1.8$ g. During this testing, the temperature difference between the surface and the fluid was found to decrease with decreasing acceleration. However, this testing was primarily in the single-phase (1-φ) region. It was determined that the ITO heaters were prone to failure at high heat loads, even with adequate cooling, due to high current densities in the thin resistive film.

Elston[40] and Elston et al.[41],[42] reported the behavior of a 16-nozzle spray array in variable gravity conditions. The test rig described in Baysinger et al.[17] and Yerkes et al.[18] was modified to test a custom-fabricated 16-nozzle spray array, cooling a TFR heater with an area of 25.4×25.4 mm^2, for the following parametric ranges: Mass flow rate, $0.0131 \leq m \leq 0.0213$ kg/s; subcooling, $1.6 \leq \Delta T_{sc} \leq 18.4$°C; heat flux, $2.9 \leq q''_{sp} \leq 25$ W/cm^2; dissolved air content, $10.1 \leq C \leq 16.8\%$; and acceleration, $0.02 \leq a \leq 2.02$ g. It was found that microgravity conditions provided enhanced spray cooling performance, indicated by a lower ΔT_{sat} for a given heat input, except at high mass flow rates, where the microgravity performance was closer to that of the terrestrial- or elevated-gravity conditions. Higher levels of subcooling tended to provide enhanced performance, and the air content did not significantly affect performance for the range of parameters tested. The qualitative performance of an improved liquid-vapor separator was also discussed.

Shedd[43] described a linear spray array designed to impact a heated surface at an angle to avoid fluid management issues and loss of heat transfer performance due to interactions between multiple spray cones associated with cooling using arrays of spray nozzles. Conrad et al.[44] reported on the use of this type of array in variable-gravity testing. This research concluded that coolant flow rate had the largest effect on spray cooling performance. It was found that reduced-gravity provided slightly increased heat transfer coefficients when compared to elevated-gravity conditions. The linear spray array used for this testing suffered a rupture in one of the seals, which redirected some of the flow away from the heater surface, so the flow rate of fluid on the heater surface may have been somewhat lower that what was reported.

Hunnel et al.[45] reported on initial experiments using a test rig to examine the effect of body forces generated using electrical fields on spray cooling. A single nozzle spraying on heated surfaces consisting of both an ITO and a Thick Film Resistor (TFR) heater mounted on glass pedestals was used to measure the heat transfer performance of spray cooling in several different orientations. The heater pedestal was surrounded by an annular sump system, and several different containment cap configurations were examined. The ITO heater was found to have slightly higher heat transfer performance than the TFR heater, and for the highest flow rate tested, the horizontal spray orientation had slightly better performance than the vertically oriented spray. For lower flow rates,

9

there was not a significant difference reported between the horizontal and vertical orientations. Because of this, the authors determined that a horizontal spray may not be adequate for predicting the behavior of sprays in a reduced gravity environment.

Glaspell[46] continued the work by Hunnel et al.[45] by examining the effect of an electric Kelvin force on the performance of spray cooling. The objective was to provide more control over the fluid management and bubble behavior. Various electrodes, heaters, and fluids were tested, and the temperature difference between the surface and the fluid was reduced by a maximum of 1.91°C by applying an electrode voltage of 23 kV. This corresponded to an increase in the heat transfer coefficient of 5.2%. Kreitzer[47] and Kreitzer et al.[48] also looked at electrical fields to try to enhance spray cooling performance. Instead of examining the electric Kelvin force, this research concentrated on the effect of the Coulomb force through inductively imparting an electrical charge on the droplets before impingement. A heat transfer improvement of up to 17% was reported, along with results for several heaters, fluids, electrodes, and nozzle types. However, variations of 5 to 14% were reported in the results obtained using different nozzles, though it was speculated that this variation may have been due to differences in nozzle alignment.

Coulomb force effects on spray cooling performance were reported by Kuhlman et al.[49] From flow visualization studies, it was determined that the characteristic time scales governing the effects of various parameters were not as short as the average time between droplet impacts. Further work to enhance spray heat transfer performance, potentially for variable-gravity environments, was discussed by Kreitzer et al.[50] In this effort, a voltage was applied to the spray nozzle itself to charge the droplets. It was reported that the spray pattern changed, but the heat transfer performance remained the same. Kreitzer and Kuhlman[51] also reported on the behavior of sprays when a voltage was applied to the nozzle, and presented the results of visualization.

As can be seen in the previous discussion, there is a wide range of results presented in the archival literature for various parameters that affect spray cooling performance. Often times, there were conflicting results presented, sometimes by the same researchers in the same publication. Table 1.1 gives a summary of the major findings of some of the studies that have examined the effects of orientation and variable-

gravity environments on spray cooling behavior. There remains much about the physical phenomena involved in spray cooling that is not well-understood. The objective of the present investigation was to continue the work presented by Baysinger et al.[17] and Yerkes et al.[18] to investigate the effects of variable-gravity on the behavior of a partially-confined, single-nozzle FC-72 spray, which was part of a recirculating closed-loop thermal management system providing cooling for a upward-facing, horizontally-oriented heated surface. FC-72 was chosen as the working fluid because it is non-toxic, non-flammable, non-corrosive and, as a dielectric, it could be sprayed directly on the electrical component to be cooled (in this case, a TFR heater). FC-72 boils at approximately 56°C at atmospheric pressure[52], which allowed the fluid lines to be maintained at reasonable temperatures to avoid burn hazards. Further details on the properties of FC-72 are given in Appendix E. The experiment was again carried out using the NASA KC-135 to impose a variable gravity environment, but the ITO heaters were replaced by TFR heaters, which were capable of handling higher heat fluxes. The behavior of the wall superheat, ΔT_{sat}, was examined by varying the following parameters: Heat flux to the spray, $21.1 \leq q''_{sp} \leq 69.0$ W/cm^2; acceleration field, $0.15 \leq a \leq 1.80$ g; coolant volumetric flow rate, $6.18 \leq V \leq 8.94$ ml/s; and coolant subcooling, $23.1 \leq \Delta T_{sc} \leq 31.7$ K. The heat fluxes tested in this effort were below q''_{CHF}, and the working fluid was nearly saturated with dissolved air, though the air content was not directly measured.

1.2. Experimental Design

The experimental apparatus used in the current research was very similar to that described by Baysinger et al.,[17] Baysinger,[39] and Yerkes et al.[18] The main differences were the addition of the TFR heater, which replaced the ITO heater, the addition of a drain loop to assist in clearing fluid from the chamber, and slight modifications to the working fluid reservoir to improve flow rate stability during variable-gravity operation.

The experimental setup was designed to be essentially self-contained, so that it could be operated aboard the NASA JSC Reduced-Gravity Research Aircraft. A structural and safety analysis was performed to ensure that the setup met the requirements imposed on experiments performed on this aircraft, and a Test Equipment Data Package was developed, following the guidance set out in various NASA documents.[53],[54],[55] A copy of this TEDP is presented in Appendix L. The rig was constructed from T-slotted

aluminum extrusions (80/20, Inc.) mounted onto an aluminum baseplate which provided the primary interface between the test rig and the aircraft. Mounting holes around the perimeter of the baseplate were used to securely bolt the test rig to the mounting points that were provided on the floor of the aircraft.

The experiment consisted of the fluid management and data acquisition systems, a test chamber which housed two opposing spray nozzles, and the heater pedestal assemblies. The entire rig is shown in Fig. 1.2. A high-speed video setup was positioned to provide limited visualization of the spray system in operation.

The spray chamber (Fig. 1.3) was fabricated from standard vacuum components. The test space within the chamber was cylindrical, with a diameter of 14.6 cm and a length of 15.2 cm. The interior walls of the chamber were lined with several layers of mesh screen and steel wool to control the location of the fluid during variable-gravity operation. The outside of the cylindrical wall of the chamber was lined with copper tubing through which water could be pumped to control the temperature, and thus the pressure, inside the chamber. This chamber pressure, P_{ch}, was measured using a pressure transducer (Omega PX303-100A5V), and was used to calculate the saturation temperature within the test chamber. A triaxial linear servo accelerometer (Columbia Research Laboratories Model SA-307HPTX) was mounted on the test chamber to provide acceleration data.

The test rig contained three flow loops: An FC-72 (nozzle) loop, a chamber drain loop, and a water loop (Fig. 1.4). The nozzle loop was used to deliver the working fluid, FC-72, through the spray nozzles and onto the heater surface. The bulk of the FC-72 inventory was stored in the reservoir, which was a custom-made stainless steel vessel with an internal stainless steel vane structure. A pad of copper wool was placed under this vane structure, and the suction line for drawing the working fluid out of the reservoir was placed in this copper wool, near the inside bottom corner of the reservoir. This arrangement was developed as an attempt to hold liquid near the suction line during variable gravity operation using capillary forces. As will be discussed later, this reservoir met with limited success, and fluid management during some of the variable-gravity operation, especially the micro-gravity periods, was unsuccessful. Elston[40] and Elston et al.[42] provided further information on the evolution of the reservoir systems used on this

test rig. The fluid was drawn out of the reservoir through an electrically controlled shut-off valve (Hoke/Simco Controls 7115G4Y with 0172L2 actuator) using a magnetically-coupled gear pump (Tuthill DDS.99PPPV2NN00000) and passed through a 40-micron filter (Swagelock) to prevent clogging of the nozzles.

After the filter, the fluid passed through a flow meter (Sponsler MF90CBPHA4X-V Lo-Flo Series flowmeter with a SP711-3 3-Wire Analog Transmitter), followed by a pressure transducer (Omega PX303-200A5V) and a pressure switch (United Electric 10-B11), which was set to shut down the power to the flow loops and heaters in the event of an over-pressure situation. The fluid then passed to a series of electrically-controlled three-way valves (Hoke/Simco Controls 7673G4Y with 0172L2F actuator). The first valve could be set to either send the fluid to the nozzles in the chamber or, if necessary, bypass the chamber. The next valve was used to select whether the fluid would be sprayed through the top or bottom nozzle. For this set of research, only the nozzle spraying on the upward-facing horizontal heater surface was used. After the three-way valves, the fluid passed through a preheater, which consisted of a length of copper tubing wrapped with a heater tape and insulation, controlled by a PID temperature controller. This was used to control the temperature of the fluid entering the nozzle. After the preheaters, the fluid was sprayed through the nozzle and onto the heater surface inside the chamber. The nozzle used in this testing was the same as that described by Baysinger et al.[17] and Yerkes et al.[18] The fluid was collected in the sump structure and removed from the chamber.

Once it left the chamber, the fluid passed through a shut-off valve (Hoke/Simco Controls 7115G4Y with 0172L2 actuator), and into a series of three liquid/air heat exchangers (Lytron 6110G1SB with MX2A3, 028316 Fans). These heat exchangers condensed and subcooled the working fluid so that there was less chance of vapor being passed through the pumps or into the reservoir. The working fluid then passed through a pressure transducer (Omega PX303-100A5V), a magnetically-coupled gear pump (Tuthill DDS1.3PPPV2NN00000), another pressure transducer (Omega PX303-200A5V), and finally another 40-micron filter (Swagelock), before being returned to the reservoir. The two pumps were arranged in this configuration to provide a push/pull effect on the chamber to attempt to provide better control of the fluid spray and

inventory. Type E thermocouples (0.16 cm diameter) were placed at strategic locations around the flow loop and in the test chamber to monitor temperatures.

A second loop was used for draining the chamber, if the sumps were unable to remove sufficient fluid during the variable-gravity operation. A fitting was installed near the bottom of the front face-plate of the chamber. If the chamber began to fill with excess working fluid, the drain loop would remove the fluid directly from the chamber to attempt to keep the chamber fluid level below the heater surface, and to maintain adequate flow of liquid back to the reservoir.

The water loop was used to control the temperature and pressure inside the chamber. The temperature of the water that was circulated through the coil around the chamber was not actively controlled. The water stayed near the ambient temperature and cooled the walls of the chamber, so that vapor that contacted the walls would condense back to liquid for removal from the chamber.

The heater used was similar to the heater/pedestal assembly described by Yerkes et al.[18] with a TFR heater instead of an ITO heater. Representative photographs of a pedestal and TFR heater are given in Fig. 1.5. The light-colored regions on the sides of the darker-colored heater in Fig. 1.5(b) are the regions of the conductive epoxy that was used to connect the copper leads to the heater to provide power to the heater. The heater had an area of $A = (1.18 \pm 0.0127) \times (1.18 \pm 0.0127)$ cm^2. The cylindrical pedestals consisted of several layers. The first three layers comprised the TFR heater and were investigated by Glaspell.[46] Table 1.2 summarizes the sizes and thermal conductivities of the heater layers, and Fig. 1.6 presents a schematic to clarify the heater geometry. This schematic includes the heat rates and a qualitative representation of the temperature profile expected through the heater.

The heater layers rested on two thin, stacked wafers of glass which were each 0.001 m thick. The glass layers sat on top of a glass pedestal, which supported and insulated the heater, in an attempt to minimize heat loss through the heater support. A small Type E thermocouple (0.0254 cm diameter) was embedded between the heater substrate and the first glass layer to measure the interface temperature, T_{int}. The surface temperature could not be measured directly without interfering with the behavior of the spray, so T_s was calculated from T_{int} utilizing a one-dimensional conduction model. As

the layers that composed the heater geometry for the TFR were very similar to those presented by Elston[40], Puterbaugh[16], Glaspell[46], and Kreitzer[47], the T_s calculation is similar to that presented by those researchers. The details of this calculation are presented in Appendix A. and the resulting expression for T_s is

$$T_s = T_{int} + \frac{q}{A}\left[\frac{H_{sub}}{k_{sub}}f + \frac{H_{htr}}{k_{htr}}\left(f - \frac{1}{2}\right) + \frac{H_{cov}}{k_{cov}}(f - 1)\right] \tag{1.1}$$

Six 0.0254 cm diameter thermocouples were also embedded between the glass layers, as shown by Yerkes et al.[18] The results of Baysinger et al.,[17] based on a comparison of a transient analytical calculation to experimental data, estimated a heat loss down a polycarbonate pedestal to be approximately $f = 1\%$. Baysinger[39] compared several different numerical solutions to estimate f, and determined the range to be $1 \leq f \leq 2.5\%$. Yerkes el al.[18] compared numerical solutions to an analytical solution, and verified this range for f. The results of Baysinger[39] and Yerkes et al.[18] suggest a slightly higher loss down the pedestal than the original estimate from Baysinger et al.[17] Since the majority of the data presented by Yerkes et al.[18] can be seen to be contained within $f = 1.5 \pm 0.5\%$, this value is used as the percentage of heat lost down the pedestal for the present configuration, which had a very similar geometry to that examined previously. A temperature limit/alarm switch module (Love Controls Model 1290 Dual Alarm) was used to limit the heater temperature to protect the heater from over-temperature conditions ($T_{int} \leq 100°C$).

The pedestal was surrounded by an annular sump structure fitted with a containment cap, as shown schematically in Fig. 1.7(a)[18], with the cap shown exploded from the rest of the sump for clarity. This structure served both as fluid containment and as a means of removing the fluid from the chamber. The nozzle was positioned just outside the opening in the top of the cap. A photograph of the nozzle placement over the cap is shown in Fig. 1.7(b). During operation, some of the liquid bounced off the surface of the heater. The cap was able to direct the majority of this fluid back down into the annular region formed by the walls of the sump and the sides of the heater pedestal, so that it would not float around in the large volume of the test chamber during variable gravity operation. However, it can be seen in Fig. 1.7(b) that the fluid tended to stick to any surface that it contacted, and there was some surface tension flow around the nozzles.

This behavior is similar to that reported by Baysinger et al.[17] The gap formed between the cap and the nozzle would allow any vapor that was generated on the heater surface to escape into the test chamber, where it could condense on the chamber walls. The slots machined into the top of the sump allowed liquid to enter the sump from the test chamber. These slots also allowed fluid to enter the test chamber from the sump, if the sump annulus became too full, so that the heater surface would not become flooded. This configuration prevented the entire region around and above the heater from being completely filled with liquid, as would be the case in a fully-confined spray system. However, it could allow some of the fluid to bounce back onto the heater surface from the walls of the sump and cap, so it is not a fully-unconfined system. Therefore, this configuration is referred to as partially-confined.

Two type E thermocouples (0.16 cm diameter) were positioned inside the sump annulus to monitor the temperature of the fluid that exited the heater. One thermocouple, measuring the upper film temperature, T_{uf}, was placed just off the surface of the heater, and a second, measuring the lower film temperature, T_{lf}, was about 1.2 cm down from the upper film temperature, near the side of the glass pedestal. The nozzle inlet temperature, T_{noz}, was also measured using the same type of thermocouple.

The thermocouples in and around the pedestal in the test chamber were all referenced through a dry-well ice point (HART Scientific 9101) to improve the stability and accuracy of the temperature readings. Additionally, these thermocouples were calibrated using an oil bath/RTD calibration setup (Hart Scientific model 5628 RTD with a model 1502A Readout). Details of this calibration are presented in Appendix C.

The heater power was measured using two different voltage measurements, as shown schematically in Fig. 1.8. The first was across the heater film itself, E_H, as close to the heater as possible to minimize voltage error from the heater leads. The second voltage measurement, E_R, was measured across a precision resistor, which had a nominal resistance of $R_p = 0.1\ \Omega$ at 25°C. The heater power is given by

$$q = E_H * \frac{E_R}{R_P} \tag{1.2}$$

The data presented here consisted of three flights of about forty parabolas each. Each parabola provided approximately 35 s of elevated gravity, at approximately $a = 1.8$

16

g, followed by about 25 s of reduced gravity. The level of the acceleration for the reduced-gravity portion of the parabola was set by the pilots flying the aircraft, depending on the flight trajectory followed. The data being taken was observed to come to steady-state within approximately 5 s, so the 25-s reduced gravity period was sufficient to collect steady-state values.

Data were routed through a data acquisition system (Agilent 34970A Data Acquisition/Switch Unit with Agilent 34901A Multiplexer modules) to a laptop computer. The scan setup for this data acquisition is shown in Appendix B. An analysis was carried out to estimate the uncertainties associated with the computed values. First, the uncertainties in the measured values were identified and quantified. The uncertainty values presented in Table 1.3 are the fixed uncertainties associated with the accuracy and calibration of the measuring devices. To determine the uncertainty in the measured values, the device uncertainty was then added to the confidence interval for each averaged measurement, as described by Montgomery and Runger.[56] The uncertainties in the calculated values could then be determined by propagating these measurement uncertainties through the method outlined by Fox and McDonald.[57] Details of these uncertainty estimate calculations are given in Appendix G. and Appendix H.

The fluid loop was filled prior to the first flight, and some air was allowed to bleed back into the system, so that the air content of the FC-72 was nearly saturated. Running the experiment with air dissolved in the FC-72 allowed for the system pressure to be close to ambient, which increased the saturation temperature in the chamber and allowed for modifications or repairs to the rig without fully pumping down the system. The air content was not measured for the present research.

1.3. Results and Discussion

The objective of this experiment was to determine the behavior of the wall superheat in a thermal management system utilizing spray cooling with a single nozzle in a recirculating closed loop when subjected to a variable-gravity environment. The dependence of ΔT_{sat} on heat flux, acceleration, subcooling, and flow rate was examined.

To determine the behavior of this system, the flow rate and level of subcooling were set at the beginning of each flight, and were maintained for the duration of that flight. The heater power and the acceleration were then varied. Each heat input level

was maintained for at least one full parabola, which consisted of an elevated-gravity period followed by a reduced-gravity period. The acceleration (gravity) reported here is the portion of the total acceleration vector which is normal to the upward-facing, horizontally-oriented heater surface. After at least one full parabola, the heater input power was adjusted to the next desired level, generally in steps of 2 to 5 W. In some cases, the same heater power was maintained for several parabolas. Data was collected by the data acquisition system approximately once every 2 s. During the flights, hand-written data sheets were created to record the nominal settings for the various parameters that were maintained, and to note any observed anomalies or events, and these data sheets are shown in Appendix F. In order to reduce the data, the transient portions, such as those during major acceleration transients, heater power adjustments, or adverse flow rate excursions, were discarded. The remaining data was divided between ten separate cases, each of which consisted of a constant flow rate, subcooling, and acceleration. The only parameter that was varied in each case was the heat input. Table 1.4 shows the ten various cases that were identified for these three flights. Table 1.5 presents a comprehensive listing of the reduced average data points that are presented in the plots in this section.

Two representative samples of transient data collected during the flight tests are shown in Fig. 1.9, which demonstrate how quickly the system was able to reach steady state after a change to one of the parameters, even during the short duration of each parabola. A sample of data collected during Flight 1, consisting of three parabolas, is presented in Fig. 1.9(a). Initially, the heat flux was $q''_{sp} = 26.8$ W/cm^2 and the acceleration was $a = 1.8$ g. At time A, the pilot initiated a reduced gravity event, which rapidly reduced the acceleration to $a = 0.15$ g. Immediately following this acceleration drop, the interface temperature decreased by 2°C to $T_{int} = 57.7$°C. At time B, the acceleration returned to $a = 1.8$ g, and the interface temperature returned to $T_{int} = 59.7$°C. During this acceleration event, both the volumetric flow rate and the heater power remained relatively constant. At time C, another reduced-gravity event was initiated, in which the acceleration was reduced to $a = 0.01$ g. Once again, though the flow rate and heater power initially remained relatively constant, the interface temperature dropped from $T_{int} = 59.4$ to 57.2°C. However, at time D, the volumetric flow rate dropped

18

dramatically from $V = 8.6$ to 1.5 ml/s, due to the pump drawing vapor from the reservoir as the liquid floated away from the suction tube, despite the vane structure and copper wool. This caused a predictable spike in the interface temperature as the flow of cooling fluid to the heater was interrupted. Between times D and E, the flow rate was still fluctuating, and the heat flux was increased to $q''_{sp} = 28.4$ W/cm^2. After time E, the flow rate became relatively stable at $V = 8.8$ ml/s and the interface temperature stabilized at approximately $T_{int} = 61°C$, which was consistent with the higher heat input. At the onset of the next reduced-gravity event, the temperature dropped to $T_{int} = 59°C$ before climbing rapidly following another interruption in the coolant flow rate.

A similar sample of data, collected during Flight 2 and consisting of three parabolas and a nominal 1-g turn, is presented in Fig. 1.9(b). At the beginning of this period, the heat flux was $q''_{sp} = 33.7$ W/cm^2, the acceleration was $a = 1.8$ g, and the interface temperature was $T_{int} = 70°C$. At time F, the acceleration dropped to $a = 0.35$ g. Though the flow rate did not change, the interface temperature dropped to $T_{int} = 65°C$. At time G, the acceleration returned to $a = 1.8$ g and the interface temperature climbed to $T_{int} = 70°C$. After this elevated-gravity period, the aircraft entered a turn period, during which the acceleration was $a = 1.0$ g. Over the course of this turn, V and q''_{sp} remained stable while the acceleration experienced several small variations. The variation in T_{int} was observed to closely follow the changes in acceleration. At H, the aircraft entered another elevated gravity period, with an acceleration change to $a = 1.8$ g and a corresponding step in interface temperature to $T_{int} = 70°C$. From I to J, the acceleration dropped to $a = 0.36$ g, with a temperature drop to $T_{int} = 65°C$. After this reduced-gravity period, the temperature returned to $T_{int} = 70°C$. At time K, the aircraft entered a reduced-gravity period, with $a = 0.01$ g. As in Fig. 1.9(a), the transition to microgravity was followed by a drastic reduction in the flow rate. However, after the acceleration was reduced the interface temperature was observed to drop to $T_{int} = 65.6°C$ before increasing rapidly following the flow rate interruption.

At acceleration levels in the microgravity range ($a \leq 0.01$ g), the flow rate was consistently interrupted due to vapor being pulled into the pump from the reservoir. While this prevented the collection of steady state data at this acceleration, it became clear from the behavior of T_{int} that a disruption of coolant flow, even for a short period of

time, can have potentially catastrophic consequences for a thermal management system employing spray cooling. Care must be taken when considering such systems to ensure that the design is robust enough to maintain the required coolant flow rates throughout the entire anticipated operating range.

The wall superheat versus acceleration for the three different flights are portrayed in Fig. 1.10. Within each flight, the flow rate and subcooling remained constant, and each individual curve represents a different heat flux. It should be noted that these curves are plotted as linear fits to the data to aid in labeling and visualization. The intent is not to imply that there is actually a linear relationship between acceleration and wall superheat. All of the curves plotted in Fig. 1.10 were observed to have a slightly positive slope, which indicated that, for a given heat flux, decreasing acceleration corresponded to decreasing wall superheat. One possible explanation for the decrease in surface temperature in reduced gravity is that, when the body forces are reduced, the impacting droplets can more easily splash the heated liquid film up and away from the surface, so that cooler incoming fluid can more easily approach the surface, providing increased cooling. A similar explanation could be applied to boiling in this system, where the bubbles can more easily eject heated fluid from the heater surface when bursting at the liquid film surface. This trend is similar to that reported by Elston[40], Yerkes et al.[18], Conrad et al.[44], and some of the results from Sone et al.[27] Other portions of Sone et al.[27], Yoshida et al.[28], and Gambaryan-Roisman et al.[30] noted an increase in temperature subsequent to a decrease in acceleration.

The effect of subcooling on the wall superheat is illustrated in Fig. 1.11. In each of these plots, the acceleration and flow rate were held constant. All of the curves had a negative slope, which indicated that for a given heat load the wall superheat was lower when there were higher values of coolant subcooling. This trend of reduced wall superheat at higher subcooling was important, since at a given heat flux the wall superheat of the device being cooled would be smaller, which is advantageous for many thermal management applications. A similar trend was reported by Elston,[40] Pais et al.,[11] and Chow et al.[3] The slopes in Fig. 1.11(a) ($a = 1.05$ g) were slightly steeper than those in Fig. 1.11(b) ($a = 1.78$ g). In each plot, the slopes remained relatively constant throughout the range of heat fluxes plotted, which was contrary to the results observed by

Elston.[40] For that multiple-nozzle experiment, the subcooling dependence was noted throughout the reduced-gravity testing. In the elevated gravity testing, the wall superheat was found to decrease with increasing subcooling for low heat fluxes, but at higher heat fluxes, there was no noted effect of subcooling on the wall superheat. This change in behavior at different heat fluxes was not observed in the current experiment, which utilized a single nozzle.

The effect of volumetric flow rate on wall superheat for three different acceleration levels can be seen in Fig. 1.12. In each plot, the subcooling and acceleration levels were kept constant. For each heat flux, the wall superheat was lower for higher values of volumetric flow rate, which was true for all acceleration levels. This trend was similar to that observed by Yoshida et al.,[28] Hunnel et al.,[45] Kim,[2] Mudawar,[1] and Estes and Mudawar.[12] Elston[40] noted this trend, but also reported that at higher flow rates in reduced gravity, there was a drastic increase in wall superheat, which was not noted in the present research. This altered behavior was likely due to the differences between single-nozzle and multiple-nozzle spray systems. There are no spray-to-spray interactions in a single-nozzle system, so fluid may be less likely to build up on the surface at higher flow rates. Again, the observed trend was important, as it suggested that, as flow rate increases, the wall superheat will be lower for a given heat flux, which can be beneficial to a thermal management application.

The heat transfer characteristics for Flight 1, consisting of cases 1, 2, and 3, are given in Fig. 1.13(a). The left-hand side of the plot (with the q''_{sp} axis, $\Delta T_{sat} = T_s - T_{sat} = 0$, as the separating line) is referred to as the single-phase region, and the right-hand side of the plot is the two-phase region. For visualization purposes, linear trend lines were applied to the single-phase and two-phase regions separately. For all three cases, ΔT_{sat} increased with increasing heat flux, as would be expected. For case 1, with the lowest value of a, ΔT_{sat} for any given heat flux is less than that for case 2 or case 3. From Table 1.4, the difference between the average values of V for these three cases was less than 3%, and the average ΔT_{sc} and T_{sat} values varied by only approximately 2%. Therefore, the acceleration was the primary difference between the parameters for cases 1, 2, and 3. There was a ΔT_{sat} shift between cases 2 and 3, but it was not as pronounced as that between cases 1 and 2. Thus, between $a = 0.15$ and 1.04 g, there was a large change in

ΔT_{sat} for a given q''_{sp}, but for between $a = 1.04$ and 1.78 g there was much less change. Another point to note is that, for Fig. 1.13(a), there was very little difference between the slopes of the single-phase and two-phase regions. The data appeared to be nearly linear throughout the entire range of ΔT_{sat}. Also, the curves were relatively parallel. There may have been a small amount of divergence as ΔT_{sat} increased, but the slopes of these cases were approximately the same. This is similar to the results presented by Estes and Mudawar[12], where there was not a significant change in slope reported through the nucleate boiling region. Therefore, it is difficult to determine how much of the heat transfer for the present research was due to single-phase convection, and how much was due to boiling.

The data for Flight 2, consisting of cases 4, 5, and 6, are shown in Fig. 1.13(b). In this data set, there were small differences between the slopes of the single-phase and two-phase regions. When viewing the three different cases plotted in Fig. 1.13(b), there was again a shift in the ΔT_{sat} data. For case 4 ($a = 0.37$ g), the wall superheat was smaller at a given heat flux when compared to case 5 ($a = 1.06$ g). However, there was also a larger shift towards increasing ΔT_{sat} between case 5 and case 6 ($a = 1.78$ g) than was noted between cases 2 and 3 in Fig. 1.13(a).

The data from Flight 3 (cases 7, 8, 9, and 10), are presented in Fig. 1.13(c). There was little difference between the two reduced-acceleration cases (case 7, at $a = 0.16$ g, and case 8, at $a = 0.36$ g). There was also little difference between case 9 ($a = 1.06$ g) and case 10 ($a = 1.76$ g). There was still a downward shift in the ΔT_{sat} values for the reduced-gravity cases (7 and 8) compared to the higher-gravity cases (9 and 10). In Fig. 1.13(c), however, there was some divergence between cases 7 and 8 and cases 9 and 10 as q''_{sp} increased, which indicated that the change in the wall superheat with a change in acceleration is greater at higher heat fluxes.

It can be noted that T_{sat} was higher for Flights 2 and 3, when compared to Flight 1. After Flight 1, it was determined that the fill level was not high enough, and the rig was topped off with additional fluid. During the topping-off process, additional air was allowed into the system, which further increased the air content and system pressure, which increased T_{sat} (and therefore ΔT_{sc}) for the remaining two flights.

Comparing Fig. 1.13(a) (Flight 1) to Fig. 1.13(b) (Flight 2) can give insight into the effect of subcooling on the acceleration dependency for the system behavior. There is a negligible difference in the flow rates between these two flights. In contrast, the subcooling temperature for Flight 1 was $\Delta T_{sc} = 25.0$ K, while the subcooling temperature for Flight 2 was $\Delta T_{sc} = 30.2$ K. In Fig. 1.13(b), the curves are spread further apart than in Fig. 1.13(a), as mentioned above. In other words, the reduction in the wall superheat due to a reduction in acceleration was more pronounced in the cases with the higher subcooling. This suggested a coupled effect of acceleration and subcooling temperature for this spray cooling system configuration, with higher subcooling levels actually enhancing the observed behavior dependence on acceleration. A similar coupling of acceleration and subcooling was reported by Elston,[40] who noted that, as the subcooling temperature decreased, the q''_{sp} versus ΔT_{sat} curves for the reduced-gravity cases approach those of the elevated-gravity cases.

Comparing Fig. 1.13(b) and Fig. 1.13(c), the effect that varying the flow rate has on the spray cooling behavior can be examined. In both, there is a good deal of separation between the low-acceleration curves and the higher-acceleration curves. However, in Fig. 1.13(b), the curves are all relatively parallel, especially in the two-phase region. On Fig. 1.13(c), it appears that the lines are much less parallel, especially on the two-phase half of the curve. This means that, in Flight 3, there was a higher heat transfer coefficient in the lower accelerations, since the slope of these curves is an indication of the convective/boiling heat transfer coefficient. One explanation for this is that the higher flow rate may tend to mask some of the dependence of the heat transfer coefficient on acceleration in the two-phase region. In all three parts of Fig. 1.13, the slope in the single-phase region was slightly higher for the lower accelerations, which would explain why there was such a temperature difference between the lower-acceleration curves and the higher-acceleration curves. It was only in Fig. 1.13(c), with the lower flow rate, that this larger slope carried over into the two-phase region.

In the open literature, researchers have presented heat flux versus surface temperature, heat flux versus $T_s - T_{noz}$ or $T_s - T_f$, or in non-dimensional terms. These alternative treatments are shown in Fig. 1.14, for the data collected during Flight 1, with Fig. 1.14(a) utilizing the non-dimensional values suggested by Yerkes et al.[18] The

curves and trends all look very similar to those in Fig. 1.13(a), and in this case, very little additional insight can be gained from these methods of showing the data. Therefore, though the extent to which the heat transfer is influenced by boiling is unknown, the two-phase convention of using $\Delta T_{sat} = T_s - T_{sat}$ will be followed. Additional plots showing these and other alternate presentations are given in Appendix I. - Appendix K.

1.4. Conclusions

The effects of variable gravity on the cooling performance of a partially-confined FC-72 spray, in a closed-loop, recirculating system, were investigated. A test rig, which had been previously flown on NASA's reduced gravity testing aircraft, was modified to test higher heat fluxes and provide a more stable flow rate. Along with the effects of acceleration, the effects of varying the coolant subcooling and the volumetric flow rate were also investigated. The wall superheat was observed to increase as the heat input was increased, as expected.

For a given heat flux, the wall superheat tended to be lower in the reduced-gravity cases than in the normal- or elevated-gravity cases. The normal-gravity cases tended to have a slightly lower wall superheat than the elevated-gravity cases for a given heat flux. This trend was observed throughout the range of heat fluxes, subcoolings, and flow rates examined. The behavior of the spray cooling performance near the critical heat flux was not investigated, and the amount of air dissolved in the working fluid was not measured.

For a given heat flux, the wall superheat tended to be lower for cases with a higher subcooling. This trend was observed throughout the range of heat fluxes tested. Higher values of coolant subcooling were also observed to enhance the effect of acceleration, as the difference in wall superheat in reduced gravity was more significant for the cases with higher subcooling.

For a given heat flux, the wall superheat tended to be lower for cases with a higher volumetric flow rate. This trend was observed throughout the range of heat fluxes tested. It was also determined that care must be exercised when designing thermal management systems for variable-gravity environments, to ensure that the system design is robust enough to maintain the necessary flow rates throughout the anticipated operating range, as even a momentary interruption in coolant flow can lead to a dramatic and potentially catastrophic temperature increase in the device being cooled.
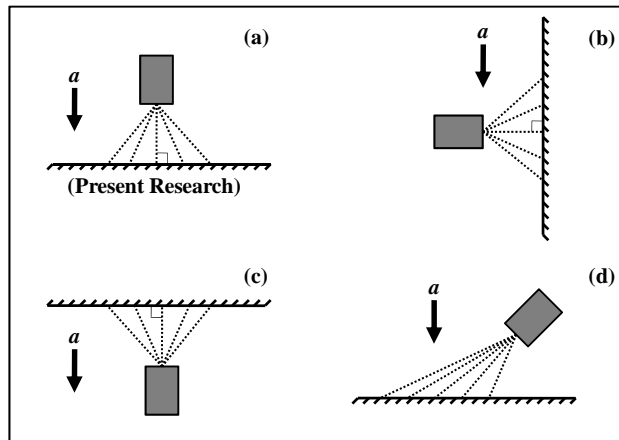
Fig. 1.1 Orientation schematics: (a) upward-facing horizontal, as in the present research; (b) vertical; (c) downward-facing horizontal; and (d) inclined spray.
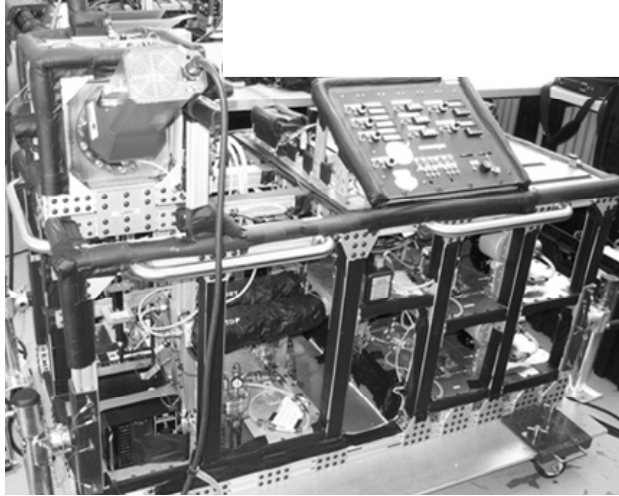
Fig. 1.2 Photograph of entire test rig.
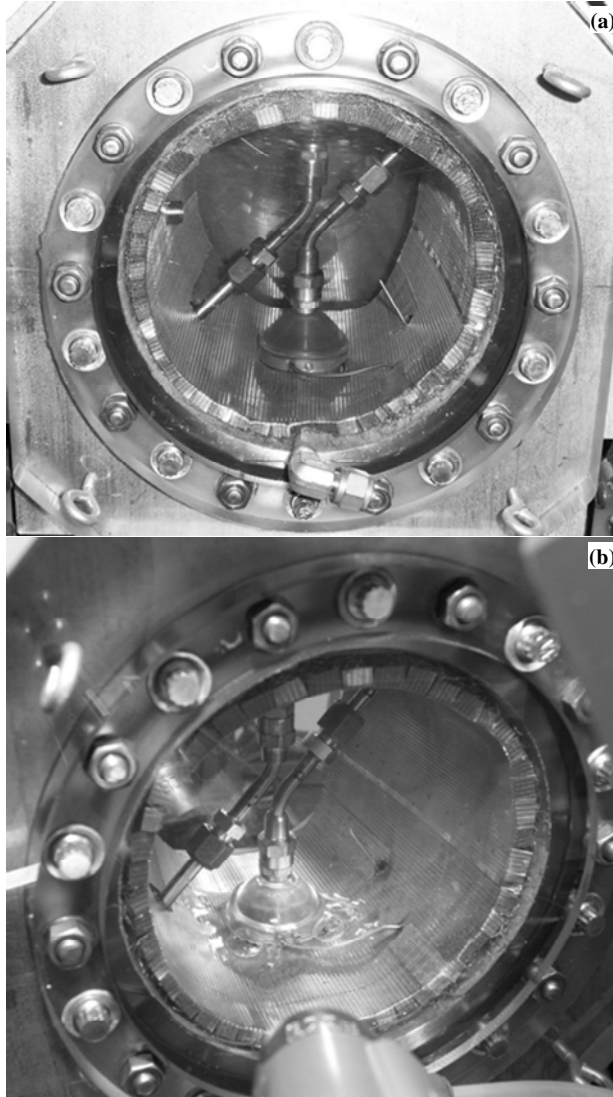
Fig. 1.3 Photographs illustrating: (a) test chamber; and (b) test chamber during operation.
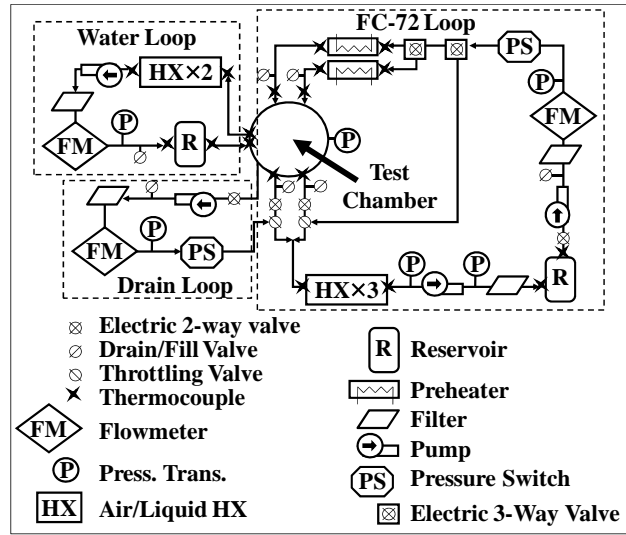
Fig. 1.4 Flow loop schematic.
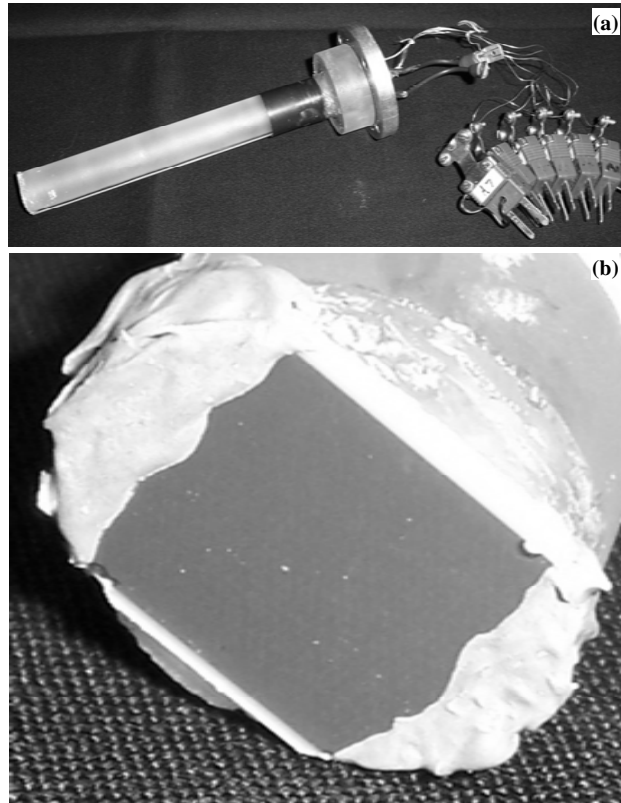
Fig. 1.5 Photographs detailing: (a) entire pedestal; and (b) close-up of TFR heater.
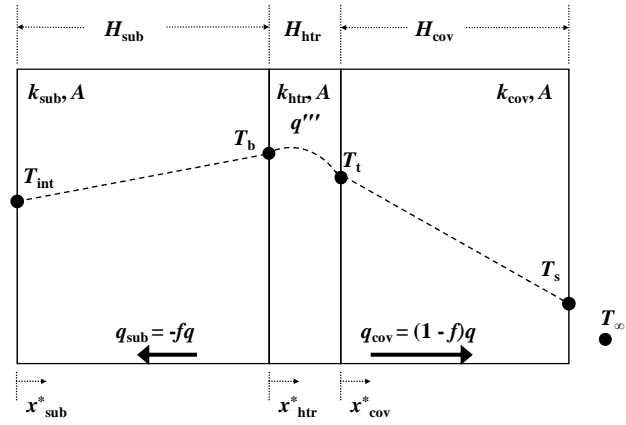
Fig. 1.6 Schematic showing heater geometry (not to scale), heat rates, and qualitative temperature distribution.
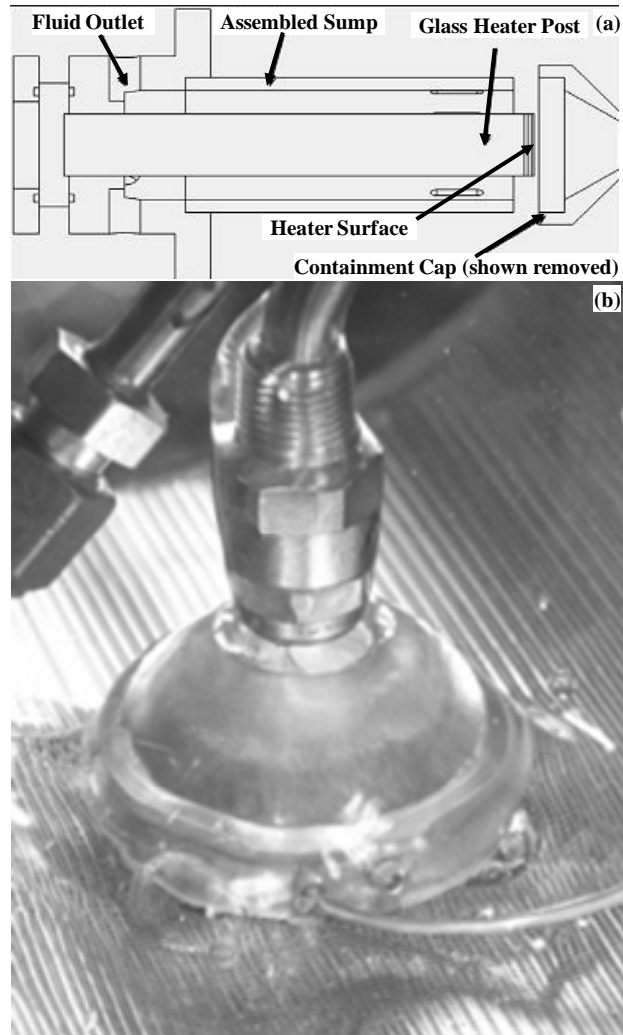
Fig. 1.7 Illustrations clarifying: (a) schematic of pedestal in sump and cap;[18] and (b) close-up photograph of nozzle/cap positioning, as well as surface tension flow during operation.
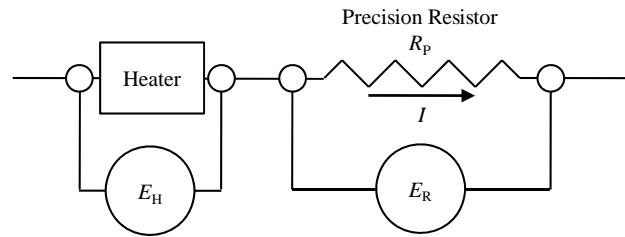
Fig. 1.8 Power measurement electrical schematic.
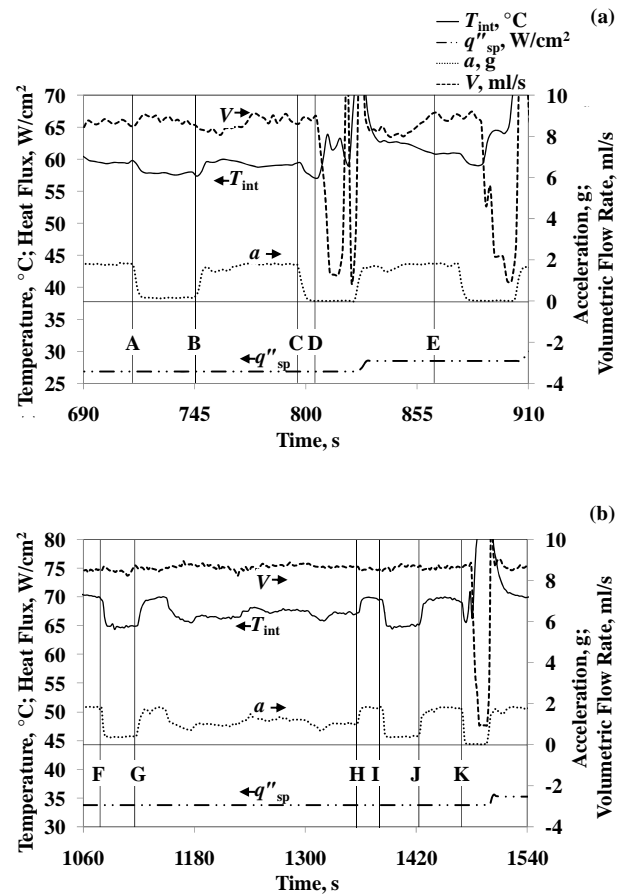
Fig. 1.9 Representative transient data traces: (a) Flight 1; and (b) Flight 2.
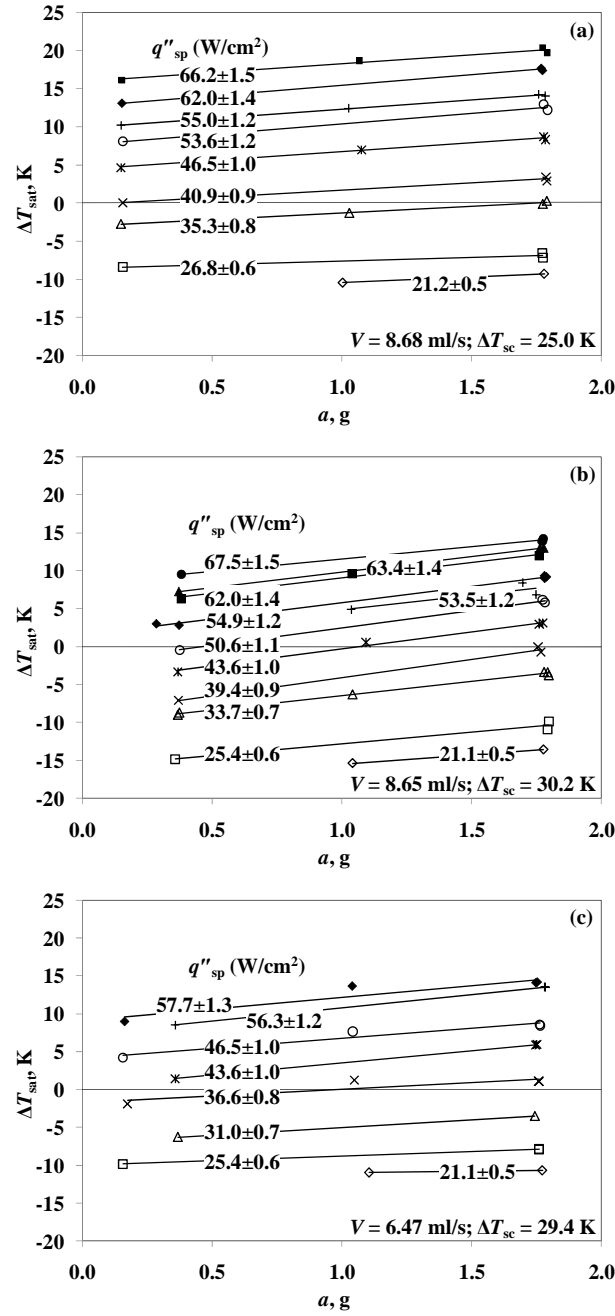
Fig. 1.10 Effect of acceleration on wall superheat: (a) Flight 1 ($V = 8.68 \pm 0.42$ ml/s, $\Delta T_{sc} = 25.0 \pm 1.1$ K, $T_{sat} = 53.7 \pm 1.1°$C); (b) Flight 2 ($V = 8.65 \pm 0.43$ ml/s, $\Delta T_{sc} = 30.2 \pm 1.0$ K, $T_{sat} = 59.3 \pm 1.0°$C); and (c) Flight 3 ($V = 6.47 \pm 0.44$ ml/s, $\Delta T_{sc} = 29.4 \pm 1.0$ K, $T_{sat} = 58.8 \pm 1.0°$C).
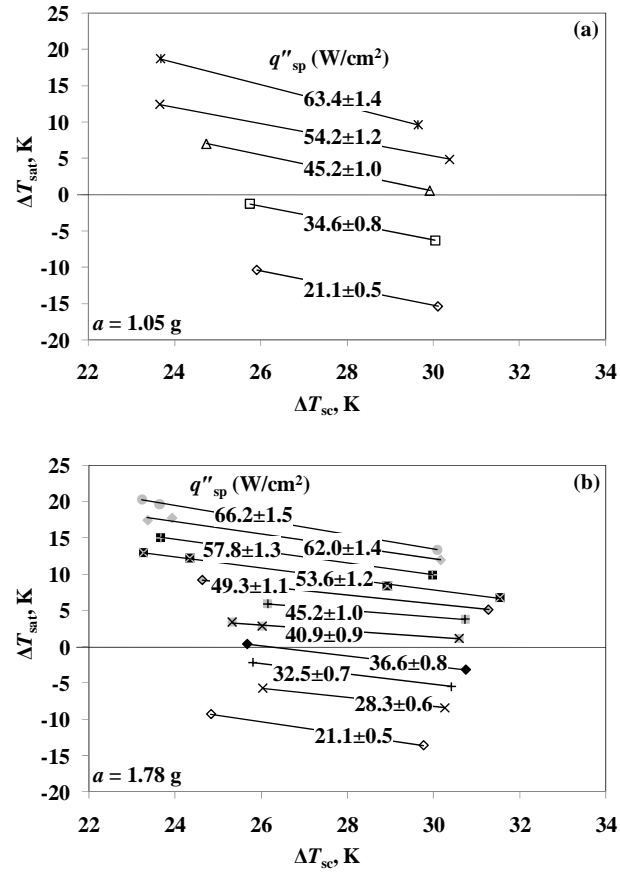
Fig. 1.11 Effect of subcooling on wall superheat ($V = 8.66 \pm 0.42$ ml/s): (a) $a = 1.05 \pm 0.04$ g; and (b) $a = 1.78 \pm 0.03$ g.
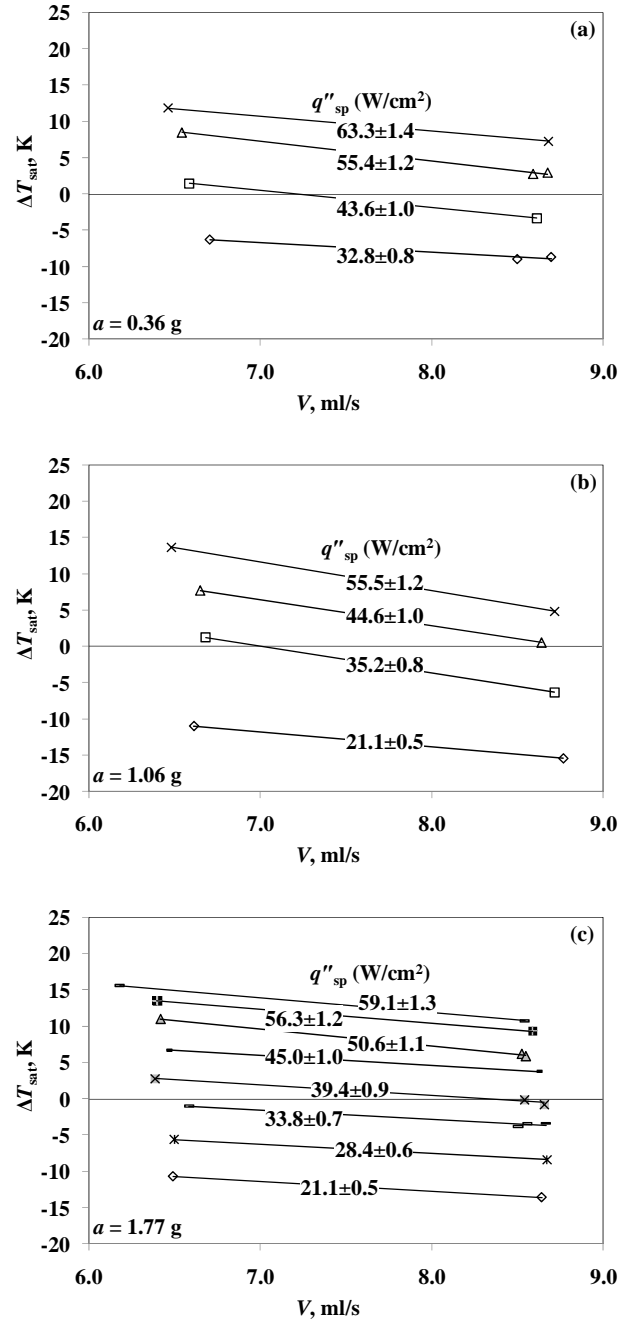
Fig. 1.12 Effect of flow rate on wall superheat ($\Delta T_{sc} = 29.9 \pm 1.5$ K): (a) $a = 0.36 \pm 0.04$ g; (b) $a = 1.06 \pm 0.04$ g; and (c) $a = 1.77 \pm 0.04$ g.
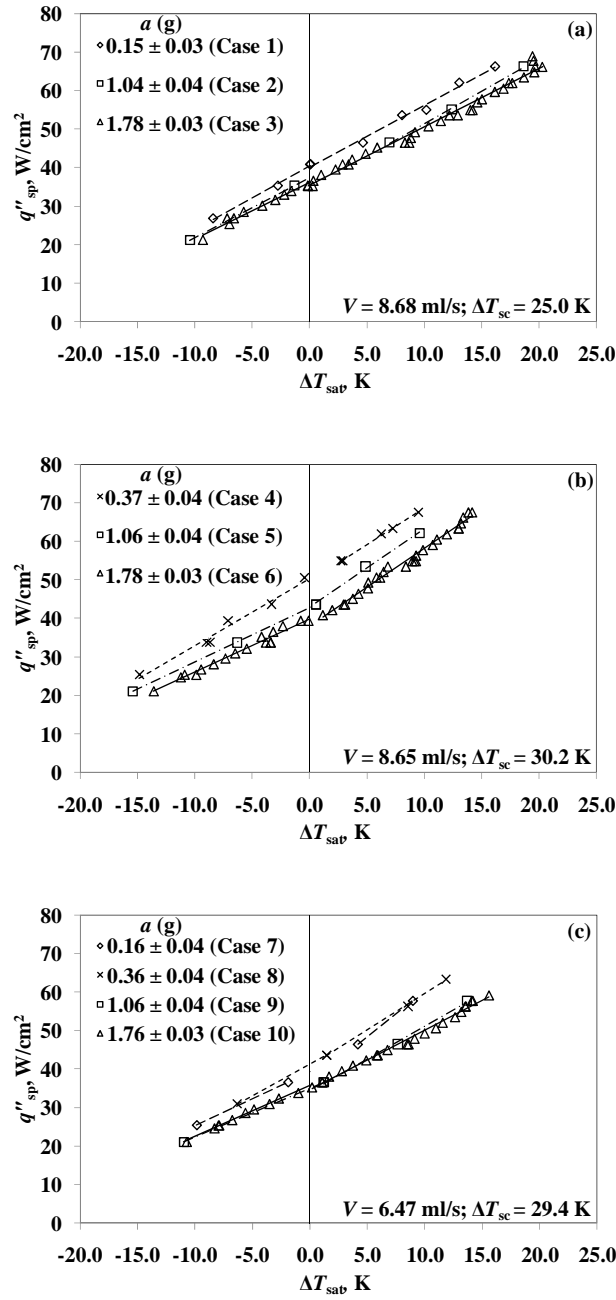
Fig. 1.13 Heat flux to spray versus wall superheat: (a) Flight 1 ($V = 8.68 \pm 0.42$ ml/s, $\Delta T_{sc} = 25.0 \pm 1.1$°C, $T_{sat} = 53.7 \pm 1.1$°C); (b) Flight 2 ($V = 8.65 \pm 0.43$ ml/s, $\Delta T_{sc} = 30.2 \pm 1.0$ K, $T_{sat} = 59.3 \pm 1.0$°C); and (c) Flight 3 ($V = 6.47 \pm 0.44$ ml/s, $\Delta T_{sc} = 29.4 \pm 1.0$ K, $T_{sat} = 58.8 \pm 1.0$°C).
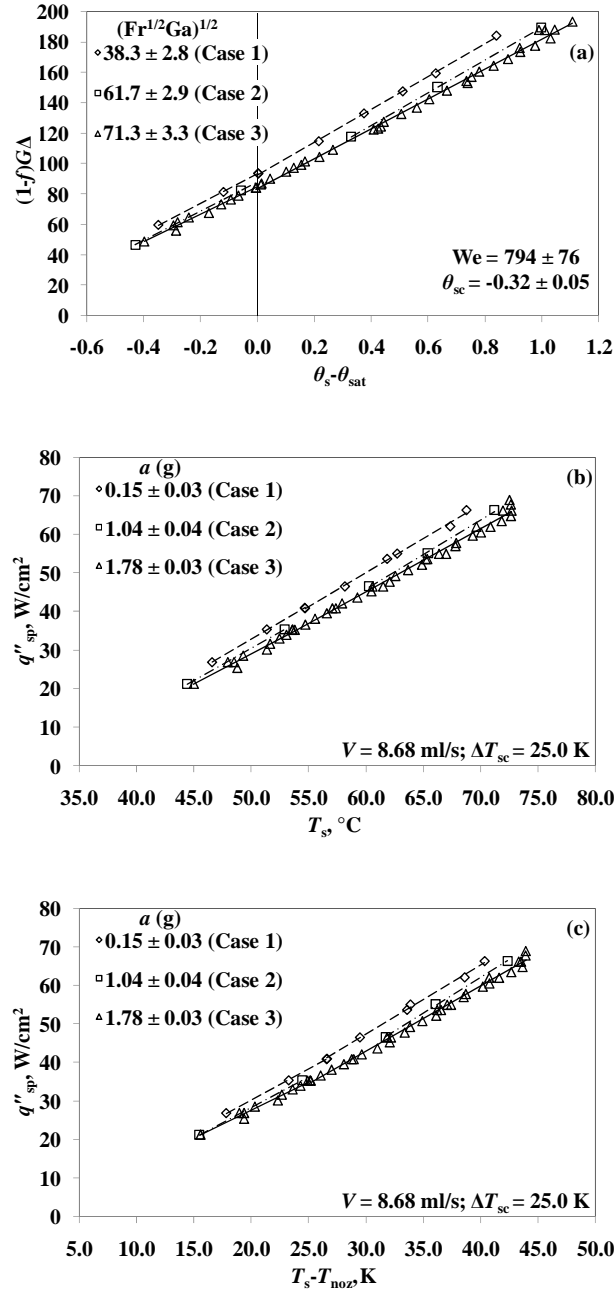
Fig. 1.14 Alternative presentations of heat flux versus temperature data for Flight 1: (a) non-dimensional terms; (b) heat flux to the spray versus surface temperature; and (c) heat flux to the spray versus temperature difference between surface and nozzle inlet temperatures.

Table 1.1 Summary of acceleration results from previous researchers

Researcher	a, g	Orientation	Nozzle Configuration	Heater size	Heater Type	Working Fluid	Flow Rate/ Volume Flux	T_{sat}, °C	ΔT_{sc}, K	q'', W/cm²	$T_s\text{-}T_{sat}$, K	q''_{CHF}, W/cm²	Orientation/ Acceleration Trends	Comments
Kato et al. (1995)[26]	1.0	Fig. 1.1 (a), (b)	Single, Unconfined, Pressure-Atomized, Uniform	19 mm Dia	Ni-Plated Cu-Block, Cartridge heaters	Water	2.0×10^{-3} to 8.5×10^{-3} m³/m²-s	100	80 to 83	30 to 400	0 to 220	170 to 400	q''_{CHF} ↑ for (b) than (a); ΔT_{sat} ↑ for (b) than (a)	More effect on ΔT_{sat} in transition boiling region
	0.01 1.0	Fig. 1.1 (a)	Single, Unconfined, Pressure Atomized, Hollow Cone			CFC-113	2.93×10^{-3} m³/m²-s	48	35 to 37	20 to 80	0 to 80	70 to 80	q''_{CHF} ↓ for a ↓, ΔT_{sat} ↓for a ↓	More effect on ΔT_{sat} in transition boiling region
	0.01 1.0 1.5	Fig. 1.1 (a)	Single, Unconfined, Pressure-Atomized, Uniform	19 mm Dia		Water	2.51×10^{-3} m³/m²-s	100	88 to 92	40 to 230	0 to 200	180 to 230	q''_{CHF} ↑ for a ↓, ΔT_{sat} ↓for a ↓	More effect on ΔT_{sat} in region below q''_{CHF}
	0.01 1.0 1.5 2.0	Fig. 1.1 (a)	Single, Unconfined, Pressure-Atomized, Uniform			Water	5.35×10^{-3} m³/m²-s	100	84 to 87	60 to 300	0 to 220	280 to 300	Little change in q''_{CHF} or ΔT_{sat} with change in a	
Um et al. (1996)[19]	1.0	Fig. 1.1 (a), (b)	Single, Air-Atomized, Unconfined, Uniform liquid flux	8 × 8 mm²	Cu-Block, Lamps	Water	0.02 to 0.04 l/min	N/A	N/A	0 to 525	$20 \le T_s \le$ 160°C	200 to 525	No effect on q''_{CHF} due to orientation	
		Fig. 1.1 (a), (b), (c)	Single, Air-Atomized, Unconfined, Non-Uniform liquid flux				0.01 to 0.03 l/min	N/A	N/A	0 to 1300	$20 \le T_s \le$ 200°C	300 to 1300	q''_{CHF} same for (a), (c); q''_{CHF} ↑ for (b)	Higher liquid mass flux at center of spray cone
Sone et al. (1996)[27]	1.0	Fig. 1.1 (a), (b), (c)	Single, Unconfined, Pressure-Atomized, Uniform	18 × 18 mm²	Pyrex Block, ITO Heater	Water	1.51×10^{-4} m³/m²-s	100	76	10 to 44	0 to 52	No	ΔT_{sat} ↓ for (a) than (b) or (c)	
	1.0	N/A	N/A	18 × 18 mm²	Pyrex Block, ITO Heater	FC-72	N/A	56	N/A	N/A	N/A	No	No effect of heater orientation reported	
	0.01 2.0	Fig. 1.1 (a)	Single, Unconfined, Pressure-Atomized, High mass flux at center	50 mm Dia	Cr-Plated Cu-Block, Cartridge heaters	Water	1.57×10^{-3} m³/m²-s	100	58 to 75	30 to 135	0 to 300	125 to 135	q''_{CHF} ↓ for a ↓, ΔT_{sat} ↓for a ↓ in transition and film boiling	Some discrepancy between plots and text
	0.01 2.0	Fig. 1.1 (a)	Single, Unconfined, Pressure-Atomized, Uniform	50 mm Dia	Cr-Plated Cu-Block, Cartridge heaters	Water	1.51×10^{-4} m³/m²-s	100	62 to 80	3 to 31	0 to 300	31	No effect on q''_{CHF}; q'' ↓ for a ↓ in high ΔT_{sat} film boiling region	
	0.01 2.0	Fig. 1.1 (a)	Single, Unconfined, Pressure-Atomized, Uniform	18 × 18 mm²	Pyrex Block, ITO Heater	Water	1.51×10^{-4} m³/m²-s	100	18	14 to 34	4 to 48	No	ΔT_{sat} ↑ for a ↓	
	0.01 2.0	Fig. 1.1 (a)	Single, Unconfined, Pressure-Atomized, High mass flux at center	50 mm Dia	Cr-Plated Cu-Block, Cartridge heaters	FC-72	1.34×10^{-3} m³/m²-s	56	29	6 to 46	12 to 78	40 to 46	q''_{CHF} ↑ for a ↓, ΔT_{sat} ↑for a ↓ in transition boiling, q'' ↑ for a ↓ in film boiling	Some discrepancy between plots and text; Opposite trend near heater edge

Table 1.1 Summary of acceleration results from previous researchers (Continued)

Researcher	a, g	Orientation	Nozzle Configuration	Heater size	Heater Type	Working Fluid	Flow Rate/ Volume Flux	T_{sat}, °C	ΔT_{sc}, K	q'', W/cm²	$T_s\text{-}T_{sat}$, K	q''_{CHF}, W/cm²	Orientation/ Acceleration Trends	Comments
	1.0	Fig. 1.1 (a), (c)		18 × 18 mm²	Pyrex Block, ITO Heater	Water	1.35×10⁻⁴ to 4.3×10⁻⁴ m³/m²-s	100	68 to 79	5 to 55	0 to 80	No	ΔT_{sat} ↓ for (c) than (a)	
	1.0	Fig. 1.1 (a), (c)		50 mm Dia	Cr-Plated Cu-Block, Cartridge heaters	Water	1.97×10⁻⁴ m³/m²-s	100	74.9	1 to 47.5	0 to 290	47.5	No orientation effect on q''_{CHF} or transition boiling; q'' ↓ for (c) than (a) in film boiling	
	1.0	Fig. 1.1 (a), (c)		18 × 18 mm²	Pyrex Block, ITO Heater	FC-72	N/A	56	29 to 37	N/A	N/A	No	ΔT_{sat} ↓ for (c) than (a)	
	1.0	Fig. 1.1 (a), (c)		50 mm Dia	Cr-Plated Cu-Block, Cartridge heaters	FC-72	2.17×10⁻³ m³/m²-s	56	30.3	0 to 11.5	0 to 95	10 to 11.5	q''_{CHF} & q''_{MHF} ↓ for (c) than (a), q'' ↓ for (c) than (a) in transition and film boiling	
Yoshida et al. (2001)[28]	0.01 1.0 2.0	Fig. 1.1 (a)	Single, Unconfined, Pressure-Atomized, Uniform Across Center	18 × 18 mm²	Pyrex Block, ITO Heater	Water	1.4×10⁻⁴ to 3.7×10⁻³ m³/m²-s	100	68 to 79	N/A	N/A	No	No effect of change in accel reported	Low volume flux - no liquid flooding, just dropwise evaporation
	0.01 1.0 2.0	Fig. 1.1 (a)		50 mm Dia	Cr-Plated Cu-Block, Cartridge heaters	Water	1.42×10⁻⁴ m³/m²-s	100	79.1	0.5 to 24	20 to 260	24	q'' & q''_{MHF} ↓ for a ↓ film boiling; no accel effect elsewhere in boiling curve	
	0.01 1.0 2.0	Fig. 1.1 (a)		50 mm Dia	Cr-Plated Cu-Block, Cartridge heaters	Water	3.7×10⁻³ m³/m²-s	100	79.1	30 to 260	10 to 210	250 to 260	q''_{CHF} ↑ for a ↓; ΔT_{sat} ↑ for a ↓ in transition boiling; no accel effect in film boiling	
	0.01 2.0	Fig. 1.1 (a)		18 × 18 mm²	Pyrex Block, ITO Heater	FC-72	2.25×10⁻⁴ m³/m²-s	56	31.5	4.3 to 6.6	8 to 38	No	No effect of change in accel reported	
	0.01 2.0	Fig. 1.1 (a)		50 mm Dia	Cr-Plated Cu-Block, Cartridge heaters	FC-72	2.2×10⁻⁴ m³/m²-s	56	31 to 36.9	1 to 19.5	20 to 80	16 to 19.5	q'' ↓ for a ↓ in film boiling for low We; no effect of accel reported elsewhere	
		Fig. 1.1 (a)				FC-87	0.0128 to 0.0204 m³/m²-s	42 to 42.5	< 0.6	5 to 90	7 to 50	68 to 90		
Lin and Ponnappan (2003)[20]	1.0	Fig. 1.1 (a)	2 × 4 Array, Pressure-Atomized, Confined	1.0 × 2.0 cm²	Cu-Block, Cartridge Heaters	FC-72	0.0122 to 0.0222 m³/m²-s	28.5 to 62.5	< 3.5	5 to 90	5 to 40	48 to 90		FC-72 with dissolved air had higher q''_{CHF}
		Fig. 1.1 (a)				Water	0.0188 to 0.0249 m³/m²-s	67 - 72	3.0 to 14.1	5 to 500	2.5 to 58	No		
		Fig. 1.1 (a)				Methanol	0.0246 to 0.0363 m³/m²-s	38.9 to 69	2.7 to 13.7	25 to 490	5 to 60	250 to 490		

Table 1.1 Summary of acceleration results from previous researchers (Continued)

Researcher	a, g	Orien-tation	Nozzle Configuration	Heater size	Heater Type	Working Fluid	Flow Rate/ Volume Flux	T_{sat}, °C	ΔT_{sc}, K	q'', W/cm²	T_s-T_{sat}, K	q''_{CHF}, W/cm²	Orientation/ Acceleration Trends	Comments
Lin et al. (2004)[21]	1.0	Fig. 1.1 (b), (c)	4 × 12 Array, Pressure-Atomized, Confined	2.54 × 7.6 cm²	Cu-Block, Cartridge Heaters	FC-72	0.505×10⁻³ to 0.880×10⁻³ kg/s per nozzle	27 to 55	< 6	10 to 60	8 to 38	30 to 60	h ↑ for (c) than (b); q''_{CHF} ↑ for (c) than (b);	
Baysinger et al. (2004)[17]	0.01 1.0 1.8	Fig. 1.1 (a), (c)	Single, Partially-confined, Pressure Atomized	17 mm Dia	Polycar-bonate Pedestal, ITO Heater	FC-72	5.3 ml/s	N/A	N/A	0 to 20 W	N/A	No	No effect of change in accel reported	Recirculating closed-loop system in variable-acceleration environment
Lin and Ponnappan (2005)[22]	1.0	Fig. 1.1 (a), (b), (c)	4 × 12 Array, Pressure-Atomized, Confined	2.54 × 7.6 cm²	Cu-Block, Cartridge Heaters	FC-72	N/A	27 to 55	< 6	N/A	N/A	32 to 60	q''_{CHF} ↑ for (c) than for (b); q''_{CHF} ↓ for (a) than (b)	
		Fig. 1.1 (b)		2.54 × 7.6 cm²	Cu-Block, Plasma Heater	Water	6.48×10⁻⁴ to 9.0×10⁻⁴ kg/s per nozzle	63.5 to 90	2 to 37	100 to 500	12 to 43	350 to 500	h ↑ for (b) large heater, q''_{CHF} ↓ for (b) large heater than (a) small heater	
Golliher et al. (2005)[6]	μ-g 1.0	Fig. 1.1 (a)	Single, Unconfined, Air-Atomized	3 in Dia	Mach-ined Al	Water	2.7 to 7.6 ml/s	N/A	N/A	N/A	N/A	N/A	Spray formed multiple, separated segments of coalesced liquid on surface in microgravity	2.2-s drop tower, results not presented for heat transfer performance
Rybicki and Mudawar (2006)[23]	1.0	Fig. 1.1 (c)	Single, Pressure-Atomized, Unconfined (Various nozzles)	1.0 × 1.0 cm²	Cu-Block, Cartridge Heaters	PF-5052	3.08 ml/s to 20.93 ml/s	50	12 to 27	10 to 237	$4 \le T_s$-$T_{noz} \le$ 50 K	128 to 237	No effect of (c) or (a) on single-phase, nucleate boiling, or q''_{CHF} correlations	(a) from previous data with Water, FC-72, FC-87
Hunnel et al. (2006)[45]	1.0	Fig. 1.1 (a), (b)	Single, Partially-confined, Pressure Atomized	16 mm Dia	Glass Pedestal, TFR and ITO Heaters	FC-72	4.8 to 9.8 ml/s	46.5 to 51.2	22.2 to 27.2	5 to 35	N/A	No	Little effect of orientation is reported	Reported that different orientations cannot simulate microgravity
		Fig. 1.1 (a), (b)	Single, Unconfined, Pressure Atomized				4.8 to 9.8 ml/s	46.5 to 51.2	22.2 to 27.2	5 to 35	N/A	No	T_s slightly ↓ for (b) than (a) at 9.8 mL/s	
Yerkes et al. (2006)[18]	0.01 0.16 0.36 1.0 1.8	Fig. 1.1 (a)	Single, Partially-confined, Pressure Atomized	16 mm Dia	Glass Pedestal, ITO Heater	FC-72	5.26 to 10.5 ml/s	56	32.6	10.1 to 39.4	N/A	No	Nu ↑ for a ↓ (θ_s-$\theta_{\infty,top}$ ↓ as a ↓)	Recirculating closed-loop system in variable-acceleration environment

Table 1.1 Summary of acceleration results from previous researchers (Continued)

Researcher	a, g	Orientation	Nozzle Configuration	Heater size	Heater Type	Working Fluid	Flow Rate/ Volume Flux	T_{sat}, °C	ΔT_{sc}, K	q'', W/cm²	T_s-T_{sat}, K	q''_{CHF}, W/cm²	Orientation/ Acceleration Trends	Comments
Gambaryan-Roisman et al. (2007)[30]	0.05 1.0 1.8	Fig. 1.1 (a)	Single, Unconfined, Pressure-Atomized	20 mm Dia	Convex Surface, Cartridge Heaters	Water	0.25 to 0.5 l/min	N/A	N/A	37.5 to 150 W	N/A	N/A	Temp. 5.1 mm below surface ↑ as a ↓ for flow above 0.4 l/min	
Elston (2008)[40]	0.01 to 2.02	Fig. 1.1 (a)	4 × 4 Nozzle Array, Confined, Pressure Atomized	25.4 × 25.4 mm²	Phenolic Base, TFR Heater	FC-72	13.1 to 21.3 g/s	37.4 to 47.2	1.6 to 18.4	2.9 to 25	-10 to 35	22 to 25	ΔT_{sat} ↓ for a ↓; q''_{CHF} ↑ for a ↓; ΔT_{sat} changed less for high m, low ΔT_{sc}; Trans. a trip q''_{CHF} prematurely	Recirculating closed-loop system in variable-acceleration environment
Conrad et al (2009)[44]	0.01 to 1.8	Fig. 1.1 (d)	Linear Nozzle Array, Confined, Pressure Atomized	25.4 × 20.6 mm²	Ohmite Resistor	FC-72	0.775 to 3.86 l/min	56	N/A	24.9 to 26.6	N/A	No	h slightly ↑ for a ↓	Reported lack of constant accel data; Damage to array seal caused uncertainty and non-uniformity of flow
Current Research (2009)	0.15 to 1.80	Fig. 1.1 (a)	Single, Partially-confined, Pressure Atomized	1.18 × 1.18 cm²	Glass Pedestal, TFR Heater	FC-72	6.18 to 8.94 ml/s	52.2 to 59.9	23.1 to 31.7	21.1 to 69.0	-15.4 to 20.3	No	ΔT_{sat} ↓ for a ↓; ΔT_{sat} ↓ for ΔT_{sc} ↑; ΔT_{sat} ↓ for V ↑	Recirculating closed-loop system in variable-acceleration environment

42

Table 1.2 Heater layer dimensions and thermal conductivities [46]

Layer	Thickness, mm	Thermal Conductivity, W/m-K
Ceramic Substrate	$H_{sub} = 0.634 \pm 0.010$	$k_{sub} = 27.0$
Heater	$H_{htr} = 0.008 \pm 0.002$	$k_{htr} = 1.04$
Glass Cover	$H_{cov} = 0.040 \pm 0.005$	$k_{cov} = 1.04$

Table 1.3 Instrument/calibration uncertainties

Measurement	Calibration Uncertainty
P_{ch}	0.25 psia
a	0.03 g
V	0.413 ml/s
E_H	$(0.000045 \times E_H + 0.0006)$ V
E_R	$(0.000040 \times E_R + 0.000007)$ V
R_p	0.00002 Ω
T_{int}	0.054°C
T_{lf}	0.065°C
T_{uf}	0.065°C
T_{noz}	0.061°C

Table 1.4 Parameters for ten cases tested during flights

Flight	Case	a, g	T_{sat}, °C	ΔT_{sc}, K	V, ml/s
1	1	0.15 ± 0.03	53.8 ± 1.2	25.4 ± 1.3	8.70 ± 0.45
	2	1.04 ± 0.04	53.8 ± 1.1	25.1 ± 1.1	8.64 ± 0.43
	3	1.78 ± 0.03	53.6 ± 1.2	24.8 ± 1.2	8.73 ± 0.43
	4	0.37 ± 0.04	59.5 ± 1.0	30.7 ± 1.0	8.63 ± 0.43
2	5	1.06 ± 0.04	59.1 ± 1.0	30.0 ± 1.0	8.70 ± 0.42
	6	1.78 ± 0.03	59.3 ± 1.0	30.3 ± 1.0	8.61 ± 0.42
	7	0.16 ± 0.04	58.9 ± 1.1	30.0 ± 1.1	6.55 ± 0.45
3	8	0.36 ± 0.04	59.2 ± 1.0	30.3 ± 1.0	6.58 ± 0.44
	9	1.06 ± 0.04	58.4 ± 1.0	29.1 ± 1.0	6.61 ± 0.42
	10	1.76 ± 0.03	58.8 ± 1.0	29.3 ± 1.0	6.43 ± 0.42

Table 1.5 Comprehensive Listing of Data Points

Case 1: $a = 0.15 \pm 0.03$ g, $V = 8.70 \pm 0.45$ ml/s, $T_{sat} = 53.8 \pm 1.2$ °C, $\Delta T_{sc} = 25.4 \pm 1.3$ K

Data Point Number	q''_{sp}, W/cm²	a, g	V, ml/s	T_{noz}, °C	T_{sat}, °C	ΔT_{sc}, K	T_s, °C	ΔT_{sat}, K
Run 1,1	26.8 ± 0.6	0.16 ± 0.04	8.79 ± 0.52	28.8 ± 0.1	55.0 ± 1.1	26.2 ± 1.1	46.6 ± 1.3	-8.4 ± 1.7
Run 1,2	35.3 ± 0.8	0.15 ± 0.05	8.80 ± 0.54	28.1 ± 0.2	54.2 ± 1.2	26.0 ± 1.2	51.4 ± 1.8	-2.8 ± 2.1
Run 1,3	40.9 ± 0.9	0.16 ± 0.04	8.77 ± 0.51	28.1 ± 0.1	54.6 ± 1.3	26.5 ± 1.3	54.7 ± 2.1	0.1 ± 2.4
Run 1,4	46.5 ± 1.0	0.15 ± 0.04	8.67 ± 0.53	28.7 ± 0.1	53.5 ± 1.3	24.8 ± 1.4	58.2 ± 2.3	4.7 ± 2.7
Run 1,5	53.6 ± 1.2	0.16 ± 0.04	8.53 ± 0.46	28.3 ± 0.1	53.8 ± 1.3	25.5 ± 1.3	61.9 ± 2.7	8.1 ± 3.0
Run 1,6	55.0 ± 1.2	0.15 ± 0.04	8.78 ± 0.57	28.8 ± 0.1	52.5 ± 1.6	23.7 ± 1.6	62.7 ± 2.8	10.2 ± 3.2
Run 1,7	62.0 ± 1.4	0.15 ± 0.05	8.56 ± 0.49	28.8 ± 0.1	54.3 ± 1.2	25.5 ± 1.2	67.4 ± 3.1	13.1 ± 3.4
Run 1,8	66.2 ± 1.5	0.15 ± 0.04	8.66 ± 0.50	28.4 ± 0.2	52.6 ± 1.3	24.2 ± 1.3	68.8 ± 3.4	16.2 ± 3.6

Case 2: $a = 1.04 \pm 0.04$ g, $V = 8.64 \pm 0.43$ ml/s, $T_{sat} = 53.8 \pm 1.1$ °C, $\Delta T_{sc} = 25.1 \pm 1.1$ K

Data Point Number	q''_{sp}, W/cm²	a, g	V, ml/s	T_{noz}, °C	T_{sat}, °C	ΔT_{sc}, K	T_s, °C	ΔT_{sat}, K
Run 2,1	21.2 ± 0.5	1.00 ± 0.04	8.71 ± 0.43	28.9 ± 0.1	54.8 ± 1.1	25.9 ± 1.1	44.4 ± 1.1	-10.4 ± 1.5
Run 2,2	35.3 ± 0.8	1.03 ± 0.07	8.82 ± 0.44	28.5 ± 0.1	54.2 ± 1.1	25.8 ± 1.1	52.9 ± 1.8	-1.3 ± 2.1
Run 2,3	46.5 ± 1.0	1.08 ± 0.05	8.54 ± 0.43	28.5 ± 0.1	53.3 ± 1.1	24.7 ± 1.1	60.3 ± 2.3	7.0 ± 2.6
Run 2,4	55.0 ± 1.2	1.03 ± 0.07	8.61 ± 0.44	29.3 ± 0.1	53.0 ± 1.1	23.7 ± 1.1	65.4 ± 2.8	12.4 ± 3.0
Run 2,5	66.2 ± 1.5	1.07 ± 0.10	8.50 ± 0.45	28.9 ± 0.1	52.5 ± 1.2	23.7 ± 1.2	71.2 ± 3.4	18.7 ± 3.6

Case 3: $a = 1.78 \pm 0.03$ g, $V = 8.73 \pm 0.43$ ml/s, $T_{sat} = 53.6 \pm 1.2$ °C, $\Delta T_{sc} = 24.8 \pm 1.2$ K

Data Point Number	q''_{sp}, W/cm²	a, g	V, ml/s	T_{noz}, °C	T_{sat}, °C	ΔT_{sc}, K	T_s, °C	ΔT_{sat}, K
Run 3,1	21.2 ± 0.5	1.78 ± 0.06	8.63 ± 0.46	29.4 ± 0.1	54.3 ± 1.1	24.8 ± 1.1	45.0 ± 1.1	-9.3 ± 1.5
Run 3,2	25.3 ± 0.6	1.79 ± 0.06	8.92 ± 0.79	29.4 ± 0.3	55.7 ± 1.2	26.3 ± 1.2	48.8 ± 3.1	-7.0 ± 3.3
Run 3,3	26.8 ± 0.6	1.77 ± 0.05	8.65 ± 0.49	29.1 ± 0.1	55.6 ± 1.2	26.5 ± 1.3	48.5 ± 1.4	-7.2 ± 1.9
Run 3,4	26.8 ± 0.6	1.77 ± 0.05	8.80 ± 0.53	29.0 ± 0.1	54.5 ± 1.2	25.5 ± 1.2	47.9 ± 1.4	-6.6 ± 1.8
Run 3,5	28.4 ± 0.6	1.78 ± 0.06	8.88 ± 0.56	29.0 ± 0.1	55.0 ± 1.3	26.0 ± 1.3	49.3 ± 1.5	-5.7 ± 1.9
Run 3,6	30.0 ± 0.7	1.75 ± 0.05	8.68 ± 0.57	29.0 ± 0.2	55.4 ± 1.4	26.4 ± 1.4	51.3 ± 1.7	-4.1 ± 2.2
Run 3,7	31.5 ± 0.7	1.76 ± 0.06	8.76 ± 0.60	28.9 ± 0.2	54.6 ± 1.5	25.6 ± 1.6	51.6 ± 1.7	-3.0 ± 2.3
Run 3,8	32.9 ± 0.7	1.77 ± 0.05	8.89 ± 0.51	28.8 ± 0.1	54.6 ± 1.3	25.8 ± 1.3	52.4 ± 1.7	-2.2 ± 2.1
Run 3,9	33.9 ± 0.7	1.78 ± 0.05	8.84 ± 0.53	28.7 ± 0.1	54.6 ± 1.3	25.9 ± 1.3	53.0 ± 1.7	-1.6 ± 2.2
Run 3,10	35.3 ± 0.8	1.77 ± 0.06	8.76 ± 0.49	28.4 ± 0.1	53.7 ± 1.1	25.3 ± 1.1	53.6 ± 1.8	-0.1 ± 2.1
Run 3,11	35.3 ± 0.8	1.79 ± 0.05	8.82 ± 0.54	28.9 ± 0.2	53.5 ± 1.2	24.6 ± 1.2	53.8 ± 1.8	0.3 ± 2.1
Run 3,12	36.6 ± 0.8	1.78 ± 0.05	8.74 ± 0.58	28.7 ± 0.2	54.4 ± 1.4	25.7 ± 1.4	54.7 ± 1.9	0.3 ± 2.3
Run 3,13	38.2 ± 0.8	1.78 ± 0.04	8.63 ± 0.48	28.6 ± 0.1	54.6 ± 1.4	26.0 ± 1.4	55.6 ± 1.9	1.0 ± 2.4
Run 3,14	39.6 ± 0.9	1.79 ± 0.05	8.64 ± 0.51	28.5 ± 0.2	54.3 ± 1.3	25.8 ± 1.3	56.6 ± 2.0	2.3 ± 2.4
Run 3,15	40.9 ± 0.9	1.79 ± 0.06	8.62 ± 0.58	28.5 ± 0.1	54.5 ± 1.3	26.0 ± 1.3	57.4 ± 2.1	2.9 ± 2.5
Run 3,16	40.9 ± 0.9	1.79 ± 0.06	8.77 ± 0.51	28.3 ± 0.1	53.7 ± 1.2	25.3 ± 1.2	57.1 ± 2.1	3.4 ± 2.4
Run 3,17	42.1 ± 0.9	1.79 ± 0.05	8.76 ± 0.52	28.3 ± 0.1	54.2 ± 1.3	25.9 ± 1.3	57.9 ± 2.1	3.7 ± 2.5
Run 3,18	43.7 ± 1.0	1.80 ± 0.06	8.62 ± 0.56	28.3 ± 0.1	54.4 ± 1.4	26.1 ± 1.4	59.3 ± 2.3	4.9 ± 2.6
Run 3,19	45.3 ± 1.0	1.79 ± 0.05	8.73 ± 0.53	28.4 ± 0.2	54.6 ± 1.4	26.2 ± 1.4	60.5 ± 2.4	5.9 ± 2.8
Run 3,20	46.5 ± 1.0	1.78 ± 0.06	8.63 ± 0.51	29.3 ± 0.1	52.8 ± 1.2	23.5 ± 1.3	61.5 ± 2.3	8.7 ± 2.7
Run 3,21	46.5 ± 1.0	1.78 ± 0.06	8.64 ± 0.60	28.7 ± 0.1	52.2 ± 1.3	23.5 ± 1.3	60.6 ± 2.4	8.3 ± 2.7
Run 3,22	47.8 ± 1.1	1.75 ± 0.05	8.69 ± 0.50	28.7 ± 0.2	53.2 ± 1.4	24.5 ± 1.4	62.1 ± 2.5	8.8 ± 2.9
Run 3,23	49.3 ± 1.1	1.78 ± 0.05	8.65 ± 0.49	28.7 ± 0.2	53.4 ± 1.5	24.6 ± 1.5	62.6 ± 2.5	9.2 ± 2.9
Run 3,24	50.8 ± 1.1	1.79 ± 0.05	8.91 ± 0.55	28.8 ± 0.2	53.3 ± 1.4	24.5 ± 1.5	63.7 ± 2.6	10.4 ± 3.0
Run 3,25	52.2 ± 1.2	1.80 ± 0.06	8.82 ± 0.53	28.8 ± 0.1	53.4 ± 1.5	24.7 ± 1.5	64.9 ± 2.7	11.5 ± 3.0
Run 3,26	53.6 ± 1.2	1.79 ± 0.04	8.71 ± 0.54	28.8 ± 0.2	53.2 ± 1.4	24.3 ± 1.4	65.4 ± 2.7	12.2 ± 3.1
Run 3,27	53.6 ± 1.2	1.78 ± 0.04	8.66 ± 0.49	29.0 ± 0.4	52.3 ± 1.2	23.3 ± 1.2	65.2 ± 2.7	12.9 ± 3.0
Run 3,28	55.0 ± 1.2	1.76 ± 0.07	8.48 ± 0.50	29.6 ± 0.1	52.8 ± 1.2	23.2 ± 1.2	67.0 ± 2.8	14.2 ± 3.0
Run 3,29	55.0 ± 1.2	1.78 ± 0.06	8.65 ± 0.51	29.3 ± 0.1	52.4 ± 1.2	23.1 ± 1.2	66.4 ± 2.8	14.0 ± 3.0
Run 3,30	57.0 ± 1.3	1.78 ± 0.05	8.79 ± 0.53	29.3 ± 0.2	53.2 ± 1.4	23.9 ± 1.5	67.8 ± 2.9	14.7 ± 3.2
Run 3,31	57.8 ± 1.3	1.78 ± 0.04	8.79 ± 0.57	29.2 ± 0.2	52.8 ± 1.4	23.7 ± 1.5	67.9 ± 2.9	15.1 ± 3.3
Run 3,32	59.7 ± 1.3	1.77 ± 0.05	8.74 ± 0.54	29.1 ± 0.2	53.1 ± 1.5	24.0 ± 1.5	69.3 ± 3.0	16.2 ± 3.4
Run 3,33	60.6 ± 1.3	1.78 ± 0.05	8.82 ± 0.53	29.3 ± 0.2	53.1 ± 1.4	23.9 ± 1.4	70.0 ± 3.1	16.9 ± 3.4
Run 3,34	62.0 ± 1.4	1.77 ± 0.05	8.94 ± 0.56	29.2 ± 0.2	53.2 ± 1.5	23.9 ± 1.5	70.9 ± 3.1	17.7 ± 3.5
Run 3,35	62.0 ± 1.4	1.77 ± 0.06	8.61 ± 0.53	28.9 ± 0.1	52.2 ± 1.2	23.4 ± 1.2	69.7 ± 3.1	17.4 ± 3.3
Run 3,36	63.5 ± 1.4	1.76 ± 0.05	8.59 ± 0.51	29.1 ± 0.2	53.1 ± 1.4	24.0 ± 1.4	71.8 ± 3.2	18.7 ± 3.5
Run 3,37	64.8 ± 1.4	1.77 ± 0.05	8.74 ± 0.53	29.0 ± 0.2	53.0 ± 1.4	24.1 ± 1.4	72.7 ± 3.3	19.6 ± 3.6
Run 3,38	66.2 ± 1.5	1.77 ± 0.14	8.64 ± 0.67	29.2 ± 0.2	52.4 ± 1.3	23.2 ± 1.3	72.7 ± 4.4	20.3 ± 4.6
Run 3,39	66.2 ± 1.5	1.79 ± 0.06	8.66 ± 0.48	28.6 ± 0.1	52.3 ± 1.2	23.6 ± 1.2	72.0 ± 3.4	19.7 ± 3.6
Run 3,40	67.8 ± 1.5	1.77 ± 0.06	8.72 ± 0.50	28.7 ± 0.2	53.1 ± 1.4	24.4 ± 1.4	72.6 ± 3.5	19.5 ± 3.8
Run 3,41	69.0 ± 1.5	1.76 ± 0.06	8.80 ± 0.65	28.6 ± 0.2	53.1 ± 1.5	24.5 ± 1.5	72.5 ± 3.5	19.5 ± 3.8

Table 1.5 Comprehensive Listing of Data Points (Continued)

Case 4: $a = 0.37 \pm 0.04$ g, $V = 8.63 \pm 0.43$ ml/s, $T_{sat} = 59.5 \pm 1.0$ °C, $\Delta T_{sc} = 30.7 \pm 1.0$ K

Data Point Number	q''_{sp}, W/cm^2	a, g	V, ml/s	T_{noz}, °C	T_{sat}, °C	ΔT_{sc}, K	T_s, °C	ΔT_{sat}, K
Run 4,1	25.3 ± 0.6	0.36 ± 0.05	8.72 ± 0.46	28.8 ± 0.1	59.8 ± 1.0	31.0 ± 1.0	44.9 ± 1.3	-14.8 ± 1.6
Run 4,2	33.7 ± 0.7	0.37 ± 0.04	8.50 ± 0.46	29.1 ± 0.1	59.9 ± 1.0	30.7 ± 1.0	50.8 ± 1.7	-9.0 ± 2.0
Run 4,3	33.7 ± 0.7	0.37 ± 0.04	8.70 ± 0.46	29.1 ± 0.1	59.5 ± 1.0	30.4 ± 1.0	50.8 ± 1.7	-8.7 ± 2.0
Run 4,4	39.4 ± 0.9	0.37 ± 0.04	8.62 ± 0.49	28.4 ± 0.2	59.8 ± 1.0	31.3 ± 1.0	52.6 ± 2.0	-7.1 ± 2.2
Run 4,5	43.6 ± 1.0	0.37 ± 0.05	8.61 ± 0.49	28.8 ± 0.1	59.2 ± 1.1	30.4 ± 1.1	55.9 ± 2.3	-3.3 ± 2.5
Run 4,6	50.5 ± 1.1	0.38 ± 0.04	8.76 ± 0.52	27.8 ± 0.1	59.5 ± 1.0	31.7 ± 1.0	59.0 ± 2.5	-0.5 ± 2.7
Run 4,7	54.9 ± 1.2	0.29 ± 0.07	8.68 ± 0.49	29.1 ± 0.1	59.6 ± 1.0	30.5 ± 1.0	62.5 ± 2.9	2.9 ± 3.1
Run 4,8	54.9 ± 1.2	0.37 ± 0.04	8.59 ± 0.48	28.9 ± 0.1	59.2 ± 1.1	30.3 ± 1.1	61.9 ± 2.8	2.8 ± 2.9
Run 4,9	61.9 ± 1.4	0.38 ± 0.04	8.56 ± 0.47	28.9 ± 0.1	59.4 ± 1.0	30.6 ± 1.0	65.7 ± 3.1	6.3 ± 3.3
Run 4,10	63.4 ± 1.4	0.37 ± 0.04	8.68 ± 0.45	29.0 ± 0.1	59.2 ± 1.1	30.2 ± 1.1	66.4 ± 3.2	7.3 ± 3.4
Run 4,11	67.5 ± 1.5	0.38 ± 0.04	8.48 ± 0.46	28.3 ± 0.1	59.3 ± 1.0	30.9 ± 1.0	68.7 ± 3.4	9.5 ± 3.5

Case 5: $a = 1.06 \pm 0.04$ g, $V = 8.70 \pm 0.42$ ml/s, $T_{sat} = 59.1 \pm 1.0$ °C, $\Delta T_{sc} = 30.0 \pm 1.0$ K

Data Point Number	q''_{sp}, W/cm^2	a, g	V, ml/s	T_{noz}, °C	T_{sat}, °C	ΔT_{sc}, K	T_s, °C	ΔT_{sat}, K
Run 5,1	21.1 ± 0.5	1.04 ± 0.05	8.77 ± 0.43	29.5 ± 0.1	59.6 ± 1.0	30.1 ± 1.0	44.2 ± 1.1	-15.4 ± 1.4
Run 5,2	33.7 ± 0.7	1.04 ± 0.06	8.71 ± 0.43	29.2 ± 0.1	59.2 ± 1.0	30.0 ± 1.0	52.9 ± 1.7	-6.3 ± 2.0
Run 5,3	43.6 ± 1.0	1.09 ± 0.05	8.64 ± 0.43	29.2 ± 0.1	59.1 ± 1.0	29.9 ± 1.0	59.6 ± 2.2	0.6 ± 2.4
Run 5,4	53.5 ± 1.2	1.04 ± 0.06	8.72 ± 0.43	28.4 ± 0.2	58.8 ± 1.0	30.4 ± 1.0	63.6 ± 2.7	4.9 ± 2.9
Run 5,5	62.1 ± 1.4	1.04 ± 0.07	8.69 ± 0.43	29.1 ± 0.1	58.7 ± 1.0	29.7 ± 1.0	68.3 ± 3.1	9.6 ± 3.3

Case 6: $a = 1.78 \pm 0.03$ g, $V = 8.61 \pm 0.42$ ml/s, $T_{sat} = 59.3 \pm 1.0$ °C, $\Delta T_{sc} = 30.3 \pm 1.0$ K

Data Point Number	q''_{sp}, W/cm^2	a, g	V, ml/s	T_{noz}, °C	T_{sat}, °C	ΔT_{sc}, K	T_s, °C	ΔT_{sat}, K
Run 6,1	21.1 ± 0.5	1.78 ± 0.06	8.64 ± 0.48	29.5 ± 0.1	59.3 ± 1.0	29.8 ± 1.0	45.7 ± 1.1	-13.6 ± 1.5
Run 6,2	24.7 ± 0.5	1.80 ± 0.06	8.78 ± 0.47	29.4 ± 0.1	59.8 ± 1.1	30.4 ± 1.1	48.6 ± 1.2	-11.2 ± 1.7
Run 6,3	25.4 ± 0.6	1.79 ± 0.05	8.79 ± 0.48	29.1 ± 0.1	59.8 ± 1.1	30.6 ± 1.1	48.9 ± 1.3	-10.9 ± 1.7
Run 6,4	25.4 ± 0.6	1.80 ± 0.05	8.61 ± 0.44	29.7 ± 0.1	59.2 ± 1.0	29.5 ± 1.0	49.3 ± 1.3	-9.9 ± 1.6
Run 6,5	26.8 ± 0.6	1.79 ± 0.06	8.71 ± 0.49	29.6 ± 0.1	59.7 ± 1.1	30.1 ± 1.1	50.2 ± 1.3	-9.5 ± 1.7
Run 6,6	28.1 ± 0.6	1.77 ± 0.05	8.67 ± 0.50	29.6 ± 0.1	59.9 ± 1.1	30.3 ± 1.1	51.5 ± 1.4	-8.4 ± 1.8
Run 6,7	29.6 ± 0.7	1.78 ± 0.06	8.58 ± 0.49	29.5 ± 0.1	59.9 ± 1.1	30.3 ± 1.1	52.5 ± 1.5	-7.3 ± 1.8
Run 6,8	30.9 ± 0.7	1.79 ± 0.06	8.66 ± 0.46	29.6 ± 0.1	59.8 ± 1.1	30.3 ± 1.1	53.3 ± 1.6	-6.5 ± 1.9
Run 6,9	32.1 ± 0.7	1.79 ± 0.05	8.63 ± 0.45	29.5 ± 0.1	59.9 ± 1.1	30.4 ± 1.1	54.4 ± 1.6	-5.5 ± 2.0
Run 6,10	33.7 ± 0.7	1.80 ± 0.05	8.51 ± 0.46	29.4 ± 0.1	59.9 ± 1.1	30.6 ± 1.1	56.1 ± 1.7	-3.8 ± 2.0
Run 6,11	33.7 ± 0.7	1.79 ± 0.05	8.56 ± 0.45	29.4 ± 0.1	59.1 ± 1.0	29.6 ± 1.0	55.6 ± 1.7	-3.4 ± 2.0
Run 6,12	33.8 ± 0.7	1.78 ± 0.05	8.67 ± 0.45	29.3 ± 0.1	59.0 ± 1.0	29.8 ± 1.0	55.6 ± 1.7	-3.4 ± 2.0
Run 6,13	35.2 ± 0.8	1.77 ± 0.06	8.63 ± 0.45	29.1 ± 0.1	59.8 ± 1.1	30.6 ± 1.1	55.6 ± 1.8	-4.2 ± 2.1
Run 6,14	36.5 ± 0.8	1.77 ± 0.05	8.54 ± 0.47	28.9 ± 0.1	59.7 ± 1.1	30.8 ± 1.1	56.5 ± 1.8	-3.2 ± 2.1
Run 6,15	38.0 ± 0.8	1.79 ± 0.05	8.51 ± 0.46	28.8 ± 0.1	59.6 ± 1.1	30.9 ± 1.1	57.3 ± 1.9	-2.3 ± 2.2
Run 6,16	39.4 ± 0.9	1.77 ± 0.07	8.66 ± 0.45	28.7 ± 0.2	59.8 ± 1.1	31.0 ± 1.1	59.0 ± 2.0	-0.8 ± 2.3
Run 6,17	39.4 ± 0.9	1.76 ± 0.05	8.54 ± 0.47	29.4 ± 0.1	59.0 ± 1.0	29.6 ± 1.0	58.9 ± 2.0	-0.1 ± 2.2
Run 6,18	40.9 ± 0.9	1.79 ± 0.06	8.57 ± 0.50	29.2 ± 0.2	59.8 ± 1.1	30.6 ± 1.1	60.9 ± 2.1	1.2 ± 2.4
Run 6,19	42.2 ± 0.9	1.79 ± 0.06	8.52 ± 0.44	29.2 ± 0.1	59.7 ± 1.1	30.6 ± 1.1	61.7 ± 2.1	2.0 ± 2.4
Run 6,20	43.6 ± 1.0	1.78 ± 0.05	8.60 ± 0.48	29.2 ± 0.1	58.8 ± 1.0	29.5 ± 1.0	61.8 ± 2.2	3.1 ± 2.4
Run 6,21	43.6 ± 1.0	1.76 ± 0.05	8.51 ± 0.46	28.8 ± 0.1	58.6 ± 1.0	29.8 ± 1.0	61.6 ± 2.2	3.0 ± 2.4
Run 6,22	45.1 ± 1.0	1.77 ± 0.05	8.61 ± 0.50	28.7 ± 0.2	59.5 ± 1.1	30.7 ± 1.1	63.2 ± 2.3	3.8 ± 2.5
Run 6,23	46.4 ± 1.0	1.77 ± 0.05	8.66 ± 0.47	28.4 ± 0.1	59.4 ± 1.1	31.1 ± 1.1	63.7 ± 2.3	4.3 ± 2.6
Run 6,24	47.8 ± 1.1	1.77 ± 0.05	8.59 ± 0.47	28.4 ± 0.1	59.4 ± 1.1	31.0 ± 1.1	64.5 ± 2.4	5.1 ± 2.7
Run 6,25	49.3 ± 1.1	1.77 ± 0.05	8.55 ± 0.47	28.1 ± 0.1	59.4 ± 1.1	31.3 ± 1.1	64.5 ± 2.5	5.1 ± 2.7
Run 6,26	50.6 ± 1.1	1.77 ± 0.06	8.52 ± 0.47	28.2 ± 0.1	59.4 ± 1.1	31.2 ± 1.1	65.6 ± 2.6	6.2 ± 2.8
Run 6,27	50.7 ± 1.1	1.78 ± 0.06	8.55 ± 0.46	28.0 ± 0.1	58.6 ± 1.0	30.6 ± 1.0	64.5 ± 2.5	5.8 ± 2.7
Run 6,28	52.1 ± 1.2	1.78 ± 0.06	8.61 ± 0.48	28.1 ± 0.3	59.5 ± 1.1	31.4 ± 1.2	65.9 ± 2.7	6.4 ± 2.9
Run 6,29	53.5 ± 1.2	1.75 ± 0.05	8.55 ± 0.50	28.2 ± 0.2	59.7 ± 1.2	31.5 ± 1.2	66.6 ± 2.7	6.8 ± 2.9
Run 6,30	53.5 ± 1.2	1.70 ± 0.20	8.70 ± 0.45	29.7 ± 0.1	58.6 ± 1.0	28.9 ± 1.0	67.0 ± 2.7	8.4 ± 2.9
Run 6,31	54.9 ± 1.2	1.78 ± 0.05	8.69 ± 0.51	29.5 ± 0.1	59.3 ± 1.1	29.8 ± 1.1	68.6 ± 2.8	9.3 ± 3.0
Run 6,32	54.9 ± 1.2	1.79 ± 0.05	8.51 ± 0.47	29.3 ± 0.1	58.6 ± 1.0	29.3 ± 1.0	67.8 ± 2.7	9.1 ± 2.9
Run 6,33	54.9 ± 1.2	1.78 ± 0.06	8.58 ± 0.44	29.1 ± 0.1	58.5 ± 1.0	29.4 ± 1.0	67.5 ± 2.7	8.9 ± 2.9
Run 6,34	56.3 ± 1.2	1.78 ± 0.06	8.59 ± 0.44	29.1 ± 0.1	59.3 ± 1.1	30.2 ± 1.1	68.5 ± 2.8	9.3 ± 3.0
Run 6,35	57.8 ± 1.3	1.78 ± 0.05	8.70 ± 0.51	29.2 ± 0.1	59.2 ± 1.1	30.0 ± 1.1	69.0 ± 2.9	9.9 ± 3.1
Run 6,36	59.1 ± 1.3	1.77 ± 0.05	8.54 ± 0.45	29.2 ± 0.1	59.3 ± 1.1	30.1 ± 1.1	70.1 ± 3.0	10.7 ± 3.2
Run 6,37	60.5 ± 1.3	1.78 ± 0.05	8.53 ± 0.47	29.2 ± 0.1	59.2 ± 1.1	30.0 ± 1.1	70.3 ± 3.0	11.1 ± 3.2
Run 6,38	61.9 ± 1.4	1.76 ± 0.06	8.63 ± 0.46	29.2 ± 0.1	59.3 ± 1.1	30.2 ± 1.1	71.3 ± 3.1	12.0 ± 3.3
Run 6,39	63.4 ± 1.4	1.78 ± 0.06	8.67 ± 0.46	29.4 ± 0.1	58.5 ± 1.0	29.1 ± 1.0	71.5 ± 3.2	13.0 ± 3.3
Run 6,40	63.4 ± 1.4	1.76 ± 0.06	8.59 ± 0.45	29.2 ± 0.1	58.5 ± 1.0	29.3 ± 1.0	71.5 ± 3.2	13.0 ± 3.3
Run 6,41	64.7 ± 1.4	1.77 ± 0.05	8.60 ± 0.47	29.0 ± 0.1	59.3 ± 1.1	30.3 ± 1.1	72.5 ± 3.3	13.2 ± 3.4
Run 6,42	66.2 ± 1.5	1.76 ± 0.05	8.60 ± 0.48	28.9 ± 0.1	59.0 ± 1.1	30.1 ± 1.1	72.4 ± 3.3	13.4 ± 3.5
Run 6,43	67.5 ± 1.5	1.77 ± 0.06	8.63 ± 0.49	28.7 ± 0.1	59.4 ± 1.1	30.7 ± 1.1	73.5 ± 3.4	14.2 ± 3.6
Run 6,44	67.5 ± 1.5	1.77 ± 0.07	8.52 ± 0.48	28.6 ± 0.2	59.1 ± 1.1	30.5 ± 1.1	73.0 ± 3.5	13.9 ± 3.7

Table 1.5 Comprehensive Listing of Data Points (Continued)

Case 7: $a = 0.16 \pm 0.04$ g, $V = 6.55 \pm 0.45$ ml/s, $T_{sat} = 58.9 \pm 1.1$ °C, $\Delta T_{sc} = 30.0 \pm 1.1$ K								
Data Point Number	q''_{sp}, W/cm^2	a, g	V, ml/s	T_{noz}, °C	T_{sat}, °C	ΔT_{sc}, K	T_s, °C	ΔT_{sat}, K
Run 7,1	25.4 ± 0.6	0.16 ± 0.04	6.52 ± 0.46	29.2 ± 0.2	59.3 ± 1.1	30.1 ± 1.1	49.4 ± 1.8	-9.9 ± 2.1
Run 7,2	36.6 ± 0.8	0.17 ± 0.05	6.62 ± 0.49	29.2 ± 0.2	59.0 ± 1.2	29.8 ± 1.2	57.1 ± 2.5	-1.9 ± 2.7
Run 7,3	46.5 ± 1.0	0.16 ± 0.05	6.59 ± 0.49	29.1 ± 0.3	58.8 ± 1.2	29.7 ± 1.2	63.0 ± 2.7	4.2 ± 3.0
Run 7,4	57.7 ± 1.3	0.16 ± 0.05	6.45 ± 0.45	28.5 ± 0.3	58.8 ± 1.2	30.3 ± 1.2	67.7 ± 3.0	9.0 ± 3.3

Case 8: $a = 0.36 \pm 0.04$ g, $V = 6.58 \pm 0.44$ ml/s, $T_{sat} = 59.2 \pm 1.0$ °C, $\Delta T_{sc} = 30.3 \pm 1.0$ K								
Data Point Number	q''_{sp}, W/cm^2	a, g	V, ml/s	T_{noz}, °C	T_{sat}, °C	ΔT_{sc}, K	T_s, °C	ΔT_{sat}, K
Run 8,1	31.0 ± 0.7	0.37 ± 0.05	6.71 ± 0.46	28.9 ± 0.2	59.1 ± 1.0	30.2 ± 1.0	52.8 ± 1.7	-6.3 ± 2.0
Run 8,2	43.6 ± 1.0	0.36 ± 0.05	6.59 ± 0.47	28.9 ± 0.2	59.4 ± 1.0	30.5 ± 1.1	60.8 ± 2.3	1.4 ± 2.5
Run 8,3	56.3 ± 1.2	0.36 ± 0.05	6.54 ± 0.46	28.7 ± 0.2	59.0 ± 1.0	30.3 ± 1.0	67.5 ± 2.9	8.5 ± 3.0
Run 8,4	63.3 ± 1.4	0.37 ± 0.04	6.46 ± 0.44	29.4 ± 0.2	59.4 ± 1.0	30.1 ± 1.0	71.2 ± 3.2	11.8 ± 3.3

Case 9: $a = 1.06 \pm 0.04$ g, $V = 6.61 \pm 0.42$ ml/s, $T_{sat} = 58.4 \pm 1.0$ °C, $\Delta T_{sc} = 29.1 \pm 1.0$ K								
Data Point Number	q''_{sp}, W/cm^2	a, g	V, ml/s	T_{noz}, °C	T_{sat}, °C	ΔT_{sc}, K	T_s, °C	ΔT_{sat}, K
Run 9,1	21.1 ± 0.5	1.11 ± 0.05	6.61 ± 0.43	29.5 ± 0.1	58.2 ± 1.0	28.7 ± 1.0	47.3 ± 1.1	-11.0 ± 1.5
Run 9,2	36.6 ± 0.8	1.05 ± 0.06	6.68 ± 0.43	29.7 ± 0.1	58.6 ± 1.0	28.9 ± 1.0	59.8 ± 1.8	1.2 ± 2.1
Run 9,3	46.5 ± 1.0	1.04 ± 0.06	6.65 ± 0.43	29.2 ± 0.1	58.5 ± 1.0	29.3 ± 1.0	66.1 ± 2.3	7.7 ± 2.5
Run 9,4	57.7 ± 1.3	1.04 ± 0.06	6.48 ± 0.43	28.9 ± 0.1	58.4 ± 1.0	29.5 ± 1.0	72.0 ± 2.9	13.6 ± 3.1

Case 10: $a = 1.76 \pm 0.03$ g, $V = 6.43 \pm 0.42$ ml/s, $T_{sat} = 58.8 \pm 1.0$ °C, $\Delta T_{sc} = 29.3 \pm 1.0$ K								
Data Point Number	q''_{sp}, W/cm^2	a, g	V, ml/s	T_{noz}, °C	T_{sat}, °C	ΔT_{sc}, K	T_s, °C	ΔT_{sat}, K
Run 10,1	21.1 ± 0.5	1.77 ± 0.06	6.49 ± 0.46	29.9 ± 0.1	58.2 ± 1.0	28.3 ± 1.0	47.5 ± 1.1	-10.7 ± 1.5
Run 10,2	24.6 ± 0.5	1.78 ± 0.06	6.39 ± 0.45	29.9 ± 0.1	59.1 ± 1.0	29.2 ± 1.0	50.8 ± 1.3	-8.3 ± 1.6
Run 10,3	25.4 ± 0.6	1.76 ± 0.06	6.47 ± 0.44	29.8 ± 0.1	58.9 ± 1.0	29.1 ± 1.1	51.0 ± 1.3	-7.9 ± 1.7
Run 10,4	25.4 ± 0.6	1.76 ± 0.06	6.44 ± 0.46	29.5 ± 0.1	58.5 ± 1.0	29.0 ± 1.0	50.5 ± 1.3	-7.9 ± 1.6
Run 10,5	26.8 ± 0.6	1.76 ± 0.06	6.42 ± 0.48	29.6 ± 0.2	59.0 ± 1.1	29.4 ± 1.1	52.2 ± 1.4	-6.8 ± 1.8
Run 10,6	28.7 ± 0.6	1.75 ± 0.06	6.50 ± 0.47	29.4 ± 0.1	58.9 ± 1.1	29.5 ± 1.1	53.3 ± 1.4	-5.6 ± 1.8
Run 10,7	29.6 ± 0.7	1.77 ± 0.06	6.56 ± 0.46	29.4 ± 0.1	58.9 ± 1.1	29.5 ± 1.1	54.0 ± 1.5	-4.9 ± 1.9
Run 10,8	31.0 ± 0.7	1.74 ± 0.06	6.51 ± 0.45	29.6 ± 0.2	59.1 ± 1.1	29.4 ± 1.1	55.5 ± 1.6	-3.5 ± 1.9
Run 10,9	32.4 ± 0.7	1.77 ± 0.05	6.53 ± 0.47	29.2 ± 0.1	58.4 ± 1.0	29.2 ± 1.0	55.7 ± 1.6	-2.7 ± 1.9
Run 10,10	33.8 ± 0.8	1.76 ± 0.05	6.59 ± 0.49	30.2 ± 0.1	59.0 ± 1.1	28.8 ± 1.1	58.0 ± 1.7	-1.0 ± 2.0
Run 10,11	35.2 ± 0.8	1.74 ± 0.06	6.50 ± 0.44	30.2 ± 0.1	59.2 ± 1.1	29.0 ± 1.1	59.3 ± 1.8	0.2 ± 2.1
Run 10,12	36.6 ± 0.8	1.76 ± 0.07	6.47 ± 0.50	29.8 ± 0.2	58.3 ± 1.0	28.5 ± 1.0	59.4 ± 1.8	1.1 ± 2.1
Run 10,13	36.6 ± 0.8	1.76 ± 0.05	6.49 ± 0.46	29.7 ± 0.1	58.4 ± 1.0	28.7 ± 1.0	59.4 ± 1.8	1.1 ± 2.1
Run 10,14	38.1 ± 0.8	1.78 ± 0.05	6.50 ± 0.49	29.7 ± 0.2	59.1 ± 1.1	29.4 ± 1.1	60.7 ± 2.0	1.7 ± 2.2
Run 10,15	39.5 ± 0.9	1.77 ± 0.05	6.39 ± 0.45	29.6 ± 0.2	59.2 ± 1.1	29.6 ± 1.1	62.0 ± 2.0	2.8 ± 2.3
Run 10,16	40.9 ± 0.9	1.77 ± 0.06	6.41 ± 0.47	29.6 ± 0.2	59.4 ± 1.1	29.7 ± 1.1	63.1 ± 2.1	3.7 ± 2.3
Run 10,17	42.3 ± 0.9	1.77 ± 0.06	6.35 ± 0.45	29.6 ± 0.2	59.4 ± 1.1	29.7 ± 1.1	64.3 ± 2.1	4.9 ± 2.4
Run 10,18	43.6 ± 1.0	1.75 ± 0.06	6.30 ± 0.47	29.6 ± 0.2	59.4 ± 1.1	29.8 ± 1.1	65.2 ± 2.2	5.8 ± 2.5
Run 10,19	43.6 ± 1.0	1.75 ± 0.07	6.51 ± 0.47	29.2 ± 0.1	58.5 ± 1.0	29.3 ± 1.0	64.4 ± 2.2	5.9 ± 2.4
Run 10,20	45.0 ± 1.0	1.77 ± 0.06	6.46 ± 0.46	29.3 ± 0.2	59.0 ± 1.1	29.8 ± 1.1	65.8 ± 2.3	6.7 ± 2.5
Run 10,21	46.5 ± 1.0	1.76 ± 0.06	6.45 ± 0.45	29.7 ± 0.1	58.1 ± 1.0	28.4 ± 1.0	66.7 ± 2.3	8.6 ± 2.5
Run 10,22	46.5 ± 1.0	1.76 ± 0.06	6.55 ± 0.46	29.5 ± 0.1	58.2 ± 1.0	28.6 ± 1.0	66.7 ± 2.3	8.5 ± 2.5
Run 10,23	47.9 ± 1.1	1.76 ± 0.05	6.36 ± 0.45	29.5 ± 0.1	58.9 ± 1.1	29.3 ± 1.1	68.0 ± 2.4	9.1 ± 2.7
Run 10,24	49.3 ± 1.1	1.77 ± 0.05	6.37 ± 0.45	29.5 ± 0.1	58.8 ± 1.1	29.3 ± 1.1	68.8 ± 2.5	10.0 ± 2.7
Run 10,25	50.6 ± 1.1	1.78 ± 0.05	6.42 ± 0.45	29.5 ± 0.2	59.0 ± 1.1	29.5 ± 1.1	70.0 ± 2.6	11.0 ± 2.8
Run 10,26	52.1 ± 1.2	1.76 ± 0.06	6.39 ± 0.45	29.5 ± 0.2	59.0 ± 1.1	29.6 ± 1.1	70.6 ± 2.6	11.6 ± 2.9
Run 10,27	53.5 ± 1.2	1.78 ± 0.05	6.27 ± 0.46	29.5 ± 0.2	59.1 ± 1.1	29.7 ± 1.1	71.8 ± 2.7	12.6 ± 2.9
Run 10,28	54.9 ± 1.2	1.78 ± 0.05	6.37 ± 0.49	29.3 ± 0.1	59.1 ± 1.1	29.8 ± 1.1	72.2 ± 2.8	13.2 ± 3.0
Run 10,29	56.3 ± 1.2	1.78 ± 0.05	6.40 ± 0.47	29.3 ± 0.1	59.1 ± 1.1	29.8 ± 1.1	72.6 ± 2.8	13.5 ± 3.1
Run 10,30	56.3 ± 1.2	1.78 ± 0.06	6.40 ± 0.43	29.1 ± 0.1	58.2 ± 1.0	29.2 ± 1.0	71.8 ± 2.8	13.5 ± 3.0
Run 10,31	57.7 ± 1.3	1.75 ± 0.07	6.38 ± 0.47	29.1 ± 0.1	58.1 ± 1.0	29.0 ± 1.0	72.2 ± 2.9	14.1 ± 3.1
Run 10,32	57.8 ± 1.3	1.75 ± 0.06	6.40 ± 0.44	29.0 ± 0.1	58.1 ± 1.0	29.1 ± 1.0	72.3 ± 2.9	14.2 ± 3.1
Run 10,33	59.2 ± 1.3	1.74 ± 0.06	6.18 ± 0.48	30.1 ± 0.1	58.9 ± 1.1	28.7 ± 1.1	74.4 ± 3.0	15.6 ± 3.2

REFERENCES

[1]Mudawar, I., "Assessment of High-Heat-Flux Thermal Management Schemes," *IEEE Transactions on Components and Packaging Technologies*, Vol. 24, No. 2, 2001, pp. 122-141.

[2]Kim, J., "Spray Cooling Heat Transfer: The State of the Art," *International Journal of Heat and Fluid Flow*, Vol. 28, No. 4, 2007, pp. 753-767.

[3]Chow, L. C., Sehmbey, M. S., and Pais, M. R., "Critical Heat Flux in Spray Cooling," *34th AIAA Aerospace Sciences Meeting and Exhibit,* AIAA, Reno, NV, 1996. AIAA 96-0727.

[4]Rini, D. P., Chen, R, and Chow, L. C., "Bubble Behavior and Nucleate Boiling Heat Transfer in Saturated FC-72 Spray Cooling," *Journal of Heat Transfer*, Vol. 124, No. 1, 2002, pp. 63-72.

[5]Kim, J., "Review of Reduced Gravity Boiling Heat Transfer: US Research," *Journal of the Japan Society of Microgravity Application*, Vol. 20, No. 4, 2003, pp. 264-271.

[6]Golliher, E. L., Zivich, C. P. and Yao, S. C., "Exploration of Unsteady Spray Cooling for High Power Electronics at Microgravity Using NASA Glenn's Drop Tower," *Proceedings of HT2005: 2005 ASME Summer Heat Transfer Conference*, ASME, San Francisco, CA, 2005. ASME HT2005-72123.

[7]Silk, E. A., Golliher, E. L., and Selvam, R. P., "Spray cooling heat transfer: Technology overview and assessment of future challenges for micro-gravity application," *Energy Conversion and Management*, Vol. 49, No. 3, 2008, pp. 453-468.

[8]Sehmbey, M. S., Chow, L. C., Pais, M. R., and Mahefkey, T., "High heat flux spray cooling of electronics," *Proceedings of the 12th symposium on space nuclear power and propulsion,* Conf. Proc. Vol. 324, AIP, Albuquerque, NM, 1995, pp. 903-909.

[9]Cader, T., and Tilton, D., "Implementing Spray Cooling Thermal Management in High Heat Flux Applications," *ITHERM '04: 9th Intersociety Conference on Thermal and*

Thermomechanical Phenomena in Electronic Systems, Vol. 2, IEEE, Las Vegas, NV, 2004, pp. 699-701.

[10]Tilton, D. E., Chow, L. C., and Mahefkey, E. T., "High Power Density Evaporative Cooling," *22nd AIAA Thermophysics Conference*, AIAA, Honolulu, HI, 1987. AIAA-87-1536.

[11]Pais, M., Tilton, D., Chow, L., and Mahefkey, E., "High Heat Flux, Low Superheat Evaporative Spray Cooling," *27th AIAA Aerospace Sciences Meeting*, AIAA, Reno, NV, 1989. AIAA 89-0241.

[12]Estes, K. A., and Mudawar I., "Correlation of Sauter mean diameter and critical heat flux for spray cooling of small surfaces," *International Journal of Heat and Mass Transfer*, Vol. 38, No. 16, 1995, pp. 2985-2996.

[13]Pautsch, A. G., and Shedd, T. A., "Spray Impingement Cooling with Single- and Multiple-Nozzle Arrays. Part I: Heat Transfer Data Using FC-72," *International Journal of Heat and Mass Transfer*, Vol. 48, No. 15, 2005, pp. 3167-3175.

[14]Shedd, T. A., and Pautsch, A. G., "Spray Impingement Cooling with Single- and Multiple-Nozzle Arrays. Part II: Visualization and Empirical Models," *International Journal of Heat and Mass Transfer*, Vol. 48, No. 15, 2005, pp. 3176-3184.

[15]Lin, L., Harris, R., Lawson, J., and Ponnappan, R., "Spray Cooling with Methanol and Water Mixtures," *9th AIAA/ASME Joint Thermophysics and Heat Transfer Conference*, AIAA, San Francisco, CA, 2006. AIAA 2006-3410

[16]Puterbaugh, R. L., "The Effect of Dissolved Air on the Cooling Performance of a Partially-Confined FC-72 Spray," Master's Thesis, Dept. of Mechanical and Materials Engineering, Wright State Univ., Dayton, OH, 2008.

[17]Baysinger, K. M., Yerkes, K. L., Michalak, T. E., Harris, R. J., and McQuillen, J., "Design of a Microgravity Spray Cooling Experiment," *42nd AIAA Aerospace Sciences Meeting and Exhibit*, AIAA, Reno, NV, 2004. AIAA 2004-966.

[18]Yerkes, K. L., Michalak, T. E., Baysinger, K. M., Puterbaugh, R. L., Thomas, S. K., and McQuillen, J., "Variable-Gravity Effects on a Single-Phase Partially Confined Spray Cooling System," *AIAA Journal of Thermophysics and Heat Transfer*, Vol. 20, No. 3, 2006, pp. 361-370.

[19]Um, J., Sehmbey, M. S., and Chow, L. C., "Effects of Gravity on Spray Cooling," *ASME International Mechanical Engineering Congress & Exhibition*, ASME, Atlanta, GA, 1996. ASME: 96-WA/HT-26.

[20]Lin, L., and Ponnappan, R., "Heat Transfer Characteristics of Spray Cooling in a Closed Loop," *International Journal of Heat and Mass Transfer*, Vol. 46, No. 20, 2003, pp. 3737-3746.

[21]Lin, L., Ponnappan, R., Yerkes, K., and Hager, B., "Large Area Spray Cooling," *42nd AIAA Aerospace Sciences Meeting and Exhibit*, AIAA, Reno, NV, 2004. AIAA 2004-1340.

[22]Lin, L., and Ponnappan, R., "Two-Phase High Capacity Spray Cooling Loop - Nozzle Orientation Effects and Performance Results," *3rd International Energy Conversion Engineering Conference*, AIAA, San Francisco,CA, 2005. AIAA 2005-5733.

[23]Rybicki, J. R., and Mudawar, I., "Single-Phase and Two-Phase Cooling Characteristics of Upward-Facing and Downward-Facing Sprays," *International Journal of Heat and Mass Transfer*, Vol. 49, No. 1, 2006, pp. 5 - 16.

[24]Mudawar, I., and Valentine, W. S., "Determination of the Local Quench Curve for Spray-Cooled Metallic Surfaces," *Journal of Heat Treating*, Vol. 7, No. 2, 1989, pp. 107-121.

[25]Mudawar, I., and Estes, K. A., "Optimizing and Predicting CHF in Spray Cooling of a Square Surface," *ASME Journal of Heat Transfer*, Vol. 118, No. 3, 1996, pp. 672-679.

[26]Kato, M., Abe, Y., Mori, Y. H., and Nagashima, A., "Spray Cooling Under Reduced Gravity Conditions," *AIAA Journal of Thermophysics and Heat Transfer*, Vol. 9, No. 2, 1995, pp. 378-381.

[27]Sone, K., Yoshida, K., Oka, T., Abe, Y., Mori, Y., and Nagashima, A., "Spray Cooling Characteristics of Water and FC-72 Under Reduced and Elevated Gravity for Space Application," *31st Intersociety Energy Conversion Engineering Conference Part 2*, IEEE, Washington, DC, 1996, pp. 1500-1505.

[28]Yoshida, K., Abe, Y., Oka, T., Mori, Y. H., and Nagashima, A., "Spray Cooling Under Reduced Gravity Condition," *ASME Journal of Heat Transfer*, Vol. 123, No. 2, 2001, pp. 309-318.

[29]Roisman, I. V., Gambaryan-Roisman, T., Kyriopoulos, O., Stephan, P., and Tropea, C., "Breakup and Atomization of a Stretching Crown," *Physical Review E*, Vol. 76, No. 2, 2007, pp. 026302-1 to 026302-9.

[30]Gambaryan-Roisman, T., Kyriopoulos, O., Roisman, I., Stephan, P., and Tropea, C., "Gravity Effect on Spray Impact and Spray Cooling," *Microgravity Science Technology*, Vol. 19, No. 3/4, 2007, pp. 151-154.

[31]Rowden, B. L., Selvam, R. P., and Silk, E. A., "Spray Cooling Development Effort for Microgravity Environments," *Space Technology and Applications International Forum*, Conf. Proc. Vol. 813, AIP, Albuquerque, NM, 2006, pp. 134-144.

[32]Selvam, R. P., Lin, L., and Ponnappan, R., "Computational Modeling of Spray Cooling: Current Status and Future Challenges," *Space Technology and Applications International Forum*, Conf. Proc. Vol. 746, AIP, Albuquerque, NM, 2005, pp. 55-63.

[33]Selvam, R. P., and Ponnappan, R., "Numerical Modeling of Nucleation Boiling in Thin Film and Effect of Droplet Impact," *15th Annual Thermal & Fluids Analysis Workshop,* Pasadena, CA, 2004.

[34]Selvam, R. P., Sarkar, M., and Ponnappan, R., "Modeling of Spray Cooling: Effect of Droplet Velocity and Liquid to Vapor Density Ratio on Heat Transfer." *16th Annual Thermal & Fluids Analysis Workshop*, Orlando, FL, 2005.

[35]Selvam, R. P., Sarkar, M., Sarkar, S., and Ponnappan, R., "Effect of Vapor Bubble Size on Heat Transfer in Spray Cooling," *Space Technology and Applications International Forum*, Conf. Proc. Vol. 813, AIP, Albuquerque, NM, 2006, pp. 145 - 152.

[36]Selvam, R. P., Sarkar, S, and Ponnappan, R., "Modeling of Spray Cooling: Convective Flow Effect on Vapor Bubble Dynamics and Heat Transfer," *9th AIAA/ASME Joint Thermophysics and Heat Transfer Conference*, AIAA, San Francisco, CA, 2006. AIAA 2006-3411.

[37]Johnston, J. E., Selvam, R. P., and Silk, E. A., "Spray Cooling Modeling: Droplet Sub-Cooling Effect on Heat Transfer," *Space Technology and Applications International Forum,* Conf. Proc. Vol. 969, AIP, Albuquerque, NM, 2008, pp. 104-111.

[38]Cole, V., Mehra, D., Lowry, S., and Gray, D., "A Numerical Spray Impingement Model Coupled With a Free Surface Film Model," *16th Thermal & Fluids Analysis Workshop*, Orlando, FL, 2005.

[39]Baysinger, K. M. "Experimental Testing and Numerical Modeling of Spray Cooling Under Terrestrial Gravity Conditions," Master's Thesis, Dept. of Mechanical and Materials Engineering, Wright State Univ., Dayton, OH, 2005.

[40]Elston, L. J. "The Effect of Variable Gravity on the Cooling Performance of a 16-Nozzle Spray Array," Master's Thesis, Dept. of Mechanical and Materials Engineering, Wright State Univ., Dayton, OH, 2008.

[41]Elston, L. J., Yerkes, K. L., Thomas, S. K., and McQuillen, J., "The Effect of Variable Gravity on the Cooling Performance of a 16-Nozzle Spray Array," *47th AIAA Aerospace Sciences Meeting Including The New Horizons Forum and Aerospace Exposition*, AIAA, Orlando, FL, 2009. AIAA 2009-1025.

[42]Elston, L. J., Yerkes, K. L., Thomas, S. K., and McQuillen, J., "Qualitative Evaluation of a Liquid-Vapor Separator Concept in Micro-Gravity Conditions." *Space Propulsion & Energy Sciences International Forum*, Conf. Proc. Vol. 1103, AIP, Huntsville, AL, 2009, pp. 3-13.

[43]Shedd, T. A., "Next Generation Spray Cooling: High Heat Flux Management in Compact Spaces," *Heat Transfer Engineering*, Vol. 28, No. 2, 2007, pp. 87-92.

[44]Conrad, B. L., Springmann, J. C., McGill, L. A., and Shedd, T. A., "Effectiveness of Linear Spray Cooling in Microgravity," *Space, Propulsion and Energy Sciences International Forum*, Conf. Proc. Vol. 1103, AIP, Huntsville, AL, 2009, pp. 67-72.

[45]Hunnell, C. A., Kuhlman, J. M., and Gray, D. D., "Spray Cooling in Terrestrial and Simulated Reduced Gravity," *Space Technology and Applications International Forum*, Conf. Proc. Vol. 813, AIP, Albuquerque, NM, 2006, pp. 126-133.

[46]Glaspell, S. L., "Effects of the Electric Kelvin Force on Spray Cooling Performance," Master's Thesis, College of Engineering and Mineral Resources, Dept. of Mechanical and Aerospace Engineering, West Virginia Univ., Morgantown, WV, 2006.

[47]Kreitzer, P. J., "Experimental Testing of Convective Spray Cooling With the Aid of an Electrical Field Using the Coulomb Force," Master's Thesis, College of Engineering and Mineral Resources, Dept. of Mechanical and Aerospace Engineering, West Virginia Univ., Morgantown, WV, 2006.

[48]Kreitzer, P. J., Glaspell, S. L., Kuhlman, J. M., Mehra, D., and Gray, D. D., "Electrical Force Effects on Spray Cooling." *SAE Power Systems Conference*, SAE, New Orleans, LA, 2006. 06PSC-61.

[49]Kuhlman, J. M., Kreitzer, P. J., Mehra, D., Gray, D. D., and Yerkes, K. L., "Influence of Coulomb Force on Spray Cooling," *Space Technology and Applications International Forum*, Conf. Proc. Vol. 880, AIP, Albuquerque, NM, 2007, pp. 100-109.

[50]Kreitzer, P. J., Kuhlman, J. M., Mehra, D., Gray, D. D., and Yerkes, K. L., "Effects of Contact Charging on Spray Impingement Heat Transfer Performance and Spray Behavior," *39th AIAA Thermophysics Conf.*, AIAA, Miami, FL, 2007. AIAA 2007-4269.

[51]Kreitzer, P. J., and Kuhlman, J. M., "Visualization of Electrohydrodynamic Effects and Time Scale Analysis for Impinging Spray Droplets of HFE-7000," *Space Technology and Applications International Forum*, Conf. Proc. Vol. 969, Albuquerque, NM, 2008, pp. 86-93.

[52]3M, "Fluorinert Electronic Liquid FC-72 Product Information," St. Paul, MN, 3M Company, 2000.

[53]Yaniec, J. S., and Del Rosso, D., *JSC Reduced Gravity Program User's Guide: AOD 33899*, Aircraft Operations Division, 2003.

[54]Yaniec, J. S., and Del Rosso, D., *Test Equipment Data Package Requirements and Guidlines NASA JSC RGO: AOD 33896*, Aircraft Operations Division, 2003.

[55]Yaniec, J. S., and Del Rosso, D., *Experiment Design Requirements and Guidelines NASA 931 KC135A: AOD 33897*, Aircraft Operations Division, 2003.

[56]Montgomery, D., and Runger, G., *Applied Statistics and Probability for Engineers*, 3rd ed., John Wiley & Sons, Inc., New York, 2003.

[57]Fox, R. W., and McDonald, A. T., *Introduction to Fluid Mechanics,* 5th ed., John Wiley & Sons, Inc., New York, 1998.

[58]Incropera, F. P., and DeWitt, D. P., *Fundamentals of Heat and Mass Transfer*, 5th ed., John Wiley & Sons, Inc., New York, 2002.

[59]Geisler, K. J. L., "Buoyancy-Driven Two Phase Flow and Boiling Heat Transfer in Narrow Vertical Channels," Ph.D. Dissertation, Univ. of Minnesota, Minneapolis, MN, 2007.

[60]Skripov, V. P., and Firsov, V. V., "Surface Tension of Perfluoroalkanes," *Russian Journal of Physical Chemistry*, Vol. 42, No. 5, 1968, pp. 653 - 656.

APPENDIX NOMENCLATURE

a Acceleration normal to surface, g

A Heater area, m^2

AVG Average value

b Radius of glass heater post assembly, m

C Percent dissolved air content by volume, $[V'_{air}/(V'_f+V'_{air})]\times100$

$C_1, C_2,...$ Constants to be determined in surface temperature formulation

C_p Specific heat, kJ/kg-K

CI Confidence interval

D Diameter, m

E Voltage, V

f Heater conduction loss fraction, $1 - (q''_{sp}/q''_H)$

F Generic function to calculate a generic value

Fr Froude number, v^2/aD_d

G $gb^2/((T_{sat}-T_{\infty,wall})k_{htr})$

$G\Delta$ Non-dimensional heat input, $q/(\pi b k_{htr}(T_{sat}-T_{\infty,wall}))$

Ga Galileo number, $aD_d^3\rho^2/\mu^2$

h Convective heat transfer coefficient, $W/(m^2\text{-K})$

H Layer thickness, m

I Electrical current, A

j Generic variable in generic function

k Thermal conductivity, W/(m-K)

K k_f/k_{htr}

m Mass flow rate, kg/s

n Number of data points used in an average

Nu Nusselt number, $h_{top}b/k_f$

P Pressure, N/m^2

q	Power, W
q''	Heat flux, W/cm^2
q'''	Volumetric heat generation, W/m^3
R	Electrical resistance, Ω
t	Constant used in Confidence Interval; Also represents time, s
T	Temperature, K
v	Droplet velocity, m/s
V	Volumetric flow rate, ml/s
V'	Volume, m^3
We	Weber number, $\rho v^2 D_d / \sigma$
x^*	Position variable used in surface temperature formulation, m

Greek Symbols

α	Constant used in Confidence Interval
δ	Uncertainty
∂	Partial derivative
ΔT	Temperature difference, K
ΔT_{sat}	Wall superheat, $T_s - T_{sat}$, K
ΔT_{sc}	Fluid subcooling temperature, $T_{sat} - T_{noz}$, K
θ	Non-dimensional temperature, $(T - T_{\infty,wall})/(T_{sat} - T_{\infty,wall})$
ρ	Density, kg/m^3
σ	Surface tension, kg/s^2
σ_{sd}	Standard deviation
μ	Absolute viscosity, kg/(m-s)

Subscripts

1,2,...i	Counting index integers
1-φ	Single-phase
2-φ	Two-phase
air	Air
b	Point between substrate and heater layers

ch	Chamber
CHF	Critical heat flux
cov	Glass cover layer
d	Droplet
f	Free-stream fluid
H	Heater
htr	Heater layer
int	Heater/pedestal interface
lf	Lower film
meas	Measured value
MHF	Minimum heat flux
noz	Nozzle inlet
p	Droplet
R	Resistor
s	Surface
sat	Saturation
sc	Subcooling
sen	Sensible heating
sp	Spray
sub	Ceramic substrate layer
t	Point between heater and cover layers
top	Surface of heater
true	True value
uf	Upper film
∞,top	Free-stream fluid flowing over heater surface
∞,wall	Free-stream fluid flowing over pedestal wall

APPENDIX A. SURFACE TEMPERATURE CALCULATION

The ITO (Indium Tin Oxide) heaters that were originally used[17][39][18] on the pedestals were not capable of reaching q''_{CHF} (critical heat flux) for the flow rates that were being tested. If the power was increased to try to reach q''_{CHF}, the heaters failed due to the high current density in the thin film of the ITO heater. These heaters were replaced by thick film resistor (TFR) heaters. This heater consisted of a ceramic substrate, a thick film resistive element, and a glass cover plate. The thicknesses and thermal conductivities of these materials are presented in Table 1.2, and Fig. A.1 presents a schematic of these layers, along with a qualitative assumed temperature profile and the heat rates through the various layers.
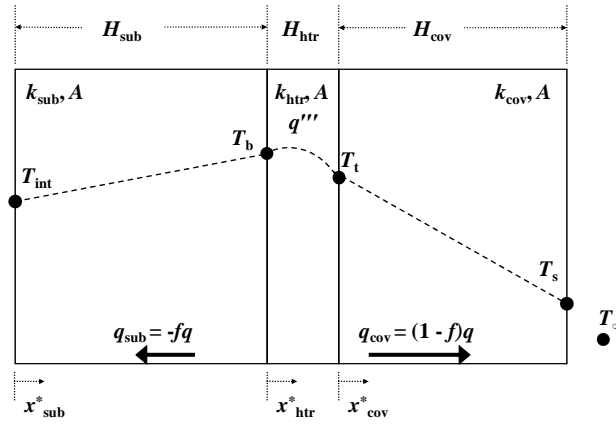
Fig. A.1 Schematic showing heater layers, heats, and temperature profile (not to scale)

The surface temperature could not be measured directly without interfering with the behavior of the spray. Thus, the temperature had to be calculated based on the temperature at the interface between the heater substrate and the supporting, insulating glass pedestal. For this calculation one-dimensional heat conduction was assumed through the substrate, heater, and glass cover layers, with a uniform volumetric heat generation term applied to the heater layer. This geometry, and thus the analysis, is similar to that presented in Glaspell[46], Kreitzer[47], Puterbaugh[16], and Elston[40]. The

governing equation for this analysis can be found in Incropera and DeWitt [58], and is given by

$$\frac{\partial}{\partial x}\left(k\frac{\partial T}{\partial x}\right) + \frac{\partial}{\partial y}\left(k\frac{\partial T}{\partial y}\right) + \frac{\partial}{\partial z}\left(k\frac{\partial T}{\partial z}\right) + q''' = \rho C_{\mathrm{p}}\frac{\partial T}{\partial t} \qquad (A.1)$$

For steady state operation, this equation becomes

$$\rho C_p \frac{\partial T}{\partial t} = 0$$
$$\frac{\partial}{\partial x}\left(k\frac{\partial T}{\partial x}\right) + \frac{\partial}{\partial y}\left(k\frac{\partial T}{\partial y}\right) + \frac{\partial}{\partial z}\left(k\frac{\partial T}{\partial z}\right) + q''' = 0 \qquad (A.2)$$

And for a one-dimensional case, this equation becomes

$$\frac{\partial T}{\partial y} = \frac{\partial T}{\partial z} = 0$$
$$\frac{\partial}{\partial x}\left(k\frac{\partial T}{\partial x}\right) + q''' = 0 \qquad (A.3)$$

And for constant thermal conductivity, this becomes the governing equation

$$k\frac{d^2 T}{dx^2} + q''' = 0 \Rightarrow \frac{d^2 T}{dx^2} + \frac{q'''}{k} = 0 \qquad (A.4)$$

Examining the substrate layer, the temperature profile can be determined in the following manner. The schematic and boundary conditions are shown in Fig. A.2.
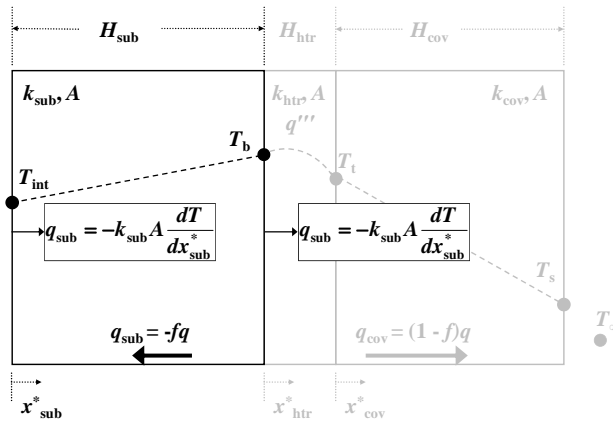
Fig. A.2 Schematic showing details of substrate layer.

For this layer, there is no heat generation, so the governing equation and boundary conditions are given by

$$\frac{d^2 T(x^*_{sub})}{dx^{*2}_{sub}} = 0$$

$$\frac{dT(x^*_{sub})}{dx^*_{sub}}\bigg|_{x^*_{sub}=0} = \frac{-q_{sub}}{Ak_{sub}}$$ (A.5)

$$\frac{dT(x^*_{sub})}{dx^*_{sub}}\bigg|_{x^*_{sub}=H_{sub}} = \frac{-q_{sub}}{Ak_{sub}}$$

Integrating the governing equation gives

$$\frac{dT(x^*_{sub})}{dx^*_{sub}} = C_1$$

$$T(x^*_{sub}) = C_1 x^*_{sub} + C_2$$ (A.6)

Applying either boundary condition in Eq. (A.5) gives the value of C_1 as

$$C_1 = \frac{-q_{sub}}{Ak_{sub}}$$ (A.7)

Applying this C_1 value to the expression for $T(x^*_{sub})$ from Eq. (A.6) gives

$$T(x^*_{sub}) = \frac{-q_{sub}}{Ak_{sub}} x^*_{sub} + C_2$$ (A.8)

Substituting the value for q_{sub} from Fig. A.2 gives the temperature in the substrate as

$$T(x^*_{sub}) = \frac{fq}{Ak_{sub}} x^*_{sub} + C_2$$ (A.9)

Examining the heater layer, the temperature profile can be determined in the following manner. The schematic and boundary conditions are shown in Fig. A.3.
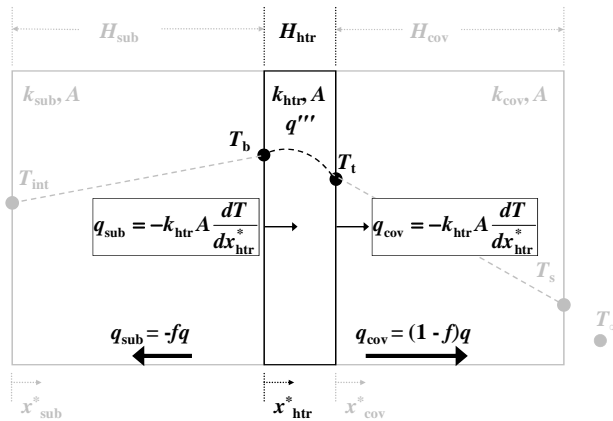
Fig. A.3 Schematic showing details of heater layer.

The governing equation and boundary conditions are given by

$$\frac{d^2 T(x^*_\mathrm{htr})}{dx^{*2}_\mathrm{htr}} + \frac{q'''}{k_\mathrm{htr}} = 0$$

$$\left. \frac{dT(x^*_\mathrm{htr})}{dx^*_\mathrm{htr}} \right|_{x^*_\mathrm{htr}=0} = \frac{-q_\mathrm{sub}}{Ak_\mathrm{htr}} \qquad \text{(A.10)}$$

$$\left. \frac{dT(x^*_\mathrm{htr})}{dx^*_\mathrm{htr}} \right|_{x^*_\mathrm{htr}=H_\mathrm{htr}} = \frac{-q_\mathrm{cov}}{Ak_\mathrm{htr}}$$

Integrating the governing equation gives

$$\frac{dT(x^*_\mathrm{htr})}{dx^*_\mathrm{htr}} = \frac{-q'''}{k_\mathrm{htr}} x^*_\mathrm{htr} + C_3$$

$$T(x^*_\mathrm{htr}) = \frac{-q'''}{2k_\mathrm{htr}} x^{*2}_\mathrm{htr} + C_3 x^*_\mathrm{htr} + C_4 \qquad \text{(A.11)}$$

Applying either boundary condition in Eq. (A.10) gives the value of C_3 as

$$C_3 = \frac{-q_\mathrm{sub}}{Ak_\mathrm{htr}} \qquad \text{(A.12)}$$

Applying this C_3 value to the expression for $T(x^*_\mathrm{htr})$ from Eq. (A.11) gives

$$T(x^*_\mathrm{htr}) = \frac{-q'''}{2k_\mathrm{htr}} x^{*2}_\mathrm{htr} + \frac{-q_\mathrm{sub}}{Ak_\mathrm{htr}} x^*_\mathrm{htr} + C_4 \qquad \text{(A.13)}$$

It should be noted that q''' can be written

$$q''' = \frac{q}{AH_\mathrm{htr}} \qquad \text{(A.14)}$$

Where q is the measured heater power. Substituting this value of q''' and the definition of q_sub from Fig. A.3 into Eq. (A.13) gives the temperature distribution in the heater layer as

$$T(x^*_\mathrm{htr}) = \frac{-q}{2Ak_\mathrm{htr}H_\mathrm{htr}} x^{*2}_\mathrm{htr} + \frac{fq}{Ak_\mathrm{htr}} x^*_\mathrm{htr} + C_4 \qquad \text{(A.15)}$$

Examining the glass cover layer, the temperature profile can be determined in the following manner. The schematic and boundary conditions are shown in Fig. A.4.
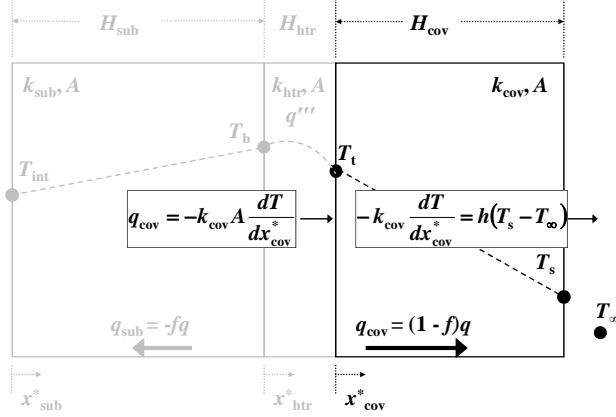
Fig. A.4 Schematic showing details of cover layer.

For this layer, there is no heat generation, so the governing equation and boundary conditions are given by

$$\frac{d^2 T(x_{cov}^*)}{dx_{cov}^{*2}} = 0$$

$$\frac{dT(x_{cov}^*)}{dx_{cov}^*}\bigg|_{x_{cov}^*=0} = \frac{-q_{cov}}{Ak_{cov}} \quad (A.16)$$

$$\frac{dT(x_{cov}^*)}{dx_{cov}^*}\bigg|_{x_{sub}^*=H_{sub}} = \frac{-h}{k_{cov}}T_s + \frac{h}{k_{cov}}T_\infty$$

Integrating the governing equation gives

$$\frac{dT(x_{cov}^*)}{dx_{cov}^*} = C_5$$
$$\quad (A.17)$$
$$T(x_{cov}^*) = C_5 x_{cov}^* + C_6$$

Applying the first boundary condition in Eq. (A.16) gives the value of C_5 as

$$C_5 = \frac{-q_{cov}}{Ak_{cov}} \quad (A.18)$$

Applying this C_5 value to the expression for $T(x^*_{cov})$ from Eq. (A.17) gives

$$T(x_{cov}^*) = \frac{-q_{cov}}{Ak_{cov}}x_{cov}^* + C_6 \quad (A.19)$$

Substituting the value for q_{cov} from Fig. A.2 gives the temperature in the substrate as

$$T(x_{cov}^*) = \frac{-(1-f)q}{Ak_{cov}}x_{cov}^* + C_6 \quad (A.20)$$

When taken together, Eqs. (A.9), (A.15), and (A.20) completely define the temperature profile through the entire three layers of the heater.   To develop an

expression for T_s based on T_{int} and the heater input power, the interface conditions that relate the temperatures in these three layers need to be accounted for. These interface conditions are given by

$$T(x^*_{sub})|_{x_{sub}=H_{sub}} = T(x^*_{htr})|_{x_{htr}=0} = T_B$$
$$T(x^*_{htr})|_{x_{htr}=H_{htr}} = T(x^*_{cov})|_{x_{cov}=0} = T_T$$

(A.21)

Substituting the expressions for $T(x^*_{sub})$ from Eq. (A.9) at $x^*_{sub} = H_{sub}$ and $T(x^*_{htr})$ from Eq. (A.15) at $x^*_{htr} = 0$ into the first interface condition from Eq. (A.21) gives

$$\frac{fq}{Ak_{sub}}H_{sub} + C_2 = \frac{-q}{2Ak_{htr}H_{htr}}(0)^2 + \frac{fq}{Ak_{htr}}(0) + C_4$$

$$C_4 = \frac{fq}{Ak_{sub}}H_{sub} + C_2$$

(A.22)

Similarly, substituting the expressions for $T(x^*_{htr})$ from Eq. (A.15) at $x^*_{htr} = H_{htr}$ and $T(x^*_{cov})$ from Eq. (A.20) at $x^*_{cov} = 0$ into the second interface condition from Eq. (A.21) gives

$$\frac{-q}{2Ak_{htr}H_{htr}}H_{htr}^2 + \frac{fq}{Ak_{htr}}H_{htr} + C_4 = \frac{-(1-f)q}{Ak_{cov}}(0) + C_6$$

$$C_6 = \frac{-q}{2Ak_{htr}}H_{htr} + \frac{fq}{Ak_{htr}}H_{htr} + C_4$$

(A.23)

Now substituting the expression for C4 from Eq. (A.22) into the expression for C6 from Eq. (A.23) yields

$$C_6 = \frac{-qH_{htr}}{2Ak_{htr}} + \frac{fqH_{htr}}{Ak_{htr}} + \frac{fqH_{sub}}{Ak_{sub}} + C_2$$

(A.24)

This expression for C_6 can be applied to the expression for $T(x^*_{cov})$ from Eq. (A.20) to yield

$$T(x^*_{cov}) = \frac{-(1-f)q}{Ak_{cov}}x^*_{cov} - \frac{qH_{htr}}{2Ak_{htr}} + \frac{fqH_{htr}}{Ak_{htr}} + \frac{fqH_{sub}}{Ak_{sub}} + C_2$$

(A.25)

The expression for $T(x^*_{sub})$ from Eq. (A.9) can be solved for C_2 to yield

$$C_2 = T(x^*_{sub}) - \frac{fq}{Ak_{sub}}x^*_{sub}$$

(A.26)

This expression for C2 can be applied to Eq. (A.25) to yield

$$T(x_{\mathrm{cov}}^*) = \frac{-(1-f)q}{Ak_{\mathrm{cov}}} x_{\mathrm{cov}}^* - \frac{qH_{\mathrm{htr}}}{2Ak_{\mathrm{htr}}} + \frac{fqH_{\mathrm{htr}}}{Ak_{\mathrm{htr}}}$$

$$+ \frac{fqH_{\mathrm{sub}}}{Ak_{\mathrm{sub}}} + T(x_{\mathrm{sub}}^*) - \frac{fq}{Ak_{\mathrm{sub}}} x_{\mathrm{sub}}^* \tag{A.27}$$

The surface temperature is the temperature from this expression for $T(x^*_{\mathrm{cov}})$ at $x^*_{\mathrm{cov}} = H_{\mathrm{cov}}$ ($T_{\mathrm{s}} = T(H_{\mathrm{cov}})$

$$T_S = \frac{-(1-f)q}{Ak_{\mathrm{cov}}} H_{\mathrm{cov}} - \frac{qH_{\mathrm{htr}}}{2Ak_{\mathrm{htr}}} + \frac{fqH_{\mathrm{htr}}}{Ak_{\mathrm{htr}}}$$

$$+ \frac{fqH_{\mathrm{sub}}}{Ak_{\mathrm{sub}}} + T(x_{\mathrm{sub}}^*) - \frac{fq}{Ak_{\mathrm{sub}}} x_{\mathrm{sub}}^* \tag{A.28}$$

Simplifying this expression yields

$$T_S = \frac{q}{A} \left[\frac{H_{\mathrm{cov}}}{k_{\mathrm{cov}}} (f-1) + \frac{H_{\mathrm{htr}}}{k_{\mathrm{htr}}} \left(f - \frac{1}{2} \right) \right.$$

$$\left. + \frac{f}{k_{\mathrm{sub}}} (H_{\mathrm{sub}} - x_{sub}^*) \right] + T(x_{\mathrm{sub}}^*) \tag{A.29}$$

Finally, to obtain an expression for T_{s} in terms of T_{int}, substitute $x^*_{\mathrm{sub}} = 0$, so that $T(x^*_{\mathrm{sub}} = 0) = T_{\mathrm{int}}$ into this expression for T_{s} to obtain

$$T_S = \frac{q}{A} \left[\frac{H_{\mathrm{cov}}}{k_{\mathrm{cov}}} (f-1) + \frac{H_{\mathrm{htr}}}{k_{\mathrm{htr}}} \left(f - \frac{1}{2} \right) + \frac{H_{\mathrm{sub}}}{k_{\mathrm{sub}}} f \right] + T_{\mathrm{int}} \tag{A.30}$$

This is the expression that will be used for calculating the surface temperature for all of the data reduction that will be done for this document.

APPENDIX B. DATA ACQUISITION SCAN SETUP SCREEN SHOTS

The following screen shots show the data acquisition scan setup as it was for the data presented in this document.

Fig. B.1 Data acquisition scan setup for flights

Sept04FlightBot - Data 05/14/08 13:07:10 - Agilent BenchLink Data Logger

File   Edit   View   Scan   Channel   Graphics   Instrument   Help

None   Off

ID	Sca	Name	Function	Range	Resoluti	Advance	Scal	Gain(M	Offset	Label	Test	High	Low	H/W Ala	Advance	Comment
209	☐	FC-72 reservoir in	Temp (type E)			Default	☐	1.0	0.0	C	Off	0.0	0.0	Alarm1		
210	☑	FC-72 reservoir out	Temp (type E)			Default	☐	1.0	0.0	C	Off	0.0	0.0	Alarm1		
211	☐	reheater in - top	Temp (type E)			Default	☐	1.0	0.0	C	Off	0.0	0.0	Alarm1		
212	☑	reheater in - bottom	Temp (type E)			Default	☐	1.0	0.0	C	Off	0.0	0.0	Alarm1		
213	☑	g-x axis	DC volts	Auto	5.5 digits	Default	☑	-.333333	0.0	g	Off	0.0	0.0	Alarm1		
214	☑	g-y axis	DC volts	Auto	5.5 digits	Default	☑	-.333333	0.0	g	Off	0.0	0.0	Alarm1		
215	☐	reheater out - top	Temp (type E)			Default	☐	1.0	0.0	C	Off	0.0	0.0	Alarm1		
216	☑	reheater out - botto	Temp (type E)			Default	☐	1.0	0.0	C	Off	0.0	0.0	Alarm1		
217	☐		Temp (type E)			Default	☐	1.0	0.0	C	Off	0.0	0.0	Alarm1		
218	☐		Temp (type E)			Default	☐	1.0	0.0	C	Off	0.0	0.0	Alarm1		
219	☑	g-z axis	DC volts	Auto	5.5 digits	Default	☑	-.333333	0.0	g	Off	0.0	0.0	Alarm1		
220	☑	ambient T/C	Temp (type E)			Default	☐	1.0	0.0	C	Off	0.0	0.0	Alarm1		
221	☐		DC current	Auto	5.5 digits	Default	☐	1.0	0.0	ADC	Off	0.0	0.0	Alarm1		
222	☐		DC current	Auto	5.5 digits	Default	☐	1.0	0.0	ADC	Off	0.0	0.0	Alarm1		
301	☐	wall temp	Temp (type E)			Advance	☑	.99359	.11368	C	Off	0.0	0.0	Alarm1		
302	☑	chamber vapor temp	Temp (type E)			Advance	☑	.99296	.09582	C	Off	0.0	0.0	Alarm1		
303	☑	bot-lower film temp	Temp (type E)			Advance	☑	.99358	.08848	C	Off	0.0	0.0	Alarm1		
304	☑	bot-upper film temp	Temp (type E)			Advance	☑	.99414	.08421	C	Off	0.0	0.0	Alarm1		
305	☑	bot-nozzle in temp	Temp (type E)			Advance	☑	.99443	.06825	C	Off	0.0	0.0	Alarm1		
306	☑	bot-wall temp (sump)	Temp (type E)			Advance	☑	.99523	.08034	C	Off	0.0	0.0	Alarm1		
307	☐	top-wall temp (sump)	Temp (type E)			Advance	☑	.99257	.11074	C	Off	0.0	0.0	Alarm1		
308	☑	bot-current	DC volts	Auto	5.5 digits	Default	☑	10	0.0	Amp	Off	0.0	0.0	Alarm1		current = voltage reading X10, M"1
309	☐	top-current	DC volts	Auto	5.5 digits	Default	☑	10	0.0	Amp	Off	0.0	0.0	Alarm1		current = voltage reading X10, M"1
310	☑	Nozzle-flow rate	DC volts	Auto	5.5 digits	Default	☑	4.41913	0.96621	gph	Off	0.0	0.0	Alarm1		
311	☑	Drain-flow rate	DC volts	Auto	5.5 digits	Default	☑	4.40992	0.30280	gph	Off	0.0	0.0	Alarm1		
312	☑	H2O-flow rate	Frequency	Auto	5.5 digits	Advance	☑	.012157	.562551	gph	Off	0.0	0.0	Alarm1		
313	☑	chamber press	DC volts	Auto	5.5 digits	Default	☑	20	-10	psia	Off	0.0	0.0	Alarm1		
314	☑	pmp3 in press	DC volts	Auto	5.5 digits	Default	☑	20	-10	psia	Off	0.0	0.0	Alarm1		
315	☑	pmp3 out press	DC volts	Auto	5.5 digits	Default	☑	40	-20	psia	Off	0.0	0.0	Alarm1		
316	☑	pmp2 out press	DC volts	Auto	5.5 digits	Default	☑	40	-20	psia	Off	0.0	0.0	Alarm1		
317	☑	pmp1 out press	DC volts	Auto	5.5 digits	Default	☑	40	-20	psia	Off	0.0	0.0	Alarm1		
318	☑	H2O pmp out press	DC volts	Auto	5.5 digits	Default	☑	20	-10	psia	Off	0.0	0.0	Alarm1		
319	☐	top heater voltage	DC volts	Auto	5.5 digits	Default	☐	1.0	0.0	VDC	Off	0.0	0.0	Alarm1		
320	☑	bot heater voltage	DC volts	Auto	5.5 digits	Default	☐	1.0	0.0	VDC	Off	0.0	0.0	Alarm1		
321	☐		DC current	Auto	5.5 digits	Default	☐	1.0	0.0	ADC	Off	0.0	0.0	Alarm1		
322	☐		DC current	Auto	5.5 digits	Default	☐	1.0	0.0	ADC	Off	0.0	0.0	Alarm1		
900	☑	bot pwr, W	Computed			Default	☑	1.0	0.0	W	Off	0.0	0.0			
901	☐	top pwr, W	Computed			Default	☑	1.0	0.0	W	Off	0.0	0.0			

Scan Setup   Graphics Setup 1   Graphics Setup 2

HP34901A   HP34901A   HP34901A   SIMULATED

Start   Sept04FlightBot ...   Sept04_1bmp - P...   1:14 PM

Fig. B.2 Data acquisition scan setup for flights

67

APPENDIX C. THERMOCOUPLE CALIBRATIONS

The thermocouples in the pedestal and the chamber were calibrated following a procedure similar to that as described in Puterbaugh[16] and Elston[40]. A Visual Basic program, written by Mr. Richard Harris (UDRI), was used to perform the calibration. This program set the temperature on the calibration bath, allowed a period of time for this temperature to stabilize, and then recorded a series of temperatures from the RTD and each of the thermocouples being calibrated. The calibrations covered the range of temperatures that were expected to be encountered during operation. The temperature reading from the RTD could be plotted against the temperature reading from each individual thermocouple, and a calibration curve (in this case linear) could be applied. The slope and intercept of this calibration curve were then input into the data acquisition system for each individual thermocouple. The following pages show the results from these calibrations for the pedestal and for the chamber thermocouples that provided data that were reported in this document, including T_{lf}, T_{uf}, and T_{noz}.

Table C.1 Pedestal thermocouple calibration data, including predictions and residuals

RTD Temp, °C	T_1, °C	Predicted T_1, °C	Abs (Residual)	T_2, °C	Predicted T_2, °C	Abs (Residual)	T_3, °C	Predicted T_3, °C	Abs (Residual)	T_4, °C	Predicted T_4, °C	Abs (Residual)
34.8	35.8	34.7	0.022	34.8	34.7	0.053	34.8	34.7	0.038	34.8	34.7	0.038
39.7	40.8	39.7	0.004	39.8	39.7	0.016	39.9	39.7	0.008	39.9	39.7	0.007
44.7	45.8	44.7	0.005	44.9	44.7	0.013	44.9	44.7	0.008	44.9	44.7	0.006
49.8	50.9	49.8	0.011	49.9	49.8	0.009	49.9	49.8	0.006	50.0	49.8	0.005
54.7	55.9	54.7	0.006	54.9	54.7	0.011	54.9	54.7	0.016	54.9	54.7	0.014
59.7	60.9	59.7	0.006	59.9	59.7	0.001	59.9	59.7	0.007	59.9	59.7	0.005
64.7	65.9	64.8	0.027	65.0	64.8	0.052	65.0	64.8	0.046	65.0	64.8	0.046
69.7	70.9	69.7	0.003	69.9	69.7	0.024	70.0	69.7	0.018	70.0	69.7	0.019
74.7	75.9	74.7	0.007	74.9	74.7	0.018	75.0	74.7	0.016	75.0	74.7	0.019
79.7	81.0	79.7	0.038	80.0	79.7	0.050	80.1	79.7	0.042	80.1	79.7	0.046
84.7	86.0	84.7	0.018	85.0	84.7	0.023	85.1	84.7	0.017	85.1	84.7	0.022
89.7	91.0	89.7	0.006	89.9	89.7	0.007	90.1	89.7	0.001	90.1	89.7	0.001
94.7	96.0	94.7	0.021	94.9	94.7	0.008	95.1	94.7	0.013	95.1	94.7	0.016
99.7	101.0	99.7	0.008	100.0	99.7	0.008	100.1	99.7	0.000	100.1	99.7	0.000
104.7	106.0	104.7	0.000	105.0	104.6	0.016	105.1	104.6	0.020	105.1	104.6	0.019
109.6	111.0	109.7	0.016	110.0	109.6	0.000	110.1	109.6	0.005	110.1	109.6	0.005
114.7	116.0	114.7	0.008	115.0	114.7	0.013	115.2	114.7	0.014	115.2	114.7	0.011
119.6	121.0	119.6	0.044	119.9	119.6	0.044	120.1	119.6	0.033	120.1	119.6	0.037
99.7	101.0	99.7	0.004	100.0	99.7	0.004	100.1	99.7	0.003	100.1	99.7	0.001
74.7	75.9	74.7	0.003	74.9	74.7	0.016	75.0	74.7	0.004	75.0	74.7	0.005
52.1	53.2	52.1	0.036	52.3	52.1	0.017	52.3	52.1	0.015	52.3	52.1	0.021

RTD Temp, °C	T_5, °C	Predicted T_5, °C	Abs (Residual)	T_6, °C	Predicted T_6, °C	Abs (Residual)	T_7, °C	Predicted T_7, °C	Abs (Residual)
34.8	34.8	34.7	0.033	34.8	34.7	0.027	34.8	34.7	0.018
39.7	39.8	39.7	0.004	39.9	39.7	0.003	39.8	39.8	0.008
44.7	44.9	44.7	0.004	44.9	44.7	0.001	44.9	44.7	0.001
49.8	49.9	49.8	0.007	49.9	49.8	0.007	49.9	49.7	0.009
54.7	54.9	54.7	0.013	54.9	54.7	0.015	54.9	54.7	0.028
59.7	59.9	59.7	0.000	60.0	59.7	0.001	59.9	59.7	0.010
64.7	65.0	64.8	0.050	65.1	64.8	0.047	65.0	64.8	0.036
69.7	70.0	69.7	0.025	70.0	69.7	0.024	70.0	69.7	0.011
74.7	75.0	74.7	0.006	75.1	74.7	0.005	75.0	74.7	0.007
79.7	80.1	79.7	0.023	80.1	79.7	0.026	80.1	79.7	0.029
84.7	85.1	84.7	0.004	85.1	84.7	0.005	85.1	84.7	0.012
89.7	90.1	89.7	0.012	90.1	89.7	0.005	90.1	89.7	0.005
94.7	95.1	94.7	0.009	95.1	94.7	0.013	95.1	94.7	0.025
99.7	100.2	99.7	0.003	100.2	99.7	0.003	100.2	99.7	0.015
104.7	105.2	104.6	0.017	105.2	104.6	0.018	105.1	104.6	0.018
109.6	110.2	109.6	0.001	110.2	109.6	0.004	110.2	109.6	0.005
114.7	115.2	114.7	0.006	115.3	114.7	0.004	115.2	114.6	0.025
119.6	120.2	119.6	0.018	120.2	119.6	0.022	120.2	119.6	0.026
99.7	100.2	99.7	0.008	100.2	99.7	0.010	100.1	99.7	0.018
74.7	75.0	74.7	0.007	75.0	74.7	0.011	75.0	74.7	0.014
52.1	52.3	52.1	0.015	52.3	52.1	0.022	52.3	52.1	0.012
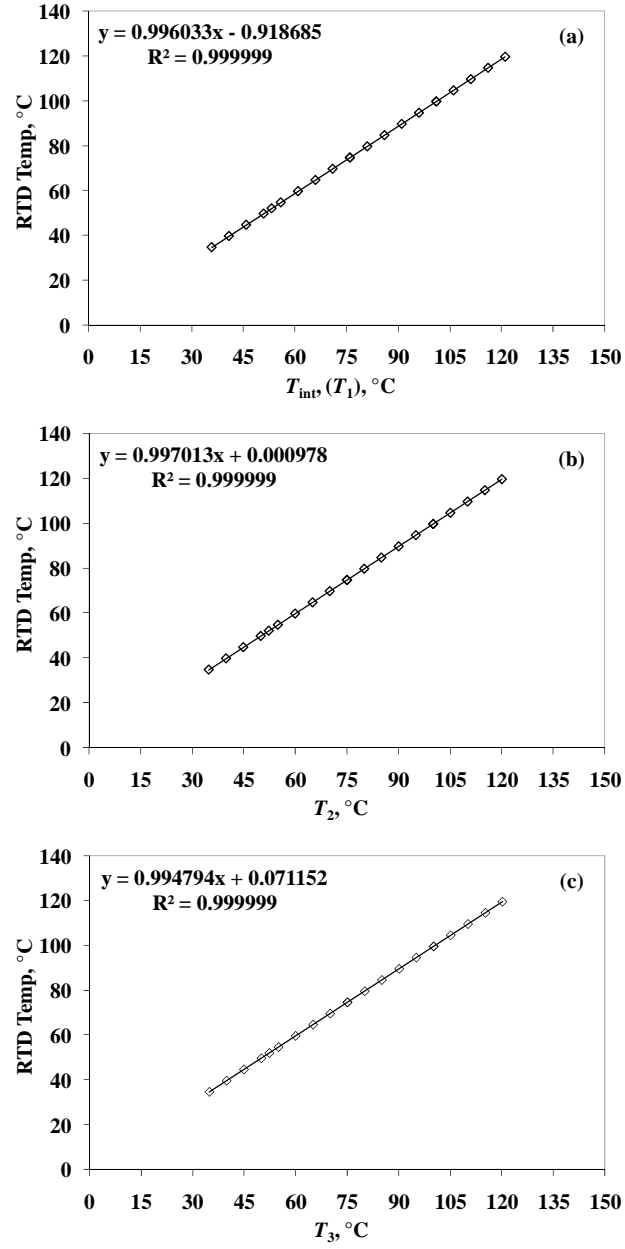
Fig. C.1 Plots showing calibration curves for the pedestal thermocouples (a) T_{int}, (b) T_2, (c) T_3
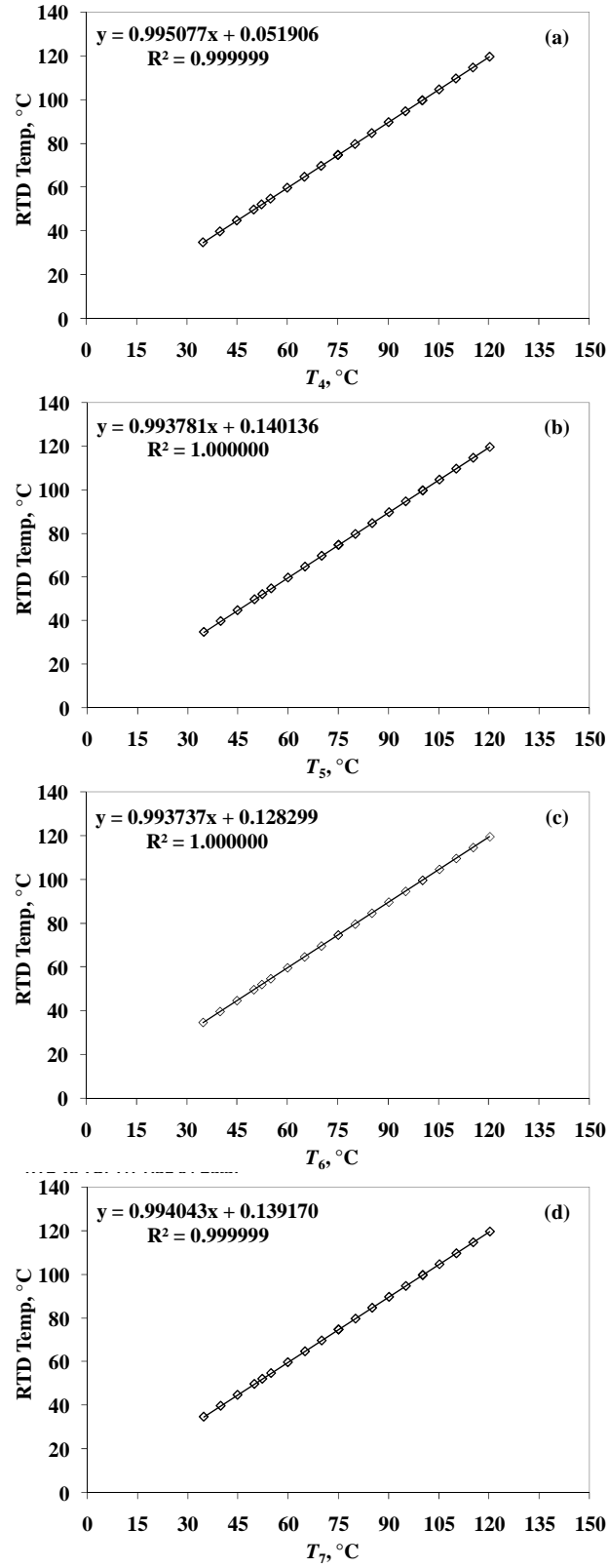
Fig. C.2 Plots showing calibration curves for the pedestal thermocouples (a) T_4, (b) T_5, (c) T_6, and (d) T_7

71

Table C.2 Chamber thermocouple calibration data, including predictions and residuals

RTD Temp, °C	T_{lf}, °C	Predicted T_{lf}, °C	Abs (Residual)	T_{uf}, °C	Predicted T_{uf}, °C	Abs (Residual)	T_{noz}, °C	Predicted T_{noz}, °C	Abs (Residual)
35.1	35.3	35.1	0.004	35.2	35.1	0.002	35.3	35.1	0.003
40.1	40.3	40.1	0.004	40.3	40.1	0.007	40.3	40.1	0.005
45.1	45.3	45.1	0.004	45.3	45.1	0.005	45.3	45.1	0.001
50.2	50.4	50.2	0.009	50.4	50.2	0.007	50.4	50.2	0.006
55.1	55.4	55.1	0.007	55.4	55.1	0.006	55.4	55.1	0.007
60.2	60.4	60.1	0.024	60.4	60.1	0.023	60.4	60.1	0.021
65.2	65.5	65.2	0.047	65.5	65.2	0.048	65.5	65.2	0.049
70.1	70.5	70.1	0.006	70.5	70.1	0.004	70.5	70.1	0.004
75.2	75.6	75.2	0.006	75.5	75.2	0.009	75.5	75.2	0.009
80.1	80.6	80.1	0.023	80.5	80.1	0.030	80.5	80.1	0.029
85.1	85.6	85.1	0.017	85.6	85.1	0.022	85.5	85.1	0.023
90.1	90.6	90.1	0.001	90.6	90.1	0.000	90.6	90.1	0.004
95.1	95.6	95.1	0.016	95.6	95.1	0.015	95.6	95.1	0.021
100.1	100.7	100.1	0.011	100.6	100.1	0.011	100.6	100.1	0.002
105.1	105.7	105.1	0.002	105.6	105.1	0.006	105.6	105.1	0.013
110.1	110.7	110.1	0.001	110.7	110.1	0.003	110.6	110.1	0.010
115.1	115.8	115.1	0.008	115.7	115.1	0.005	115.7	115.1	0.009
120.1	120.7	120.0	0.055	120.6	120.0	0.055	120.6	120.0	0.049
117.6	118.2	117.5	0.040	118.2	117.5	0.041	118.1	117.5	0.042
112.6	113.2	112.6	0.004	113.2	112.6	0.003	113.2	112.6	0.006
107.6	108.2	107.6	0.006	108.1	107.6	0.005	108.1	107.6	0.001
102.6	103.1	102.6	0.005	103.1	102.6	0.005	103.1	102.6	0.002
97.6	98.2	97.6	0.036	98.1	97.6	0.036	98.1	97.6	0.036
92.6	93.1	92.6	0.001	93.1	92.6	0.004	93.1	92.6	0.006
87.6	88.1	87.6	0.019	88.0	87.6	0.020	88.0	87.6	0.021
82.7	83.1	82.7	0.024	83.1	82.7	0.023	83.1	82.7	0.026
77.6	78.0	77.6	0.009	78.0	77.6	0.010	78.0	77.6	0.012
72.6	73.0	72.6	0.006	72.9	72.6	0.006	72.9	72.6	0.001
67.6	67.9	67.6	0.016	67.9	67.6	0.015	67.9	67.6	0.022
62.7	63.1	62.8	0.036	63.0	62.7	0.033	63.0	62.7	0.032
57.6	57.9	57.6	0.053	57.8	57.6	0.048	57.8	57.6	0.051
52.7	52.9	52.6	0.030	52.9	52.6	0.034	52.9	52.6	0.034
47.6	47.9	47.7	0.023	47.9	47.7	0.027	47.9	47.7	0.024
42.7	42.8	42.7	0.012	42.8	42.7	0.013	42.8	42.6	0.015
37.7	37.8	37.6	0.018	37.8	37.6	0.023	37.8	37.6	0.022
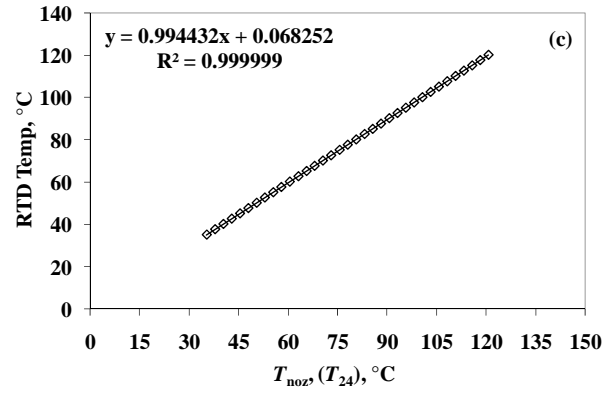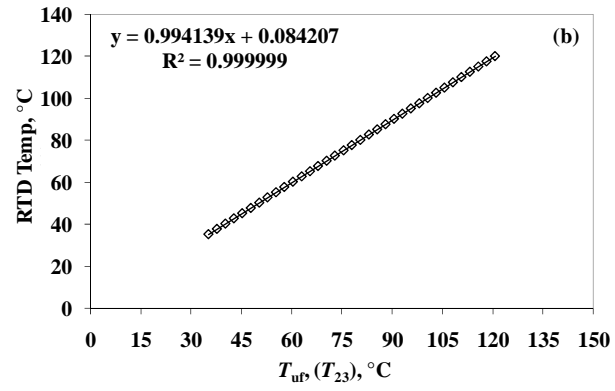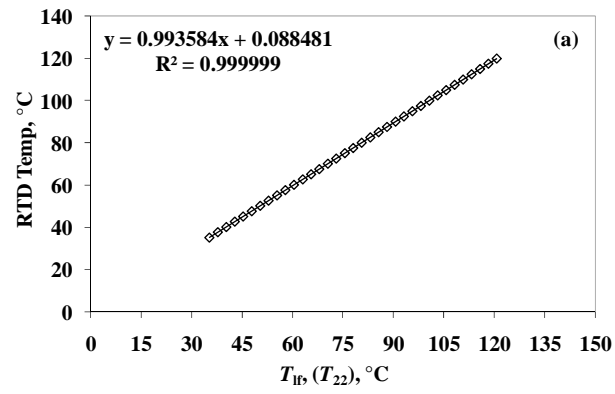
Fig. C.3 Plots showing calibration curves for the chamber thermocouples (a) T_{lf}, (b) T_{uf}, and (c) T_{noz}

APPENDIX D. MANUFACTURER FLOWMETER CALIBRATION

The calibration curves in the data acquisition system for the flowmeter were developed from data supplied by the manufacturer. As mentioned previously, the flowmeter was a Sponsler MF90CBPHA4X-V Lo-Flo Series flowmeter with a SP711-3 3-Wire Analog Transmitter. The manufacturer supplied calibration data that related a frequency output from the flowmeter itself, and this data, along with the associated linear fit and residuals, are shown in Fig. D.1(a) and Table D.1. The manufacturer also supplied calibration data for the Analog Transmitter which related the input frequency to an output voltage. The curve fit from Fig. D.1(a) was used to convert these input frequencies to flow rates. This calculated flow rate was then related to the output voltage from the Analog Transmitter data to obtain the required flow rate/voltage curve fit as shown in Fig. D.1(b). This curve was then input into the data acquisition system to convert measured voltage to flow rate.

Table D.1 Manufacturer calibration data and residuals for flowmeter

Manufacturer Flow Rate, gpm	Manufacturer Frequency, Hz	Predicted Flow, gpm	Abs(Residual), gpm	Abs(Residual), gph
0.846	1834	0.844	0.0015	0.088
0.797	1727	0.796	0.0015	0.088
0.770	1682	0.776	0.0052	0.312
0.722	1564	0.722	0.0004	0.022
0.674	1480	0.684	0.0104	0.626
0.642	1383	0.640	0.0014	0.087
0.608	1308	0.607	0.0008	0.045
0.607	1308	0.607	0.0000	0.001
0.537	1152	0.536	0.0002	0.012
0.476	1012	0.473	0.0028	0.165
0.462	983	0.460	0.0020	0.122
0.463	984	0.460	0.0026	0.156
0.399	839	0.395	0.0040	0.241
0.329	685	0.325	0.0037	0.219
0.328	684	0.325	0.0028	0.171
0.247	507	0.245	0.0019	0.112
0.208	421	0.206	0.0019	0.114
0.191	386	0.191	0.0008	0.049
0.058	107	0.065	0.0062	0.371
0.027	37	0.033	0.0056	0.337

Manufacturer Frequency, Hz	Calculated Flow, Curve Fit From Above, gpm	Manufacturer Volts Out, V	Predicted Flow, Curve Fit From Transmitter Data, gpm	Predicted Flow, Curve Fit From Transmitter Data, gph
0	0.016	0	0.016	0.966
408	0.200	2.5	0.200	12.014
816	0.384	5	0.384	23.062
1223	0.568	7.5	0.568	34.110
1631	0.753	10	0.753	45.158

gpm			gph	
Manufacturer's Slope, gpm/V	Manufacturer's Intercept, gpm		Manufacturer's Slope, gph/V	Manufacturer's Intercept, gph
0.073652	0.016104		4.419134	0.966212
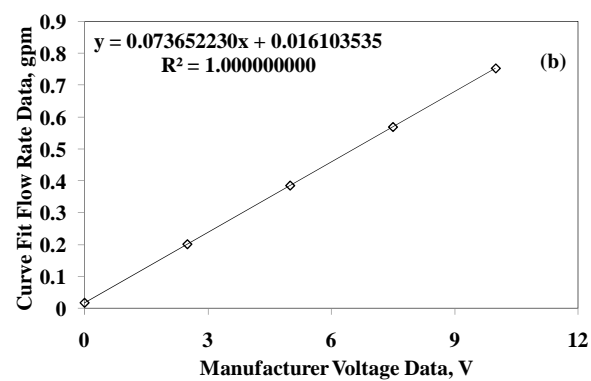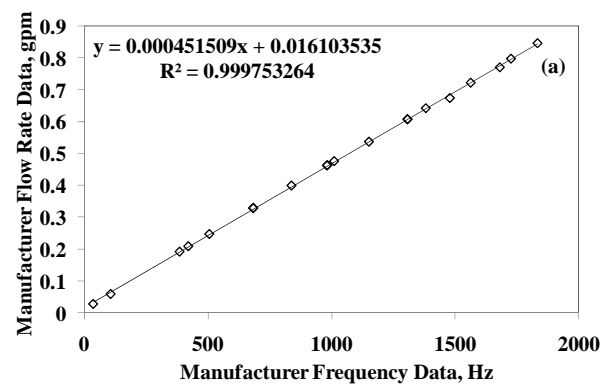
Fig. D.1 Plots showing curve fits for flowmeter calibrations (a) flow rate versus flow meter frequency and (b) calculated flow rate versus voltage output

APPENDIX E. FC-72 PROPERTY DATA

The various properties for FC-72 that are presented herein are based on property information given in Geisler[59]. Geisler references a data sheet from 3M from 1990. Several attempts were made to obtain this data sheet, but were unsuccessful. Therefore, data and equations from Geisler were used. Formulas were given for specific heat, thermal conductivity and surface tension, and a parametric table presented data for saturation pressure, viscosity, and density. Where it was possible, the data from Geisler was checked against equations found in a 3M data sheet from 2000,[52] and the surface tension data was checked against data from Skripov and Firsov.[60] For saturation pressure, viscosity, and density, curves were fit to the parametric data, which were used along with the given equations for specific heat, thermal conductivity and surface tension, to determine FC-72 properties in the present research. The following plots and tables show the details of these property calculations. The equations listed on the plots are either the given formula for the property, or a curve fit to the parametric data.

Table E.1 Specific heat formula comparison

Temperature, °C	Specific Heat, Geisler (2007)[59], J/(kg-K)	Specific Heat, 3M (2000)[52], J/(kg-K)	Abs(Difference), 3M Formula to Data, J/(kg-K)	% Difference
0	1011	1014	2.99	0.30
5	1019	1022	3.04	0.30
10	1026	1030	3.09	0.30
15	1034	1037	3.14	0.30
20	1042	1045	3.19	0.31
25	1050	1053	3.24	0.31
30	1057	1061	3.28	0.31
35	1065	1068	3.33	0.31
40	1073	1076	3.38	0.32
45	1080	1084	3.43	0.32
50	1088	1092	3.48	0.32
55	1096	1099	3.53	0.32
56.6	1098	1102	3.54	0.32
60	1104	1107	3.58	0.32
65	1111	1115	3.63	0.33
70	1119	1123	3.67	0.33
75	1127	1131	3.72	0.33
80	1135	1138	3.77	0.33
85	1142	1146	3.82	0.33
90	1150	1154	3.87	0.34
95	1158	1162	3.92	0.34
100	1165	1169	3.96	0.34

$$y = 1.5443*(T+273.15) + 589.18$$
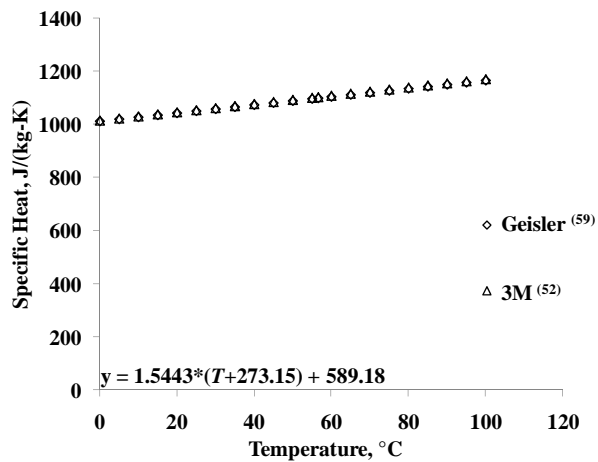
Fig. E.1 Specific heat versus temperature

Table E.2 Thermal conductivity formula comparison

Temperature, °C	Thermal Conductivity: Geisler (2007)[59], W/(m-K)	Thermal Conductivity: 3M Sheet (2000)[52], W/(m-K)	Abs(Difference), 3M Formula to Data, W/(m-K)	% Difference
0	5.88E-02	6.00E-02	1.23E-03	2.09
5	5.82E-02	5.95E-02	1.27E-03	2.18
10	5.76E-02	5.89E-02	1.30E-03	2.26
15	5.70E-02	5.84E-02	1.33E-03	2.33
20	5.64E-02	5.78E-02	1.37E-03	2.43
25	5.59E-02	5.73E-02	1.40E-03	2.51
30	5.53E-02	5.67E-02	1.44E-03	2.61
35	5.47E-02	5.62E-02	1.47E-03	2.69
40	5.41E-02	5.56E-02	1.50E-03	2.77
45	5.35E-02	5.51E-02	1.54E-03	2.88
50	5.29E-02	5.45E-02	1.57E-03	2.97
55	5.23E-02	5.40E-02	1.61E-03	3.08
56.6	5.22E-02	5.38E-02	1.61E-03	3.09
60	5.18E-02	5.34E-02	1.64E-03	3.17
65	5.12E-02	5.29E-02	1.67E-03	3.26
70	5.06E-02	5.23E-02	1.71E-03	3.38
75	5.00E-02	5.18E-02	1.74E-03	3.48
80	4.94E-02	5.12E-02	1.78E-03	3.60
85	4.88E-02	5.07E-02	1.81E-03	3.71
90	4.83E-02	5.01E-02	1.84E-03	3.81
95	4.77E-02	4.96E-02	1.88E-03	3.94
100	4.71E-02	4.90E-02	1.91E-03	4.06

$$y = -0.0001168*(T+273.15) + 0.090672$$
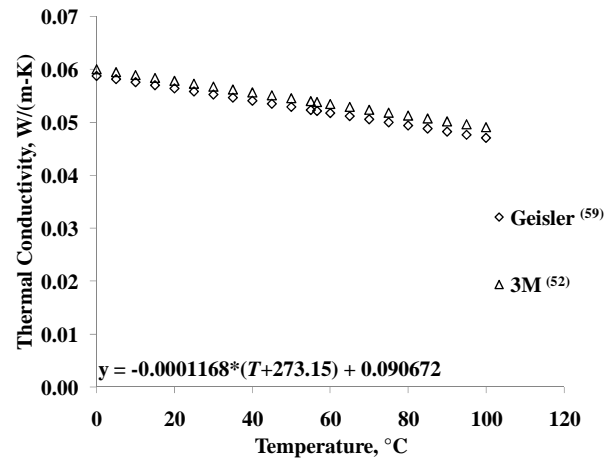
Fig. E.2 Thermal conductivity versus temperature

Table E.3 Surface tension formula comparison

Temperature, °C	Surface Tension, Geisler (2007)[59], kg/s²	Surface Tension, Skripov and Firsov (1968)[60], dynes/cm	Surface Tension, Skripov and Firsov (1968)[60], kg/s²	Abs(Difference), J/(kg-K)	% Difference
0	1.33E-02				
5	1.29E-02				
10	1.24E-02				
15	1.20E-02				
20	1.15E-02	11.00	1.10E-02	4.96E-04	4.32
25	1.10E-02				
30	1.06E-02				
35	1.01E-02				
40	9.71E-03				
41	9.62E-03	9.44	9.44E-03	1.81E-04	1.88
45	9.27E-03				
50	8.84E-03				
55	8.41E-03				
56.6	8.27E-03				
59.4	8.04E-03	7.78	7.78E-03	2.56E-04	3.18
60	7.98E-03				
65	7.56E-03				
70	7.15E-03				
74.6	6.77E-03	6.60	6.60E-03	1.72E-04	2.54
75	6.74E-03				
80	6.33E-03				
81.6	6.21E-03	6.04	6.04E-03	1.65E-04	2.66
85	5.93E-03				
90	5.54E-03				
93.4	5.27E-03	4.85	4.85E-03	4.23E-04	8.02
95	5.15E-03				
100	4.77E-03				

$$y = 0.042705*(1.0-((273.15 + T))/451.65))^{(1.2532)}$$
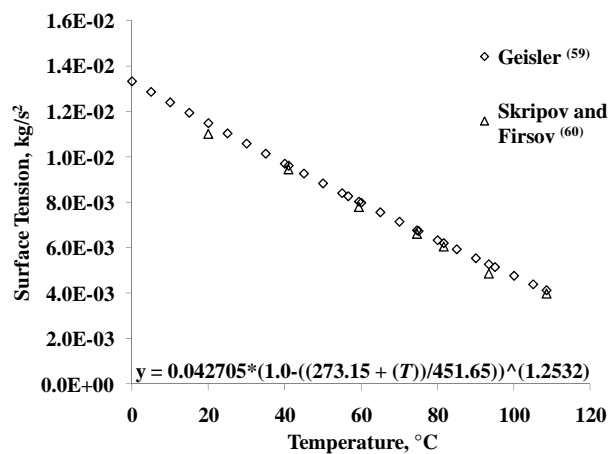
Fig. E.3 Surface tension versus temperature

Table E.4 Saturation temperature curve fit comparison

Pressure, kPa	Pressure, atm	Pressure, psia	Temperature: Geisler (2007)[59], °C	3rd Order Curve Fit, °C	Abs(Difference): Fit to Data, °C	% Difference	Temperature: Formula, 3M Sheet (2000)[52], °C	Abs(Difference): 3M Formula to Data	% Difference
23.5	0.23	3.4	20	20.3	0.33	1.64	18.4	1.61	8.03
30.0	0.30	4.4	25	25.1	0.07	0.27	24.3	0.73	2.93
36.6	0.36	5.3	30	29.5	0.53	1.75	29.2	0.77	2.56
45.7	0.45	6.6	35	35.0	0.05	0.14	35.0	0.00	0.01
54.7	0.54	7.9	40	39.7	0.28	0.71	39.8	0.17	0.43
67.2	0.66	9.7	45	45.4	0.38	0.84	45.5	0.52	1.15
79.5	0.79	11.5	50	50.1	0.09	0.18	50.4	0.36	0.72
96.0	0.95	13.9	55	55.3	0.28	0.51	55.9	0.91	1.66
101	1.00	14.7	56.6	56.8	0.15	0.27	57.5	0.93	1.64
112	1.11	16.3	60	59.6	0.36	0.59	60.7	0.74	1.23
134	1.32	19.4	65	64.8	0.23	0.36	66.2	1.20	1.85
155	1.53	22.5	70	70.2	0.15	0.22	71.0	1.00	1.42

$$y = 5.27781\text{E-}03P^3 - 2.93346\text{E-}01P^2 + 7.07482\text{E+}00P - 5.97600\text{E-}01$$
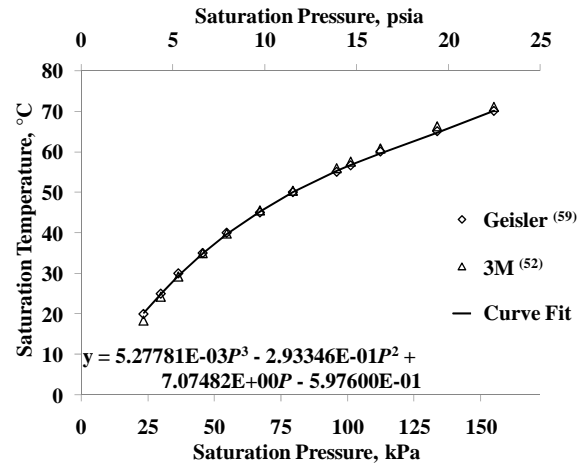
Fig. E.4 Saturation temperature versus pressure

Table E.5 Absolute viscosity curve fit comparison

Temperature, °C	Geisler (2007)[59]				3M (2000)[52] (Points from Graphical Data)		
	Absolute Viscosity: Geisler (2007)[59], kg/(m-s)	3rd Order Curve Fit, kg/(m-s)	Abs(Difference): Fit to Data, kg/(m-s)	% Difference	Kinematic Viscosity: 3M (2000)[52], m²/s	Density: Linear Formula, 3M (2000)[52], kg/m³	Absolute Viscosity: 3M (2000)[52], kg/(m-s)
0	9.50E-04	9.33E-04	1.68E-05	1.771			
3	-	8.93E-04	-	-	5.00E-07	1732	8.66E-04
5	8.74E-04	8.67E-04	6.77E-06	0.775			
9	-	8.19E-04	-	-	4.50E-07	1717	7.72E-04
10	8.00E-04	8.07E-04	7.07E-06	0.884			
15	7.43E-04	7.51E-04	8.49E-06	1.142			
18	-	7.20E-04	-	-	4.00E-07	1693	6.77E-04
20	6.87E-04	7.00E-04	1.36E-05	1.987			
25	6.44E-04	6.54E-04	1.00E-05	1.558			
29	-	6.19E-04	-	-	3.50E-07	1664	5.83E-04
30	6.01E-04	6.11E-04	1.00E-05	1.666			
35	5.68E-04	5.72E-04	4.37E-06	0.769			
40	5.35E-04	5.37E-04	1.97E-06	0.368			
45	5.09E-04	5.06E-04	3.50E-06	0.688	3.00E-07	1623	4.87E-04
50	4.83E-04	4.77E-04	5.97E-06	1.236			
53	-	4.61E-04	-	-	2.80E-07	1602	4.48E-04
55	4.61E-04	4.52E-04	9.17E-06	1.989			
56.6	4.54E-04	4.44E-04	9.63E-06	2.123			
60	4.39E-04	4.29E-04	9.91E-06	2.258			
61	-	4.25E-04	-	-	2.60E-07	1581	4.11E-04
65	4.18E-04	4.09E-04	9.63E-06	2.301			
70	3.98E-04	3.91E-04	7.44E-06	1.868	2.40E-07	1557	3.74E-04
75	3.80E-04	3.75E-04	4.97E-06	1.309			
80	3.62E-04	3.61E-04	8.56E-07	0.236			
85	3.43E-04	3.49E-04	5.39E-06	1.571			
90	3.25E-04	3.38E-04	1.27E-05	3.923			
95	3.20E-04	3.28E-04	8.38E-06	2.623			
100	3.14E-04	3.19E-04	5.07E-06	1.615			

$$y = -2.9921\text{E-}10T^3 + 1.0440\text{E-}07T^2 - 1.3585\text{E-}05T + 9.3278\text{E-}04$$
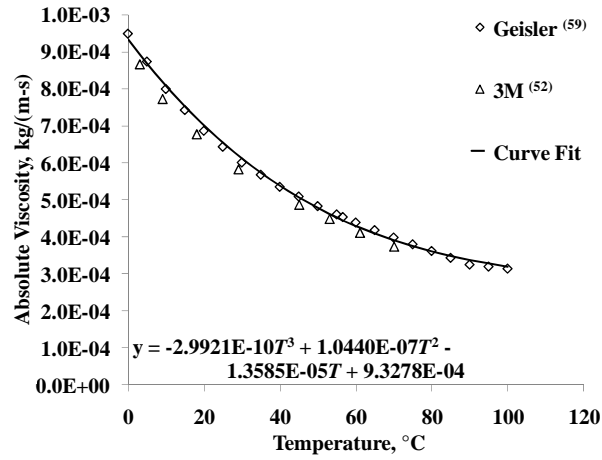
Fig. E.5 Absolute viscosity versus temperature

Table E.6 Density curve fit comparison

Temperature, °C	Density: Geisler (2007)[59], kg/m³	3rd Order Curve Fit, kg/m³	Abs(Difference), Fit to Data, kg/m³	% Difference	Density: Linear Formula, 3M (2000)[52], kg/m³	Abs(Difference), 3M Formula to Data, kg/m³	% Difference
0	1755	1764	9.2	0.52	1740	15.3	0.87
5	1738	1741	3.7	0.21	1727	10.6	0.61
10	1720	1721	1.1	0.06	1714	5.9	0.34
15	1706	1703	2.5	0.15	1701	4.8	0.28
20	1692	1688	3.9	0.23	1688	3.7	0.22
25	1680	1674	6.2	0.37	1675	5.6	0.33
30	1669	1662	6.8	0.41	1662	7.4	0.44
35	1659	1652	7.5	0.45	1649	10.8	0.65
40	1650	1643	7.1	0.43	1636	14.1	0.85
45	1641	1634	6.5	0.40	1623	18.0	1.10
50	1631	1626	5.4	0.33	1610	22.0	1.35
55	1623	1618	4.3	0.26	1596	26.1	1.61
56.6	1620	1616	3.9	0.24	1592	27.5	1.69
60	1614	1610	3.2	0.20	1583	30.3	1.88
65	1603	1602	1.3	0.08	1570	33.1	2.06
70	1593	1593	0.0	0.00	1557	36.0	2.26
75	1581	1583	2.3	0.15	1544	36.9	2.33
80	1569	1572	3.3	0.21	1531	37.8	2.41
85	1554	1560	5.5	0.36	1518	35.9	2.31
90	1539	1545	5.9	0.38	1505	34.1	2.21
95	1520	1528	8.2	0.54	1492	28.1	1.85
100	1501	1509	8.1	0.54	1479	22.1	1.47

$$y = -3.94076\text{E-}04T^3 + 6.34153\text{E-}02T^2 - 4.95353\text{E+}00T + 1.76448\text{E+}03$$
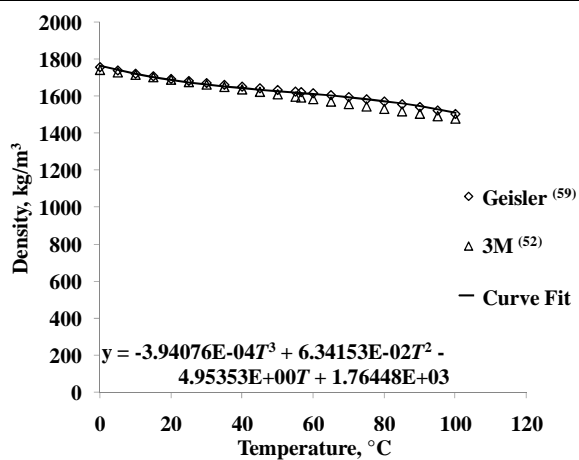
Fig. E.6 Density versus temperature

83

APPENDIX F. DATA SHEETS FROM FLIGHTS

During the flights, hand-written data sheets were created to record the nominal settings for the various parameters that were maintained, and to note any observed anomalies or events. The following figures are scans of these data sheets, and are included here for the sake of completeness.

14 SEPT 04

Elapsed Time	Top/Bot Nozzle	FC-72 Flow (gph)	H2O Flow (gph)	Reh In (°C)	Reh Out (°C)	Q (=VI) (W)	T_{int} (°C)	Nozzle Temp (°C)	(chamber press)	Comments
58:30	BOT	8.085				76				8H SET 96
59:30	BOT		10.9	20.0	30.4	78	91	29.7	13.0	TURN
1:00:30			10.9	20.0	30.6	80	91	29.3	13.0	
1:02:41			10.9	19.5	30.8	82	93	29.4	13.1	
1:03:90			10.9	19.4	30.0	84	95	29.2	13.3	
1:10:20			10.9	19.4	30.7	86	97	29.6	13.1	
			10.8	19.2	30.8	88	96	29.0	12.6	
1:14:00			10.8	19.4	31.6	90	98	29.3	13.0	
1:18:30			10.8	19.2	30.4	92	100	29.0	13.0	
1:17:00			10.8	19.2	30.4	94	99.7	28.6	13.1	TURN
1:22:40			10.8	19.0	30.1	96	100	28.6	12.6	
1:24:10			10.8	19.8	30.2	98	101	28.5	12.6	
										OVERTEMP KICKING
										→ OFF

14 sept 04

Elapsed Time	Top/Bot Nozzle	FC-72 Flow (gph)	H2O Flow (gph)	Reh In (°C)	Reh Out (°C)	Q (=VI) (W)	T_{int} (°C)	Nozzle Temp (°C)	chamber pressure psi	Comments
9-14-04										
0	Bot	8p-8.5	11.2	25	30	30	30	29	13.	T_{amb}=23.7 °C
7:58										Start record → ②
9:52										Stop record
14:30						40				Start record → ②
15:02										Stop record
24:50						50.1				Start record lunar → ③
25:46										Stop record
33:48						59.9				Start → ④
34:52										Stop
52:40						70				Start → ⑤
53:50										Stop
1:07:10						81.0				Start → ⑥
1:08:22						82.2				Stop
1:14:58						90.3				Start → ⑦
1:16:35						92.1				Stop

15 Sept 04

Elapsed Time	Top/Bot Nozzle	FC-72 Flow (gph)	H2O Flow (gph)	Reh In (°C)	Reh Out (°C)	Q (=VI) (W)	T_{int} (°C)	Nozzle Temp (°C)	Chamber Press PSIA	Comments
0	BOT	8.0-8.5	10.4 11.2	21.5	52.1	30 35	53.8	30.2	16.4	Rehat 70°C Set point / Reheat 75°C 3:55
0:8:00			11.4	33.2	31.1	35	59	29.5	16.4	
8:55			11.3	22.9	30.9	36	55.5	28.7	16.4	Partial Rehat 80C
11:14				22.6	31.2	38	61.4	29.6	16.4	
12:34			11.3	22.6	31.5	40	63.5	29.6	16.4	
13:45			11.4	22.6	31.2	42	64.9	29.5	16.6	
15:00			11.4	22.5	31.4	44	66.5	29.6	16.5	
16:10				22.5	31.8	46	68.5	30.0	16.7	
17:26				22.4	31.0	48	70.5	29.4	16.6	partial
18:99				22.4	31.2	58	69.9	29.3	16.0	
25:02				22.1	31.2	50	72.4	29.7	16.6	
26:23				21.9	30.9	52	72.3	29.1	16.6	
27:40				21.7	30.6	54	73.6	29.0	16.6	

15 Sept 04

Elapsed Time	Top/Bot Nozzle	FC-72 Flow (gph)	H2O Flow (gph)	Reh In (°C)	Reh Out (°C)	Q (=VI) (W)	T_{int} (°C)	Nozzle Temp (°C)	Chamber Press PSIA	Comments
30:20	BOT	8.0-8.5	11.4	21.3	31.8	56	79.4	29.5	16.0	Reheat 85° 29:50
31:35				21.3	31.3	58	80.3	29.6	16.6	
32:52				21.3	30.7	60	79.7	29.2	16.6	
34:10				21.4	30.9	62	81.1	29.3	16.6	partial
44:40				21.0	30.6	62	80.0	28.8	15.7	
45:26				20.6	31.3	64	84.4	29.8	16.5	
46:42				20.3	29.5	66	84.3	28.6	16.4	
47:56				20.1	30.3	68	85.6	28.5	16.3	
49:12				19.9	29.6	70	85.4	28.0	16.2	
50:26				19.8	30.5	72	85.2	29.0	16.3	partial
51:48				19.7	29.8	72	85.7	27.9	15.8	
53:00				19.8	29.4	74	89.0	28.4	16.4	
56:00				19.9	29.5	76	85.1	27.9	15.8	Reheat 95°C 57:00
59:40				19.9	30.8	78	92.9	30.5	16.4	partial (2)
1:03:50				19.2	30.1	80	93.5	29.1	16.4	
1:05:08				19.3	31.0	82	93.3	29.4	16.3	
1:06:24				19.3	30.4	84	96.5	28.6	16.4	
1:07:40				19.3	31.1	86	95.6	29.4	16.3	
1:09:00				19.2	30.6	88	98.4	29.6	16.4	partial
1:13:54				19.6	31.1	90	95.5	29.1	15.8	partial
1:15:40				19.4	30.9	90	98.1	29.3	15.8	
1:16:54				19.2	30.3	92	100.8	29.5	16.4	
1:18:10				18.9	30.8	94	99.1	29.3	16.1	
1:19:24				19.7	29.7	96	100.0	28.9	16.3	
1:20:48				18.6	29.9	96	101.0	28.5	16.0	partial lost Pore

43

	Elapsed Time	Top/Bot Nozzle	FC-72 Flow	H2O Flow	Reh In	Reh Out	Q (=VI)	T_{int}	Nozzle Temp		Comments
	9-15-04		(gph)	(gph)	(°C)	(°C)	(W)	(°C)	(°C)		
setting:	φ	Bot	8.0-8.5	10.4			30	30			Tamb = ΔQ≈2-5 W
start 1	100						30				Normal g
end	200										
start 2	625						30				1st parabola
end	736										
3	852						30				
	1010										
4	1228						40				
	1400										
5	1613						46				
	1738										
6	1851						48				
	1928										
New tape start	2121										} New tape run
	2144										at normal g Qetw parq...
7	2505						50-52				
	2651										
8	2857						56				Marsian
	3040										
10	3251						60				
	3417										was not stopped
D/R	3541										When stop here, it's 62 W

	Elapsed Time	Top/Bot Nozzle	FC-72 Flow	H2O Flow	Reh In	Reh Out	Q (=VI)	T_{int}	Nozzle Temp		Comments
			(gph)	(gph)	(°C)	(°C)	(W)	(°C)	(°C)		
start 1	4528						64				
end	4700										
start 2	4700						66				
	4826										
3	4916						70				
	5054										
4	5305						74				1st 2 7815 in marsian
	5423										
5	10410						80				
	10510										
6	10756						86				
	10905										
7	11817						94				
	11913										tape stopped before the end of mg

17 Sep 04

Elapsed Time	Top/Bot Nozzle	FC-72 Flow	H2O Flow	Reh In	Reh Out	Q (=VI)	T_{int}	Nozzle Temp	Chamber press	Comments	
	B	(gph)	(gph)	(°C)	(°C)	(W)	(°C)	(°C)	PSI	Vapor	Reh Set
Start ~	Lot	6.06.5	10.9	21.8	31.1	30	30	29.7	15.4	25.8	75
			11.1	21.3	30.9	30		29.6	29.1	15.4	26.0	75.0
			11.1	21.3	30.8	30	30.1	55.4	15.4	26.0	75.0
			11.1	21.2	30.9	30	36.4	29.9	15.5	26.3	800
			11.1	21.0	31.5	35	62.3	30.0	16.0	28.2	
			11.1	20.7	32	36	63.5	30.0	16.1	28.4	
			11.2	20.3	31.4	38	65.0	30.0	16.0	28.0	
			11.2	20.5	31.5	40	65.4	29.4	15.9	28.0	
			11.2	20.4	30.8	42	66.5	29.4	15.8	28.1	
			11.2	20.2	31.4	44	69.8	30.0	16.1	28.3	
			11.2	20.2	30.5	46	69.3	29.2	15.6	27.8	85
			11.2	20.3	32.1	46	72.3	30.5	16.1	28.6	
			11.2	20.2	31.5	48	72.0	30.0	16.0	28.8	
			11.2	20.1	31.6	50	74.4	30.2	16.1	29.1	
			11.2	20.2	31.6	52	77.4	30.4	16.1	29.3	
TURN			Made Switch - Kirk took some video								
			11.2	19.7	31.0	52	71.1	29.1	16.1	26.3	
Zero			Start Video (25 30) (10) 30 (Partial?)							(26.45)	12 10
Start			11.2	19.7	31.8	54	73.5	30.0	16.1	29.1	Start Vid	13 10
Stop			11.2	19.5	31.0	56	79.0	30.0	16.1	29.3	Start	13 14
Stop			11.2	19.3	31.0	58	80.1	29.6	16.1	29.6	Vid 30.07	14 15
Stop 30.00			11.2	19.2	30.8	60	84.0	29.6	16.2	29.6	Start 30 (2)	14 15
Stop 31.13											
Mach on			11.2	19.2	30.7	62	83	29.5	16.2	29.9	Start 31.34	15 16

Elapsed Time	Top/Bot Nozzle	FC-72 Flow	H2O Flow	Reh In	Reh Out	Q (=VI)	T_{int}	Nozzle Temp	Chamber press	Comments	
		(gph)	(gph)	(°C)	(°C)	(W)	(°C)	(°C)	PSI	Vapor	Reh Set
	Bot	6.06.5									80
7 secs			11.2	19.2	30.6	62	81.2				Vid 35.41	16 17
37.06.51			11.2	19.1	30.4	64	84.3	29.2	15.9	29.1	Vid 34.18	17 18
30.17			11.2	19.0	30.1	66	86.0	29.1	16.0	28.7		18
37.45										90	18 19
Swap			11.1	19.0	31.2	66	80.7	28.9	15.9	28.5	Vid 41.25	18
Zero			11.1	18.8	32.0		94					
04 42.41			11.1	18.7	31.0	68	88.1	29.3	15.7	29.1	ON 42.53	19 20
04 43.26			11.1	18.6	31.3	70	89.6	29.2	15.9	28.9	Vid 44.10	19 21
04 45.13			11.1	18.5	30.3	72	91.1	29.4	15.9	29.4	Vid 45.31	20 22
04 46.30			11.1	18.5	30.6	74	93.1	29.4	16.0	29.6	Vid 46.46	22 23
04 47.48			11.1	18.4	31.0	76	95.7	29.3	16.0	29.7	48.06	23 24
04 49.03			11.1	18.4	30.4	78	95.5	29.2	16.0	29.7	49.00	24 25
04 50.00			11.1	18.3	3	80	96.2	29.3	16.1	29.7	50.32	25 26
Mach on			11.1	18.1	30.1	80	95.1	29.1	15.5	29.6	Vid 52.46	26 27
Turn	Bot	04 53.52	11.1	18.3	30.3	82	99.0	29.5	16.1	29.5		

Elapsed Time	Top/Bot Nozzle	FC-72 Flow (gph)	H2O Flow (gph)	Reh In (°C)	Reh Out (°C)	Q (=VI) (W)	T_int (°C)	Nozzle Temp (°C)	Scale Pres psi	Scale Temp °C	Comments °C
Lunar	Bot	6.69	11.20	18.3	30.0	82	91.9	28.3	16.00	26.3	90
On 98.30			11.0	18.0	30.1	82.1	96.4	29.1	15.5	27.6	95
			11.0	17.9	31.5	84	98.9	30.2	15.5	29.4	On 99.7
1:0.49			11.0	17.7	30.1	86	99.5	30.0	15.7	30.1	On 1:01.0
2:06			11.0	17.6	30.4	88	100.2	30.0	15.9	30.7	On 02.46
3:24	Martian Nozzle		11.0	17.5	30.5	90	101.3	29.9	16.1	30.5	3:40
							77.5				
4:48			10.9	17.4	28.3	90	99.3	25.7	15.5	Reh Off	On 6:24
			10.9	17.3	18.4	92	91.7	17.6	15.4	25.8	
7:34			10.9	17.3	17.7	94	92.4	16.9	15.3	24.5	On 7:46
8:41			END	OF	DAY						

Elapsed Time	Top/Bot Nozzle	FC-72 Flow (gph)	H2O Flow (gph)	Reh In (°C)	Reh Out (°C)	Q (=VI) (W)	T_int (°C)	Nozzle Temp (°C)		Comments
3 sec	bot	6.065								Before parabola
1.20						30w				not recording yet
5.37										
5.69										
5.80										
7.49										
757										Lunar
1030										
1035										
11.48										
11.52										
13.06										
1310										
14.24										
1427										Martian
17.00										
1707										
1818										
1823										
1940										

89

APPENDIX G. UNCERTAINTY IN MEASURED VALUES

In general, a conservative estimation of the uncertainty in a measured value is taken to be the uncertainty associated with the measurement added to the confidence interval over a given set of steady-state data. The confidence interval was determined following the method outlined in Montgomery and Runger (2003)[56]. Due to the unique experimental environment, namely the length of time of each parabola and the sampling rate of the data acquisition system, the number of data points per steady-state data set was fairly limited. For this reason, it was decided to use a confidence interval based on the two-tailed t-Distribution for the average values calculated from the measured values. This confidence interval CI, based on a confidence level of $100(1-\alpha)\%$, for a data set consisting of n points, with a measured average value AVG_{meas} and a standard deviation σ_{sd}, is calculated as

$$CI = \frac{t_{\frac{\alpha}{2},n-1} \times \sigma_{sd}}{\sqrt{n}} \qquad (G.1)$$

The value of $t_{\alpha/2,n-1}$ can be found from Table IV in the appendix of [56] or from the built-in function TINV(α,n-1) in Microsoft Excel®. For all of the CI calculated for this data reduction, a confidence level of 95%, giving α=0.05, was chosen. The interpretation of this calculated CI is such that the interval AVG_{meas} - $CI \leq AVG_{true} \leq AVG_{meas}$ + CI will bracket the true average, AVG_{true}, with a confidence of 95% (pg251 of Montgomery and Runger 2003[56]).

G.1. Uncertainty in temperature measurement

The temperatures for this experiment were measured using Type E thermocouples. To find the uncertainty in the temperature measurements, the calibration uncertainty for each thermocouple and the confidence interval for the steady state data were accounted for as follows:

$$\delta T = (\text{Calibration } \delta) + (CI \text{ of Data}) \qquad (G.2)$$

The thermocouples were calibrated using a Hart Model 5628 RTD with a Hart Model 1502A Readout. The calibration uncertainty was calculated as the sum of the

RTD uncertainty and the maximum deviation of the calibration curve to the RTD values for each thermocouple. The RTD / readout combination had an uncertainty of $\pm\ 0.01°C$. The four temperatures most of interest in this data reduction were the interface temperature, T_{int}, the lower film temperature, T_{lf}, the upper film temperature, T_{uf}, and the nozzle temperature, T_{noz}. The following table gives the calibration curve, R^2 value, and maximum calibration curve deviation for each of these thermocouples.

Table G.1 Curve fit details for temperature measurements

Thermocouple	Curve Fit	R^2 Value	Maximum Deviation
T_{int}	y = 0.996032990x - 0.918685057	0.999999436	0.044
T_{lf}	y = 0.993583527x + 0.088480511	0.999999213	0.055
T_{uf}	y = 0.994139141x + 0.084207114	0.999999180	0.055
T_{noz}	y = 0.994432013x + 0.068251535	0.999999165	0.051

For one set of steady-state data, consisting of 12 data points, the average and standard deviation for T_{int} were calculated to be 57.8 °C and 0.14 °C, respectively. This gives $CI = +\ 0.087$ °C, which gives a total uncertainty in T_{int} of $\delta T_{int} = \pm\ 0.141$ °C.

G.2. Uncertainty in flow rate measurement

To find the uncertainty in the flow rate measurement, V, the uncertainty in the calibration curve and the confidence interval for the steady-state V were accounted for as follows:

$$\delta V = (\text{Calibration Curve } \delta) + (CI \text{ of Data}) \tag{G.3}$$

For V, the calibration curve was fit to data provided by the manufacturer of the flow meter, which was a Sponsler MF90CBPHA4X-V Lo-Flo Series flowmeter with a SP711-3 3_Wire Analog Transmitter. The manufacturer supplied flow rate and frequency data for flow rates up to approximately 50 gph. A linear trend line was applied to this frequency/V data, and this trend line was then converted to a voltage/V fit, using data provided by the manufacturer about the transmitter. The range of interest for these experiments was taken to be $V < 20$ gph. On this range, the maximum deviation of the linear fit to the manufacturer's data was 0.371 gph. The manufacturer listed an uncertainty of 0.11% on the calibration data, which gives a maximum uncertainty of 0.022 gph on the range of interest. Therefore, the uncertainty of the calibration curve is approximately 0.393 gph. This uncertainty is added to the confidence interval for each

block of steady-state data to find the total uncertainty in the V measurement, δV. For one set of steady-state data, consisting of 12 data points, the average and standard deviation for V were calculated to be 8.36 gph and 0.15 gph, respectively. This gives $CI = \pm\, 0.095$, which gives a total uncertainty in V of $\delta V = \pm\, 0.490$ gph.

The calibration curve was spot-checked using a stopwatch, scale, and graduated cylinder, and the flow rate results of this spot check were found to be within several percent of the flow rate reported by the calibration curve, which is within the uncertainty limits as given above.

G.3. Uncertainty in chamber pressure

To find the uncertainty in the chamber pressure, P_{ch}, the accuracy of the P_{ch} measurement and the confidence interval for the steady-state P_{ch} data were accounted for as follows:

$$\delta P_{ch} = (\text{Accuracy of } P_{ch} \text{ Measurement}) + (CI \text{ of Data}) \qquad \text{(G.4)}$$

P_{ch} was measured using an Omega PX303-100A5V pressure transducer, with a range of 0 to 100 psia and a full-scale accuracy of 0.25%, which results in an uncertainty in P_{ch} of $\pm\, 0.25$ psia. This uncertainty is added to the confidence interval for each block of steady-state data to find the total uncertainty in the P_{ch} measurement, δP_{ch}. For one set of steady-state data, consisting of 12 data points, the average and standard deviation of P_{ch} were found to be 13.8 psia and 0.035 psia, respectively. This gives $CI = \pm\, 0.022$ psia, and a total uncertainty $\delta P_{ch} = \pm\, 0.27$ psia.

G.4. Uncertainty in acceleration

To find the uncertainty in the acceleration normal to the heater surface, a, the accuracy of the a measurement and the confidence interval for the steady-state a data were accounted for as follows:

$$\delta a = (\text{Accuracy of } a \text{ Measeurement}) + (CI \text{ of Data}) \qquad \text{(G.5)}$$

a was measured using a Columbia Research Laboratories, Inc. Triaxial Linear Servo Accelerometer, model number SA-307HPTX. The output was -7.5 to 7.5 Volts, and the scale factor was set at the factory to give a reading of -2.5 to 2.5 g. The tolerance of this scale factor was given as $\pm\, 1\%$, and since it was linear, this gives approximately a

± 1% uncertainty in the acceleration measurement. Therefore, the maximum uncertainty of the acceleration measurement would be ± 0.025 g. This uncertainty is added to the confidence interval for each block of steady-state data to find the total uncertainty in the a measurement, δa. For one set of steady-state data, consisting of 12 data points, the average and standard deviation of a were found to be 0.156 g and 0.016 g, respectively. This gives $CI = \pm 0.010$ g, and a total uncertainty $\delta a = \pm 0.04$ g.

G.5. Uncertainty in heater voltage

To find the uncertainty in the heater voltage, E_H, the accuracy of the voltage measurement and the confidence interval for the steady state E_H data was accounted for as follows:

$$\delta E_H = (\text{Accuracy of } E_H \text{ Measurement}) + (CI \text{ of Data}) \tag{G.6}$$

E_H was measured using the AGILENT 34970A Data Acquisition/Switch Unit with an Agilent 34901A 20-Channel Multiplexer using the auto range feature. For this set of data, E_H was always on the 100 V range. The largest uncertainty given by the manufacturer for this range is 0.0045% of the reading plus 0.0006% of the range. This gives an accuracy of the E_H measurement of $\pm (0.000045*(\text{Average } E_H) + 100*0.000006)$ V. This uncertainty is added to the confidence interval for each block of steady-state data to find the total uncertainty in the E_H measurement, δE_H. For one set of steady-state data, consisting of 12 data points, the average and standard deviation of E_H were found to be 21.9 V and 0.00033V, respectively. The accuracy for this measurement is ± 0.0016V, and the $CI = \pm 0.00021$ V. This gives a total uncertainty $\delta E_H = \pm 0.0018$ V.

G.6. Uncertainty in precision resistor voltage

To find the uncertainty in the precision resistor voltage, E_R, the accuracy of the voltage measurement and the confidence interval for the steady state E_R data was accounted for as follows:

$$\delta E_R = (\text{Accuracy of } E_R \text{ Measurement}) + (CI \text{ of Data}) \tag{G.7}$$

E_R was measured using the AGILENT 34970A Data Acquisition/Switch Unit with an Agilent 34901A 20-Channel Multiplexer using the auto range feature. For this set of data, E_R was always on the 1.0 V range. The largest uncertainty given by the manufacturer for this range is 0.0040% of the reading plus 0.0007% of the range. This

gives an accuracy of the E_R measurement of $\pm$ (0.000040*(Average E_R) + 1.0*0.000007) V. This uncertainty is added to the confidence interval for each block of steady-state data to find the total uncertainty in the E_R measurement, δE_R. For one set of steady-state data, consisting of 12 data points, the average and standard deviation of E_R were found to be 0.174 V and 3.4×10^{-6} V, respectively. The accuracy for this measurement is $\pm 1.4 \times 10^{-5}$ V, and the $CI = \pm 2.16 \times 10^{-6}$ V. This gives a total uncertainty $\delta E_R = \pm 1.61 \times 10^{-5}$ V.

APPENDIX H. UNCERTAINTY IN CALCULATED VALUES

The uncertainty calculations for the calculated values are described below:

The method that was used for propagating uncertainties from measured values to calculated values is described in detail in Appendix F of Fox and McDonald (5th Ed)[(57)]. For a calculated value F that is a function of variables $(j_1, j_2, \ldots, j_i)$, the relative uncertainty in F, $\delta F/F$, due to the individual uncertainties in the variables $(\delta j_1, \delta j_2, \ldots, \delta j_i)$ can be found from the following equation

$$\frac{\delta F}{F} = \left[\left(\frac{j_1}{F}\frac{\partial F}{\partial j_1}\frac{\delta j_1}{j_1}\right)^2 + \left(\frac{j_2}{F}\frac{\partial F}{\partial j_2}\frac{\delta j_2}{j_2}\right)^2 + \cdots + \left(\frac{j_i}{F}\frac{\partial F}{\partial j_i}\frac{\delta j_i}{j_i}\right)^2\right]^{\frac{1}{2}} \quad \text{(H.1)}$$

The δj values are the uncertainties that were found following the method outlined previously, so that they account for the precision of the measurement as well as the *CI* associated with the measurement. In this way, all of those individual uncertainties can be accounted for in the uncertainty of F. This method is used for calculating the uncertainties for all of the calculated values that are functions of two or more variables.

H.1. Uncertainty in calculated saturation temperature

To find the uncertainty in the saturation temperature, T_{sat}, the maximum deviation of the T_{sat} versus P_{sat} curve-fit equation from the original tabular data was added to the uncertainty associated with T_{sat} due to δP_{ch}.

$$\delta T_{sat} = (\text{Max Curve Fit Deviation}) + (\delta \text{ in } T_{sat} \text{ due to } \delta P_{ch}) \quad \text{(H.2)}$$

The saturation temperature was calculated from the following equation, which was found using the data from Geisler (2007)[(59)]:

$$T_{sat}(P_{ch}) = 5.27781 \times 10^{-3} \times P_{ch}^3 - 0.293346 \times P_{ch}^2$$
$$+ 7.07482 \times P_{ch} - 0.5976 \quad \text{(H.3)}$$

This equation is valid over the range of $3.4 \leq P_{ch} \leq 22.5$ psia, and on this range, the maximum deviation of the curve fit from the given data was 0.53 °C (1.75%).

The uncertainty in T_{sat} due to δP_{ch} was found by calculating T_{sat} at P_{ch}, $P_{ch}+\delta P_{ch}$, and $P_{ch}-\delta P_{ch}$. The differences $[T_{sat}(P_{ch}+\delta P_{ch}) - T_{sat}(P_{ch})]$ and $[T_{sat}(P_{ch}-\delta P_{ch}) - T_{sat}(P_{ch})]$ were calculated, and the maximum absolute value from these differences was taken as the uncertainty in T_{sat} due to δP_{ch}. For the set of P_{ch} data mentioned above, this gave

Table H.1 Uncertainty in T_{sat} due to δP_{ch}

Chamber Pressure (psia)	Calculated Saturation Temperature (°C)	Absolute Value of Deviation from $T_{sat}(P_{ch})$ (°C)
13.8 - 0.27 = 13.5	54.5	0.54
13.8 + 0.27 = 14.1	55.6	0.53

The maximum uncertainty in T_{sat} associated with δP_{ch} is therefore $\pm$ 0.54 °C. The total uncertainty in the calculation of T_{sat} for this set of data is therefore $\pm$ 1.07 °C.

H.2. Uncertainty in calculated droplet velocity

The droplet velocity, v, was calculated from the volumetric flow rate, V, using the following curve fit equation, which was found using the data from Yerkes et al.[18] This data was generated using a Dantek Two-Axis Phase Doppler Anemometer.

$$v(V) = 9.4467 \times 10^{-2} \times V^2 - 0.41430 \times V + 7.2713 \qquad \text{(H.4)}$$

This second-order curve fit was based on three data points, so there is no deviation from the curve fit to the given data.

The uncertainty in v due to δV was found by calculating v at V, $V+\delta V$, and $V-\delta V$. The differences $[v(V+\delta V) - v(V)]$ and $[v(V-\delta V) - v(V)]$ were calculated, and the maximum absolute value from these differences was taken as the uncertainty in v due to δV. For one set of V data mentioned above, this gave

Table H.2 Uncertainty in T_{sat} due to δP_{ch}

Flow Rate V (gph)	Calculated Velocity v (m/s)	Absolute Value of Deviation from $v(V)$ (m/s)
8.36 – 0.82 = 7.54	9.52	0.89
8.36 + 0.82 = 9.18	11.43	1.02

The maximum uncertainty in v associated with δV is $\delta v = \pm$ 1.02 m/s.

H.3. Uncertainty in calculated temperature of free stream fluid flowing over the heater surface

The temperature of the free-stream fluid flowing over the heater surface, $T_{\infty,\text{top}}$, is the fluid temperature used for calculating the fluid properties. This average fluid temperature is calculated from the following equation

$$T_{\infty,\text{top}} = \frac{T_{\text{noz}} + T_{\text{uf}}}{2} \qquad (\text{H.5})$$

Following the uncertainty propagation procedure given in Fox and McDonald[57], the uncertainty in this temperature, $\delta T_{\infty,\text{top}}$, is

$$\delta T_{\infty,\text{top}} = T_{\infty,\text{top}} \left[\left(\frac{\delta T_{\text{noz}}}{T_{\text{noz}} + T_{\text{uf}}} \right)^2 + \left(\frac{\delta T_{\text{uf}}}{T_{\text{noz}} + T_{\text{uf}}} \right)^2 \right]^{\frac{1}{2}} \qquad (\text{H.6})$$

For one set of data, the average $T_{\infty,\text{top}}$ was 29.7 °C. The associated T_{noz}, δT_{noz}, T_{uf}, and δT_{uf} were 28.8 °C, 0.094 °C, 30.7 °C, and 0.121 °C, respectively. This gave an uncertainty in $T_{\infty,\text{top}}$ of $\delta T_{\infty,\text{top}} = 0.08$ °C.

H.4. Uncertainty in calculated density

To find the uncertainty in the density, ρ, the maximum deviation of the ρ versus $T_{\infty,\text{top}}$ curve-fit equation from the original tabular data was added to the uncertainty associated with ρ due to $\delta T_{\infty,\text{top}}$.

$$\delta\rho = (\text{Max Curve Fit Deviation}) + (\delta \text{ in } \rho \text{ due to } \delta T_{\infty,\text{top}}) \qquad (\text{H.7})$$

The density was calculated from the following equation, which was found using the data from Geisler (2007) [59]:

$$\begin{aligned}
\rho\left(T_{\infty,\text{top}}\right) &= -3.94076 \times 10^{-4} \times T_{\infty,\text{top}}^3 + 6.34153 \times 10^{-2} \\
&\quad \times T_{\infty,\text{top}}^2 - 4.95353 \times T_{\infty,\text{top}} + 1764.48
\end{aligned} \qquad (\text{H.8})$$

The maximum deviation of the curve fit from the given data was 9.19 kg/m³ (0.52%).

The uncertainty in ρ due to $\delta T_{\infty,\text{top}}$ was found by calculating ρ at $T_{\infty,\text{top}}$, $T_{\infty,\text{top}} + \delta T_{\infty,\text{top}}$, and $T_{\infty,\text{top}} - \delta T_{\infty,\text{top}}$. The differences $[\rho(T_{\infty,\text{top}} + \delta T_{\infty,\text{top}}) - \rho(T_{\infty,\text{top}})]$ and $[\rho(T_{\infty,\text{top}} - \delta T_{\infty,\text{top}}) - \rho(T_{\infty,\text{top}})]$ were calculated, and the maximum absolute value from these differences was taken as the uncertainty in ρ due to $\delta T_{\infty,\text{top}}$. For one set of $T_{\infty,\text{top}}$ data, this gave

Table H.3 Uncertainty in ρ due to $\delta T_{\infty,top}$

$T_{\infty,top}$ (°C)	Calculated Density (kg/m^3)	Absolute Value of Deviation from $\rho(T_{\infty,top})$ (kg/m^3)
29.7 - 0.08 = 29.6	1663.0	0.17
29.7 + 0.08 = 29.8	1662.7	0.17

The maximum uncertainty in ρ associated with $\delta T_{\infty,top}$ is therefore $\pm$ 0.17 kg/m^3. The total uncertainty in the calculation of ρ for this set of data is therefore $\delta\rho = \pm$ 9.36 kg/m^3.

H.5. Uncertainty in calculated viscosity

To find the uncertainty in the viscosity, μ, the maximum deviation of the μ versus $T_{\infty,top}$ curve-fit equation from the original tabular data was added to the uncertainty associated with μ due to $\delta T_{\infty,top}$.

$$\delta\mu = \text{(Max Curve Fit Deviation)} + (\delta \text{ in } \mu \text{ due to } \delta T_{\infty,top}) \quad \text{(H.9)}$$

The viscosity was calculated from the following equation, which was found using the data from Geisler (2007) [59]:

$$\mu(T_{\infty,top})$$
$$= -2.9921 \times 10^{-10} \times T_{\infty,top}^3 + 1.0440 \times 10^{-7} \quad \text{(H.10)}$$
$$\times T_{\infty,top}^2 - 1.3585 \times 10^{-5} \times T_{\infty,top} + 9.3278 \times 10^{-4}$$

The maximum deviation of the curve fit from the given data was 1.68×10^{-5} Pa-s (1.77%).

The uncertainty in μ due to $\delta T_{\infty,top}$ was found by calculating μ at $T_{\infty,top}$, $T_{\infty,top} + \delta T_{\infty,top}$, and $T_{\infty,top} - \delta T_{\infty,top}$. The differences $[\mu(T_{\infty,top} + \delta T_{\infty,top}) - \mu(T_{\infty,top})]$ and $[\mu(T_{\infty,top} - \delta T_{\infty,top}) - \mu(T_{\infty,top})]$ were calculated, and the maximum absolute value from these differences was taken as the uncertainty in μ due to $\delta T_{\infty,top}$. For one set of $T_{\infty,top}$ data, this gave

Table H.4 Uncertainty in μ due to $\delta T_{\infty,top}$

$T_{\infty,top}$ (°C)	Calculated Viscosity (Pa-s)	Absolute Value of Deviation from $\mu(T_{\infty,top})$ (Pa-s)
29.7 - 0.08 = 29.6	6.14×10^{-4}	6.27×10^{-7}
29.7 + 0.08 = 29.8	6.13×10^{-4}	6.26×10^{-7}

98

The maximum uncertainty in μ associated with $\delta T_{\infty,top}$ is therefore $\pm\ 6.27\times10^{-7}$ Pa-s. The total uncertainty in the calculation of μ for this set of data is therefore $\delta\mu =$ $1.74\times10^{-5} \pm$ Pa-s.

H.6. Uncertainty in calculated surface tension

To find the uncertainty in the surface tension, σ, the uncertainty associated with σ due to $\delta T_{\infty,top}$ was accounted for.

$$\delta\sigma = (\text{Uncertainty in } \sigma \text{ due to } \delta T_{\infty,top}) \tag{H.11}$$

The surface tension was calculated from the following equation, given in Geisler $(2007)^{(59)}$:

$$\sigma(T_{\infty,top})$$

$$= 0.042705\left(1.0 - \left(\frac{\left(273.15\ +\ \left(T_{\infty,top}\right)\right)}{451.65}\right)\right)^{1.2532} \tag{H.12}$$

This equation was given in the paper, so there was no tabular data to compare it to for determining the maximum deviation of the curve fit from the given data.

The uncertainty in σ due to $\delta T_{\infty,top}$ was found by calculating σ at $T_{\infty,top}$, $T_{\infty,top}+\delta T_{\infty,top}$, and $T_{\infty,top}-\delta T_{\infty,top}$. The differences $[\sigma(T_{\infty,top}+\delta T_{\infty,top}) - \sigma(T_{\infty,top})]$ and $[\sigma(T_{\infty,top}-\delta T_{\infty,top}) - \sigma(T_{\infty,top})]$ were calculated, and the maximum absolute value from these differences was taken as the uncertainty in σ due to $\delta T_{\infty,top}$. For one set of $T_{\infty,top}$ data, this gave

Table H.5 Uncertainty in μ due to $\delta T_{\infty,top}$

$T_{\infty,top}$ (°C)	Calculated Surface Tension (N/m)	Absolute Value of Deviation from $\sigma(T_{\infty,top})$ (N/m)
29.7 - 0.08 = 29.6	1.062×10^{-2}	6.863×10^{-6}
29.7 + 0.08 = 29.8	1.061×10^{-2}	6.862×10^{-6}

The maximum uncertainty in σ associated with $\delta T_{\infty,top}$ is therefore $\pm\ 6.863 \times 10^{-6}$ N/m. This is used as the total uncertainty in the calculation of σ, $\delta\sigma$.

There was surface tension data given in the Skripov and Firsov$^{(60)}$, and this data agrees well with the surface tension given by the equation found in Geisler $(2007)^{(59)}$.

H.7. Uncertainty in calculated fluid thermal conductivity

To find the uncertainty in the fluid thermal conductivity, k_f, the uncertainty associated with k_f due to $\delta T_{\infty,\text{top}}$ was accounted for.

$$\delta k_f = (\text{Uncertainty in } k_f \text{ due to } \delta T_{\infty,\text{top}}) \tag{H.13}$$

The fluid thermal conductivity was calculated from the following equation, given in Geisler (2007)[59]:

$$k_f(T_{\infty,\text{top}}) = -0.0001168(T_{\infty,\text{top}} + 273.15) + 0.090672 \tag{H.14}$$

This equation was given in the paper, so there was no tabular data to compare it to for determining the maximum deviation of the curve fit from the given data.

The uncertainty in k_f due to $\delta T_{\infty,\text{top}}$ was found by calculating k_f at $T_{\infty,\text{top}}$, $T_{\infty,\text{top}}$ $+\delta T_{\infty,\text{top}}$, and $T_{\infty,\text{top}}$ - $\delta T_{\infty,\text{top}}$. The differences $[k_f(T_{\infty,\text{top}}+\delta T_{\infty,\text{top}}) - k_f(T_{\infty,\text{top}})]$ and $[k_f(T_{\infty,\text{top}}-\delta T_{\infty,\text{top}}) - k_f(T_{\infty,\text{top}})]$ were calculated, and the maximum absolute value from these differences was taken as the uncertainty in k_f due to $\delta T_{\infty,\text{top}}$. For one set of $T_{\infty,\text{top}}$ data, this gave

Table H.6 Uncertainty in k_f due to $\delta T_{\infty,\text{top}}$

$T_{\infty,\text{top}}$ (°C)	Calculated Fluid Thermal Conductivity (W/m-K)	Absolute Value of Deviation from $k_f(T_{\infty,\text{top}})$ (W/m-K)
29.7 - 0.08 = 29.6	5.530×10^{-2}	8.96×10^{-6}
29.7 + 0.08 = 29.8	5.528×10^{-2}	8.96×10^{-6}

The maximum uncertainty in k_f associated with $\delta T_{\infty,\text{top}}$ is therefore $\pm\, 8.96 \times 10^{-6}$ N/m. This is used as the total uncertainty in the calculation of k_f, δk_f.

H.8. Uncertainty in calculated heater power

The heater power, q, is calculated from a voltage measurement across the heater, E_H, a voltage measurement across a precision resistor, E_R, and the resistance of the precision resistor, R_P, using the following equation

$$q = E_H \left(\frac{E_R}{R_P}\right) \tag{H.15}$$

Following the uncertainty propagation procedure given in Fox and McDonald[57], the uncertainty in the heater power, δq, is

$$\delta q = q \left[\left(\frac{\delta E_H}{E_H}\right)^2 + \left(\frac{\delta E_R}{E_R}\right)^2 + \left(\frac{\delta R_P}{R_P}\right)^2\right]^{\frac{1}{2}} \tag{H.16}$$

H.9. Uncertainty in calculated heat flux to the spray

The heat flux to the spray, q''_{sp}, is calculated using the following equation

$$q''_{sp} = \frac{(1-f)q}{A} \tag{H.17}$$

Following the uncertainty propagation procedure given in Fox and McDonald[57], the uncertainty in the heat flux to the spray, $\delta q''_{sp}$, is

$$\delta q''_{sp} = q''_{sp} \left[\left(\frac{-\delta f}{1-f}\right)^{\frac{1}{2}} + \left(\frac{\delta q}{q}\right)^{\frac{1}{2}} + \left(\frac{-\delta A}{A}\right)^{\frac{1}{2}} \right]^{\frac{1}{2}} \tag{H.18}$$

H.10. Uncertainty in calculated surface temperature

The surface temperature, T_s, is calculated using the following equations

$$T_s = T_{int} + qY$$

$$Y = \frac{1}{A} \left[\frac{H_{cov}}{k_{cov}}(f-1) + \frac{H_{htr}}{k_{htr}}\left(f - \frac{1}{2}\right) + \frac{H_{sub}}{k_{sub}}f \right] \tag{H.19}$$

Following the uncertainty propagation procedure given in Fox and McDonald[57], the uncertainty in the surface temperature, δT_s, is

$$\delta T_s = [(\delta T_{int})^2 + (Y\delta q)^2 + (q\delta Y)^2]^{\frac{1}{2}} \tag{H.20}$$

and the uncertainty in the constant term, δY, is calculated from

$$\delta Y$$

$$= Y \left\{ \left[\frac{-\delta A}{A}\right]^2 + \left[\frac{\delta f}{YA}\left(\frac{H_{cov}}{k_{cov}} + \frac{H_{htr}}{k_{htr}} + \frac{H_{sub}}{k_{sub}}\right)\right]^2 \right.$$

$$\left. + \left[\frac{\delta H_{cov}}{YA}\frac{(f-1)}{k_{cov}}\right]^2 + \left[\frac{\delta H_{htr}}{YA}\frac{\left(f-\frac{1}{2}\right)}{k_{htr}}\right]^2 + \left[\frac{\delta H_{sub}}{YA}\frac{f}{k_{sub}}\right]^2 \right\}^{\frac{1}{2}} \tag{H.21}$$

The uncertainties in the thermal conductivity values were assumed to be negligible for determining the uncertainty in the surface temperature.

H.11. Uncertainty in calculated temperature difference

The temperature difference, ΔT_{sat}, is calculated using the following equation

$$\Delta T_{sat} = T_s - T_{sat} \tag{H.22}$$

Following the uncertainty propagation procedure given in Fox and McDonald[57], the uncertainty in the temperature difference, $\delta \Delta T_{sat}$, is

$$\delta \Delta T_{\text{sat}} = \Delta T_{\text{sat}} \left[\left(\frac{\delta T_{\text{s}}}{T_{\text{s}} - T_{\text{sat}}} \right)^2 + \left(\frac{-\delta T_{\text{sat}}}{T_{\text{s}} - T_{\text{sat}}} \right)^2 \right]^{\frac{1}{2}} \tag{H.23}$$

H.12. Uncertainty in calculated two-phase heat transfer coefficient

The two-phase heat transfer coefficient, $h_{2\text{-}\varphi}$, is calculated using the following equation

$$h_{2\text{-}\varphi} = \frac{(1-f)q'' - q''_{\text{sen}}}{\Delta T_{\text{sat}}} \tag{H.24}$$

Following the uncertainty propagation procedure given in Fox and McDonald[57], the uncertainty in the two-phase heat transfer coefficient, $\delta h_{2\text{-}\varphi}$, is

$$\delta h_{2\text{-}\varphi} = h_{2\text{-}\varphi} \left[\left(\frac{\delta(1-f)q''}{(1-f)q'' - q''_{\text{sen}}} \right)^2 + \left(\frac{\delta \Delta T_{\text{sat}}}{\Delta T_{\text{sat}}} \right)^2 \right]^{\frac{1}{2}} \tag{H.25}$$

The value q''_{sen} is the average value of the intercepts from the linear trendlines applied to the single-phase and two-phase regions of the q''_{sp} vs. ΔT_{sat} plot, and there is no way to accurately estimate the uncertainty associated with this value, so the uncertainty $\delta q''_{\text{sen}}$ was neglected for the uncertainty analysis on $\delta h_{2\text{-}\varphi}$.

H.13. Uncertainty in calculated non-dimensional grouping $(\text{Fr}^{1/2}\text{Ga})^{1/2}$

The non-dimensional grouping, $(\text{Fr}^{1/2}\text{Ga})^{1/2}$, is calculated using the following equation

$$\left(\text{Fr}^{\frac{1}{2}}\text{Ga} \right)^{\frac{1}{2}} = \left(\frac{v a^{\frac{1}{2}} D_{\text{d}}^{\frac{5}{2}} \rho^2}{\mu^2} \right)^{\frac{1}{2}} \tag{H.26}$$

Following the uncertainty propagation procedure given in Fox and McDonald[57], the uncertainty in the non-dimensional grouping, $\delta(\text{Fr}^{1/2}\text{Ga})^{1/2}$, is

$$\delta \left(\text{Fr}^{\frac{1}{2}}\text{Ga} \right)^{\frac{1}{2}} = \left(\text{Fr}^{\frac{1}{2}}\text{Ga} \right)^{\frac{1}{2}} \left[\left(\frac{1}{2} \frac{\delta v}{v} \right)^2 + \left(\frac{1}{4} \frac{\delta a}{a} \right)^2 \right.$$
$$\left. + \left(\frac{5}{4} \frac{\delta D_{\text{d}}}{D_{\text{d}}} \right)^2 + \left(\frac{\delta \rho}{\rho} \right)^2 + \left(-\frac{\delta \mu}{\mu} \right)^2 \right]^{\frac{1}{2}} \tag{H.27}$$

The value D_{d} is an average value of the droplet diameters listed in Table 1 in Yerkes et al.[18] The uncertainty in D_{d} is taken to be approximately 1×10^{-6} m for the purposes of this uncertainty analysis.

H.14. Uncertainty in calculated subcooling temperature

The subcooling temperature, T_{sc}, is calculated using the following equation

$$\Delta T_{sc} = T_{sat} - T_{noz} \tag{H.28}$$

Following the uncertainty propagation procedure given in Fox and McDonald[57], the uncertainty in the subcooling temperature, $\delta \Delta T_{sc}$, is

$$\delta \Delta T_{sc} = \Delta T_{sc} \left[\left(\frac{\delta T_{sat}}{T_{sat} - T_{noz}} \right)^2 + \left(\frac{-\delta T_{noz}}{T_{sat} - T_{noz}} \right)^2 \right]^{\frac{1}{2}} \tag{H.29}$$

H.15. Uncertainty in calculated Weber number

The Weber number, We, is calculated using the following equation

$$We = \frac{\rho v^2 D_d}{\sigma} \tag{H.30}$$

Following the uncertainty propagation procedure given in Fox and McDonald[57], the uncertainty in the Weber number, δWe, is

$$\delta We = We \left[\left(\frac{\delta \rho}{\rho} \right)^2 + \left(2 \frac{\delta v}{v} \right)^2 + \left(\frac{\delta D_d}{D_d} \right)^2 + \left(-\frac{\delta \sigma}{\sigma} \right)^2 \right]^{\frac{1}{2}} \tag{H.31}$$

As above, the uncertainty in D_d is taken to be approximately 1×10^{-6} m for the purposes of this uncertainty analysis.

H.16. Uncertainty in calculated free-stream fluid flowing over the side of the pedestal

The temperature of the free-stream fluid flowing over the side of the pedestal, $T_{\infty,wall}$, was calculated from the following equation

$$T_{\infty,wall} = \frac{T_{uf} + T_{lf}}{2} \tag{H.32}$$

Following the uncertainty propagation procedure given in Fox and McDonald[57], the uncertainty in this temperature, $\delta T_{\infty,wall}$, is

$$\delta T_{\infty,wall} = T_{\infty,wall} \left[\left(\frac{\delta T_{uf}}{T_{uf} + T_{lf}} \right)^2 + \left(\frac{\delta T_{lf}}{T_{uf} + T_{lf}} \right)^2 \right]^{\frac{1}{2}} \tag{H.33}$$

H.17. Uncertainty in calculated non-dimensional surface temperature

The non-dimensional surface temperature, θ_s, is calculated using the following equation

$$\theta_s = \frac{T_s - T_{\infty,wall}}{T_{sat} - T_{\infty,wall}} \tag{H.34}$$

Following the uncertainty propagation procedure given in Fox and McDonald[57], the uncertainty in the non-dimensional surface temperature, $\delta\theta_s$, is

$$\delta\theta_s = \theta_s \left[\left(\frac{\delta T_s}{T_s - T_{\infty,\text{wall}}} \right)^2 \right.$$
$$\left. + \left(\frac{\delta T_{\infty,\text{wall}}(T_s - T_{\text{sat}})}{(T_s - T_{\infty,\text{wall}})(T_{\text{sat}} - T_{\infty,\text{wall}})} \right)^2 + \left(\frac{-\delta T_{\text{sat}}}{T_{\text{sat}} - T_{\infty,\text{wall}}} \right)^2 \right]^{\frac{1}{2}} \tag{H.35}$$

H.18. Uncertainty in calculated non-dimensional saturation temperature

The non-dimensional saturation temperature, θ_{sat}, is calculated using the following equation

$$\theta_{sat} = \frac{T_{\text{sat}} - T_{\infty,\text{wall}}}{T_{\text{sat}} - T_{\infty,\text{wall}}} = 1 \tag{H.36}$$

Since this value is always $\theta_{\text{sat}}=1$, the uncertainty in this non-dimensional temperature, $\delta\theta_{\text{sat}}$, is taken to be $\delta\theta_{\text{sat}}=0$.

H.19. Uncertainty in calculated non-dimensional temperature difference

For the non-dimensional temperature difference, $\theta_s - \theta_{\text{sat}}$, the uncertainty propagation procedure given in Fox and McDonald[57] gives an uncertainty in the non-dimensional temperature difference, $\delta(\theta_s - \theta_{\text{sat}})$, of

$$\delta(\theta_s - \theta_{\text{sat}}) = (\theta_s - \theta_{\text{sat}}) \left(\frac{\delta\theta_s}{(\theta_s - \theta_{\text{sat}})} \right) = \delta\theta_s \tag{H.37}$$

H.20. Uncertainty in calculated non-dimensional heat input

The non-dimensional heat input, $(1-f)G\Delta$, is calculated using the following equation

$$(1 - f)\text{G}\Delta = \frac{(1 - f)q}{\pi b(T_{\text{sat}} - T_{\infty,\text{wall}})k_{\text{htr}}} \tag{H.38}$$

Following the uncertainty propagation procedure given in Fox and McDonald[57], the uncertainty in this non-dimensional heat input, $\delta(1-f)G\Delta$, is

$$\delta(1 - f)\text{G}$$
$$= (1 - f)\text{G}\Delta \left[\left(\frac{-\delta f}{(1 - f)} \right)^2 + \left(\frac{\delta q}{q} \right)^2 + \left(\frac{-\delta b}{b} \right)^2 \right.$$
$$\left. + \left(\frac{-\delta T_{\text{sat}}}{T_{\text{sat}} - T_{\infty,\text{wall}}} \right)^2 + \left(\frac{\delta T_{\infty,\text{wall}}}{T_{\text{sat}} - T_{\infty,\text{wall}}} \right)^2 \right]^{\frac{1}{2}} \tag{H.39}$$

The uncertainty in the value of π and the uncertainty in the heater thermal conductivity have been neglected for this uncertainty analysis.

H.21. Uncertainty in calculated non-dimensional subcooling temperature

The non-dimensional subcooling temperature, θ_{sc}, is calculated using the following equation

$$\theta_{sc} = \frac{\Delta T_{sc} - T_{\infty,wall}}{T_{sat} - T_{\infty,wall}} \tag{H.40}$$

Following the uncertainty propagation procedure given in Fox and McDonald[57], the uncertainty in the non-dimensional subcooling temperature, $\delta\theta_{sc}$, is

$$\delta\theta_{sc} = \theta_{sc} \left[\left(\frac{\delta\Delta T_{sc}}{\Delta T_{sc} - T_{\infty,wall}} \right)^2 \right.$$
$$\left. + \left(\frac{\delta T_{\infty,wall}(\Delta T_{sc} - T_{sat})}{(\Delta T_{sc} - T_{\infty,wall})(T_{sat} - T_{\infty,wall})} \right)^2 + \left(\frac{-\delta T_{sat}}{T_{sat} - T_{\infty,wall}} \right)^2 \right]^{\frac{1}{2}} \tag{H.41}$$

APPENDIX I. ALTERNATE FORMS OF HEAT VERSUS TEMPERATURE

There are several ways of presenting the characteristic heat transfer plots in literature, and the following plots present the data that was taken during this flight week in those other forms, so that it can be more easily compared to data presented by other researchers. The heat flux to the spray is plotted versus the surface temperature in Fig. I.1, and Fig. I.2 presents the heat flux to the spray versus the temperature difference between the surface temperature and the nozzle inlet temperature. As mentioned previously, there is not a great deal of additional insight that can be gained from these plots above and beyond the trends identified by Fig. 1.13 for the present research.
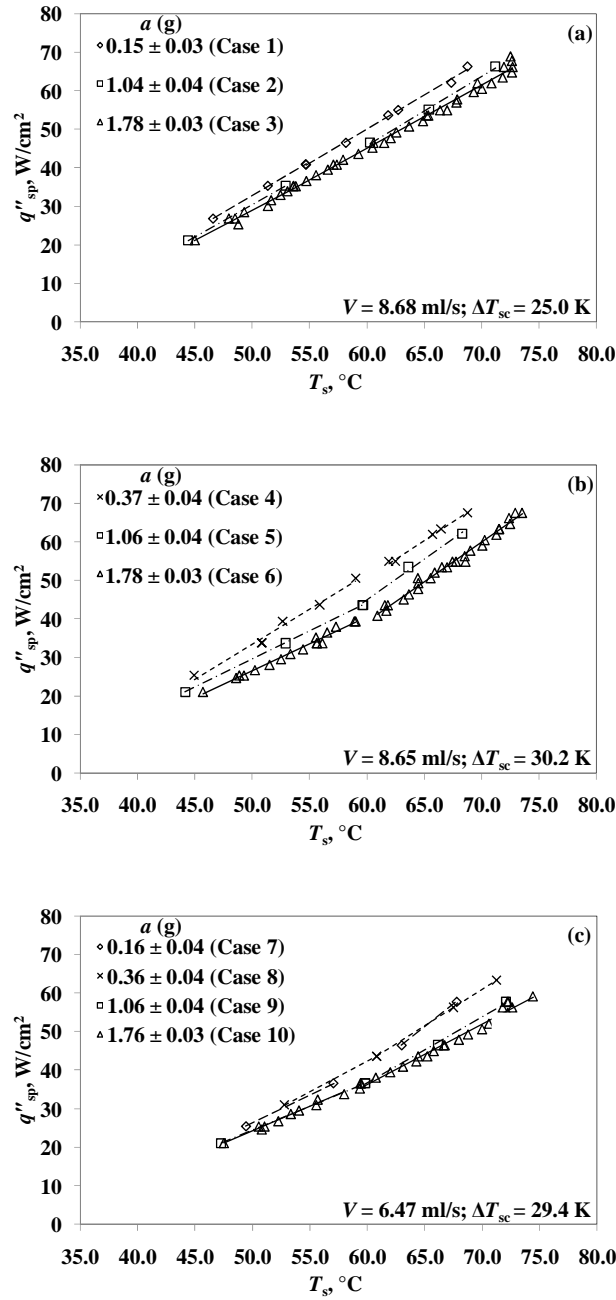
Fig. I.1 Plots showing heat flux versus surface temperature: (a) Flight 1 ($V = 8.68 \pm 0.42$ ml/s, $\Delta T_{sc} = 25.0 \pm 1.1$ K, $T_{sat} = 53.7 \pm 1.1$°C); (b) Flight 2 ($V = 8.65 \pm 0.43$ ml/s, $\Delta T_{sc} = 30.2 \pm 1.0$ K, $T_{sat} = 59.3 \pm 1.0$°C); and (c) Flight 3 ($V = 6.47 \pm 0.44$ ml/s, $\Delta T_{sc} = 29.4 \pm 1.0$ K, $T_{sat} = 58.8 \pm 1.0$°C).

107
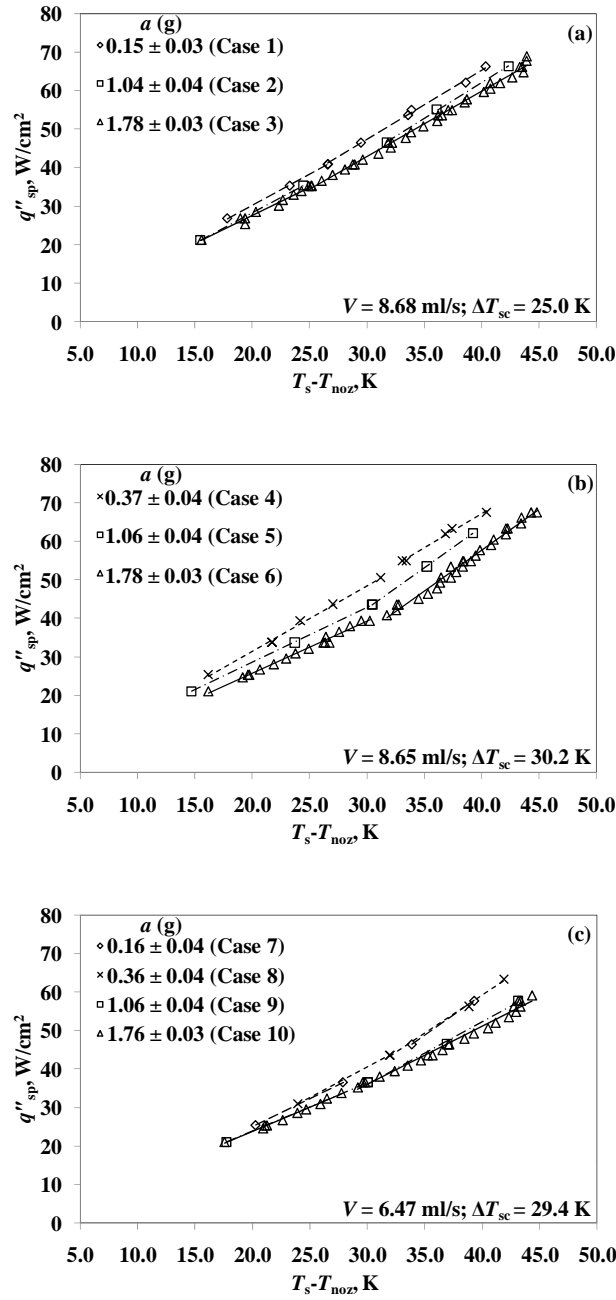
Fig. I.2 Plots showing heat flux versus temperature difference between surface and nozzle inlet: (a) Flight 1 ($V = 8.68 \pm 0.42$ ml/s, $\Delta T_{sc} = 25.0 \pm 1.1$ K, $T_{sat} = 53.7 \pm 1.1$°C); (b) Flight 2 ($V = 8.65 \pm 0.43$ ml/s, $\Delta T_{sc} = 30.2 \pm 1.0$ K, $T_{sat} = 59.3 \pm 1.0$°C); and (c) Flight 3 ($V = 6.47 \pm 0.44$ ml/s, $\Delta T_{sc} = 29.4 \pm 1.0$ K, $T_{sat} = 58.8 \pm 1.0$°C).

APPENDIX J. ADDITIONAL FIGURES

The following figures are similar to those in the main body, but did not provide a great deal of additional insight. They were placed in this appendix for reference, but they would not have been appropriate to include in the main body.

The effect of subcooling is demonstrated in Fig. J.1. The heat flux to the spray versus the wall superheat for cases 2 and 5 are compared in Fig. J.1(a). These two cases had similar flow rates but different subcooling temperatures, with case 2 at $\Delta T_{sc} = 25.1$ K and case 5 at $\Delta T_{sc} = 30.0$ K. Similarly, Fig. J.1(b) compares the heat flux to the spray versus the temperature difference for cases 3 ($\Delta T_{sc} = 24.8$) and 6 ($\Delta T_{sc} = 30.3$). In both Fig. J.1(a) and Fig. J.1(b), it is revealed that the higher subcooling provided a smaller wall superheat for any given heat load, demonstrating that the amount of heat that can be removed by a given ΔT_{sat} was greater.

The effects of flow rate on the performance of the spray cooling system can be seen in Fig. J.2. The heat flux to the spray versus the temperature difference for cases 4 and 8 is shown in Fig. J.2(a). The difference between these two curves is in the volumetric flow rate, with $V = 8.63$ ml/s for case 4 and $V = 6.58$ ml/s for case 8. Similarly, Fig. J.2(b) illustrates the data for cases 5 ($V = 8.70$ ml/s) and 9 ($V = 6.61$ ml/s). Finally, Fig. J.2(c) epitomizes the data for cases 6 ($V = 8.61$ ml/s) and 10 ($V = 6.43$ ml/s). In all three of these plots, the volumetric flow rate and subcooling were held constant. In all the data, the higher flow rate gives a lower ΔT_{sat} for the same heat flux, or a higher heat flux for a given ΔT_{sat}. This is indicative of enhanced heat transfer performance at higher flow rates, as would be expected.

The data at similar heat fluxes from Fig. 1.10(a) and (b) is combined in Fig. J.3, to show the effects of subcooling on the wall superheat versus acceleration behavior. Similarly, the data at similar heat fluxes from Fig. 1.10(b) and (c) are combined in Fig. J.4, to show the effects of volumetric flow rate on the wall superheat versus acceleration behavior.
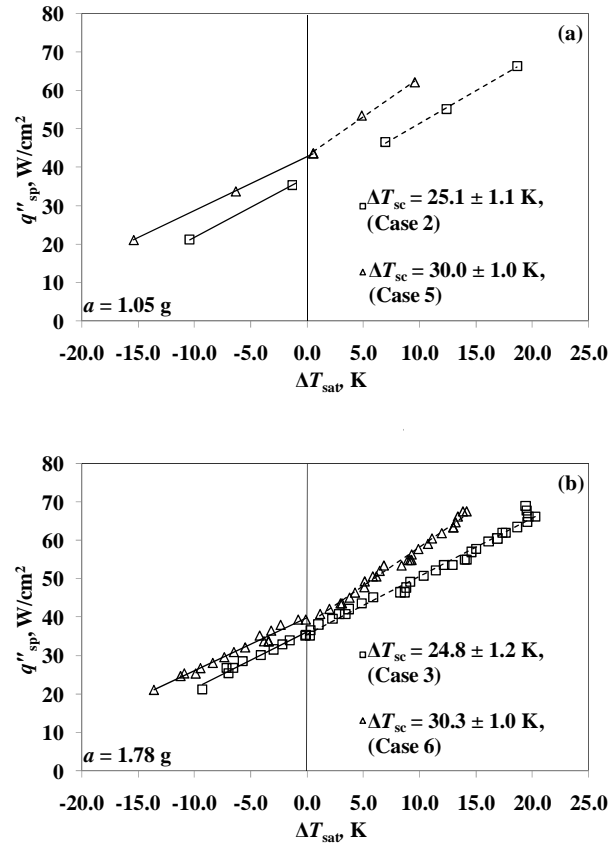
Fig. J.1 Effect of subcooling on heat flux ($V = 8.66 \pm 0.42$ ml/s): (a) $a = 1.05 \pm 0.04$ g (Cases 2 and 5); and (b) $a = 1.78 \pm 0.03$ g (Cases 3 and 6).
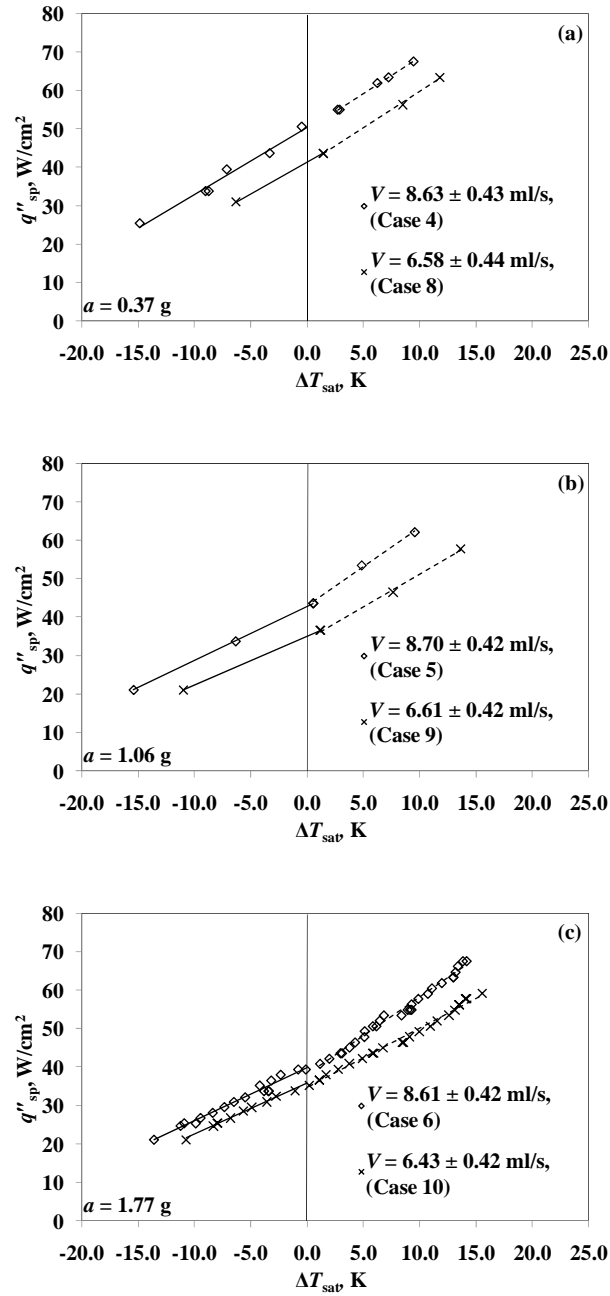
(a)

q''_{sp}, W/cm^2

$V = 8.63 \pm 0.43$ ml/s, (Case 4)

$V = 6.58 \pm 0.44$ ml/s, (Case 8)

$a = 0.37$ g

ΔT_{sat}, K

(b)

q''_{sp}, W/cm^2

$V = 8.70 \pm 0.42$ ml/s, (Case 5)

$V = 6.61 \pm 0.42$ ml/s, (Case 9)

$a = 1.06$ g

ΔT_{sat}, K

(c)

q''_{sp}, W/cm^2

$V = 8.61 \pm 0.42$ ml/s, (Case 6)

$V = 6.43 \pm 0.42$ ml/s, (Case 10)

$a = 1.77$ g

ΔT_{sat}, K

Fig. J.2 Effect of flow rate on heat flux ($\Delta T_{sc} = 30.0 \pm 1.4$ K, $T_{sat} = 59.1 \pm 1.2$°C): (a) $a = 0.37 \pm 0.03$ g (Cases 4 and 8); (b) $a = 1.06 \pm 1.04$ g (Cases 5 and 9); and (c) $a = 1.77 \pm 0.03$ g (Cases 6 and 10).

111
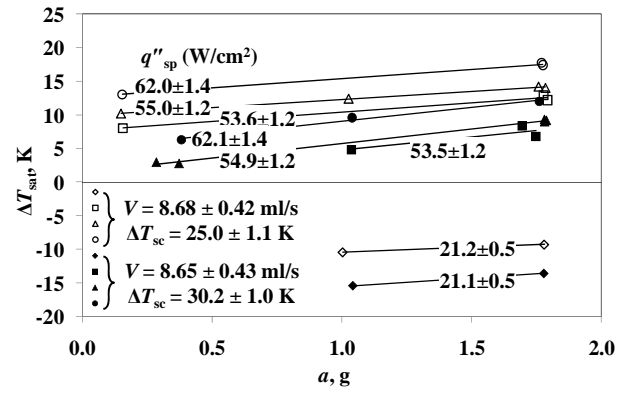
Fig. J.3 Effect of subcooling on wall superheat at various accelerations.
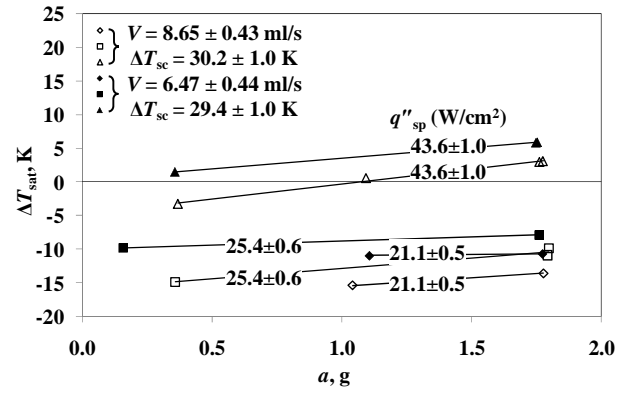
Fig. J.4 Effect of flow rate on wall superheat at various accelerations.

APPENDIX K. NON-DIMENSIONAL FIGURES

The following figures are the non-dimensional versions of many of the plots seen throughout the rest of the main body and appendices of this document.

Many of the same trends can be seen in Fig. K.1(a) as in Fig. 1.13(a). The non-dimensional temperature difference θ_s-θ_{sat} tends to increase as the non-dimensional heat flux $(1-f)G\Delta$ increases. There is still a difference between cases 1 and 2, showing that the lower acceleration of case 1 drops the value of θ_s-θ_{sat} at a given $(1-f)G\Delta$ when compared to case 2. However, there is a slightly more pronounced difference between case 2 and case 3 when the non-dimensional data is observed, as compared to the dimensional data of Fig. 1.13(a). The slopes in Fig. K.1(a) behave very similarly to those observed in Fig. 1.13(a), with the curves being relatively linear and parallel. Similar statements can be made concerning the data presented in Fig. K.1(b) and (c) when compared to Fig. 1.13(b) and (c). Additionally, Fig. K.2 is analogous to Fig. 1.10, but presented in non-dimensional form. Also, Fig. K.3 and Fig. K.4 are analogous to Fig. J.3 and Fig. J.4.
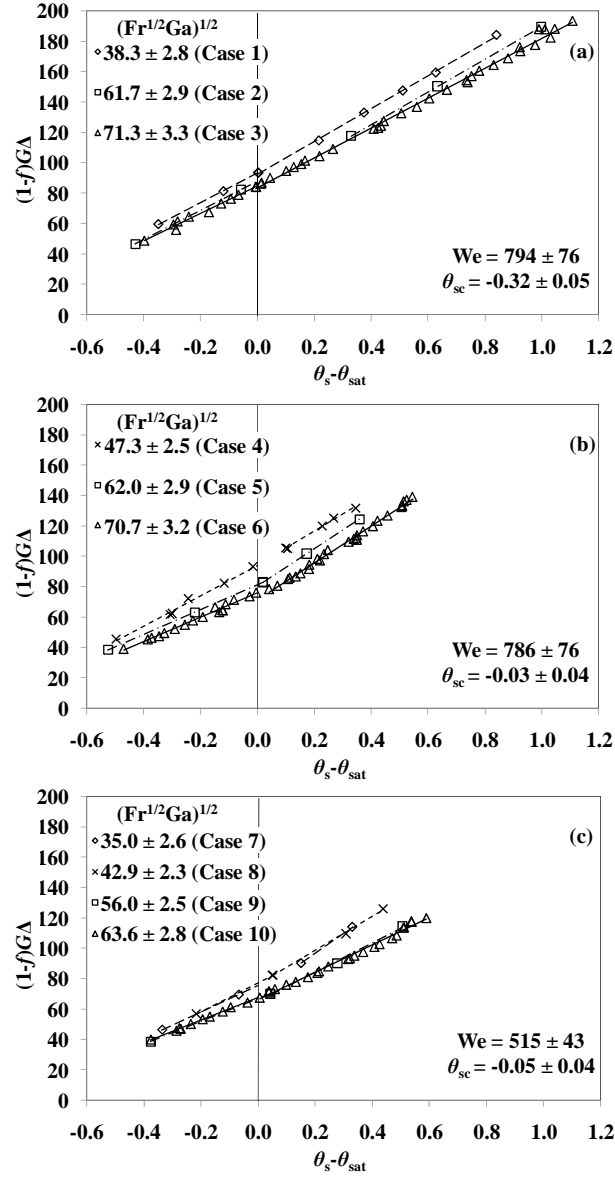
Fig. K.1 Non-dimensional heat input versus non-dimensional temperature difference showing (a) Flight 1 (repeating Fig. 1.14), (b) Flight 2, and (c) Flight 3

114

We = 794 ± 76
$\theta_{sc} = -0.32 \pm 0.05$

(a)

$(1-f)G\Delta$

188±12

170±12

151±9

140±9

118±6

96.5±5.4

82.5±4.0

60.1±3.1

46.7±2.1

$\theta_s - \theta_{sat}$

$(Fr^{1/2}Ga)^{1/2}$

We = 786 ± 76
$\theta_{sc} = -0.03 \pm 0.04$

(b)

$(1-f)G\Delta$

136±6

130±5 124±5

109±4 103±4

95.8±3.8

83.1±3.0 73.8±2.9

63.0±2.3

46.3±1.7 38.5±1.3

$\theta_s - \theta_{sat}$

$(Fr^{1/2}Ga)^{1/2}$

We = 515 ± 43
$\theta_{sc} = -0.05 \pm 0.04$

(c)

$(1-f)G\Delta$

115±4 112±5

90.6±3.4

83.5±3.4

70.3±2.6

57.5±2.1

46.9±1.8

38.8±1.3

$\theta_s - \theta_{sat}$
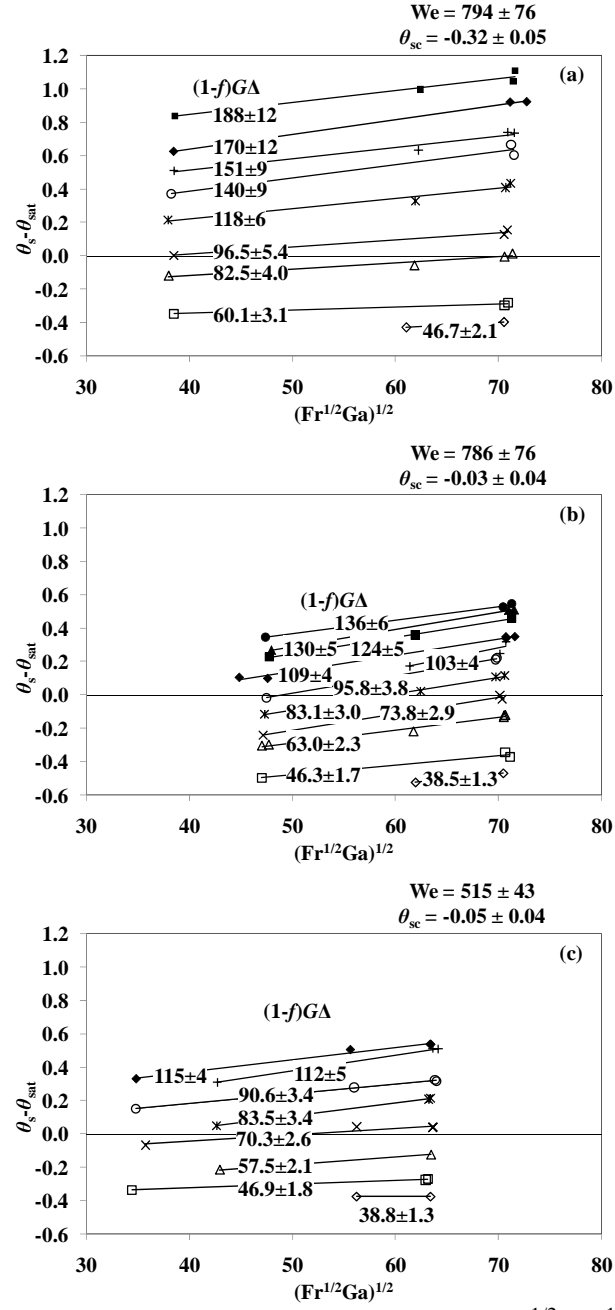
$(Fr^{1/2}Ga)^{1/2}$

Fig. K.2 Non-dimensional temperature difference versus $(Fr^{1/2}Ga)^{1/2}$ showing (a) Flight 1, (b) Flight 2, and (c) Flight 3

115
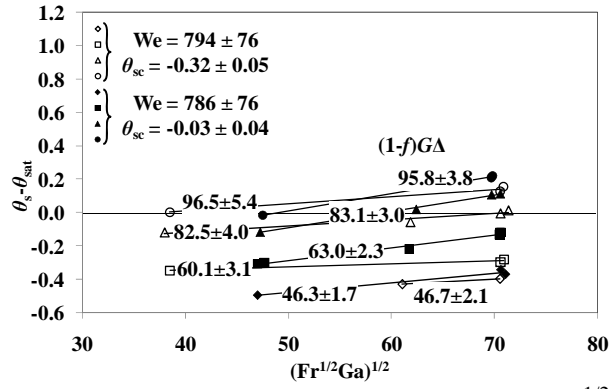
Fig. K.3 Non-dimensional temperature difference versus $(Fr^{1/2}Ga)^{1/2}$ (Effect of Subcooling)
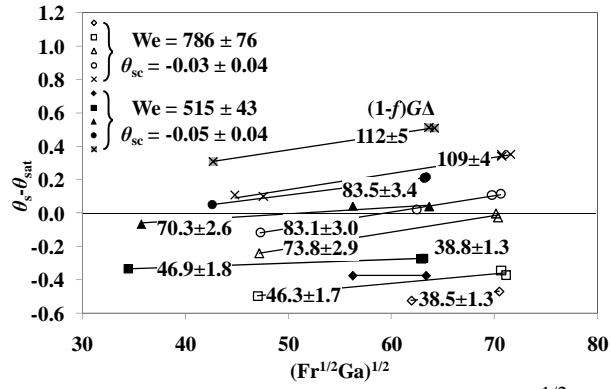
Fig. K.4 Non-dimensional temperature difference versus $(Fr^{1/2}Ga)^{1/2}$ (Effect of Flow)

APPENDIX L. TEST EQUIPMENT DATA PACKAGE

The following Test Equipment Data Package (TEDP) is a document that was required by NASA for any experiments that were flown on the reduced gravity testing platform. The formatting of this document has not been modified, other than making the figures black and white, and adding page numbers to coincide with the rest of this thesis. Therefore, the formatting may not entirely match that from the rest of this thesis, but the TEDP is being included for historical reference, and changing the formatting of this stand-alone document would have been inappropriate.

TEST EQUIPMENT DATA PACKAGE
FOR
THE MICROGRAVITY
SPRAY COOLING EXPERIMENT

Kirk Yerkes
Air Force Research Laboratory, Propulsion Directorate
Wright Patterson Air Force Base
1950 Fifth Street
WPAFB, OH 45433-7251
PH (937)255-5721
FAX (937)656-7529

2 August 2004

Revisions

Rev. 2, 4 October 2003

System Weight

Original TEDP listed weight as 642 pounds. Upon arrival at GRC, rig weighed in at 742 pounds. Additional items were placed on rig including brackets, 80/20 channel, wiring, laptop power supply, and handle bars. Several structural calculations were redone.

Original pg #	Rev 2 pg #	Change
i	i	Quick Reference Sheet: Overall Weight
6	6	Rig Frame Analysis: Calculation for M_{Total} and Margin of Safety
7	7	Table 3: Additional Components listed and some weight adjustment
7	7	Table 5: Moment Load value
8 8		Calculation for $P_{t, max}$ and Margin of Safety
8	9	Calculation for load carrying capacity
11	11	Table 9: Tabulation of weights and moment arms
11 12		Calculation for $P_{t, max}$ and P_s
12	12	Calculation for Margin of Safety
12	13	Calculation for Combined Shear/Tensile Loading
N/A	46–48	Document additional load testing on 80/20 channel vertical risers and bracing.

Plumbing Schematic

As a result of the Technical Readiness Review conducted at WPAFB on September 16, 2003, it was suggested, and consequently, implemented to install additional fill/drain valves to facilitate filling the FC-72 past the filters and with the subsequent degassing. The new plumbing schematic is illustrated below:

Drainfill Valve Connections

Reheater: ¼"Copper tubing

3-way valve

Reheater: ¼"Copper tubing

3-way valve

Press. Trans

Pressure Relief Switch

Pressure Relief Switch

Air/Liq Hx

Air/Liq Hx

Chamber

Press. Trans

Press. Trans

Pump

Drainfill Valve Connections

Fl. M

Fl. M

Reservoir

Filter

Filter

Drain Valve Connection

Throttling Valves

Filter

Press. Trans

Drainfill Valve Connections

Fl. M

Air/Liq Hx

Pump

Pump

Air/Liq Hx

Air/Liq Hx

Press. Trans

Pump

Press. Trans

Filter

Reservoir

Va

3/8" Polyflow; 350psi@ 21C, 240psi@ 43C

1/4" Polyflow; 400psi@ 21C, 260psi@ 43C

3/8" St.Steel; 4100 psi

1/4" St.Steel; 4400 psi

3/8" Copper; 1840 psi

*Connections consist of standard, brass or steel compression fittings with metal ferrules (rated to that of the tubing).

*Metal tube pressures are maximum suggested working pressures, as noted in the Parker catalog.

*Copper tubing pressure includes a temperature derating factor, as noted in the Parker catalog.

*Dotted pink lines indicate areas of low pressure. All other regions are "high" pressure regions.

*Maximum expected pressure: 80 psi

ii

Rev. 3, 5 April 2004

Changes

A few minor changes were made to the package that flew in October. The watt transducers were replaced by precision resistors. Changes in the FC-72 flow loop included larger pump heads and the addition al of optiona l che ck valves. Additiona l optica l m ounting brackets were added for additional cam era m ounting. The test cham ber was m odified with an internal annular screen and the sump heater mounting assembly was redesigned.

Rev 2 pg #	Rev 3 pg #	Change
iii	v	Quick Reference Sheet: Changed Flight Dates and Proposed Researchers
1	1	Changed Flight Manifest
2	2	Deleted "mounted in a port replicator"
6	6	Table 2: Deleted watt transducer
6	6	Moment equations: (now) 9649.51 (was) 9727.56, (now) 86845.59 (was) 87548.04, margin of safety (now) .34 (was) .33
7	7	Table 3: Level Four (now) 27.6, 30.81, 850.36 (was) 34.3, 30.75, 1054.73
		Added "Optical Mounting"
		Total (now) 17.86, 9649.51 (was) 18.00, 9727.46
11	11	Table 9: Rig (now) 19.0, 10879.40 (was) 19.1, 10953.84
		Total (now) 14.9, 11054.13 (was) 15.0, 11128.64
12	12	Tipping tensile load equation: (now) 14.9, 503.3 (was) 15.0, 506.7
		Margin of safety equations: (now) 503.3, 6.7 (was) 506.7, 6.6
13	13	Combined shear/tensile loading: (now) 503.3, .0035, .35 (was) 506.7, .0036, .36
14	14	Flow Schematic: (now) 100 °C (was) 70 °C
15	15	Changed pressure switches' setting (now) 105 psiA (was) 82 psiA. Changed the pressure at which the FC-72 loop will be tested to 132 psiG from 111 psiG.
19	19	Hazard Control(s): (now) will monitor heater temperature, to not exceed 100 °C (was) will monitor temperature, to not exceed 70 °C
20	20	Hazard Control(s): Test chamber: (now) "in the chamber" (was) "at the heater", deleted "(should the chamber temperature reach the 70 °C)"
		FC-72 Nozzle inlet: deleted "The test chamber will be pressure tested to 111 psiG", flow components pressure tested (now) 132 psiG (was) 111 psiG
		Pressure switches set to (now) 105 psiA (was) 85 psiA
		Added, "Note: Maximum working pressure for FC-72 system is 100 psiA. Maximum working pressure for water system is 75 psiA."
21	21	Hazard Control(s): heater operating temperature (now) 100 °C (was) 70 °C
		Added "by shutting down the experiment"

iii

22 22		Hazard Control(s): (now) 132 psiG (was) 111 psiG
28	28	(now) heater temperatures will be limited to 100 °C (was) experiment temperatures will be limited to 70 °C
33–40 33–41		Updated electrical schematics
48–52	49–53	Updated views of rig
53	55	Changed view of chamber to show the screen and new sump
57–58	59–63	Updated views of sump
59	64	Updated flow schematic

Rev. 4, 2 August 2004

Changes

A few m inor changes w ere m ade to the packag e that flew in May. O ne of the FC-72 supply lines was changed to a drain line. Portions of the document were changed to clarify meanings.

Rev 3 pg #	Rev 4 pg #	Change
iii	iii	Change table, first item Rev 3 pg # (now) v (was) iv
v	vi	Quick Reference Sheet: Changed Flight Dates and Proposed Researchers
1	1	Changed Flight Manifest
1	1	Added "thick film resistance heaters"
1,2	1,2	Deleted ITO references to heaters
1	2	Equipment Description: (now) glass or polycarbonate pedestals (was) polycarbonate pedestals
7	7	Table 5: (now) 375 in·lbs (was) 225 in·lbs
8	8	Total rig analysis (now) c.g. is 18.5 in. (was) c.g. is 18.6 in.
10	10	Shelf Attachment to Frame: added "…, from Table 5,…" and "…, using a joint strength value of 375 in·lbs from Table 5,…"
13	13	Electrial Emergency Flow Shutdown Switch: (now) In addition, individual items… (was) All items…
14,15	14,15	Flow Schematic: (now) test chamber will set… (was) test chamber set… (now) The maximum temperature will be at the heater and is 100 °C. The maximum chamber temperature is set for 70 °C, which corresponds to a chamber pressure of 25 psiA. (was) The maximum temperature will be at the heater and is 100 °C which corresponds to a maximum of 25 psiA if the entire chamber should the chamber temperature reach the 70 °C.
15	15	Flow Schematic: (now) volume of the chamber will… (was) volume of the chamber combined will…
N/A	16	Added "Flow Containment Plan" section.
19	19	Hazard Controls(s): added "Should a leak occur, the flow system is designed to be able to isolate the FC-72 either in the test chamber or the reservoir."
20	20	Hazard Control(s): (now) "volume of the chamber combined…" (was) "volume of the chamber…", added "or isolation of the FC-72 in the event of a leak"
21	21	Hazard Control(s): added "This will allow high heat flux testing at the heater without significantly altering the chamber temperature."
30	30	Leak Shut Down Procedure: Added step to isolate FC-72. Added methods to mop-up leak. Emergency Shut Down Procedure: Added methods to mop-up leak.
64	64	Updated flow schematic

KC-135 Quick Reference Data Sheet

Principal Investigator:
Kirk Yerkes
AFRL/PRPS
1950 Fifth Street
WPAFB, OH 45433-7251
PH: (937)255-5721
FAX: (937)656-7529
E-mail: kirk.yerkes@wpafb.af.mil
Experiment Title: Microgravity Spray Cooling
Flight Dates: 13–17 September 2004

Category	Data	See page
Overall Assembly Weight	742 lbs	11
Assembly Dimensions:	44"×64.5"×44"	
Equipment Orientation Requests:	Lengthwise along axis of aircraft	
Floor Mounting Strategy	Bolts	
Gas Cylinder Requests	No	
Overboard Vent Requests	No	
Power Requirements	115 VAC, 60 Hz	14
Free Float Experiment	No	
Proposed Researchers	Kirk Yerkes, AFRL	1
	Lt Ryan Claycamp, AFRL	
	Kerri Baysinger, AFRL	
	Travis Michalak, AFRL	
	Quinn Leland, AFRL	
	Levi Elston, AFRL	
	John McQuillen, NASA GRC	
	Eric Golliher, NASA GRC	
	Mark Kobel, NASA GSFC	
	A.J. Mastropietro, NASA GSFC	

Table of Contents

List of Tables

List of Figures

Flight Manifest

Name	Affiliation	Preferred Days of Flight	Previous Flyer
Kirk Yerkes	AFRL	Tu-F	Yes, May 2004
Lt Ryan Claycamp	AFRL	Tu,Th,F	Yes, May 2004
Kerri Baysinger	AFRL	Tu,W,F	Yes, May 2004
Travis Michalak	AFRL	Tu,W,Th	Yes, May 2004
Quinn Leland	AFRL	Alternate	No
Levi Elston	AFRL	Alternate	Yes, May 2004
John McQuillen	NASA GRC		Yes
Eric Golliher	NASA GRC		Yes, May 2004
Mark Kobel	NASA GSFC		No
A.J. Mastropietro	NASA GSFC		No

Table 1: Flight Manifest

Experiment Background

Two-phase spray cooling is an example of a thermal management technique that may be utilized in high heat flux acquisition and high thermal energy transport concepts. It is one of many possible alternatives to the prevalent passive thermal management technologies, such as heat pipes and capillary pumped loops, which are currently used in space applications. Many researchers have investigated the utility of two-phase sprays for the thermal management of devices generating high heat fluxes. However, there has been little research addressing the physics and ultimate performance of two-phase spray cooling in the micro-gravity environment.

Experiment Description

The experiment consists of two primary components as shown in the equipment drawings. The first component is a rotatable spray test chamber containing the spray nozzles, heaters, primary condenser surface, and sump configuration to collect the liquid and condensate. The second component is the flow loop system that consists of two flow loops to manage the working fluid, FC-72, and a water loop to cool the spray test chamber. The experiment will be operated by applying electrical power to the Indium Tin Oxide (ITO) heaters or thick film resistance heaters, to generate heat, and spray cooling the heaters. Data will be collected on the heat transfer performance and thermophysics of spray cooling of the heaters in both high-g and micro-g environments.

Equipment Description

The entire experiment is constructed of an aluminum framework made of "8020" with a 0.5-inch thick aluminum base plate which serves as the mounting plate and a containment pan should any fluid leaks develop during flight tests. The spray test chamber is rotatable pressure vessel and will be fixed in one orientation during a flight test (see Figure 1). The spray test chamber consists of two opposed spray nozzles, heaters, and sump sys-

1

tems. Target heaters are mounted on glass or polycarbonate pedestals as part of the sump system to remove unconstrained liquid from the test chamber. The inside surface of the chamber is lined with a wick structure as the primary condensation surface for the condensate liquid to return to the sump system. Liquid is collected in the sump and returned to the fluid delivery loop. The exterior surface of the chamber is liquid cooled using a separate water loop coupled to liquid-air heat exchangers. Thermocouples mounted in the pedestals are used to determine the heat loss through the underside of the heaters.
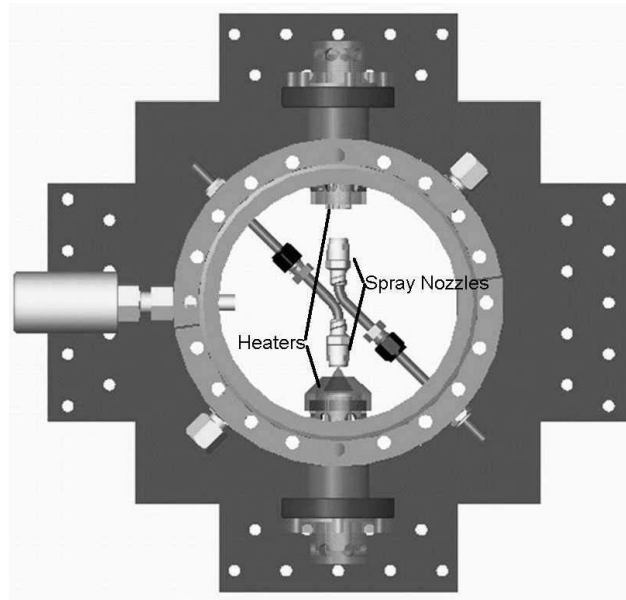

Figure 1: Illustration of Test Chamber

The flow loop consists of the pumps, flow meters, pressure and temperature transducers, pressure relief switches, reservoirs, electrical valves, liquid-air heat exchangers, reheaters, and associated plumbing. These components serve to move the cooling water and the FC-72 working to and from the spray test chamber while monitoring flow rate, temperatures, and pressure. Various power supplies are also mounted to the experimental framework to provide electrical power to the various fluid motive components in the flow loop, heaters, and, instrumentation transducers.

The experiment will be operated and monitored via a control panel and data acquisition system. The data acquisition system consists of a laptop coupled to an HP Data Acquisition/Switch Unit. Various safety features limit the maximum heater temperature and system pressure in order to maintain the experiment within safe operating parameters during the flight test. Both software and mechanical safety features allow for the safe shutdown in the event of a temperature or pressure excursion above allowable limits.

2

Structural Analysis

The experimental hardware is configured to be installed on the KC-135 with the long axis of the experiment rig parallel to the longitudinal axis of the aircraft. Figure 2 illustrates the axis/orientation that will be used in this test series.
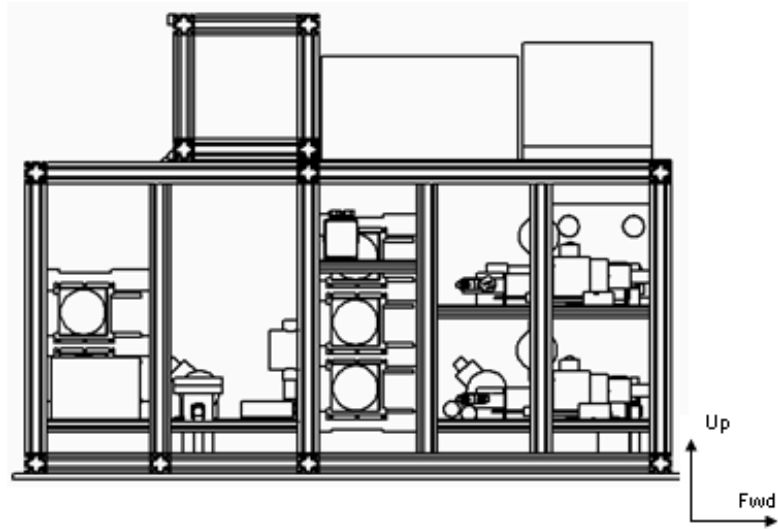

Figure 2: Equipment Orientation

Load Factors

This report analyzes the effects of emergency load factors specified by the *JSC Reduced Gravity Program User's Guide*. The components are analyzed with emergency load factors in all appropriate orientations.

Direction	Load Factor
Forward	9g
Aft	3g
Lateral	2g
Up	2g
Down	6g

Frame Components

Provided is the detailed analysis to the extent that the component warranted. This will serve as an example as to how the other components in Table 2 were analyzed.

FC-72 Reservoir

The FC-72 reservoir is mounted to the base plate and a shelf with four ¼-20 bolts and weighs 17.66 lbs. when filled with F C-72 to its operational level. Figure 3 shows the 9g forward load factor results.

Applied g loading:

Direction	Load (lbs)
Forward	159.0
Aft	53.0
Up/Lateral	35.3
Down	106.0

Tensile/shear loading: The independent tensile/shear loading per bolt was calcu lated as shown here:

$$\frac{(applied\ load)}{\#\ of\ bolts}$$

Direction	Load (lbs/bolt)
Forward	39.75
Aft	13.25
Up/Lateral	8.83
Down	26.5

Margins of Safety: The ultimate tensile margin of safety is calculated as shown here:

$$MS_{UT} = \frac{F_{UT}}{(applied\ load)(FS)} - 1$$

Where,

F_{UT} = Ultimate te nsile f ailure load (oth er option s in clude F_{YT} = Yield tensile failure load, F_{SU} = Ultim ate shea r f ailure load, and F_{SY} = Yield s hear failure load)

FS = Factor of safety

Established NASA factors of safe ty are 2.0 or greater for all st ructural or fracture critical elements.

The tensile and shear loads for a grade 8 ¼-20 bolt are:

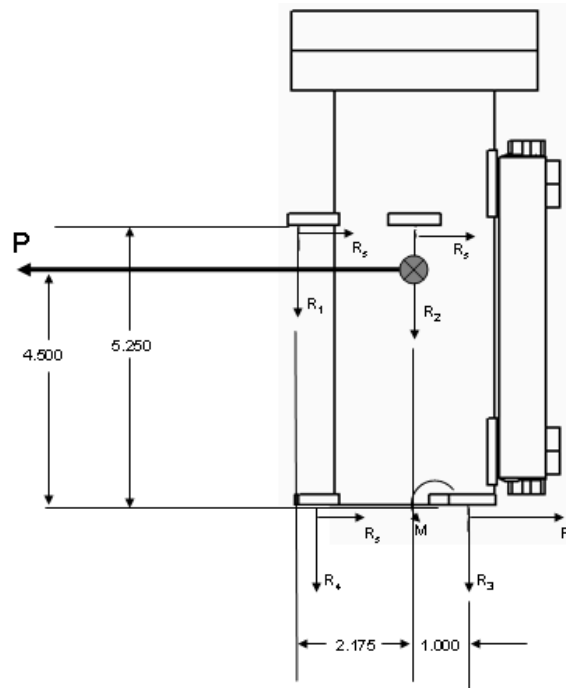$$F_T = 4770\ \text{lbs} \qquad F_S = 2860\ \text{lbs}$$

4

Figure 3: Reactions to 9g Forward Load Factor—FC-72 Reservoir

Shear ultimate margin of safety:

$$MS_S = \frac{2860}{(39.75)(2)} - 1 = 35$$

With a m argin of safety of 35, it is clear th at the applied g-loads in any direction are small in co mparison with the f ailure or yie ld loads for the bolts. All tensile/she ar loads are two orders of m agnitude below the failure loads an d th us indicate large m argins of safety for any force acting on this component.

Component Table

Table 2 contains all data pertin ent to the analysis of the remaining frame components. It is evident from the ultim ate tensile m argins of safety that none of the com ponents approach the failure loads of the bolts restraining them and therefore, no further analysis of these components is warranted.

Component	Weight (lbs)	Applied g-load (9g for-ward – lbs)	Bolt	Tensile/shear loading (lbs/bolt)	F_S (lbs)	MS F_S
Power Supply (480W)	3.85	34.7	10-32	8.7	1525	87
Power Supply (100W)	1.60	14.4	10-32	3.6	1525	210
Power Supply (chamber heater)	3.15 2	8.4	10-32	7.1	1525	106
Heat Exchanger Fan	3.35	30.2	10-32	5.0	1525	150
Heat Exchanger Assembly – Water Loop	10.5 9	4.5	MS51959	3.9	1525	192
Heat Exchanger Assembly – FC-72 Loop	14.2 1	27.8	MS51959	5.3	1525	142
Water Reservoir	14.0	126.0	Grade 8 ¼-20	25.2	2860	55.8
Test Section	70.0	630.0	80/20 ¼-20	26.3	3300	61.9

Table 2: Component Analysis

Rig Frame Analysis

This section will include a detailed analysis of the frame. The loads and moments acting on the rig frame base members are presented in Table 3. Therefore, the weight in Table 3 does not include the weight of the 80/20 extrus ions below the lower joints and the center of gravity distance is measured from the top of those 80/20 extrusions.

The rig fram e is constructed of 2020 extrusions from 80/20 Inc. All joints were assem -bled with their recomm ended bolt kits and al l fasteners wer e torqued ac cording to th eir specifications. The corner connections use the m anufacturer's 90° joining plates (P/N 4128) with two inside corner brackets (P/N 4114). Table 4 contains the extrusion proper-ties and Tab le 5 has the joint strength values. 80/20 did not have docum entation for the joints we are using with the 2020 extrusions. We perform ed static testing to develop our own figures and document the result in Appendix B. The frame is bolted to the base plate with MS51959-81 screws.

The total m oment load resulting f rom the 9g f orward load f actor is r eacted at e ighteen joints connecting the vertical members to the base members (ignoring, conservatively, the effects of the eighteen joints at the top of the fram e and the bracing that the shelves pro-vide). The total moment load, as determined from the data of Table 3, is:

$$M_{Total} = 9g\left(\sum M\right) = 9(9649.51) = 86,845.59 \text{ in·lbs}$$

Dividing this total m oment am ong the eighteen joints at the base of the fram e yields a moment load per joint of 4824.76 in·lbs. Co mparing this load to the joint ultim ate strength:

$$MS_{Ult} = \frac{9700}{(4824.76)(1.5)} - 1 = .34$$

This gives us a positive margin of safety.

6

	Weight (lbs)	Z from top of 80/20 base (in)	Mz
Frame 111.6		18.25	2036.70
Shelf Supports	13.6	7.55	102.68
Shelves 50.7		8.11	411.18
Fasteners 41.3		12.00	495.60
Water Loop	10.5	14.99	157.40
FC72 Loop	14.2	12.29	174.52
Level One	49.9	5.47	272.95
Level Two	29.1	23.11	672.50
Level Three	2.6	20.50	53.30
Level Four	27.6	30.81	850.36
Test Section	70.0	35.00	2450.00
Optical Mountings	1.5	21.01	31.52
Wiring & Connectors	43.0	18.25	784.75
Plumbing & Fittings	48.2	18.25	879.65
Miscellaneous 26.5		10.43	276.40
Total	**540.3**	**17.86**	**9649.51**

Table 3: Experiment Rig Loads and Moments

	2020	1010
Material	6105-T5 Aluminum	6105-T5 Aluminum
Yield Strength	35000 psi	35000 psi
Tensile Strength	38000 psi	38000 psi
Elastic modulus	10,2000,000 psi	10,2000,000 psi
Moment of inertia (x-x and y-y)	.5513 in^4	.04413 in^4
Section area	1.223 in^2	.435in^2

Table 4: Extrusion Properties

	Double 90° Joining Plate with 90° Corner Brackets – 2020	Corner Bracket – 1010
Direct (shear) load		325 lb
Moment load	9700.0 in·lbs	375 in·lbs
Torsion load		180 in·lbs

Table 5: Joint Strength Values

With the tipping moment factored into the situation under 9gs forward, the tensile load on the bolts in the row farthest from the line of rotation will experience the highest load and that load can be calculated with this formula:

$$P_{t,\max} = \frac{FLd_k}{\sum_i nd_i^2}$$

Where

F = overturn load

L = vertical distance from overturn line to center of gravity

7

d_k = distance from overturn line to furthest bolt(s)

n = number of bolts in a row

d_i = distance from overturn line to row

The total rig, including the 80/ 20 extrusions left out of th e above calculation, w eighs 572.6 lb and the center of gravity is 18.5 inches fr om the top of the base plate. This will result in the reactions illustrated in F igure 4. Substituting the known values into this for-mula

$$P_{t,\max} = \frac{(9)(572.6)(18.5)(62)}{10(.5^2 + 1.5^2 + 61^2 + 62^2) + 4(3^2 + 6^2 + 8^2 + 11^2 + 14^2 + 17^2 + 20^2 + 23^2 + 26^2) + \cdots} = 27$$
$$\cdots + 4(29^2 + 32^2 + 35^2 + 38^2 + 41^2 + 44^2 + 47^2 + 50^2 + 53^2 + 56^2 + 59^2) + \cdots$$
$$\cdots + 11(12.5^2 + 13.5^2 + 27^2 + 28^2) + 9(38.5^2 + 39.5^2)$$

$P_{t,\max}$ = tipping tensile load = 27 lbs/bolt

Margin of Safety: Using the margin of safety calculation stated earlier in this report, the ultimate and yield margins of safety in the tipping tensile load on the bolts in the row far-thest from the line of rotation can be calculated by:

For MS51959 screws: F_T = 2540 lbs and F_S = 1525 lbs

$$MS_T = \frac{2540}{(27)(2)} - 1 \approx 46$$

With the large m argins of safety, it is eviden t that the tensile load on th e bolts in th e row receiving the most tension during tipping will not be critical for bolt failure.

Combined Shear/Tensile Loading: The com bined tipp ing shear and te nsile load ing is analyzed with the following formula:

$$\left(\frac{P_S}{F_S}\right)^3 + \left(\frac{P_t}{F_t}\right)^2 \leq 1$$

Where

P_S = applied shear load

F_S = shear failure load

P_t = applied tensile load (tipping)
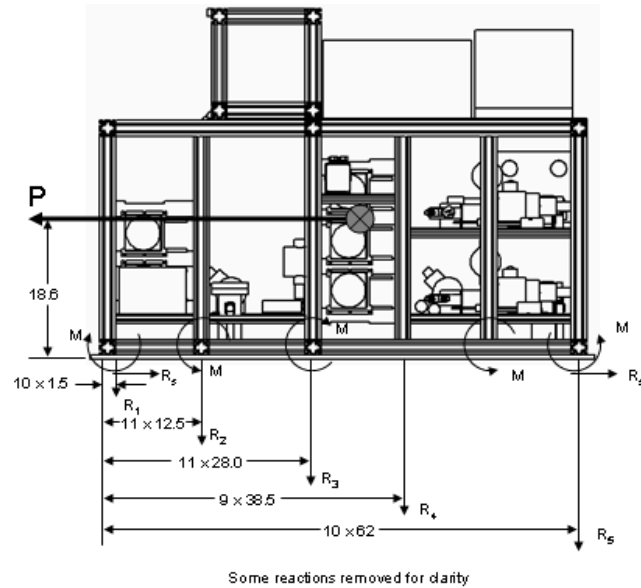
F_t = tensile failure load

8

Figure 4: Reactions to 9g Forward Load Factor—Rig Frame

The combined shear/tensile loading is analyzed below:

With a forward load of 572.6 at 9gs, which equals 5153.4 lbs, being held by 182 screws, the shear loading per screw is 28.3 lbs.

$$\left(\frac{28.3}{1525}\right)^3 + \left(\frac{27}{2540}\right)^2 = .00012 = .012\% \text{ of load carrying capacity used}$$

Shelves

Table 6 contains all data pertinent to the analysis of the shelves.

Shelf	Weight (including components – lbs)	Applied mass (9g forward – lbs)	Shear Loading (lbs/bolt)	Bolt	F_s (lbs)
1	17.8	160.2	7.0	¼-20	3300
2	17.2	154.8	5.2	¼-20	3300
3	10.1	90.9	4.1	¼-20	3300
4	36.5	328.5	8.0	¼-20	3300
5	29.2	262.8	6.0	¼-20	3300

Table 6: Shelf Loading

Shear Margin of Safety: The shear margin of safety for the first shelf is calculated as shown here:

$$MS_S = \frac{3300}{(7.0)(2)} - 1 \approx 235$$

9

138

With a margin of safety of 235, it is clear that the applied g-loads in any direction are small in comparison with the failure or yield loads for the bolts. All tensile/shear loads are two orders of magnitude below the failure loads and thus indicate large margins of safety for any force acting on this shelf.

Shelf Attachment to Frame: The shelves are attached to 1010 extrusions that are attached to the 2020 frame with corner brackets (P/N 4121 and 4122, right and left brackets respectively).

Shelf 4 is used to show the calculations for the shelves. It is supported by 8 extrusions and the 9g forward load factor results in reactions shown in Figure 5. The 328.5 lb load spread over the 8 joints results in an individual loading of 41.06 lb. With a joint strength value of 325 lb, from Table 5, the margin of safety is:

$$MS = \frac{325}{41.06 \cdot 1.5} - 1 = 4.3$$

The center of gravity of the components on the shelf is at 2.75 in. This creates a moment load of:

$$M_{total} = 9g(36.5)(2.75) = 903.38$$

Dividing this total moment among the eight joints yields a moment load per joint of 112.9 in·lbs. This gives a margin of safety, using a joint strength value of 375 in·lbs from Table 5, of:

$$MS = \frac{375}{112.9 \cdot 1.5} - 1 = 1.2$$

By symmetry, the 3g aft and 2g lateral load factors are not considered critical for failure in the structure. The results of the calculations for the remaining shelves are shown in Table 7.
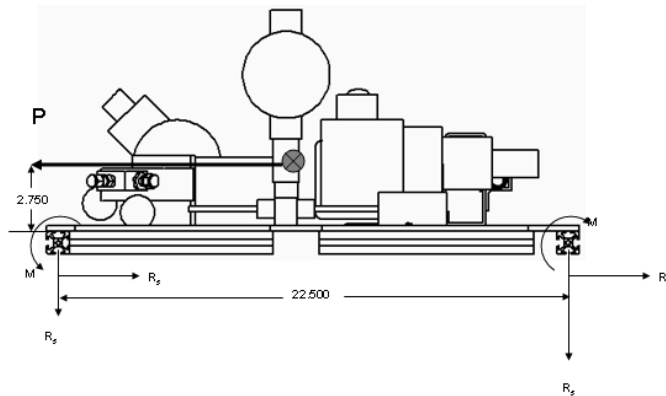

Figure 5: Reactions to 9g Forward Load Factor—Shelf

10

Shelf	Weight (including components – lbs)	Applied mass (9g forward – lbs)	Shear load MS	Moment load MS
1 17.8		160.2	9.8	3.5
2 17.2		154.8	10.2	1.7
3 10.1		90.9	8.5	3.0
4 36.5		328.5	4.3	1.2
5 29.2		262.8	5.6	1.8

Table 7: Shelf Margins of Safety

Pull Testing

Components of the installation were pull tested. Data gathered from the pull tests are contained in Table 8. All components passed the pull test.

Component	Location	Weight (lbs)	Forward (lbs)	Aft (lbs)	Left (lbs)	Right (lbs)	Up (lbs)
Pump	Shelves 2,4,5	7.35	(132.3,135)	(44.1,135)	(29.4,135)	(29.4,135)	(29.4,60)
Flow meter	Shelves 2,4,5	3.75	(67.5,80)	(22.5,80)	(15,80)	(15,80)	(15,20)
2-way valve	Shelves 3,4,5	2.55	(45.9,60)	(15.3,60)	(10.2,60)	(10.2,60)	(10.2,15)
3-way valve	Shelves 4,5	2.85	(51.3,60)	(17.1,25)	(11.4,20)	(11.4,20)	(11.4,15)

Note: Format is (target, actual). All hold times are fifteen seconds.

Table 8: Pull Test Results

Analysis of Microgravity Experiment Rig as One Object

The weight and moment arm of the entire rig is in Table 9. It was calculated that the vertical center of gravity of the rig is 15.0 in. Th e base plate of the rig is bolted to the floor of the aircraft with 8 steel AN6 bolts. The independent shear/tensile load on the 8 bolts holding the base plate to the aircraft floor is calculated as:

Forward: 5538 lbs   Up/Lateral: 1231 lbs

Description	Weight (lbs)	Z from airfcraft floor (in)	Moment Arm (lbs·in)
Rig 572.6		19.0	10879.40
Reservoirs 31.1		4.5	139.95
Base Plate	139.1	0.25	34.78
Total	**742.8**	**14.9**	**11054.13**

Table 9: Assembly Weight and Moment Arm

The normal-gravity load per attach point is computed as 92.9 lb, well below the m axi-mum allowable load of 200 lb. per attach point . The 9g forward load f actor results in reactions shown in Figure 6.

The tipping tensile load under 9gs forward on the bolts farthest from the line of rotation is calculated as:

$$P_{t,max} = \frac{(9)(742.8)(14.9)(62.25)}{2(2.25^2 + 22.25^2 + 42.25^2 + 62.25^2)} = 503.3 \text{ lbs}$$

The shear load per bolt is:
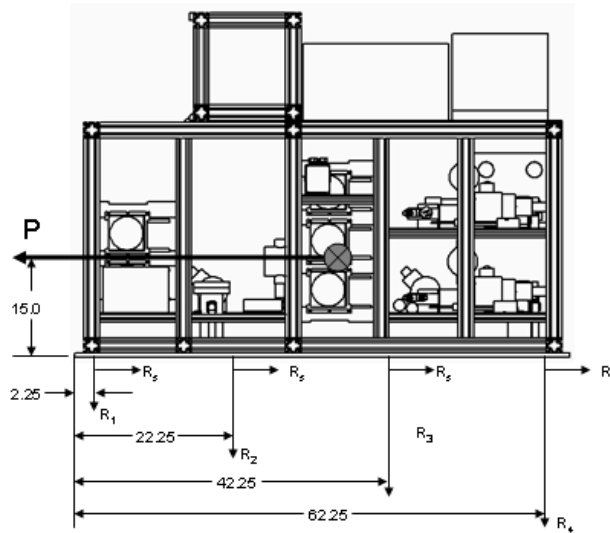
$$P_S = \frac{(9)(742.8)}{8} = 835.7 \text{ lbs}$$

Figure 6: Reactions to 9g Forward Load Factor—Assembly

Margin of Safety: Using the margin of safety calculation stated earlier in this report, the ultimate and yield margins of safety in the tipping tensile load on the bolts in the row farthest from the line of rotation can be calculated by:

For AN6 bolts: $F_{UT} = 10100$ lbs and $F_{YT} = 7740$ lbs

$$MS_{UT} = \frac{10100}{(503.3)(2)} - 1 = 9.0$$

$$MS_{YT} = \frac{7740}{(503.3)(2)} - 1 = 6.7$$

The ultimate shear strength for AN6 bolts is: $F_{SU} = 8280$ lbs. The margin of safety for shear loading is:

12

141

$$MS_{UT} = \frac{8280}{(835.7)(2)} - 1 = 4.0$$

With the large margins of safety, it is evident that the tensile load on the bolts in the row receiving the most tension during tipping will not be critical for bolt failure. The margin of safety for shear loading is large too.

Combined Shear/Tensile Loading: The combined tipping shear and tensile loading is analyzed with the following formula:

$$\left(\frac{835.7}{8280}\right)^3 + \left(\frac{503.3}{10100}\right)^2 = .0035 = .35\% \text{ of load carrying capacity used}$$

With the results above, the combined shear/tensile loading during 9gs forward, including tipping moment, is not critical for bolt failure.

As shown through this structural analysis, the Microgravity Experiment Rig will sustain the 9g forward loading with large margins of safety, indicating large margins in all other directions and planes.

Electrical Analysis

Electrical Schematic

Appendix A contains the electrical schematics for the microgravity experiment and shows the overall power distribution, fuses, and wire sizes.

Electrical Load

The Microgravity Spray Cooling Experiment requires 115 VAC, 60 Hz power for operation. The component requirements are in Table 10.

Electrical Emergency Flow Shutdown Switch

In the event that an emergency shutdown is required by failure of the test section or any other unforeseen circumstance, there is a large "emergency flow shutdown" switch that automatically shuts off power to all valves, heaters and pumps. This switch essentially shuts down the flow and the system can only be reset by pulling this button back up. The computer, display, and instrumentation are not affected by this emergency shutoff and thus permit the monitoring of the experiment if it is necessary.

In addition, individual items can be shut off by shutting off the main power switches on the control panel located on top of the frame.

13

Circuit	Power	Component	Load (amps)
1	115 VAC, 60 Hz	Water Heater	2
		FC Reheaters (2)	12
		Total Circuit 1	**14**
2	115 VAC, 60 Hz	Power Supply	7
		Heater	4.5
		Total Circuit 2	**11.5**
3	115 VAC, 60 Hz	Power Supply	7
		Heater	4.5
		Total Circuit 3	**11.5**
4	115 VAC, 60 Hz	Power Supply	2
		Fans (5)	1
		Watt Transducers (2)	.004
		PID Controller (3)	.03
		Data Acquisition System	.5
		Zero-Point Dry Well	1
		Laptop Computer	1.5
		Total Circuit 4	**6.034**

Table 10: Component Requirements

Loss of Electrical Power

In the even t of a loss in electrical p ower, all valves, pum ps, heaters and instrum entation will shut down. There will be no flow.

Pressure System

Flow Schematic

Appendix C contains the flow sche matic for the microgravity experiment rig. Hose sizes are specified on the flow schematic.

Relief valve set pressures were determ ined using the following rationale. Although it is not standard procedure, if the operating pre ssures are set at ground level, the gauge read-ing is converted into an absolute reading. Under normal operating conditions, cabin pres-sure is 11 to 12 psia. In the event of a rapid cabin depressurization, cabin pressure at alti-tude can fall to 4 psia. Therefore, the set pre ssure (SP) for the relief valves are set using the following function of the WP (in absolute pressure):

$$SP = 1.10 \cdot (WP - 4\,\mathrm{psia})$$

The pneumatic pressure (PP) of components is set using the following:

$$PP = 1.25 \cdot 1.1 \cdot (WP - 4\,\mathrm{psia}) + 14.7\,\mathrm{psia}$$

Both the se t pressu re a nd pneum atic pressu re are dif ferential pressu res and the set-ting/testing occurs at a difference relative to ambient pressure.

The tem perature within the tes t ch amber w ill set the system pressure. The m aximum temperature will be at th e heater and is 100 °C. The m aximum chamber tem perature is

14

set for 70 °C, which corresponds to a chamber pressure of 25 psiA. In order to drive flow through the spray nozzles, the pump needs to provide FC-72 at a pressure of 75 psiA.

Pressure switches will b e set at 105 psiA a nd will shut off the heaters and pum ps in the event of an overpres sure situation. Shutti ng do wn the heaters and pum ps will s erve to remove the heat source and allow the pres sure to equalize through the flow loop across the pum ps resulting in a system   pressure no more than 25 psiA. T he volum e of the chamber will also a ct as a fluid overflow reservoir to a llow excess expansion of the FC-72.

All water flow com ponents will be pressure tested to 111 psiG. All FC- 72 flow compo-nents, including the test chamber, will be pressure tested to 132 psiG.

Pressure certification has been completed. Results are available on request.

Flow Component Listing

Table 11 contains a listing of the flow components.

Table 11: Flow Components

Description MFG		Model Number	Maximum Working Pressure (psig unless otherwise noted)
Water Loop			
Heat Exchanger	Lytron	6110G1SB	250
Fan Lytron		MX2A3, 028316	n/a
Heat Exchanger	Lytron	6110G1SB	250
Fan Lytron		MX2A3, 028316	n/a
Pump Tuthill		DDS.68PPPV2NN3700	200
Filter Swagelock		140 micron	2150
Flow Meter	Omega	FTB9505	5000
Pulse Amplifier	Omega	FLSC-64	n/a
Pressure Transducer	Omega	PX303-100A5V	100 (proof-200) psia
Reservoir/Sight Glass	MDC Vacuum/Lube Devices Inc.		290
FC-72 Loop			
Heat Exchanger	Lytron	6110G1SB	250
Fan Lytron		MX2A3, 028316	n/a
Heat Exchanger	Lytron	6110G1SB	250
Fan Lytron		MX2A3, 028316	n/a
Heat Exchanger	Lytron	6110G1SB	250
Fan Lytron		MX2A3, 028316	n/a
Pump Tuthill		DDS.68PPPV2NN3700	200
Pump Tuthill		DDS.57PPPV2NN3700	250
Pump Tuthill		DDS.57PPPV2NN3700	250
Filter Swagelock		40 micron	2150
Filter Swagelock		15 micron	2150
Filter Swagelock		15 micron	2150

15

Description MFG		Model Number	Maximum Working Pressure (psig unless otherwise noted)
Flow Meter	Omega	FTB-9504	5000
Pulse Amplifier	Omega	FLSC-64	n/a
Flow Meter	Omega	FTB-9504	5000
Pulse Amplifier	Omega	FLSC-64	n/a
Pressure Transducer	Omega	PX303-200A5V	200 (proof-400) psia
Pressure Transducer	Omega	PX303-200A5V	200 (proof-400) psia
Pressure Transducer	Omega	PX303-200A5V	200 (proof-400) psia
Pressure Transducer	Omega	PX303-100A5V	100 (proof-200) psia
Reservoir/Sight Glass	MDC Vacuum/Lube Devices Inc.		290
2-way valve	Hoke/Simco Controls	7115G4Y	6000
Actuator Hoke/Sim	co Controls	0172L2	n/a
2-way valve	Hoke/Simco Controls	7115G4Y	6000
Actuator Hoke/Sim	co Controls	0172L2	n/a
2-way valve	Hoke/Simco Controls	7115G4Y	6000
Actuator Hoke/Sim	co Controls	0172L2	n/a
2-way valve	Hoke/Simco Controls	7115G4Y	6000
Actuator Hoke/Sim	co Controls	0172L2	n/a
3-way valve	Hoke/Simco Controls	7673G4Y	6000
Actuator Hoke/Sim	co Controls	0172L2F	n/a
3-way valve	Hoke/Simco Controls	7673G4Y	6000
Actuator Hoke/Sim	co Controls	0172L2F	n/a
Drain valve	Swagelock		1000
Drain valve	Swagelock		1000
Pressure Switch	United Electric Cont	10-B11	12000
Pressure Switch	United Electric Cont	10-B11	12000
Accelerometer		SA307HPTX	n/a

Chamber

Pressure Transducer	Omega	PX303-100A5V	100 (proof-200) psia

Fluid Containment Plan

The test fluid is FC-72. FC-72 is a non-t oxic and non-corrosive fl uid. The total volum e of FC-72 in the system is approximately 1.5 liters. The test chamber can hold 2.6 liters of FC-72, while the fluid reservoir between the two cut-off valves can hold approxim ately 1.5 liters. In the event of a leak in either the test chamber or the fluid reservoir, the FC-72 can be pumped into the other cham ber. There are prov isions to isolate the legs of the flow loop in the event of a leak.

There is a separate cooling loop which circulates water through a copper coil surrounding the test chamber to condense FC-72 vapor.

The junction between the rig and the baseplate has been sealed with RTV to contain any overnight leaks of fluid. Any penetrations th rough this plate, including those for test sec-

16

tions, tanks, etc, have also been sealed with RTV. The approximate volume, based on the height of the 80/20 channel an d the enclosed area of the base plate, is 44.75 liters. The base of the rig is divided into four cells. The smallest cell has an approximate volume of eight liters.

The majority of the plumbing within the flow loops is either metallic or polyflow and has been pressure certif ied to 1.25x (pneum atically) the Maxim um Absolute W orking Pressure (MAWP).

The experiment will be leak-ch ecked prior to installation aboard the aircraf t. Af ter any test section or fluid change out, and prior to any flight, the rig will be leak-checked.

Absorbent PIGs, Ki mwipes and Ziploc baggies will be strategically located around the rig to provide clean-up capability in the even t of a leak. Used PIGs and Kim wipes will be sealed in the Ziploc baggies.

Laser Certification

No lasers will be used with this experiment.

Parabola Details and Crew Assistance

Forty parabolas per flight of 0.01g are requested. No modifi cations to either the tim ing between trajectories or the time duration of turns are anticipated.

Institutional Review Board

There are no plans to u se human or animal test subjects and these tests are not of a biological nature.

KC-135 Hazards Analysis

This section consists of AOD Forms 70 and 71.

17

HAZARD SOURCE CHECKLIST

Enumerate or mark N/A

N/A Flamm   able/combustible material, fluid (liquid, vapor, or gas)
1 Toxic/noxious/corrosive/hot/cold   material, fluid (liquid, vapor, or gas)
2____   High pressure system (static or dynamic)
N/A____   Evacuated container (implosion)
N/A Frangible   material
N/A____   Stress corrosion susceptible material
N/A____   Inadequate structural design (i.e., low safety factor)
N/A____   High intensity light source (including laser)
N/A Ionizing/electrom   agnetic radiation
N/A Rotating   device
N/A____   Extendible/deployable/articulating experiment element (collision)
N/A____   Stowage restraint failure
N/A____   Stored energy device (i.e., mechanical spring under compression)
N/A____   Vacuum vent failure (i.e., loss of pressure/atmosphere)
3____   Heat transfer (habitable area over-temperature)
4 Over-tem   perature explosive rupture (including electrical battery)
5____   High/Low touch temperature
6____   Hardware cooling/heating loss (i.e., loss of thermal control)
N/A Pyrotechn   ic/explosive device
N/A____   Propulsion system (pressurized gas or liquid/solid propellant)
N/A____   High acoustic noise level
N/A____   Toxic off-gassing material
N/A Mercury/m   ercury compound
N/A____   Other JSC 11123, Section 3.8 hazardous material
N/A Organic/m   icrobiological (pathogenic) contamination source
7 Sharp   corner/edge/protrusion/protuberance
N/A Flamm   able/combustible material, fluid ignition source (i.e., short circuit;
____   under-sized wiring/fuse/circuit breaker)
8____   High voltage (electrical shock)
N/A____   High static electrical discharge producer
9____   Software error or compute fault
N/A Carcinogenic   material
Other:____
Other:____
Other:____

AOD Form 71 (Jul 2002)   Verify that this is the correct version before use.

18

147

DETAILED HAZARD DESCRIPTION

Use the following format for describing each identified hazard in detail.

Hazard Number: 1

Title:
Toxic fluid – FC-72

Hazard Description:
Water is not a health hazard.

FC-72 is non-toxic and inert; the quantity used in this experiment will not affect the aircraft environment

At room temperature: Eye contact--Contact with the eyes during product use is not expected to result in significant irritation. Skin contact--Contact with the skin during product use is not expected to result in significant irritation. Inhalation--No health effects are expected. Ingestion--No health effects are expected

At temperature >200°C: hydrogen fluoride and perfluoroisobutylene is generated.

Hazard Cause(s):

Leak, spill, or component failure causes release of test fluid from closed experimental system. Over temperature of FC-72 in excess of 200°C.

Hazard Control(s):

Pressure-testing of equipment of at least 1.25 times the operating pressure will ensure adequate containment of fluids.

Safety cut-out measures will monitor heater temperature, to not exceed 100°C, and shut down operation in potentially-hazardous circumstances.

Should a leak occur, the flow system is designed to be able to isolate the FC-72 either in the test chamber or the reservoir.

AOD Form 70 (Jul 2002)   Verify that this is the correct version before use.

DETAILED HAZARD DESCRIPTION

Use the following format for describing each identified hazard in detail.

Hazard Number: 2

Title:
High pressure system

Hazard Description:
Over pressurization of flow system causes a component to fail; releasing test fluids and possibly injuring nearby personnel.

Hazard Cause(s):

Flow system blockage, or cabin depressurization causes unexpected pressure differential across an experiment component.

Hazard Control(s):

Test chamber: Temperature within the chamber will set the pressure. A maximum working temperature of 70 °C in the chamber will result in a maximum of 25 psiA.
FC-72 Nozzle inlet: Inlet pressure to the spray nozzle will be limited to 75 psiA
Water flow components will be pressure tested to 111 psiG.*
FC-72 flow components, including the test chamber, will be pressure tested to 132 psiG.*
Pressure switches will be set at 105 psiA and will shut off the heaters and pumps in the event of an overpressure situation. Shutting down the heaters and pumps will serve to remove the heat source and allow the pressure to equalize through the flow loop across the pumps resulting in a system pressure no more than 25 psiA. The volume of the chamber will also act as a fluid overflow reservoir to allow excess expansion of the FC-72 or isolation of the FC-72 in the event of a leak.
*All noncommercial components will be pneumatically pressure tested to at least 1.25 times the maximum working pressure. Note: Maximum working pressure for FC-72 system is 100 psiA.
Maximum working pressure for water system is 75 psiA.

AOD Form 70 (Jul 2002)   Verify that this is the correct version before use.

20

DETAILED HAZARD DESCRIPTION

Use the following format for describing each identified hazard in detail.

Hazard Number: 3

Title:
Heat transfer

Hazard Description:
Increase in temperature of habitable area surrounding experiment causes discomfort and/or burning in personnel on board

Hazard Cause(s):

Overheat on one or more components causes an increase in the temperature surrounding the experiment package.

Spill or leak of heated fluid causes an increase in the temperature surrounding the experiment package.

Hazard Control(s):

Maximum expected heater operating temperature of 100 °C and test chamber temperature of 70 °C – minimal heat load, will not significantly alter the environment surrounding the experiment package. This will allow high heat flux testing at the heater without significantly altering the chamber temperature.

Over-temperature controls and safety cut-out measures prevent overheating by shutting down the experiment.

AOD Form 70 (Jul 2002)   Verify that this is the correct version before use.

21

150

DETAILED HAZARD DESCRIPTION

Use the following format for describing each identified hazard in detail.

Hazard Number: 4

Title:
Over temperature explosive rupture

Hazard Description:
Increase in temperature within the test cell will result in an increase in pressure. Should this increase in temperature result in a pressure exceeding the rating of the viewport to the test chamber, an explosive rupture may occur.

Hazard Cause(s):

The temperature in the chamber is balanced by the heat input from the heaters and the water coil around the chamber walls. The test chamber is controlled at a temperature consistant with a desired pressure. The maximum allowable chamber temperature is 70°C, which will result in a chamber pressure of 25 psiA.

Hazard Control(s):

The test chamber is constructed with 1-inch Lexan viewports mounted to the test chamber. In addition, over-temperature switches will shut off the heaters in the event of a temperature excursion in the test chamber. The Lexan viewports have been structurally analyzed to verify structural integrity in the event of a pressure excursion. The test chamber along with the FC-72 flow components will be tested to 132 psiG.

AOD Form 70 (Jul 2002)   Verify that this is the correct version before use.

22

DETAILED HAZARD DESCRIPTION

Use the following format for describing each identified hazard in detail.

Hazard Number: 5

Title:
High touch temperature

Hazard Description:
Components or surfaces feel hot to the touch; may cause minor burns to personnel who come in contact with them.

Hazard Cause(s):

Improperly insulated surfaces expose personnel to hot surfaces.

Hazard Control(s):

High temperature components will be insulated or thermally shielded from the environment.

The test chamber, as well as potentially exposed components and surfaces, will be insulated.

AOD Form 70 (Jul 2002)   Verify that this is the correct version before use.

23

DETAILED HAZARD DESCRIPTION

Use the following format for describing each identified hazard in detail.

Hazard Number: 6

Title:
Hardware cooling loss

Hazard Description:
Planned cooling measures fail, resulting in overheating of hardware, potentially resulting in hazardout temperatures in and around the experimental test package

Hazard Cause(s):

Line blockages

Pump failure

Heat exchanger fan failure

Hazard Control(s):

Safety cutout measures will ensure temperature control, < 70°C, including a manual emergency-shutdown-switch, which will shut down all potentially dangerous components.

AOD Form 70 (Jul 2002)   Verify that this is the correct version before use.

24

DETAILED HAZARD DESCRIPTION

Use the following format for describing each identified hazard in detail.

Hazard Number: 7

Title:
Sharp corners

Hazard Description:
Sharp corners or other surfaces on experimental test package cause minor cuts/abrasions to personnel.

Hazard Cause(s):

Unintentional contact with sharp corners may cause minor cuts/abrasions.

Hazard Control(s):

A safety/grab rail will be installed along the perimeter of the experimental test package frame.

Any remaining exposed sharp edges or corners will be padded.

AOD Form 70 (Jul 2002)   Verify that this is the correct version before use.

DETAILED HAZARD DESCRIPTION

Use the following format for describing each identified hazard in detail.

Hazard Number: 8

Title:
High voltage

Hazard Description:
Potentially lethal voltages will be used to power the experiment.

Hazard Cause(s):

1. Wire breaking and shorting to chassis.
2. Shorting of voltage potential to ground.
3. Breakdown of wire because of high current load.

Hazard Control(s):

1. All power lines are protected using circuit breakers and/or fuses.
2. All voltage potentials are shielded and proper connectors are used.
3. Experiment package is chassis grounded.
4. All wiring is rated for operating currents.

AOD Form 70 (Jul 2002)   Verify that this is the correct version before use.

26

155

DETAILED HAZARD DESCRIPTION

Use the following format for describing each identified hazard in detail.

Hazard Number: 9

Title:
Software error

Hazard Description:
Loss of experimental control (ie: temperature/pressure control) due to software error.

Hazard Cause(s):

Computer failure causes software not to work

Aircraft power loss/malfunction.

Hazard Control(s):

Computer operates on battery backup in case of power loss.

All safety cut-out measures will be controlled via hardware, rather than software.

Tool Requirements

Tools supplied by the Reduced Gravity Office   should be sufficient for loading and re-moval of the experiment from the aircraft.

Photo Requirements

None

Aircraft Loading

The experiment can be loaded with a forklift and either directly on its own pallet or the lifting pallet/basket supplied by the Reduced Gr avity Office. The experim ent assembly contains casters that are removable.

Ground Support Requirements

It is necessary to have access to 115 VAC, 60 Hz in order to operate the assembly, either for final functional checks or the Test Readiness Review.

Hazardous Materials

FC-72 will be the primary working fluid. Te mperatures exceeding 200 °C will res ult in FC-72 generating hazardous m aterials, hydrogen fluoride and perfluor oisobutylene. Be-cause the heater tem peratures will b e limited to 100 °C there will be no hazardous m a-terial generation.

Material Safety Data Sheets

See Appendix E for the material safety data sheet (MSDS) for the FC 72.

28

Test Procedures

Loading Checklist

1. Verify that all mounting bolts are tight.
2. Verify power connections, 115 VAC 60 Hz.

Pre-test Checklist

1. Ascertain that the coolant and water systems are filled with sufficient liquids.
2. Plug in cords for the four AC circuits, 20 amp capacity for circuit 1 and 15 amp capacity for circuits 2, 3 and 4.
3. Turn on Breakers 1, 2, 3 and 4, verify green indicators for each.
4. Verify that all toggle switches are in the off (down) position and all potentiometers are at 0 (fully counterclockwise).
5. Press the Start button and verify red indicators for the pumps and target heaters and red and blue indicators for the flow bypass.

Testing Checklist

1. Turn on the laptop computer, log in and start the data acquisition program.
2. Verify system pressures are appropriate for coolant temperature.
3. Turn on the water pump and set the flow rate as indicated on the computer display using the potentiometer; verify green indicator.
4. Turn on the coolant pumps and set the flow rates as indicated on the computer display using the potentiometers; verify green indicators and flow rate on the digital readouts.
5. Switch the bypass toggle switches to the up position and verify spray in the chamber.
6. Set the reheater PID controllers to the desired temperature and set the alarm cutout temperatures.
7. Switch the PID controllers on; verify green indicators.
8. When the fluids are at operating temperature, the reheater indicators will be cycling.
9. Verify that the over-temperature PID controller alarm settings are correctly adjusted.
10. Turn on the video cameras and place them in record mode.
11. Turn on the target heater switches and verify green indicators.
12. Set the target heater wattage using the potentiometers.
13. Take data as appropriate to the flight test plan.

29

Post-test Checklist

1. Switch off target heaters and set potentiometers to the 0 position.
2. Switch off reheater switches.
3. Switch bypass toggle switches to the down position.
4. Switch off all pumps and set potentiometers to the 0 position.
5. Switch off video cameras.
6. Stop data acquisition and shut down computer.
7. Switch off the four Breakers.

Leak Shut Down Procedure

1. Identify the location of the leak and use the pump to isolate FC-72 away from leak into either the chamber or the fluid reservoir and close the appropriate valves.
2. Hit Panic button to shutdown the system and allow the system to come to a low pressure equilibrium.
3. Assess source of leak for fixability. If fixable, (e.g., wrong valve is open), seal leak; otherwise.
4. Use either absorbent PIGs or Kimwipes to mop-up leak. Place wet materiel into zip lock baggie or vent tank.

Emergency Shut Down Procedure

1. Hit Panic button.
2. Ensure all power is off.
3. Visually verify and contain any leaks using absorbent PIGs or Kimwipes. Place wet materiel into zip lock baggie or vent tank.

30

Appendix A: Electrical Schematic

31

NASA Spray Experiment
Circuit 1

33
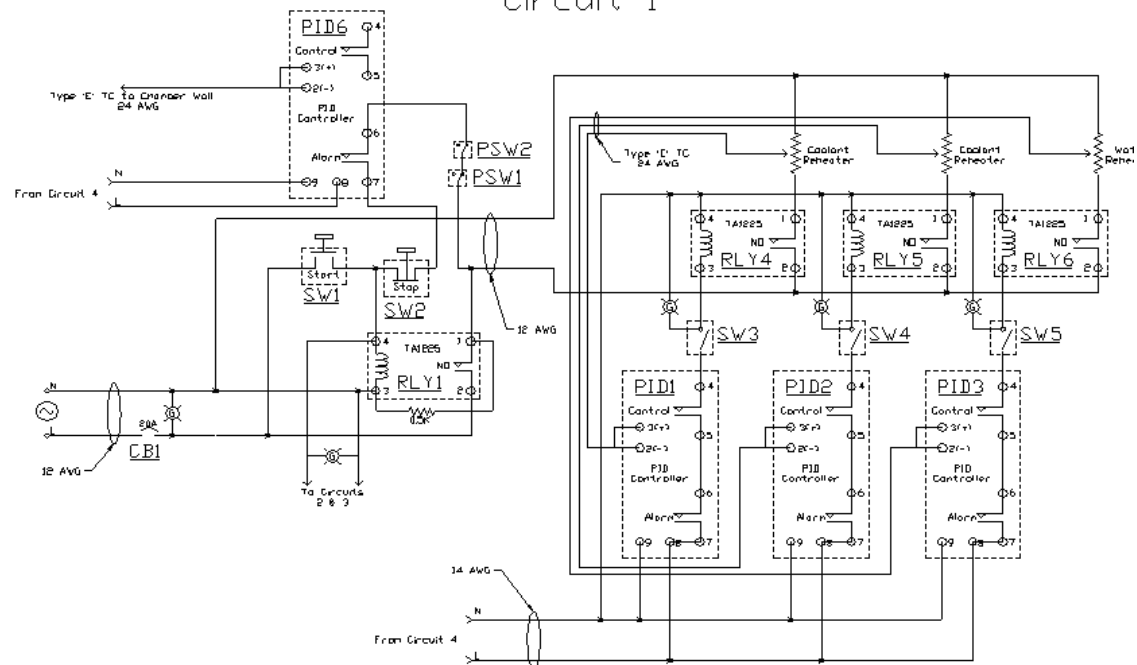
NASA Spray Experiment
Circuit 2
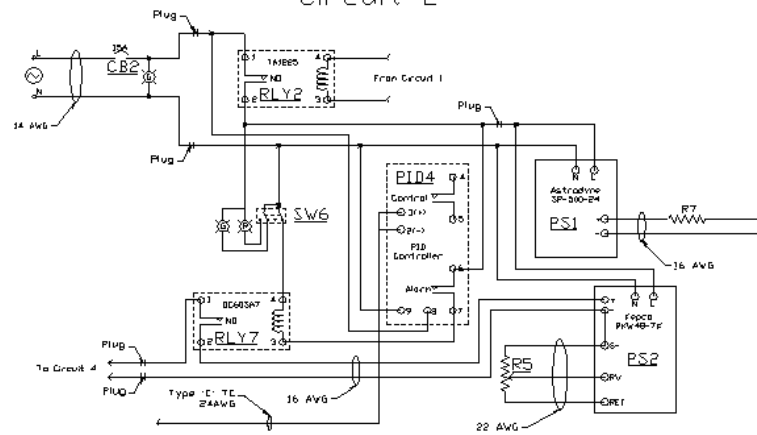
NASA Spray Experiment
Circuit 3
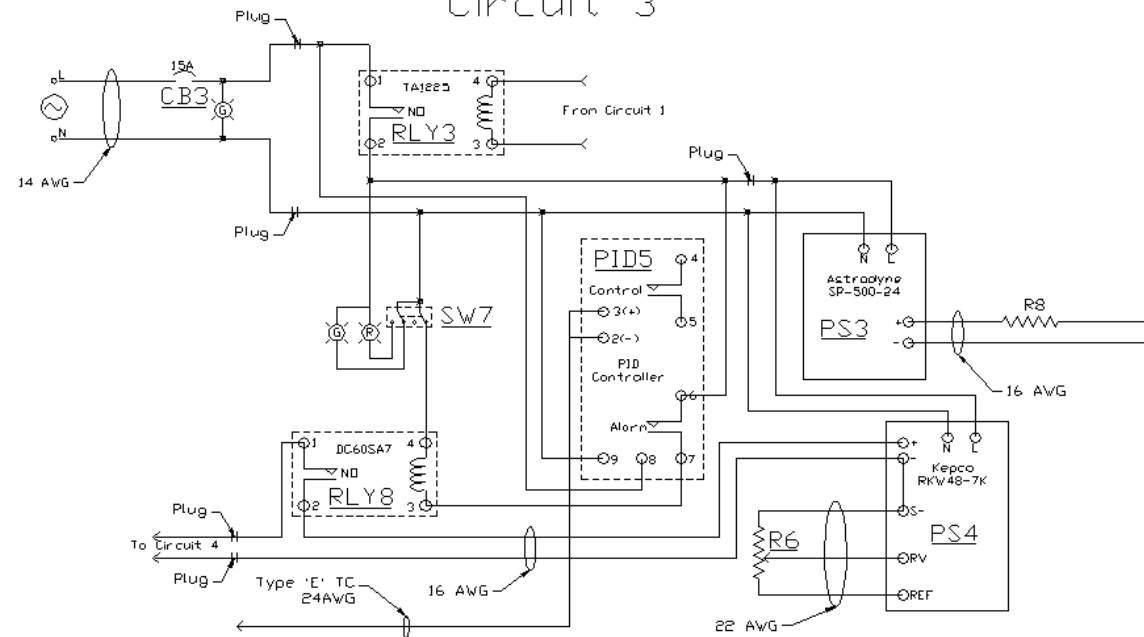
NASA Spray Experiment
Circuit 4
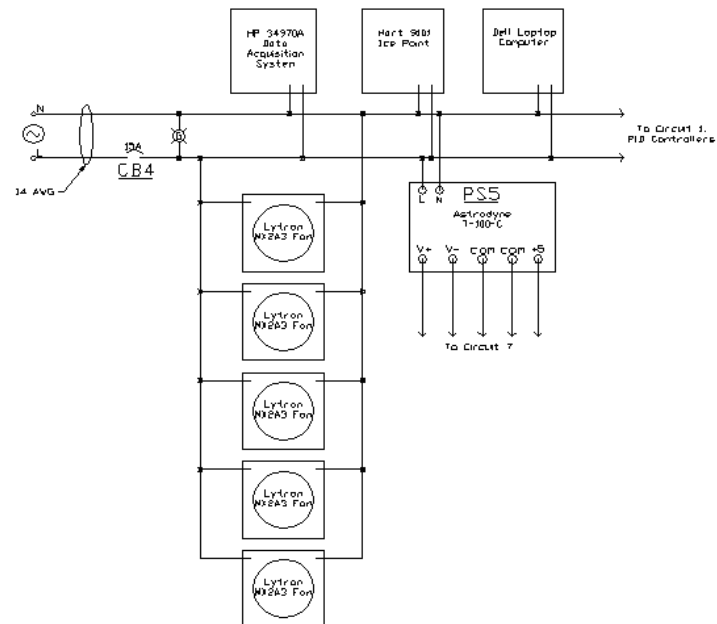
NASA Spray Experiment
Circuit 5

NASA Spray Experiment
Circuit 6

38

NASA Spray Experiment
Circuit 7

18 AWG

From Circuit 4

V+
V−
com
com
v5

22 AWG

Accelerometer

Pulse Amplifier
Pulse Amplifier
Pulse Amplifier

Pressure Transducer
Pressure Transducer
Pressure Transducer
Pressure Transducer
Pressure Transducer
Pressure Transducer
Pressure Transducer

Video Camera
Video Camera

DVM1
DVM2
DVM3
DVM4
DVM5

39

168
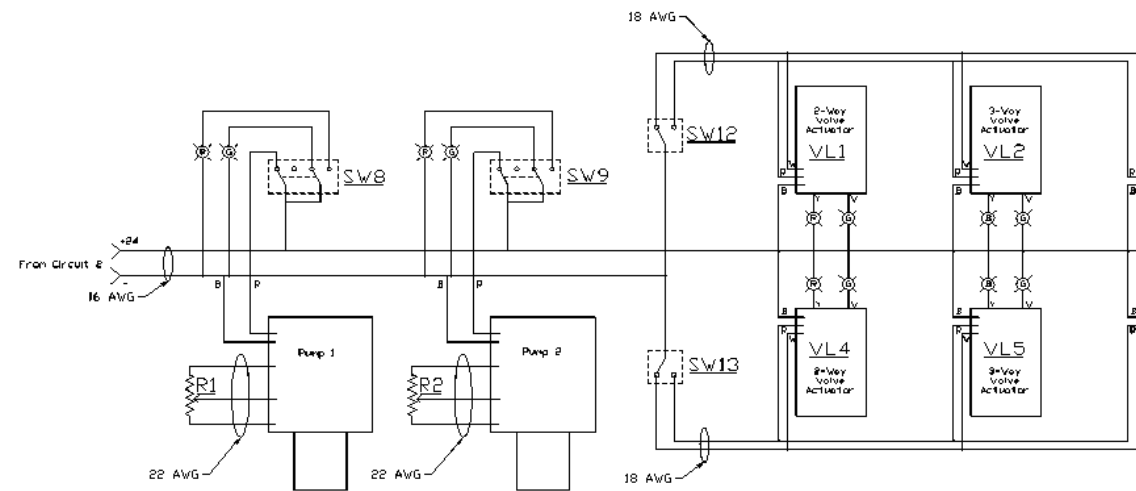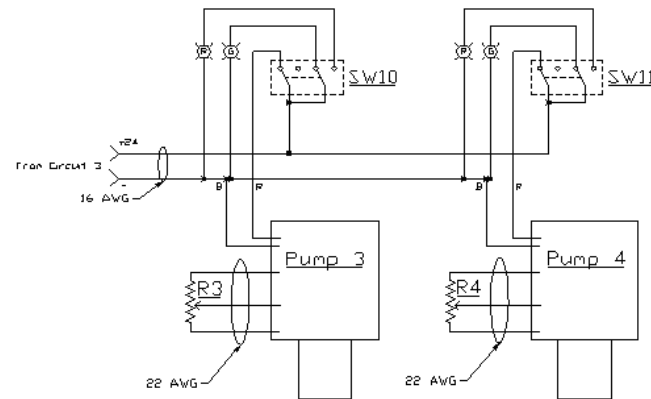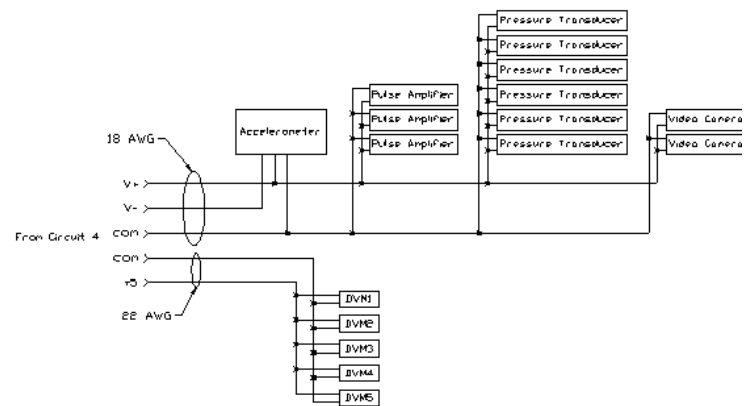
Control Panel
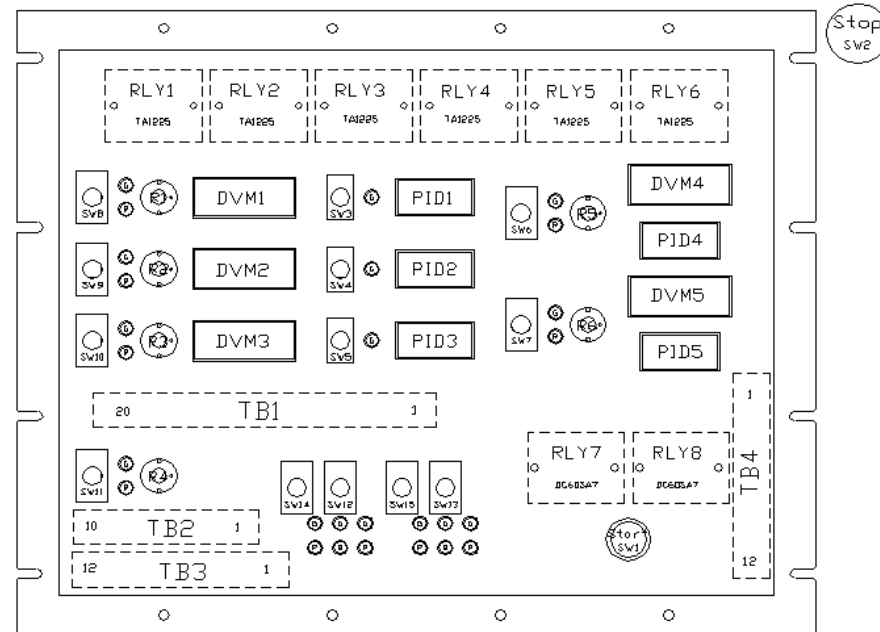
Power Panel
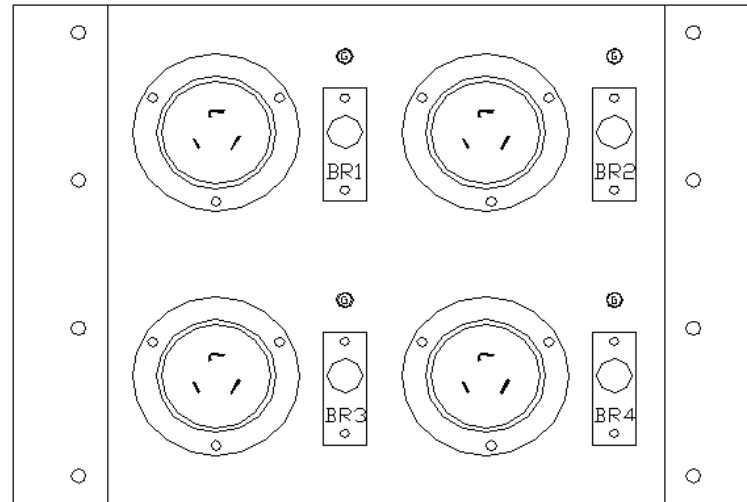
Appendix B: 2020 Joint Fastener Static Testing

The joint fastener strength values in the 80/20 literature were insufficient for the joint fasteners used on the frame. Static tests were conducted on a test structure. The first structure, shown in Figure B 1 and Figure B2, wa s assembled from 2020 extrusions and two 90° joining plates (P/N 4128) and two 90° corn er brackets (P/N 4114). All screws were torqued to 90 in·lbs.

Figure B1: Corner Joint

Figure B2: Corner Joint

A load, composed from three F-class weights—44.1 lbs, 55.1 lbs and 110.2 lbs, was placed 36 in ches from the joint, as shown in Figure B3. The load was left in place for fifteen minutes. The results are tabulated in Table B1. After the last load was removed, the beam returned to a position of 2.2 inches compared to the s tarting position of 2.55 inches. Some of the deflection m ay be because of clam ping arrangement. Disassembly did not show any visible deformation in the parts, i.e. plates and joints. The joint did not have ultimate failure.
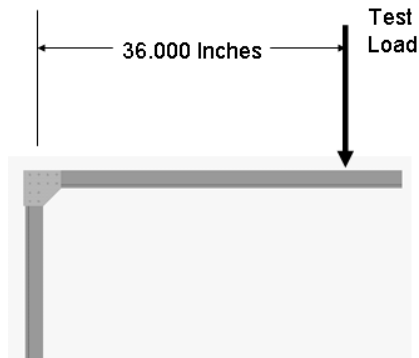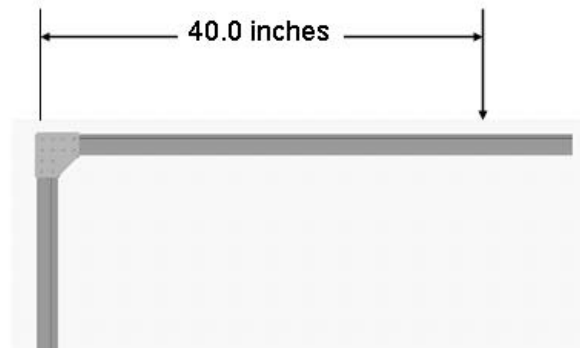
Figure B3: Corner Joint Load Point

Mass (lbs)	Moment (in·lbs)	Deflection (initial-final) inches
110.2	3967.2	(2.55-1.75) = 0.80
165.3	5950.8	(2.55-1.15) = 1.40
209.4	7538.4	(2.55-0.55) = 2.0

Table B1: Corner Bracket Loads

The second joint tested was the tee joint. It consists of a tee joint (P/N 4125) and two 90° corner brackets (P/N 4114). The joint is show n in Figure B4. This configuration was loaded in a sim ilar manner to the corner joint, as shown in Figure B 5. The results are in Table B2. After the last load was rem oved, the beam returned to 6.8 inches from a start-ing position of 7.55 inches. Som e of the de flection m ay be because of clam ping ar-rangement. Disassembly did not show any visible deformation in the parts, i.e. plates and joints. The joint did not have ultimate failure.

Mass (lbs)	Moment (in·lbs)	Deflection (initial-final) inches
110.2	3967.2	(7.55-6.8) = 0.75
165.3	5950.8	(7.55-6.0) = 1.55
209.4	7538.4	(7.55-5.25) = 2.30

Table B2: Tee Bracket Loads

44
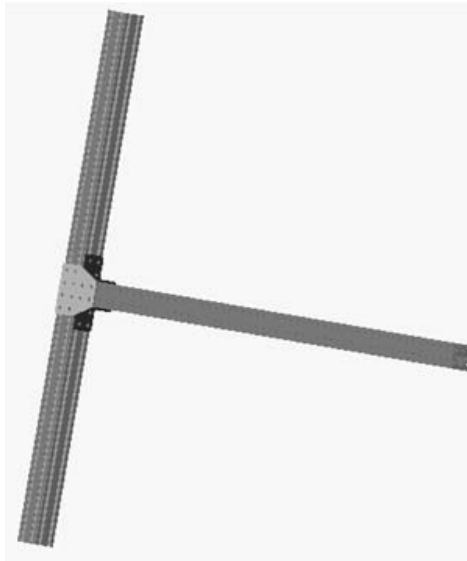
Figure B4: Tee Joint
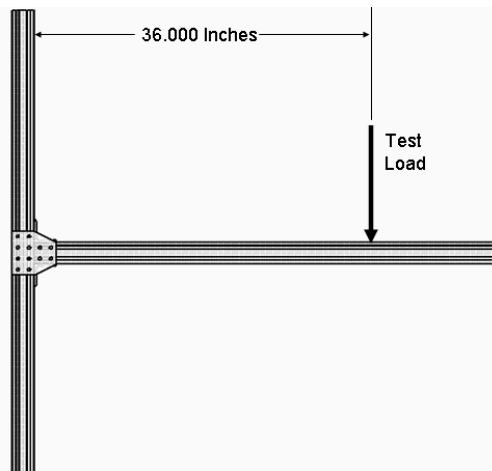
Figure B5: Tee Joint Point Load

A second structure, shown in Figure B6 a nd Figure B7, was assem bled from 2020 extru-sions and three 90° joining plates (P /N 4128) and three 90° corner brackets (P/N 4114). All screws were torqued to 90 in·lbs.

Figure B6: Corner Joint

Figure B7: Corner Joint

A load, composed from five F-class weight s—11.02, 22.05, 44.1 lbs, 55. 1 lbs and 110.2 lbs, was pla ced 40 inches f rom the joint, as sho wn in Figure B8. The load was lef t in place for fifteen m inutes. The resu lts are tabu lated in Tab le B3. Som e of the def lection may be bec ause of clamping arrangem ent. Disassembly did not show any visible defor- mation in the parts, i.e. plates and joints. The joint did not have ultimate failure.

46

Figure B8: Corner Joint Load Point

Mass (lbs)	Moment (in·lbs)	Deflection (initial-final) inches
110.43	4417.2	(45-44) = 1.0
209.43 8377.2		(45-42.5) = 2.50
242.5	9700.0	(45-42) = 3.0

Table B3: Corner Bracket Loads

The second joint tested was the tee joint. It consists of a tee joint (P/N 4125) and two 90° corner brackets (P/N 4114). The joint is show n in Figure B9. This configuration was loaded in a similar manner to the corner joint, as shown in Figure B10. The results are in Table B4. Som e of the deflection m ay be because of clamping arrangement. Disassem bly did not show any visi ble deformation in the parts, i.e. plates and joints. The joint did not have ultimate failure.

Mass (lbs)	Moment (in·lbs)	Deflection (initial-final) inches
110.43 4417.2		(48.5-48.0) = 0.5
209.43	8377.2	(48.5-45.25) = 3.25
242.5	9700.0	(48.5-44.25) = 4.25

Table B4: Tee Bracket Loads

47

176
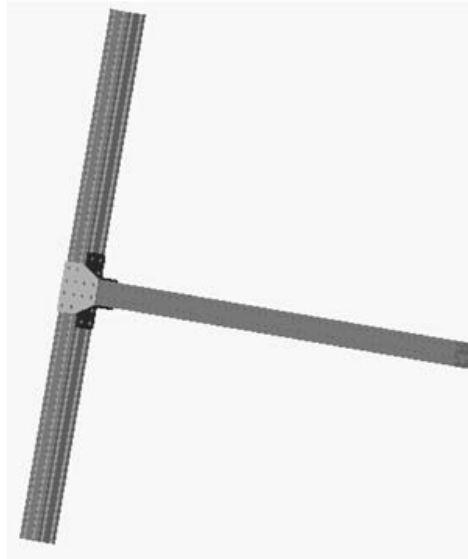
Figure B9: Tee Joint
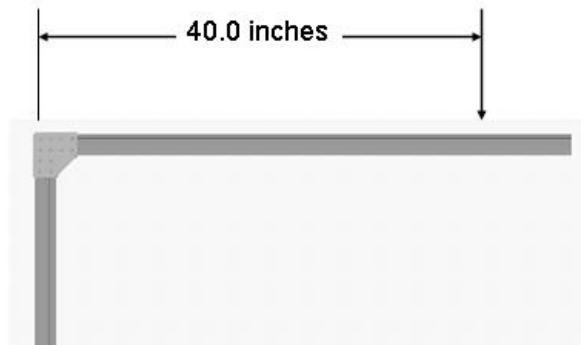
Figure B10: Tee Joint Point Load

48

Appendix C: Experiment Drawings and Flow Schematic
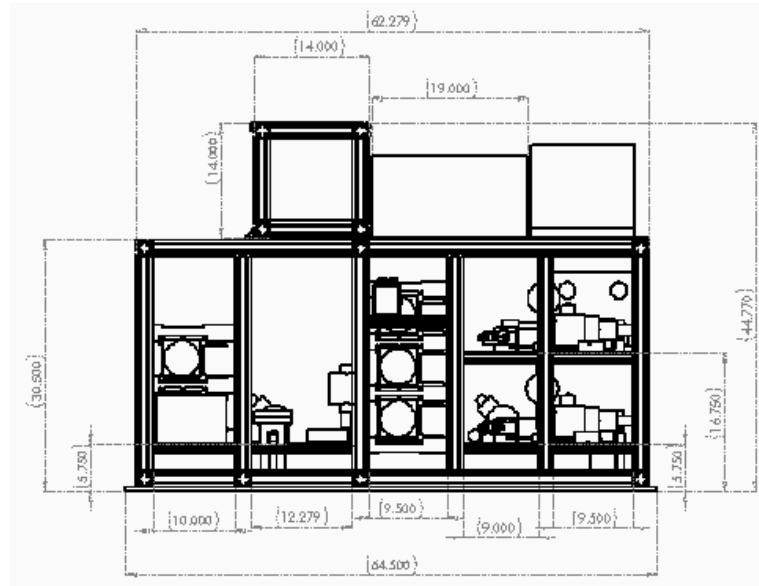
Figure C1: Side View of Rig
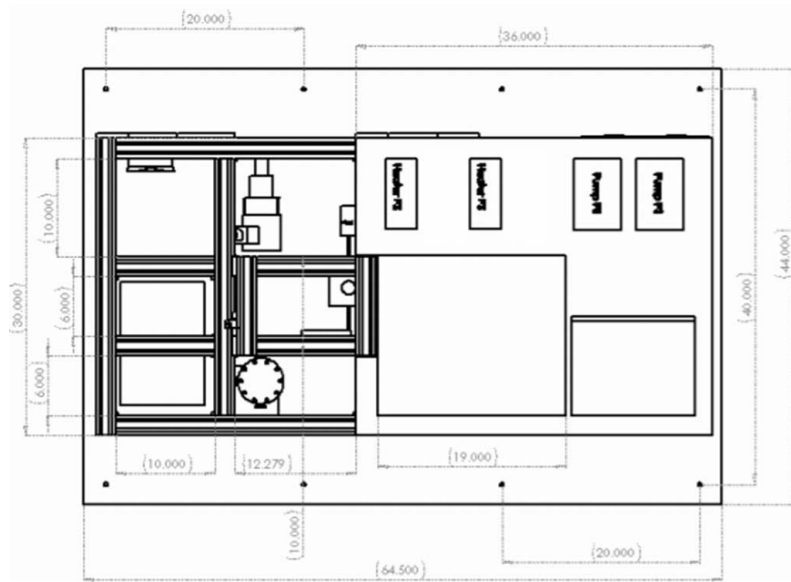
Figure C2: Top View of Rig
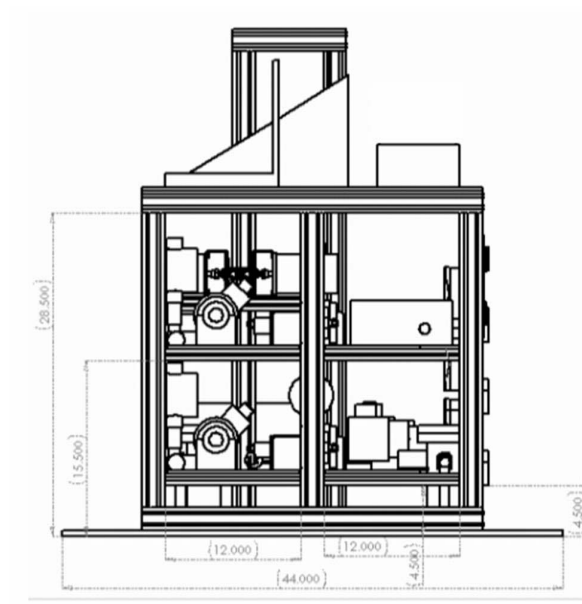
Figure C3: Rear View of Rig

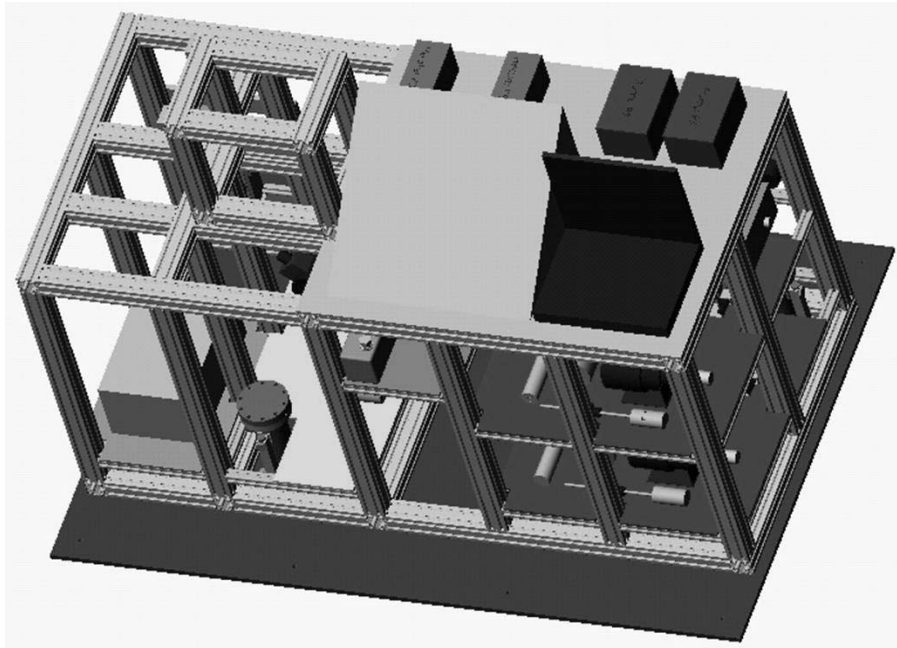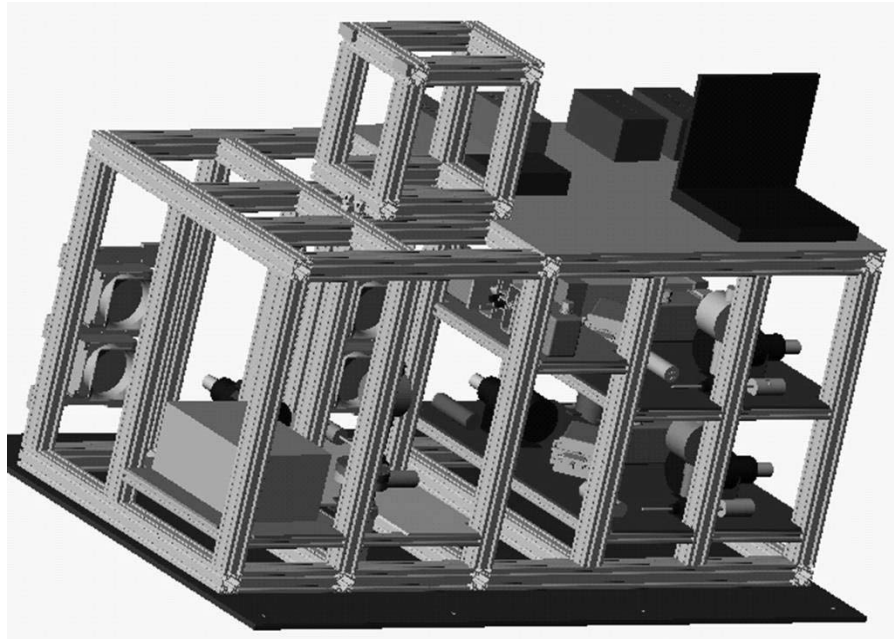50
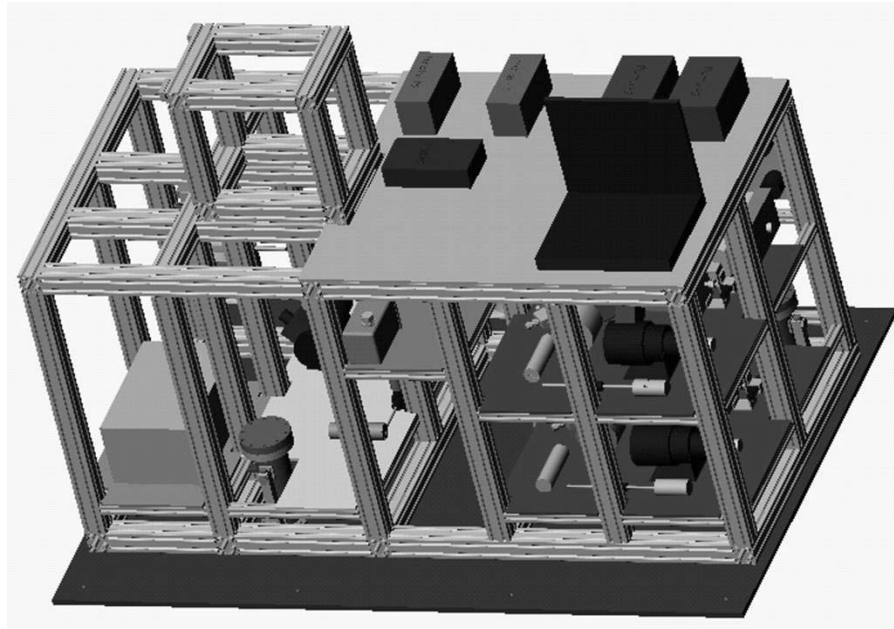
Figure C4: Three-dimensional View of Rig

Figure C5: Three-dimensional View of Rig

52

Figure C6: Three-dimensional View of Rig

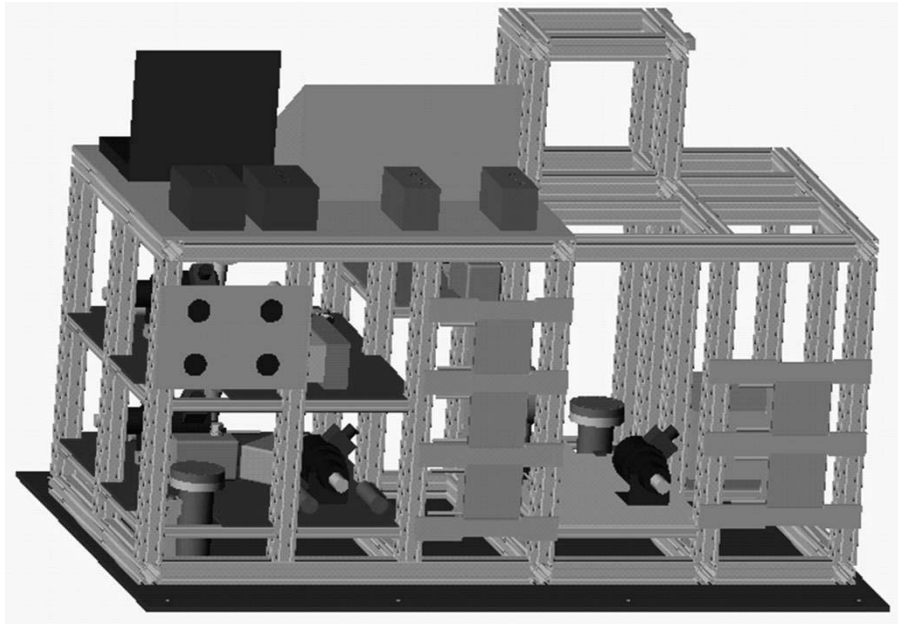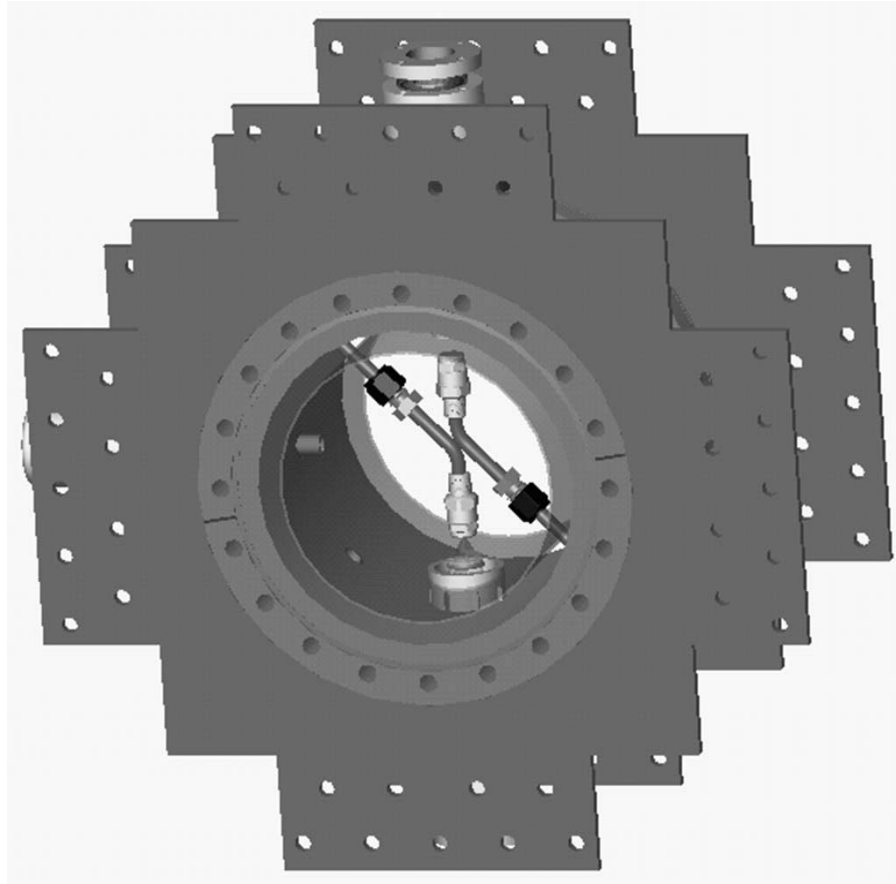**Figure C7: Three-dimensional View of Rig**
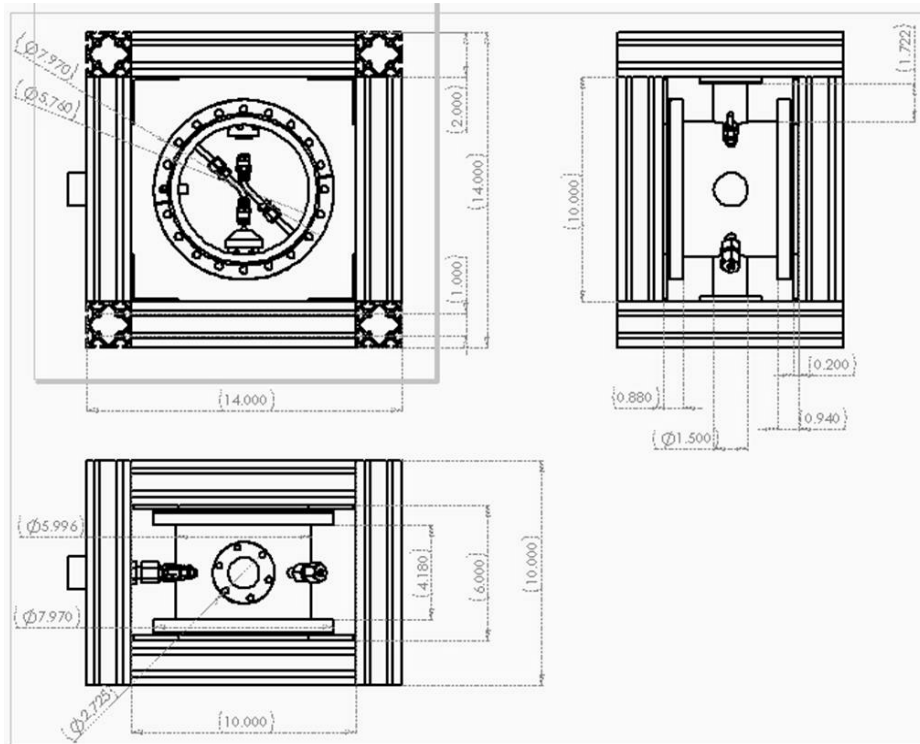
54

Figure C8: Three-dimensional View of Chamber With Screen
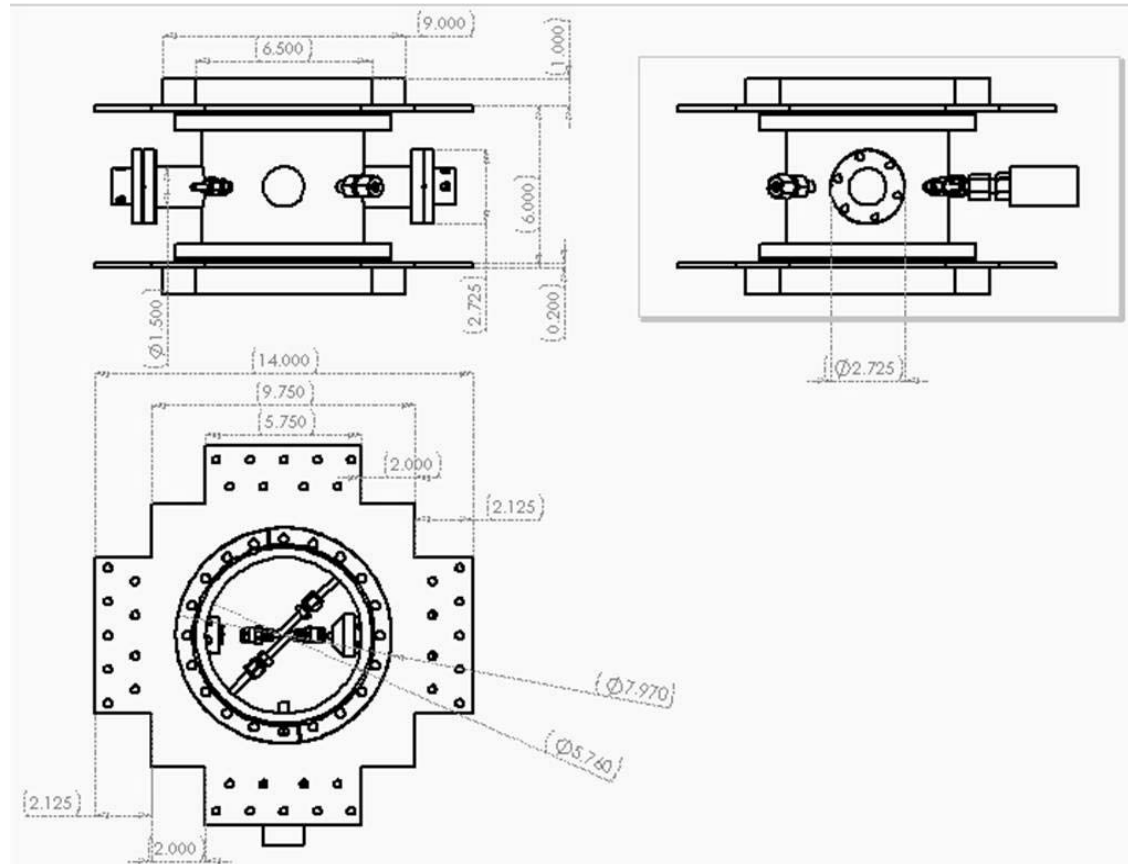
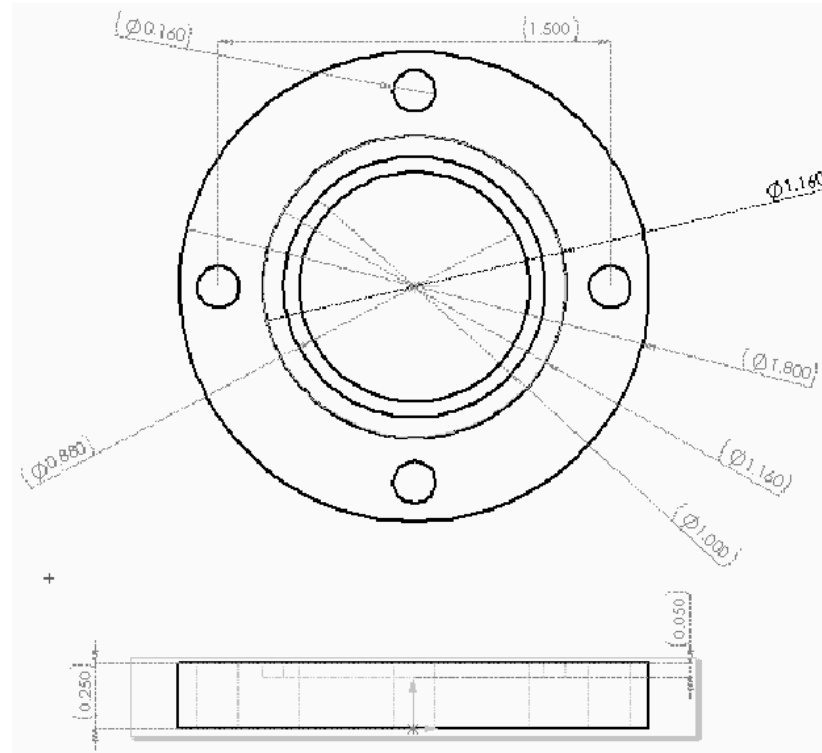**Figure C9: Test Chamber in Mounting Structure**

Figure C10: Test Chamber

58

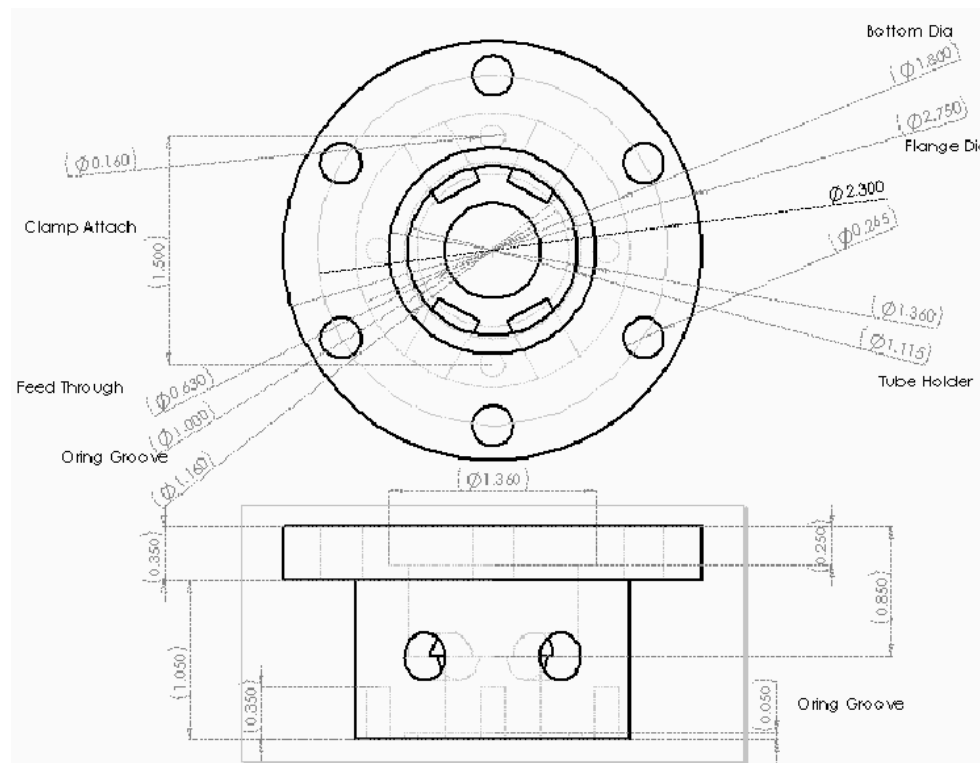**Figure C11: Sump for Test Chamber — Side View**

59

188

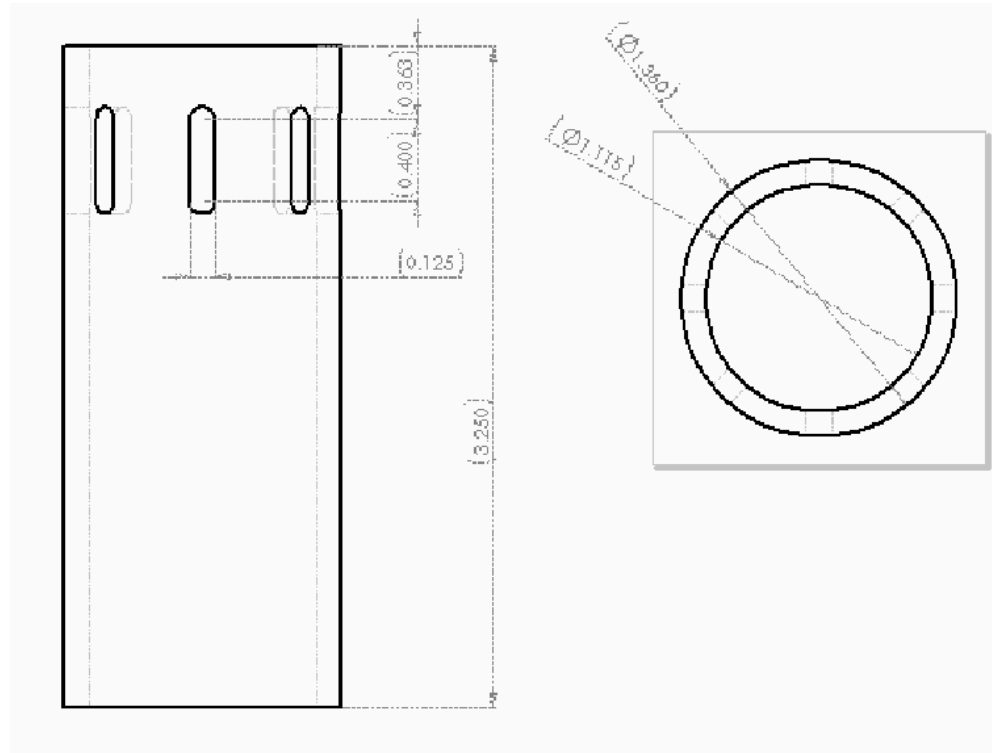**Figure C12: Sump for Test Chamber — Side View**

60

189

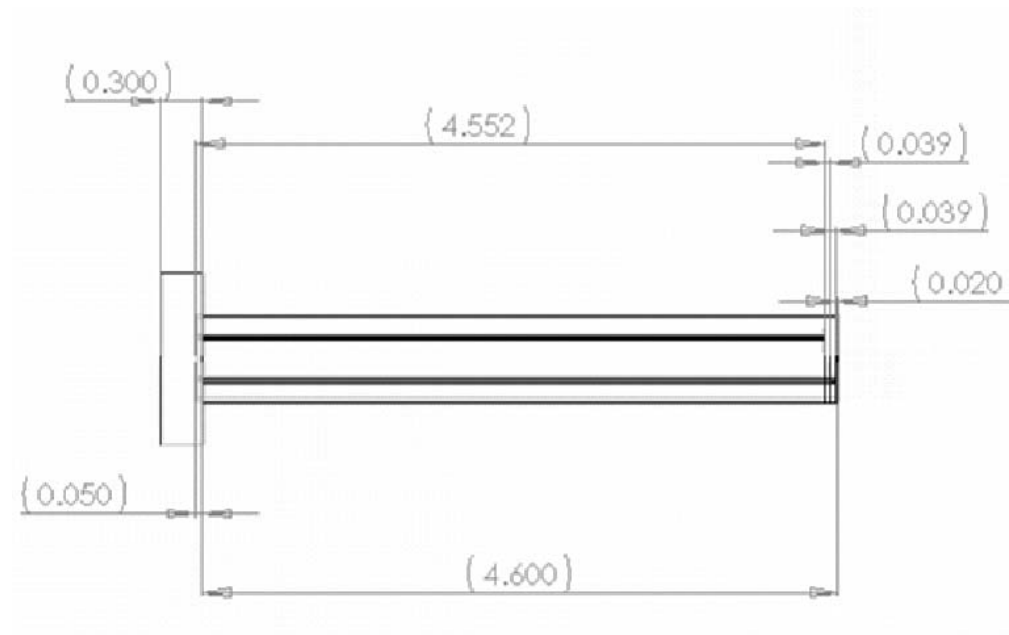**Figure C13: Sump for Test Chamber — Side View**

Figure C14: Pedestal for Test Chamber — Side View
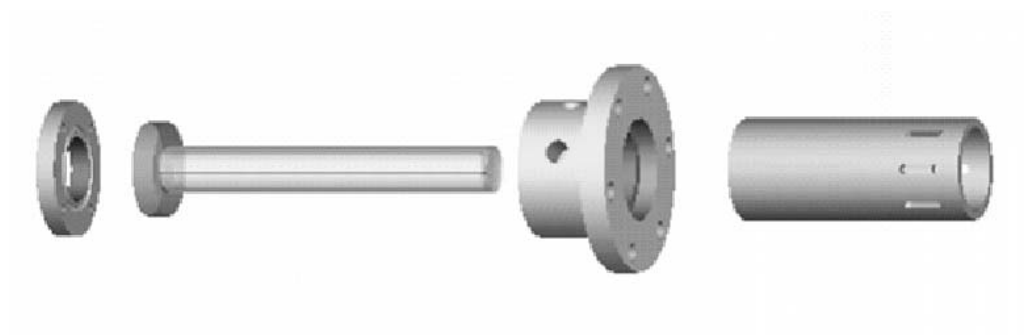
62

Figure C15: Exploded View of Sump
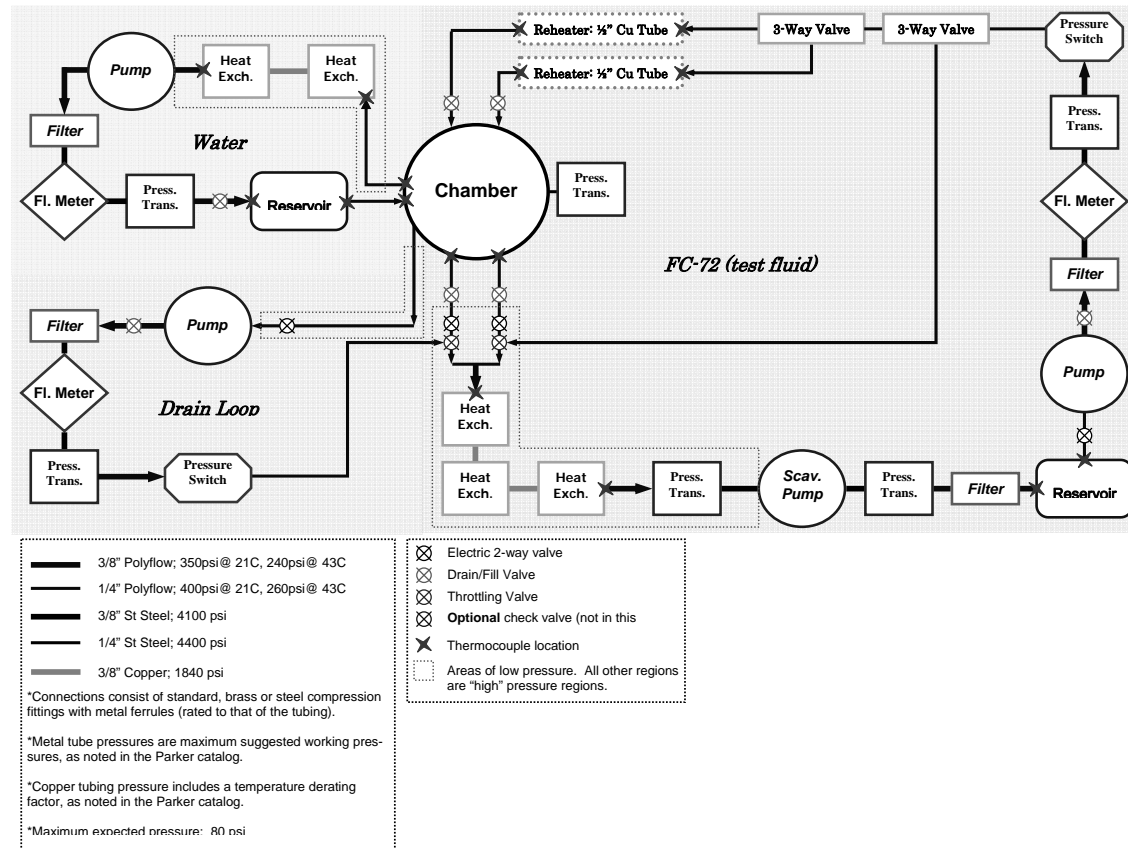
Figure C16: Flow Schematic

Appendix D: Pressure Certification

Results from the pneum atic tests will be pres ented at or prior to the Test Readin ess Re-view.

The requirements and planned test pressure are in the following table:

Components	Maximum Working Pressure	Planned Pneumatic Test Pressure
Test chamber	100 psiA	132 psiG
FC-72 Nozzle inlet (high pressure side of FC-72 flow system)	100 psiA	132 psiG
Water flow components	75 psiA	111 psiG

65

Appendix E: Material Safety Data Sheet

66

3M

Material Safety Data Sheet

SECTION 1: PRODUCT AND COMPANY IDENTIFICATION

PRODUCT NAME: FC-72 FLUORINERT Brand Electronic Liquid
MANUFACTURER: 3M
DIVISION: 3M Specialty Materials

ADDRESS: 3M Center
St. Paul, MN 55144-1000

EMERGENCY PHONE: 1-800-364-3577 or (651) 737-6501 (24 hours)

Issue Date: 09/05/2002
Supercedes Date: 01/24/2001

Document Group: 10-3789-4

Product Use:
Intended Use: For industrial use only. Not intended for use as a medical device or drug.
Specific Use: Testing Fluid or Heat Transfer Fluid for Electronics.

SECTION 2: INGREDIENTS

Ingredient	C.A.S. No.	% by Wt
PERFLUORO COMPOUNDS, (PRIMARILY COMPOUNDS WITH 6 CARBONS)	86508-42-1	100

SECTION 3: HAZARDS IDENTIFICATION

3.1 EMERGENCY OVERVIEW

Specific Physical Form: Liquid
Odor, Color, Grade: Colorless, odorless liquid.
General Physical Form: Liquid
Immediate health, physical, and environmental hazards: None known.

3.2 POTENTIAL HEALTH EFFECTS

196

Eye Contact:
Contact with the eyes during product use is not expected to result in significant irritation.

Skin Contact:
Contact with the skin during product use is not expected to result in significant irritation.

Inhalation:
No health effects are expected.

Ingestion:
No health effects are expected.

3.3   POTENTIAL ENVIRONMENTAL EFFECTS

This compound is completely fluorinated (perfluorinated), or it contains perfluorinated portions. Perfluoroalkyl groups resist degradation in most natural environments. This low-solubility substance has insignificant toxicity to aquatic organisms (Lowest LL50 or EL50 is >1000 mg/L). LL50 (Lethal Level) and EL50 are similar to LC50 and EC50, but tests the water phase from incompletely-miscible mixtures. Take precautions to prevent direct release of this substance to the environment.

ATMOSPHERIC FATE:
Perfluoro compounds (PFCs) are photochemically stable and expected to persist in the atmosphere for more than 1000 years. PFCs have high global warming potentials (GWP), exceeding 5000 (100-yr-ITH). The Ozone Depletion Potential (ODP) is Zero.

SECTION 4: FIRST AID MEASURES

4.1   FIRST AID PROCEDURES

The following first aid recommendations are based on an assumption that appropriate personal and industrial hygiene practices are followed.

Eye Contact: Flush eyes with large amounts of water. If signs/symptoms persist, get medical attention.

Skin Contact: Wash affected area with soap and water. If signs/symptoms develop, get medical attention.

Inhalation: If signs/symptoms develop, remove person to fresh air.   If signs/symptoms develop, get medical attention.

If Swallowed: No need for first aid is anticipated.

SECTION 5: FIRE FIGHTING MEASURES

5.1   FLAMMABLE PROPERTIES

Autoignition temperature	*Not Applicable*
Flash Point	*Not Applicable*
Flammable Limits - LEL	Nonflammable
Flammable Limits - UEL	Nonflammable

197

5.2 EXTINGUISHING MEDIA
Material will not burn.

5.3 PROTECTION OF FIRE FIGHTERS

Special Fire Fighting Procedures: Wear full protective clothing, including helmet, self-contained, positive pressure or pressure demand breathing apparatus, bunker coat and pants, bands around arms, waist and legs, face mask, and protective covering for exposed areas of the head. Water may be used to blanket the fire. Exposure to extreme heat can give rise to thermal decomposition.

Unusual Fire and Explosion Hazards: No unusual fire or explosion hazards are anticipated. No unusual effects are anticipated during fire extinguishing operations. Avoid breathing the products and substances that may result from the thermal decomposition of the product or the other substances in the fire zone. Keep containers cool with water spray when exposed to fire to avoid rupture.

> **Note: See STABILITY AND REACTIVITY (SECTION 10) for hazardous combustion and thermal decomposition information.**

SECTION 6: ACCIDENTAL RELEASE MEASURES

Accidental Release Measures: Observe precautions from other sections. Call 3M- HELPS line (1-800-364-3577) for more information on handling and managing the spill. Evacuate unprotected and untrained personnel from hazard area. The spill should be cleaned up by qualified personnel. Ventilate the area with fresh air. Contain spill. Working from around the edges of the spill inward, cover with bentonite, vermiculite, or commercially available inorganic absorbent material. Mix in sufficient absorbent until it appears dry. Collect as much of the spilled material as possible. Clean up residue with an appropriate organic solvent. Read and follow safety precautions on the solvent label and MSDS. Place in a metal container approved for transportation by appropriate authorities. Seal the container. Dispose of collected material as soon as possible.

> **In the event of a release of this material, the user should determine if the release qualifies as reportable according to local, state, and federal regulations.**

SECTION 7: HANDLING AND STORAGE

7.1 HANDLING
Avoid skin contact with hot material. For industrial or professional use only. No smoking: Smoking while using this product can result in contamination of the tobacco and/or smoke and lead to the formation of the hazardous decomposition products mentioned in the Reactivity Data section of this MSDS. Store work clothes separately from other clothing, food and tobacco products. Use general dilution ventilation and/or local exhaust ventilation to control airborne exposures to below Occupational Exposure Limits. If ventilation is not adequate, use respiratory protection equipment.

7.2 STORAGE
Store away from heat. Keep container tightly closed. Keep container in well-ventilated area.

SECTION 8: EXPOSURE CONTROLS/PERSONAL PROTECTION

8.1 ENGINEERING CONTROLS
Provide appropriate local exhaust when product is heated. Provide appropriate local exhaust ventilation on open containers. For those situations where the fluid might be exposed to extreme overheating due to misuse or equipment failure, use with appropriate local exhaust ventilation sufficient to maintain levels of thermal decomposition products below their exposure guidelines.

69

8.2 PERSONAL PROTECTIVE EQUIPMENT (PPE)

8.2.1 Eye/Face Protection
Avoid eye contact.
The following eye protection(s) are recommended: Safety Glasses with side shields.

8.2.2 Skin Protection
Avoid skin contact with hot material. Wear appropriate gloves, such as Nomex, when handling this material to prevent thermal burns.
Avoid skin contact.
Select and use gloves and/or protective clothing to prevent skin contact based on the results of an exposure assessment. Consult with your glove and/or protective clothing manufacturer for selection of appropriate compatible materials.
Gloves made from the following material(s) are recommended: Nitrile Rubber.

8.2.3 Respiratory Protection
Under normal use conditions, airborne exposures are not expected to be significant enough to require respiratory protection. Avoid breathing of vapors, mists or spray.
Select one of the following NIOSH approved respirators based on airborne concentration of contaminants and in accordance with OSHA regulations: Half facepiece or fullface air-purifying respirator with organic vapor cartridges. Consult the current 3M Respiratory Selection Guide for additional information or call 1-800-243-4630 for 3M technical assistance. If thermal degradation products are expected, use fullface supplied air respirator.

8.2.4 Prevention of Swallowing
 Do not eat, drink or smoke when using this product. Wash exposed areas thoroughly with soap and water.

8.3 EXPOSURE GUIDELINES

None Established

SECTION 9: PHYSICAL AND CHEMICAL PROPERTIES

Specific Physical Form:	Liquid
Odor, Color, Grade:	Colorless, odorless liquid.
General Physical Form:	Liquid
Autoignition temperature	*Not Applicable*
Flash Point	*Not Applicable*
Flammable Limits - LEL	Nonflammable
Flammable Limits - UEL	Nonflammable
Boiling point	50 - 60 ºC
Density	1.7 g/ml
Vapor Density	Approximately 11.7 [@ 20 ºC] [*Ref Std:* AIR=1]
Vapor Pressure	Approximately 232 mmHg [@ 20 ºC]
Specific Gravity	Approximately 1.7 [*Ref Std:* WATER=1]
pH	*Not Applicable*
Melting point	*Not Applicable*
Solubility in Water	Nil
Evaporation rate	> 1 [*Ref Std:* BUOAC=1]
Volatile Organic Compounds	Exempt
Percent volatile	Approximately 100 %
VOC Less H2O & Exempt Solvents	Exempt
Viscosity	Approximately 0.42 centistoke [@ 20 ºC]

_____Page 4 of 8

199

SECTION 10: STABILITY AND REACTIVITY

Stability: Stable.

Materials and Conditions to Avoid: Finely divided active metals; Alkali and alkaline earth metals; Heat(greater than 200 °C)

Hazardous Polymerization: Hazardous polymerization will not occur.

Hazardous Decomposition or By-Products

Substance	Condition
Hydrogen Fluoride	At Elevated Temperatures - greater than 200 °C
Perfluoroisobutylene (PFIB)	At Elevated Temperatures - greater than 200 °C

Hazardous Decomposition: If the product is exposed to extreme condition of heat from misuse or equipment failure, toxic decomposition products that include hydrogen fluoride and perfluoroisobutylene can occur.

Hydrogen fluoride (CAS No. 7664-39-3) has an ACGIH Threshold Limit Value - Ceiling of 3 ppm (as fluoride), an OSHA Permissible Exposure Limit - Time Weighted Average of 3 ppm (as fluoride) and a revoked OSHA Permissible Exposure Limit - Short Term Exposure Limit (which is enforced by some State Right-To-Know programs) of 6 ppm (as fluoride). Hydrogen fluoride may cause respiratory tract irritation, dental or skeletal fluorosis and irritation or burns to the eyes or skin, particularly when dissolved in water (hydrofluoric acid). The odor threshold for HF is 0.04 ppm, providing good warning properties for exposure.

Perfluoroisobutylene(CAS No. 382-21-8) has an ACGIH Threshold Limit Value - Ceiling of 0.01 ppm. Perfluoroisobutylene may cause respiratory tract irritation, pulmonary edema, cyanosis, and effect on the hematopoietic system.

SECTION 11: TOXICOLOGICAL INFORMATION

Product-Based Toxicology Information:

A Material Toxicity Summary Sheet (MTSS) has been developed for this product. Please contact the address listed on the first page of this MSDS to obtain a copy of the MTSS for this product.

> Please contact the address listed on the first page of the MSDS for Toxicological Information on this material and/or its components.

SECTION 12: ECOLOGICAL INFORMATION

ECOTOXICOLOGICAL INFORMATION

Test Organism	Test Type	Result
Fathead Minnow, Pimephales promelas	96 hours Lethal Concentration 50%	>1000 mg/l
Water flea, Daphnia magna	48 hours Effect Concentration 50%	>1500 mg/l

CHEMICAL FATE INFORMATION

Test Type	Result	Protocol
20 days Biological Oxygen Demand	Nil	
Chemical Oxygen Demand	Nil	

SECTION 13: DISPOSAL CONSIDERATIONS

Waste Disposal Method: Reclaim if feasible. As a disposal alternative, incinerate in an industrial or commercial facility in the presence of a combustible material. Combustion products will include HF. Facility must be capable of handling halogenated materials. To reclaim or return, check product label for contact.

EPA Hazardous Waste Number (RCRA): Not regulated

Since regulations vary, consult applicable regulations or authorities before disposal.

SECTION 14:TRANSPORT INFORMATION

ID Number(s):
98-0211-0216-9, 98-0211-0217-7, 98-0211-0267-2, 98-0211-1795-1, 98-0211-8068-6, 98-0212-2992-1, ZF-0002-0305-7, ZF-0002-0321-4, ZF-0002-0354-5, ZF-0002-0802-3, ZF-0002-1162-1

Please contact the emergency numbers listed on the first page of the MSDS for Transportation Information for this material.

SECTION 15: REGULATORY INFORMATION

US FEDERAL REGULATIONS

Contact 3M for more information.

311/312 Hazard Categories:
Fire Hazard - No   Pressure Hazard - No   Reactivity Hazard - No   Immediate Hazard - No   Delayed Hazard - No

STATE REGULATIONS

Contact 3M for more information.

CHEMICAL INVENTORIES

The components of this product are in compliance with the chemical notification requirements of TSCA.

All applicable chemical ingredients in this material are listed on the European Inventory of Existing Chemical Substances (EINECS),

Page 6 of 8

201

or are exempt polymers whose monomers are listed on EINECS.

The components of this product are listed on the Canadian Domestic Substances List.

The components of this product are listed on the Australian Inventory of Chemical Substances.

The components of this product are listed on Japan's Chemical Substance Control Law List (also known as the Existing and New Chemical Substances List.)

Contact 3M for more information.

INTERNATIONAL REGULATIONS

Contact 3M for more information.

This MSDS has been prepared to meet the U.S. OSHA Hazard Communication Standard, 29 CFR 1910.1200.

SECTION 16: OTHER INFORMATION

NFPA Hazard Classification
    Health: 3   **Flammability:** 0   **Reactivity:** 0   **Special Hazards:** None

National Fire Protection Association Hazard Codes are designed for use by firefighters, sheriffs, or other emergency response teams who are concerned with the hazards of materials under emergency conditions. These NFPA codes are intended to include the hazards of the products of decomposition or combustion in a fire situation.

HMIS Hazard Classification
    Health: 0   **Flammability:** 0   **Reactivity:** 0   **Protection:** X - See PPE section.
Hazardous Material Identification System (HMIS(r)) hazard ratings are designed to inform employees of chemical hazards in the workplace. These ratings are based on the inherent properties of the material under expected conditions of normal use and are not intended for use in emergency situations. HMIS(r) ratings are to be used with a fully implemented HMIS(r) program. HMIS(r) is a registered mark of the National Paint and Coatings Association (NPCA).

No revision information is available.

DISCLAIMER: The information in this Material Safety Data Sheet (MSDS) is believed to be correct as of the date issued. 3M MAKES NO WARRANTIES, EXPRESSED OR IMPLIED, INCLUDING, BUT NOT LIMITED TO, ANY IMPLIED WARRANTY OF MERCHANTABILITY OR FITNESS FOR A PARTICULAR PURPOSE OR COURSE OF PERFORMANCE OR USAGE OF TRADE. User is responsible for determining whether the 3M product is fit for a particular purpose and suitable for user's method of use or application. Given the variety of factors that can affect the use and application of a 3M product, some of which are uniquely within the user's knowledge and control, it is essential that the user evaluate the 3M product to determine whether it is fit for a particular purpose and suitable for user's method of use or application.

3M provides information in electronic form as a service to its customers. Due to the remote possibility that electronic transfer may have resulted in errors, omissions or alterations in this information, 3M makes no representations as to its completeness or accuracy. In addition, information obtained from a database may not be as current as the information in the MSDS available directly from 3M.

3M MSDSs are available at www.3M.com

203